Multiscale modelling of conjugated polymers for use in energy applications.

Drew Pearce

Department of Physics,

Imperial College London

This thesis is submitted for the degree of

Doctor of Philosophy

Declaration

All work in this thesis, unless otherwise stated and appropriately cited, is my own work undertaken between 2014 and 2019.

Copyright declaration

The copyright of this thesis rests with the author and is made available under a Creative Commons Attribution Non-Commercial No Derivatives licence. Researchers are free to copy, distribute or transmit the thesis on the condition that they attribute it, that they do not use it for commercial purposes and that they do not alter, transform or build upon it. For any reuse or redistribution, researchers must make clear to others the licence terms of this work.

Abstract

Organic materials offer unique advantages to improve the sustainability of applications within many realms of technology. In this work I use a range of computational methods for modelling materials to investigate systems within the application space of energy materials. I specifically investigate a class of emerging linear conjugated polymers for use as photocatalysts for water splitting, and molecular dynamics is used to identify solvation as a key explanation for differing hydrogen evolution rates. I then proceed to uncover the role solvation plays in the stabilisation of the hydrogen evolution reaction, finding that the first charge separation becomes energetically favourable as the polarity of the medium increases. In addition to this I investigate polymers in solution that have been explored for applications in which charge transport is important (such as OFETs and OPV). I also look at how chemical structure impacts the conformation in solvent and how that correlates to device level performance.

Acknowledgements

A PhD is a long and complex process and as such there are many people to whom I owe my thanks as without them I could not have completed it.

First and foremost my supervisor, Jenny. It usually goes without saying that a PhD would not be possible without the PhD supervisor but Jenny has consistently gone above and beyond to look after me both academically and personally throughout. I am hugely grateful for her support and mentorship, and its impact on my work and personal development.

I must also thank Anne for her help and support during the PhD, particularly helping with and sharing some of the computational difficulties and frustrations that arose from this work. My work is heavily computational and I have relied on the experience and skill of all those who maintain and run the high performance computing systems at Imperial; for all these people I am incredibly grateful.

Throughout my time at Imperial there have been many people who have passed through the Jenny Nelson group who have made my time there enjoyable and have always provided a mixture of technical advice, personal support, or just a friendly chat. In particular, Alise, Beth, Jarv, Michelle, Sam and Xingyuan.

I would also like to thank all the members of TSM Cohort 5 who came along on this journey with me. Of particular note are Andy, Beth, Farnaz and Freda who have been close and supportive friends, always there for both advice and distraction when it was needed (and sometimes when it wasn't).

My sincere thanks also to Nicolas Harrison and Denis Andrienko for taking the time to read and examine this thesis, and for all of their insights and suggestions that made this work stronger and clearer.

To my Mum, Dad and family I would also like to say thank you for all the love and support you have provided me both throughout my PhD and before.

Of course I can go no further without acknowledging Laura. One of the few people to have

read my thesis multiple times, including from a hospital bed. From learning elements of LaTeX in order to help correct my section references, to the hours of proof reading, you have done so much to encourage and support me. Outside of work you have never failed to bring joy and happiness into my life. I am yours, always.

Finally, I would like to thank all those people whose names I do not and will never know, whose silent kindness and dedication enables others to succeed and thrive, and who so often go unrecognised.

1 Introduction **1**

1.1 New Challenges: The need for new materials 1

1.2 New Materials: Functional Organic Materials 3

1.3 New Methods: Multiscale Modelling for computational design of materials for devices 4

1.4 Overview of Thesis 5

2 Theoretical Background **7**

2.1 Organic Materials: Conjugated Polymers 7

2.1.1 Polymers 12

2.1.2 Electronic Structure of Organic Materials 13

2.1.3 Generation and Recombination of Excitations 16

2.1.4 Microstructure of Polymer systems 19

2.1.5 Polyfluroene 21

2.2 Photocatalyic Water Splitting 21

2.2.1 Fundamentals of Water Splitting 21

2.2.1.1 Measuring Device Performance 23

2.2.2 Metal Oxide Systems 24

2.2.3 Organic Photocatalyst Systems 25

2.2.3.1 Carbon Nitride Systems 25

2.2.3.2 Other Organic Systems 26

3 Methods of Computational Materials **29**

3.1 *Ab initio* Methods 29

3.1.1 Quantum Theory 29

3.1.2 Hartree-Fock 30

3.1.3 Density Functional Theory 32

3.1.3.1 Exchange-Correlation Approximations 33

3.1.4 Limitations 38

3.2 Atomistic Molecular Dynamics 38

3.2.1 Nuts and Bolts of MD 39

3.2.2 Force Field Design and Optimisation 40

3.2.2.1 OPLS 41

3.2.2.2 Ensembles 42

3.2.3 Computational Implementation 43

3.2.3.1 Periodic Boundary Conditions . . . 43
3.2.3.2 Interaction Cut-Offs . . . 44
3.2.3.3 Numerical Integrator . . . 45
3.2.3.4 Constraints . . . 46
3.2.3.5 Thermostats and Barostats . . . 46
3.2.4 Analysis Tools . . . 49
3.2.4.1 Radial Distribution Function . . . 49
3.2.4.2 Radius of Gyration . . . 50
3.2.4.3 Free Energy Calculations . . . 50
3.2.5 Procedures . . . 50
3.2.6 Limitations . . . 52
3.3 Summary . . . 52

4 MD of Solvent Systems 55
4.1 Introduction . . . 55
4.2 Force Field Choice and Development . . . 55
4.3 Single Phase Solvent Solutions . . . 61
4.3.1 Water . . . 61
4.3.2 TEA . . . 63
4.3.3 Methanol . . . 65
4.3.4 Chloroform . . . 66
4.3.5 Decalin . . . 68
4.4 Two-phase Solvent Solutions . . . 70
4.4.1 Water-Methanol . . . 71
4.4.2 TEA-Methanol . . . 74
4.4.3 Water-TEA . . . 76
4.4.4 Conclusions: Metrics of Solubility in MD . . . 79
4.5 Three-phase Solvent Solutions: Reaction Mixture . . . 79
4.6 Conclusions . . . 81

5 Behaviour of Oligomers in Solution 83
5.1 Introduction . . . 83
5.1.1 Experimental Context . . . 84
5.2 Force field Development . . . 87
5.2.1 Solvents . . . 87

5.2.2 Polyfluorene . . . 87
5.2.3 IDTBT . . . 92
5.3 Conformational Behaviour of Isolated Oligomers . . . 93
5.3.1 Persistence Length . . . 96
5.4 Using Molecular Dynamics to understand Beta Phase in PFO . . . 102
5.4.1 Beta Phase Simulations . . . 102
5.4.2 Free Energy of Planarisation . . . 103
5.5 Conclusions . . . 104

6 MD of conjugated polymer photocatalysts 107
6.1 Introduction: Differential Hydrogen Evolution . . . 107
6.2 Systems of Study . . . 108
6.3 Investigating differential hydrogen evolution . . . 110
6.3.1 Electronic Structure . . . 110
6.3.2 Exciton Lifetimes and Particle Sizes . . . 111
6.3.3 Differential Co-catalyst amounts . . . 115
6.3.4 Absorption Spectra . . . 116
6.4 Molecular Dynamics of Solvation . . . 119
6.4.1 Introduction and Choice of Method . . . 119
6.4.2 Force Field Development of Polymers . . . 120
6.4.2.1 Overview . . . 120
6.4.2.2 Data for Force Fields . . . 121
6.4.2.3 Final Force Fields . . . 126
6.4.3 Results: Single Oligomers in Solution . . . 131
6.4.3.1 Water-TEA . . . 131
6.4.3.2 Reaction Mixture . . . 133
6.5 Towards Aggregates: Multiple Oligomers in Solution . . . 136
6.5.1 Introduction . . . 136
6.5.2 Solvation Environments of Bi-Oligomer Aggregates . . . 136
6.6 Conclusions . . . 141

7 Hydrogen Evolution Pathway 143
7.1 Introduction . . . 143
7.2 Triethylamine: Hydrogen evolution pathway . . . 144
7.2.1 DFT calculations of driving forces in TEA pathway . . . 147

7.3 Test of dependence on level of theory . . . 151
7.4 Trial Set of Polymers . . . 155
7.4.1 Introduction . . . 155
7.4.2 Outline of Set . . . 155
7.4.3 Comparing DFT driving forces with HER performance . . . 156
7.4.4 Quantifying Local Environment with Molecular Dynamics . . . 158
7.4.5 Driving Forces in Multi-Phasic Environment . . . 166
7.4.5.1 Polarity of Binary Mixtures . . . 167
7.4.5.2 Results . . . 168
7.5 Ternary Enviroments: Full Reaction Mixture Model . . . 169
7.5.1 Molecular Dynamics . . . 170
7.6 Summary . . . 176

8 Conclusions and Future Work 179
8.1 Conclusions . . . 179
8.2 Future Work . . . 180

1.1 This schematic shows a summary of the different methods used in materials research problems in the literature. The common scales accessible by each of the techniques are shown and are a function of the amount of readily available computational power. 4

2.1 This figure shows the s and p_x, p_y, p_z and orbitals and the sp^2 hybridised molecular orbitals that play such a crucial role in organic materials, particularly conjugated ones. 9

2.2 This figure shows how a combination of the p_z and sp^2 orbitals combine to form σ and π bonds in conjugated materials. In this case an ethene is shown. 9

2.3 This figure shows a selection of commonly used and studied conjugated organic materials. (a) shows Polyfluorene (PFO) (b) shows Poly(3-hexylthiophene-2,5-diyl), P3HT, (c) shows indacenodithiophene-co-benzothiadiazole (IDTBT), (d) shows a C60 buckminsterfullerene, (e) shows Perylene diimide (f) shows Pentacene. (a), (b) and (c) are classified as polymers where as (d), (e), and (f) are classified as small molecules. Purple atoms show points for sidechains to be attached. 11

2.4 This figure shows the different type of excitation in organic materials: (a) shows excitons, (b) shows polarons, and (c) shows bi-polarons. As shown polarons (and bi-polarons) exist for both positive and negative charge. From [1]. 15

2.5 A figure showing how the ground state total energy of a system varies as a nuclear coordinate is changed, in this case the inter-monomer torsion. The nuclear coordinate is shown in (a) and the potential energy surface in (b). 16

2.6 This diagram shows a Jablonski diagram. It shows the ground state, a singlet state labelled S_0, the first and second singlet excited states, S_1 and S_2, and the first triplet excited state T_1. For each state there exists a number of closely ($\backsim 0.1$eV) spaced energy levels corresponding to different vibrational modes. Different types of radiative and non radiative decays are shown. 19

2.7 This figure, from [2], shows different microstructures for semiconducting polymer systems with (a) semi-crystalline, (b) weakly ordered and (c) completely amorphous character. Large scale crystallinity is not vital for charge transport but a minimal amount of aggregation is. Transport pathways are highlighted in red. 20

2.8 This figure shows the ideal experimental set-up of a single system in (a) and two system in (b) with a photocatalyst (and most likely a co-catatlyst) immersed in water and overall water splitting occuring. (c) shows a basic schematic of the reaction that would be taking place in the absence of a co-catalyst; when a co-catalyst is used the oxidation and/or the reduction occurs at the surface of it with the main catalyst acting as the photo-absorber. 22

2.9 This figure shows the experimental set-up when hydrogen evolution is investigated using a Sacrificial Electron Donor that absorbs the charge and goes on to break down into products. One key difference is that the reaction occurs in a mixture of water and SED (and sometimes additional mixing agents) which will affect the Ph and polarity. 24

3.1 This depicts the chemical understanding of levels of theory, based on that of Perdew [3], and its relation to the ideal "heaven" of chemical accuracy. Larger rungs represent different levels of DFT. We carry out our entire study around the fourth main rung and do this because of the complex nature of what we want to investigate. Smaller rungs represent improvements within that DFT treatment such as more complete basis sets or functionals that contain long-range corrections. 37

3.2 A diagrammatic representation of the atom-atom interactions in MD that must be specified in what is known as a force field. 40

3.3 This schematic shows the procedure for generating production molecular dynamics trajectories for (a) systems of solvents only and (b) systems of oligomers and solvents. In (b) a convergence test is used to ensure that energy is conserved and the dihedral autocorrelations have reduced to zero. In some simulations, particularly persistence length calculations, would typically need longer than 5ns of equilibriation (~15-20ns). 51

4.1 This figure outlines the force field used, from [4], for Triethylamine. a) shows the labelling scheme used, b) the partial charges, q, and Van der Waals parameters (σ, ε) for each atom, c) the bond equilibrium distance r_0 and spring constant k_r and d) the equilibrium angle (θ_0) and spring constant (k_θ) and dihedral Fourier parameters (V_1,V_2,V_3). 56

4.2 This figure outlines the TIP4P OPLS forcefield[5]. a) shows the labelling scheme used, b) the partial charges, q, and Van der Waals parameters (σ, ε) for each atom, c) the bond equilibrium distance r_0 and spring constant k_r and d) the equilibrium angle (θ_0) and spring constant (k_θ) and dihedral Fourier parameters (V_1,V_2,V_3). M is a virtual site whose position is held constant at 0.015nm away from the oxygen atom in the same direction as the two hydrogens. 57

4.3 This figure outlines the force field used, from [6], for methanol. a) shows the labelling scheme used, b) the partial charges, q, and Van der Waals parameters (σ, ε) for each atom, c) the bond equilibrium distance r_0 and spring constant k_r and d) the equilibrium angle (θ_0) and spring constant (k_θ) and dihedral Fourier parameters (V_1,V_2,V_3). 58

4.4 This figure outlines the OPLS force field for cis-decalin. a) shows the labelling scheme used, b) the partial charges, q, and Van der Waals parameters (σ, ε) for each atom, c) the bond equilibrium distance r_0 and spring constant k_r and d) the equilibrium angle (θ_0) and spring constant (k_θ) and (e) dihedral Fourier parameters (V_1,V_2,V_3). 59

4.5 This figure outlines the OPLS force field for trans-decalin. a) shows the labelling scheme used, b) the partial charges, q, and Van der Waals parameters (σ, ε) for each atom, c) the bond equilibrium distance r_0 and spring constant k_r and d) the equilibrium angle (θ_0) and spring constant (k_θ) and dihedral Fourier parameters (V_1,V_2,V_3). 60

4.6 This figure outlines the OPLS force field for chloroform[7]. a) shows the labelling scheme used, b) the partial charges, q, and Van der Waals parameters (σ, ε) for each atom, c) the bond equilibrium distance r_0 and spring constant k_r and d) the equilibrium angle (θ_0) and spring constant (k_θ) and dihedral Fourier parameters (V_1,V_2,V_3). 61

4.7 (a) shows the final state of the box of 686 water molecules, shown as Van der Waals Spheres, and a comparison between experimental RDFs[8] and MD RDFs for (b) oxygen-oxygen interactions, (c) oxygen-hydrogen interactions and (d) hydrogen-hydrogen interactions. 63

4.8 (a) shows the final state of the box of 277 TEA molecules, shown as Van der Waals Spheres and MD RDFs for (b) carbon-carbon interactions, (c) nitrogen-nitrogen interactions and (d) hydrogen-hydrogen interactions. 64

4.9 (a) shows the final state of the box of 402 methanol molecules, shown as Van der Waals Spheres, and a comparison between experimental RDFs[9] and MD RDFs for (b) carbon-carbon interactions, (c) oxygen-oxygen interactions and (d) non-methyl-hydrogen-non-methyl-hydrogen interactions. 66

4.10 (a) shows the final state of the box of 203 chloroform molecules, shown as Van der Waals Spheres, and a comparison between experimental RDFs[10] and MD RDFs for (b) carbon-carbon interactions, (c) chlorine-chlorine interactions and (d) hydrogen-hydrogen interactions. 68

4.11 This figure shows the final state of the box of 402 decalin molecules, shown as Van der Waals Spheres coloured by atom in (a) and according to whether it is cis or trans in (b), and MD RDFs for (c) trans-cis interactions and (d) cis-cis and trans-trans interactions. 69

4.12 This figure shows snapshots of the MD simulations of water with methanol at (a) 1.87% (b) 4.66% (c) 7.65% (d) 9.32% (e) 18.54% (f) 33.33% (g) 50.00% by volume concentration in water. The average number of clusters per methanol molecule at each concentration is shown in (h). 72

4.13 (a) shows the final state of the box with 1:1 water:methanol by volume, shown as Van der Waals Spheres, and MD RDFs for (b) methanol-water interactions, (c) carbon-oxygen interactions and (d) methyl-oxygen-water-oxygen interactions. Water is shown as red and methanol as orange. 73

4.14 This figure shows snapshots of the MD simulations of TEA in methanol at (a) 1.87% (b) 4.66% (c) 7.65% (d) 9.32%(e) 18.54% (f) 33.33% (g) 50.00% by volume concentration in water. The average number of clusters per methanol molecule at each concentration is shown in (h). 75

4.15 This figure shows snapshots of the MD simulations of TEA in water at (a) 1.87% (b) 4.66% (c) 7.65% (d) 9.32% (e) 18.54% (f) 33.33% (g) 50.00% by volume concentration in water. The average number of clusters per TEA molecule at each concentration is shown in (h). 77

4.16 This figure shows the molecular dynamics simulation of a box of water and TEA with 1:1 concentration by volume, a snapshot of the final system is shown in (a), and radial distribution functions between the centre of masses of (b) TEA and water (c) TEA and TEA (d) water and water are shown. 78

4.17 This figure shows the very different behaviour of three binary mixtures: TEA in water (blue), TEA in methanol (red) and methanol in water (cyan) which are understood to have limited solubility, good solubility and full miscibility respectively. 79

4.18 This figure shows (a) a snapshot of the MD simulation of a ternary mixture of water (red), methanol (orange) and TEA (blue) at equal volumes, and RDFs from the centre of mass of TEA to the centre of mass of (b) water (c) methanol and (d) TEA. 80

4.19 This shows a comparison of the RDFs between water and TEA between the systems with and without methanol and at two concentrations of TEA in water to make comparisons easier to see. 81

5.1 This figure displays the backbone structure of the polymers we consider in this chapter, namely (a) PFO and (b) IDTBT. Purple Atoms represent positions where sidechains are added. 84

5.2 Two different conformations of the PFO chain, α and β-phase. Taken as snapshots from MD simulations. The relevant dihedral is highlighted (blue) showing it must be $180°$ in the β-phase. Sidechains are not shown. Below each are absorption (PL) measurements of the different phases showing the experimentally probe-able conformational markers[11]. 85

5.3 This figure shows the different parts of β-phase formation and the two paths in solution that can be taken depending on whether aggregation or planarisation occurs first. How these factors influence each other is a source of much discussion. 86

5.4 Figure showing a) charges, b) inter-monomer torsion 88

5.5 PFO backbone force field. a) nomenclature used. b) atom types, partial charges and Van der Waals parameters. c) shows bond, angle and proper dihedral parameters where X,Y,Z represent all C-C-H angles. i,j,k,l represent all intra-monomer C-C-C-H/C-C-C-C angles. d) shows the improper dihedrals which are added to account for planar stiffness due to conjugation. R represents the sidechain of choice and the parameters are outlined separately in Figures 5.6 and 5.7. 89

5.6 Octyl (and 16 by extending the number of C3s) sidechain force field. a) nomenclature used. b) atom types, partial charges and Van der Waals parameters. c) shows bond, angle and proper dihedral parameters where X,Y,Z represent all C-C-H angles. i,j,k,l represent all intra-monomer C-C-C-H angles. 90

5.7 Ethylhexyl sidechain force field. a) nomenclature used. b) atom types, partial charges and Van der Waals parameters. c) shows bond, angle and proper dihedral parameters where X,Y,Z represent all C-C-H angles. i,j,k,l represent all intra-monomer C-C-C-H/C-C-C-C angles. d) shows the improper dihedrals which are added to account for planar stiffness due to conjugation. 91

5.8 Polyethylene Glycol sidechain, commonly called PEG force field used in Section 7.4.4. a) nomenclature used. b) atom types, partial charges and Van der Waals parameters. c) shows bond, angle and proper dihedral parameters where X,Y,Z represent generic sequential carbons (e.g. 1,2,3 or 4,5,6). 92

5.9 This figure shows snapshots of polyflourene with octyl (C_8H_{17}) sidechains in (a) chloroform, (b) a mixture of cis- and trans-decalin and (c) water. 93

5.10 This figure shows snapshots of polyflourene with hexadecyl (C_16H_{33}) sidechains in (a) chloroform, (b) a mixture of cis- and trans-decalin and (c) water. 94

5.11 This figure shows snapshots of polyflourene with ethylhexyl ($C_2H_7(C_6H_{13})$) sidechains in (a) chloroform, (b) a mixture of cis- and trans-decalin and (c) water. 94

5.12 This plot shows the calculated free energy of solvation values for PFO in each of the solvents and how poor solvation corresponds with a decrease in the radius of gyration. 96

5.12 These plots show the results of the correlation function of monomer angles and the resultant fit used to determine the MD stiffness measure for PFO with (a), (b), (c): octyl sidechains, (d), (e), (f): ethylhexyl sidechains and (g), (h), (i): hexadecyl sidechains in (a), (d), (g): decalin, (b), (e), (h): chloroform and (c), (f) and (i): water. 99

5.13 These plots show the results of the correlation function of monomer angles and the resultant fit used to determine the MD stiffness measure for IDTBT, from [12] with (a), (b): ethylhexyl sidechains and (c), (d): hexadecyl sidechains in (a), (c): chloroform and (b), (d): water 100

5.14 This figure shows snapshots from MD where PFO has been simulated in decalin with (a) no intermonomer dihedral restraints and (b) dihedral restraints that force PFO to planarise its backbone in a manner similar to the solid state beta-phase conformation. 102

5.15 This figure shows representative angle probability distributions of the intermonomer dihedral of an octomer in chloroform. We can see that when not forced to be planar it samples the minima of the torsional potential. 103

6.1 This figure shows the chemical structures of all the polymers considered experimentally, P1, P7, P10 and FSM. The latter was less well studied experimentally but is included for the computational study. 108

6.2 This figure summarises the experimental observations from [13] and [14], namely that (i) P7 and P10 evolve hydrogen whilst P1 does not and (ii) that this evolution correlates to a TAS signal, believed to be an electron polaron on the polymer. (a) Shows the relative TAS signal at 600nm after 100μs compared with the HER. (b) Shows the TAS spectrum at 100μs for P1, P7 and P10. Data reproduced from [14]. 109

6.3 This figure shows a method from the literature of determining the likelihood of hydrogen evolution occuring. We determine the EA, IP*, EA* and IP values relative to the SHEL. From this we can deduce a "driving force" by looking at the difference between IP* (some people approximate this using EA) and the hydrogen evolution potential. (a) plots the experimental HER versus the calculated driving force. (b) shows the levels relative to the SHEL. 111

6.4 This figure shows the spatial distribution of the electron in the Kohn-Sham HOMO and LUMO states for FSM and for P10. These have been calculated using DFT with the ωB97XD functional and the aug-cc-pVDZ basis set. 112

6.5 This figure shows the magnitude and direction of the dipole moments in Debeye found using the ωB97XD functional and the aug-cc-pVDZ basis set for monomers of P1, FSM, P7 and P10. 112

6.6 This figure shows the hydrogen evolution rates (HERs) for P1, P7 and P10 plotted against (a) average exciton lifetime from TAS data[14], (b) active volume, calculated from Equation 6.3 as a percentage. 113

6.7 This figure shows how exciton lifetime and diffusion affect how much polymer in the material is active for contributing to hydrogen evolution. The active area is highlighted in orange, and represents the average length that excitons can travel within its given lifetime. Thus, excitons generated inside the orange region have the potential to generate hydrogen whilst those in the grey region do not. In the schematic we show a case where the diffusion length is much smaller than the particle size. 114

6.8 This figure shows the spectrum of the Xe lamp used (a Newport Model 6258) in the hydrogen evolution experiments. For reference the solar spectrum at sea-level is also plotted. 117

6.9 Normalised experimentally measured absorbance spectra are shown on the left. The right shows the absorbed photon flux by each polymer, based on the experimental absorption and spectrum of the lamp used in the HER experiments. . . . 117

6.10 Absorption, predicted theoretically using TD-DFT calculations, is shown on the left. The right shows the absorbed photon flux by each polymer, based on the theoretically predicted absorption and lamp spectra of the lamp used in the HER experiments. . . . 118

6.11 This figure shows both experimental (solid line) and theoretical (dashed) predicted total photon absorbance of P1, P7 and P10 compared with the experimental HERs. We see that increased number of photons is only 1.64 times going from P1 to P10 whereas the HER is 2026 times. . . . 119

6.12 This figure shows the average partial charge on each monomer of a) a 6-mer of P1, b) 8-mer of FSM, c) 8-mer of P7 and d) 8-mer of P10. Whilst we notice some edge effects, we see that it is small (less than two hundreths of an electron charge) and thus neglect it in our model. . . . 122

6.13 This figure shows the fitting of the intermonomer torsion from DFT for (a) P1, (b) FSM, (c) P7 and (d) P10. . . . 123

6.14 This figure shows the fitting of the intermonomer out-of-plane bond bending from DFT for (a) P1, (b) FSM, (c) P7 and (d) P10. . . . 124

6.15 This figure shows the fitting of a hydrogen bond being bent out of the plane of conjugation from DFT for (a) P1, (b) FSM, (c) P7 and (d) P10. . . . 125

6.16 This figure shows the fitting of a carbon atom being bent out of the plane of conjugation from DFT for (a) P1, (b) FSM, (c) P7 and (d) P10. . . . 126

6.17 P1 Force field. a) nomenclature used. b) atom types, partial charges and Van der Waals parameters. c) shows bond, angle and proper dihedral parameters where X,Y,Z represent all C-C-H angles. i,j,k,l represent all intra-monomer C-C-C-H/C-C-C-C angles. d) shows the improper dihedrals which are added to account for planar stiffness due to conjugation. . . . 127

6.18 FSM Force field. a) nomenclature used. b) atom types, partial charges and Van der Waals parameters. c) shows bond, angle and proper dihedral parameters where X,Y,Z represent all C-C-H angles. i,j,k,l represent all intra-monomer C-C-C-H/C-C-C-C angles. d) shows the improper dihedrals which are added to account for planar stiffness due to conjugation. . . . 128

6.19 P7 Force field. a) nomenclature used. b) atom types, partial charges and Van der Waals parameters. c) shows bond, angle and proper dihedral parameters where X,Y,Z represent all C-C-H angles. i,j,k,l represent all intra-monomer C-C-C-H/C-C-C-C angles. d) shows the improper dihedrals which are added to account for planar stiffness due to conjugation. 129

6.20 P10 Force field. a) nomenclature used. b) atom types, partial charges and Van der Waals parameters. c) shows bond, angle and proper dihedral parameters where X,Y,Z represent all C-C-H angles. i,j,k,l represent all intra-monomer C-C-C-H/C-C-C-C angles. d) shows the improper dihedrals which are added to account for planar stiffness due to conjugation. 130

6.21 This figure shows the results of MD of P1, FSM, P7 and P10 in a 50:50 mixture of water and TEA. It shows snapshots of the final state in (a)-(d) with close ups of the local environments in (e)-(h) and finally the centre-of-mass RDFs of the oligomers to the solvents are shown in (i)-(l). In all cases red represents water and blue represents TEA. 132

6.22 This figure shows local environments by volume of each of the oligomers, which are calculated through the cumulative RDF and the molar volumes of each of the components. Red and blue represent water and TEA respectively. 133

6.23 This figure shows the results of MD of single oligomers of FSM, P1, P7 and P10 in a 1:1:1 mixture of water, methanol and TEA. It shows snapshots of the final state in (a)-(d) with close-ups of the local environments in (e)-(h) and finally the centre-of-mass RDFs of the oligomers to the solvents are shown in (i)-(l). In all cases red represents water, blue represents TEA and orange represents methanol. 134

6.24 This figure shows local environments in a 1:1:1 water:TEA:methanol mixture, by volume, of each of the oligomers, which are calculated through the cumulative RDF and the molar volumes of each of the components. Orange, red and blue represent methanol, water And TEA respectively. 135

6.25 This figure shows the results of MD of an aggregated pair of P1, FSM, P7 and P10 in a 1:1 mixture of water and TEA. It shows snapshots of the final state in (a)-(d) with close-ups of the local environments in (e)-(h) and finally the centre-of-mass RDFs of the oligomers to the solvents are shown in (i)-(l). In all cases red represents water, blue represents TEA. 137

6.26 This figure shows the results of MD of aggregated pairs of P1, FSM, P7 and P10 in a 1:1:1 mixture of water, methanol and TEA. It shows snapshots of the final state in (a)-(d) with close-ups of the local environments in (e)-(h) and finally the centre-of-mass RDFs of the oligomers to the solvents are shown in (i)-(l). In all cases red represents water, blue represents TEA and orange represents methanol. 138

6.27 This figure shows the calculated average local environment for aggregated pairs of oligomer in a 1:1 mixture of water and TEA. The dashed line shows the equivalent TEA line for the single oligomers. Blue and red represent TEA and water respectively. 139

6.28 This figure shows the calculated average local environment for aggregated pairs of oligomer in a 1:1:1 mixture of water, methanol and TEA. Above the orange dashed line lies the methanol phase for a single oligomer, between the orange and red dashed lines lies the water phase for a single oligomer, and below the red dashed line lies the TEA phase for a single oligomer. Blue, red and orange represent TEA, water and methanol respectively. 140

7.1 This figure shows part of the reaction that leads to the photo-induced decomposure of TEA into the products DEA, ADH and protons (which eventually recombine into hydrogen). The polymer (FSM) shown represents whichever polymer photocatalyst is present. 145

7.2 This figure shows two active polymers (P7 and P10) and two inactive polymers (FSM and P1) from the previous chapter. The total energy at each step in Figure 7.1 is shown in both TEA (dashed) and in water (full line). These calculations were performed using the **b3lyp** functional and the **6-311g(d,p)** basis set. It can be seen from these that it appears to be solvation and not chemical structure that strongly affects the thermodynamics of these steps. 148

7.3 This figure shows two active polymers (P7 and P10) and two inactive polymers (FSM and P1) from the previous chapter. The total energy at each step in Figure 7.1 is shown in both TEA (dashed) and in water (full line). These calculations were performed using the **wB97XD** functional and the **cc-pVDZ** basis set. It can be seen from these that it appears to be solvation and not chemical structure that strongly affects the thermodynamics of these steps. 149

7.4 This schematic shows the ways of modelling the polymer and the different ways in which I have relaxed different assumptions in order to test the robustness of the approach. By examining each of these levels we isolate the minimal model that adequately explains the phenomenon in order to isolate a prospective screening method. Finally, in red the chosen model is shown. 152

7.5 This figure shows the dependence of the energy of the charge separation step (Step 1) under some of the different situations shown in Figure 7.4 for (a) the b3lyp functional and pople basis set and (b) the ωB97XD functional with the Dunning correlation-consistent basis sets. 154

7.6 This figure shows the make up of the new set of polymers used to stress-test the theoretical connection we have isolated between solvation and hydrogen evolution. 156

7.7 This figure shows how correlated the hydrogen evolution rate (in μg H_2/hr per monomer) is with the difference between a polymer's free energy of solvation in water and its free energy of solvation in TEA as calculated using b3lyp/6-311+g(d,p) in blue, ωB97XD/aug-cc-pVDZ in red and M06HF/aug-cc-pVDZ in cyan. Polymers that lie on the left of zero preferentially want to lie in water and this correlates strongly with performance. 157

7.8 This figure shows how correlated the hydrogen evolution rate (in μg H_2/hr per monomer) is with the calculated charge separation "driving force" in water as calculated using b3lyp/6-311+g(d,p) in blue, ωB97XD/aug-cc-pVDZ in red and M06HF/aug-cc-pVDZ in cyan. We can see that there is no strong correlation. . . 158

7.9 This figure shows the snapshots of a) FSM 6mer, b) P1 12mer, c) P2 4mer, d) P3 4mer, e) P4 4mer, f) P6 4mer, g) P7 4mer and h) P10 6mer surrounded by a 1:1 mixture of water and TEA at 300K. 160

7.10 This figure shows the snapshots of a) FSMPEG, b) FSMOCT, c) FPPEG, d) FPOCT, e) FS5PEG and f) FS5OCT surrounded by a 1:1 mixture of Water and TEA at 300K. 161

7.11 This figure shows the local solvent environment of a) FSM 6mer, b) P1 12mer, c) P2 4mer, d) P3 4mer, e) P4 4mer, f) P6 4mer, g) P7 4mer and h) P10 6mer in a 1:1 mixture of water and TEA at 300K. 162

7.12 This figure shows the local solvent environment of a) FSMPEG, b) FSMOCT, c) FPPEG, d) FPOCT, e) FS5PEG and f) FS5OCT oligomer in a 1:1 mixture of water and TEA at 300K. 163

7.13 This figure shows the local environment (taken at a cutoff radius of 2nm from the center of mass of the oligomers' backbone) of the oligomers studied with MD. . 164

7.14 This figure shows the correlation between water volume in the surrounding environment on the oligomer from water/TEA(1:1) MD systems and the experimental HER values (performed in water/TEA/methanol solution in 1:1:1 ratio by volume). 165

7.15 This figure shows the fundamental system assumed by each of the two main effective medium models, the Maxwell-Garnett[15] and Bruggeman[16]. The former uses different regions of each medium for a given mole fraction, whereas in contrast the Maxwell-Garnett model considers one of the mediums as the base medium and then adds small inclusions of the second medium. 168

7.16 This figure shows the improved correlation of experimental HER data, in μg H_2/hr per monomer, with the charge separation driving force weighted by amount of water in the local environment from MD simulations. Results using b3lyp/6-311+g(d,p), ωB97XD/aug-cc-pVDZ and M06HF/aug-cc-pVDZ are shown in blue, red and cyan respectively. 169

7.17 This figure shows the whole simulation box of a) FSM 6mer, b) P1 12mer, c) P2 4mer, d) P3 4mer, e) P4 4mer, f) P6 4mer, g) P7 4mer, and h) P10 4mer solvated in TEA, water and methanol in 1:1:1 ratio by volume. Water, TEA and methanol are shown in Red, Blue and Orange respectively but because of the level of mixing the definition between solvents is hard to see. 171

7.18 This figure shows the whole simulation box of a) FSMPEG 6mer, b) FSMOCT 6mer, c) FPPEG 4mer, d) FPOCT 4mer, e) FS5OCT 3mer, and f) FS5PEG 3mer solvated in TEA, water and methanol in 1:1:1 ratio by volume. Water, TEA and methanol are shown in Red, Blue and Orange respectively but because of the level of mixing the definition between solvents is hard to see. 172

7.19 This figure shows the local environment of a) FSM 6mer, b) P1 12mer, c) P2 4mer, d) P3 4mer, e) P4 4mer, f) P6 4mer, g) P7 4mer, and h) P10 4mer solvated in TEA, water and methanol in 1:1:1 ratio by volume. Water, TEA and methanol are shown in Red, Blue and Orange respectively but because of the level of mixing the definition between solvents is hard to see. 173

7.20 This figure shows the local environment of a) FSMPEG 6mer, b) FSMOCT 6mer, c) FPPEG 4mer, d) FPOCT 4mer, e) FS5OCT 3mer, and f) FS5PEG 3mer solvated in TEA, water and methanol in 1:1:1 ratio by volume. Water, TEA and methanol are shown in Red, Blue and Orange respectively but because of the level of mixing the definition between solvents is hard to see. 174

7.21 This figure shows the local environment (taken at the cutoff of 2nm) of the oligomers studied with MD. 175

8.1 This figure shows the main reaction pathway for hydrogen evolution when Triethanolamine (TEOA) is used as the SED. The pathway is almost identical to that of the main SED of study in this work, TEA. It should be noted that there is an additional dead-end step not shown here that may limit performance. 182

3.1 This table shows the different types of MD, outlining the minimal unit of each, how the forces are derived and consquently how that type formally scales computationally. It should be noted that, as discussed previously, linear scaling of *ab initio* methods is available and thus in practice ab initio MD can be performed with $\mathcal{O}(\mathrm{NlogN})$. It is worth also noting that the overall cost of *ab initio* MD is much higher even if the scaling behaviour can be similar to Atomistic MD. 39

4.1 This table shows results drawn from MD in comparisons with experimental data, where it is available, and DFT, performed using the infinite basis set approximation of the Dunning correlation consistent and the ωB97XD functional. 62

4.2 This table shows some physical properties (density, self-diffusion, free energy of solvations) of TEA calculated using MD alongside experimental data where it exists and DFT calculations (performed with b3lyp/6-311g(d,p)). The average errors are shown. 64

4.3 This table shows data used to check the validity of the force field for methanol compared with experimental data where it exists and DFT (b3lyp/6-311g(d,p)) where it does not. 65

4.4 This table shows data used to check the validity of the force field for chloroform compared with experiment where it exists and DFT (b3lyp/6-311g(d,p)) where it does not. 67

4.5 This table shows data used to check the validity of the force field for methanol compared with experimental data where it exists and DFT (b3lyp/6-311g(d,p) where it does not. It is shown separately for cis and trans conformers. 70

4.6 This table shows the computed free energy of solvation for cis- and trans-decalin in chloroform, methanol and water, in eV, computed using MD and using DFT, using b3lyp/6-311g(d,p). In the final column the average difference between DFT and MD is shown as a percentage. 70

5.1 This table shows the average radius of gyration for both the backbone and sidechains of PFO and IDTBT for a spectrum of solvents and sidechains. It is worth noting that these numbers represent a single sampling, and a more fuller picture would require multiple different starting configurations or through a technique like blocking[17] to properly represent the errors in these values. 95

5.2 This table shows the free energy of solvation of polyfluorene in three different solvents: chloroform, decalin and water, as calculated using molecular dynamics. 96

5.3 This table shows the results of the correlation function fit obtaining the MD stiffness measure, with IDTBT values taken from [12] with permission. The errors given represent only the fitting error which we note is not a good representation of all sources of error. 101
5.4 This table shows calculated free energy of planarisation for PFO oligomers with different sidechains and different solvents. 104

7.1 A table showing calculation percentage of the volume at 2nm from the oligomer backbone. 165
7.2 A table showing driving forces when weighted by the MD volume fraction alongside the unweighted values in water. 168
7.3 A table showing the calculated percentage of the volume at a r_{cutoff} of 2nm from the oligomers' backbone. 176

1

Introduction

1.1 New Challenges: The need for new materials

The pace of human technological progress has been drastic and can be defined by two major and sweeping changes: the industrial revolution[18, 19] and the silicon revolution[20, 21]. The industrial revolution is the impact of the invention and transition to a highly mechanised society, originally through the use of the steam engine before being replaced largely by general combustion engines and fossil fuel based power. The silicon revolution refers to the invention of silicon based transistors and the subsequent explosion and reliance on logic systems (computers). It is difficult to understand the vast and wide ranging impact that both of these changes have made to individuals and humanity in general. The effects of these on life expectancy and other measures of quality of life have been the subject of wide-ranging discussion and study[22, 19]. Their changes have been largely powered by fossil fuels and inorganic materials (metals and their derivatives primarily). These advances have generated a number of costs: air and water pollution[23, 24, 25], depletion of vital resources[26], loss of biodiversity[27] and potentially catastrophic climate change[28, 29]. Of particular pressing concern is the risk of severe climate change as a result of greenhouse gases that have been released, and continue to be released at alarming rates[30], into the atmosphere causing an increase in the average global temperature. This is a consequence of direct activities such as burning fossil fuels for electricity and energy[31], land use change[31, 32, 33] and resource extraction[31, 34, 35]. As such research to offset this impact has focused on three different strands: energy generation without the use of fossil fuels, ways of reproducing the same devices we currently rely on with much less energy usage (energy saving), and in new materials to replace or mitigate the need for raw earth extraction through the utilisation of sustainable earth abundant materials. As climate research has developed, the goal for decarbonisation has become both more severe and more urgent[36, 37].

This thesis works in the application area of devices that are able to generate energy from sunlight (photovoltaics and photocatalytic water splitting) as well as devices that have the potential to reproduce exisiting technology using sustainable materials. The bulk of this work relates directly to water splitting and we shall now place the desire of this technology in context. Solar Photovoltaics (PV) and other renewables have seen an impressive research development but also more recently an equally impressive industrial roll-out with renewable electricity generation now reaching cost parity with fossil-fuel based electricity production[38, 39]. The PV systems being readily deployed are primarily based on silicon and can be energy intensive to produce. In addition, in order to maintain an electricity grid which operates broadly as we have now, i.e. one where there are few contraints on demand to allow supply to match, we require a way of storing energy or a way of sustainably generating electricity on demand. Research in this subject can be framed into three categories: generation of a sustainable fuel that can be burnt on demand[40, 41], electricity storage such as batteries[42, 43, 44], and demand management[45, 46]. Water splitting takes place in the first of these. Other options for renewable fuel sources include biofuel which involves producing a fuel from biomass such as crops or biowaste. The former of these raises issues of land-use given the changing of, for example, forest to farmland[47]. With land use being a direct cause of climate change this is problematic and, in addition, raises issues of competition of land resource with food production[48].

Photocatalytic water splitting works by absorbing sunlight and directing that energy to split water molecules into hydrogen and oxygen gas. The hydrogen gas would then be stored and used in a fuel cell to convert into electricity or to replace the internal combustion engine in transport applications[49, 50]. The advantage of this approach is that the waste product of the fuel cell would then be water. This alongside the water-cycle could provide a closed (renewable) loop of fuel[51]. In addition to these advantages hydrogen possesses another key factor in its favour in that it has a very high gravimetric energy density, making it of particular interest to areas where weight is a factor in efficiency such as air (and space) travel[52, 53]. Conversely, hydrogen has a very poor volumetric energy density meaning that the same energy takes up a lot of volume. Researchers have been looking at ways of increasing that number by, for example, dissolving the hydrogen into a metal[54].

1.2 New Materials: Functional Organic Materials

All of this work belongs in the field of organic materials, a class of material that is made of earth abundant materials that have been increasingly studied for a variety of applications. Organic electronic materials are semiconductors based on light molecular materials which can absorb light and conduct charge[55]. If functionalised to the same quality as inorganic semiconductors they could be used for OLEDs[56, 57, 58] and OFETs[59] to provide digital displays and computer processing (logic circuitry) in an efficient, sustainable way. Indeed, OLED displays have now been fully deployed and are already the standard for high-end displays. Meanwhile OFETs have been hampered by low charge mobilities and low environmental and operational stability[60] but recent research has significantly narrowed the gap between OFETs and traditional inorganic equivalents[59]. Organic electronic materials are expected to be cheap and sustainable due to the ability for them to be produced in a roll to roll type 'printing' procedure[61]. They have the added benefit of being flexible.

In the arena of energy generation, organic materials have been investigated for photovoltaic applications (OPVs). In addition to OPVs there has also been some interest for sunlight induced electrolysis of water (water splitting)[62, 63].

As touched upon, there are significant potential advantages to using these materials: they are cheaper to make[58], able to be produced from solution[61] and potentially biodegradable[64]. They are flexible which can be useful especially in niche applications such as compact electronic devices. The exact properties of the material is highly dependent on structural properties which, to some degree, can be controlled by certain controllable parameters during the synthesis. This is one of the biggest advantages of this category of materials, but also one of the biggest challenges. Determining the exact relationship between such parameters and the final performance of a device remains an open research question[65].

With such advantages come a significant amount of challenges for both experimental techniques and for theoretical understanding. Such variability of behaviour and large phase space

of possible chemical structures inhibits experimental 'exploratory' type investigation[66]. This makes developing computational tools and deep physical understanding of the processes vital. On the simulation side there are also difficulties: the materials are complex and the phenomena involved are highly multi-scale, ranging from charge distributions over single molecules on an electronic scale, through atomistic interactions to structural, device-scale behaviour. In the next section we discuss a realm of materials modelling which may provide a toolbox for dealing with these problems: Multiscale Modelling.

1.3 New Methods: Multiscale Modelling for computational design of materials for devices

As mentioned in the last section the materials of study are often highly complex and take place in a large phase space that makes identifying materials that have the desired properties a difficult and complex task. The processes of interest often take place over different length and time-scales, and in addition these processes can also be interdependent on one another[67, 68]. It is for this reason that computational modelling plays such a key role in the research of new materials. In particular, multi-scale modelling might play a key role in the future of materials research. Multiscale modelling is modelling where multiple different scales (either time or length) are important and thus the modelling must have information flow between different scales. In Figure 1.1 we show a schematic outlining the different types of multiscale modelling used in the literature.

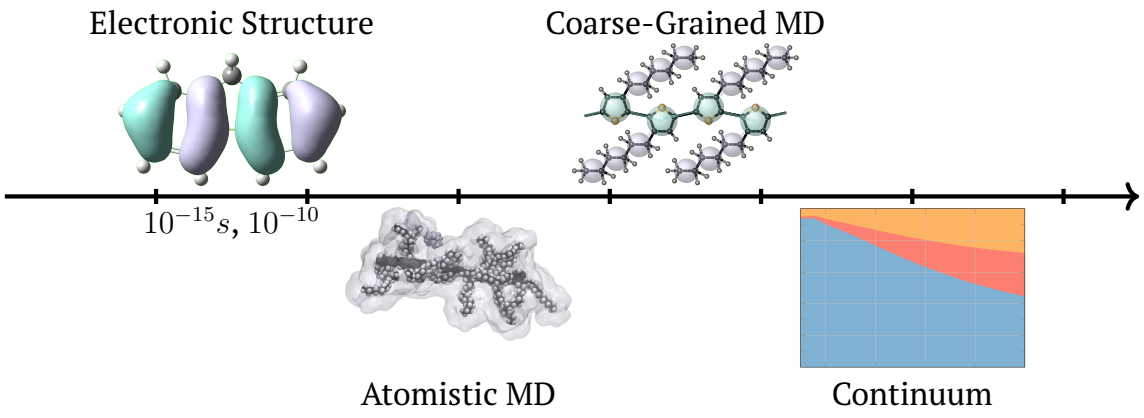


Figure 1.1: This schematic shows a summary of the different methods used in materials research problems in the literature. The common scales accessible by each of the techniques are shown and are a function of the amount of readily available computational power.

We can see from this figure that there are a number of different methods for accessing differ-

ent scales and managing information flow between them. It is vital to think carefully about the physics of the system in question, about what elements are important, and thus to choose appropriate methods. Due to the systems we study, and this work being so intrinsically multi-scale, we summarise the multi-scale methods in this section. This work uses a number of methods within one scale, including:

- Molecular Dynamics - these are a key part of our studies of conformation of conjugated polymers that we undertake on Polyfluorene and IDTBT in Chapter 5 and on Polymer Photocatalysts in Chapter 6
- Electronic structure - this is fundamentally important to the study of hydrogen evolution reactions in Chapter 7

Using methods at different scales however is not, in itself, multi-scale. This takes information being used from one scale to inform and model processes occuring at another. The crescendo of this work involves a truly multi-scale approach bringing together information from the electronic structure, nanoscale molecular dynamics information, and continuum electrostatics. We use a mathematical model using continuum methods to derive a cut-off value to determine the local environment of the polymer in molecular dynamics which is then fed back into DFT calculations in Chapter 7 to uncover the driving forces for hydrogen evolution.

1.4 Overview of Thesis

This thesis is structured as follows: in Chapter 2 we cover the theoretical underpinnings of the work, covering what research has been done up to this point. In Chapter 3 we cover the workings of the computational methods we use to study these problems. Next, in Chapter 4, we use simulations to investigate the behaviour of various liquids and their multi-phase behaviour. We next look, in Chapter 5, at simple systems of polymer and single solvents that are important materials for the production of organic devices that involve charge transport (such as OFETs). Chapters 6 and 7 contain the work on photocatalytic water splitting, with Chapter 6 using molecular dynamics to look at the solvation properties alongside the aggregation effects. In Chapter 7 we study in depth the mechanisms of hydrogen evolution with a particular focus on how the results from Chapter 6 impact them. We do this with an eye to create a method of predicting the performance of polymers as organic photocatalysts.

2

Theoretical Background

The work in this thesis involves the application of a variety of computational methods to simulate the properties of organic conjugated polymers on different length and time scales, in order to better understand their performance when applied to charge transport and photocatalytic solar energy conversion. In this chapter I provide the research context of each element of my research. In Section 1.3 we have already presented a minimal introduction to a relatively new strand of computational materials modelling, multi-scale modelling. In this chapter we discuss the problems we consider in this work and outline why they are intrinsically multi-scale problems that require such methods. In Section 2.1 we provide a brief, wider, overview of the study of conjugated polymers and their applications before focusing on the specific polymers and applications we study in this work. Finally, in Section 2.2, we briefly outline research in the field of photocatalytic water splitting before focusing on the very new application of organic materials as photocatalysts.

2.1 Organic Materials: Conjugated Polymers

Technology, particularly electronic technology, has traditionally relied on inorganic semiconductor materials[69]. In the last two decades there has been increasing focus on the potential use of organic semiconducting compounds for electronic applications. Most organic materials are insulators; there is however a class of materials that behave as semiconductors and they have been of great research and industrial interest.

Organic semiconductors possess a number of potential benefits: reliance on earth abundant materials and the potential for them to be produced from solution or by other high volume processes, making the resulting products cheap and reducing energy demand in manufacture. Organic semiconductor materials have made a substantial impact in some areas already, for example OLEDs TV sales have been in substantial increase in the last few years and as mentioned

in Section 1.2 OLEDs are the standard for high-end displays[45]. Organic Field Effect Transistors (OFETs) for electronics are also being actively pursued, being held back by low charge mobilities and poor stability[60]. The gap between OFET and traditional FET performances has been narrowing over the last few years[70, 71]. The application of organic semiconductors to solar photovoltaic energy conversion, Organic Photovoltaics (OPV), has attracted intense research and industrial interest over the last few years and stimulated much new materials development. OPV technology is being developed commercially, albeit for different applications than typical mainstream PV power generation [72]. Organic electronic devices are expected to be produced through a 'roll-to-roll' printing process and as a result they are expected to be cheap to produce. They have the added benefit of being flexible, making them more adaptable to different applications; this feature is utilised already in making OLED TVs curved to match more closely what is natural for the eye.

Most organic materials are insulators[73]. There is however a class of materials that behave as semiconductors and they have been of great research and industrial interest[74, 75]. To understand how the semiconducting properties of organic electronic materials arise we first must discuss the electronic structure of organic materials. Electronic states in crystalline inorganic materials tend to form well defined bands that are delocalised over the entire crystal due to the periodicity of the lattice. The set of bands is partially filled with electrons, resulting in an insulator, metal or semiconductor depending on the occupation of the highest filled band and the energy gap between bands. In contrast, organic materials tend to have more localised orbitals, because of the lack of periodicity and the strong coupling of electronic and vibrational degrees of freedom. To discuss the structure of orbitals in organics we first consider the orbitals in a carbon atom, plotted in Figure 2.1.

We can see from Figure 2.1 that in carbon the four valence electrons exist in the 2s and three degenerate 2p orbitals. Different combinations of these valence orbitals lead to different types of hybridised orbitals, namely the sp, sp^2 and sp^3 which are blends of the 2s orbital with one, two and three of the 2p orbitals, respectively. The unhybridised p_z orbitals for each type of hybridisation are left unchanged. We now show how this might look for two covalently bonded carbon atoms in Figure 2.2.

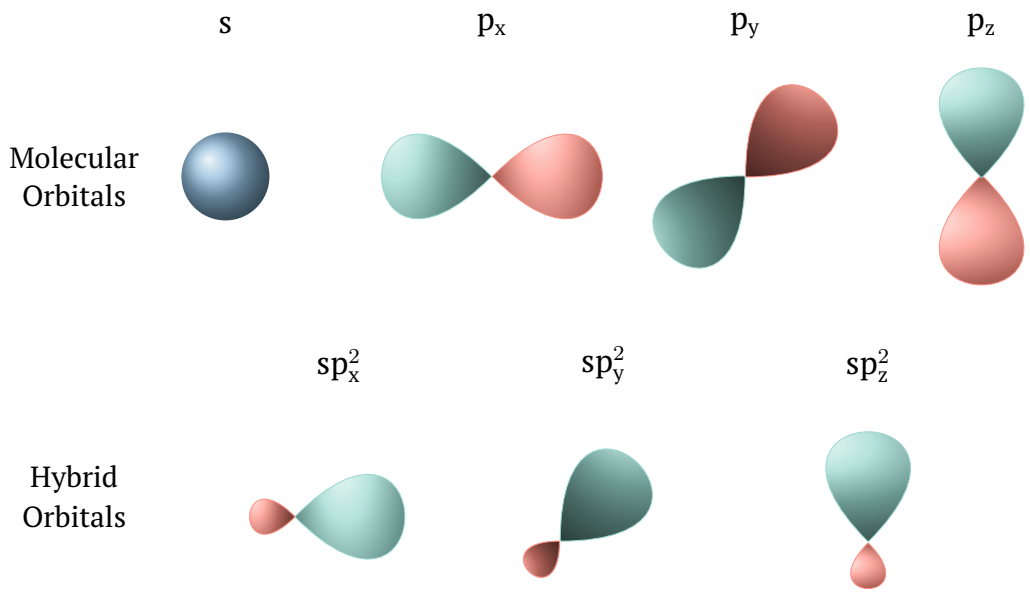


Figure 2.1: This figure shows the s and p_x, p_y, p_z and orbitals and the sp^2 hybridised molecular orbitals that play such a crucial role in organic materials, particularly conjugated ones.

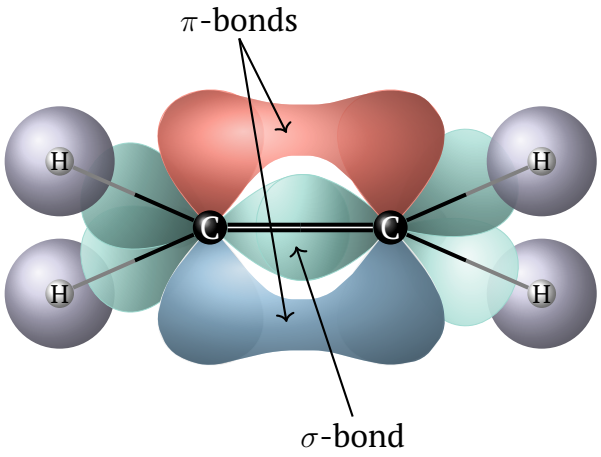


Figure 2.2: This figure shows how a combination of the p_z and sp^2 orbitals combine to form σ and π bonds in conjugated materials. In this case an ethene is shown.

We see in Figure 2.2 that what allows organic materials to act as semiconductors when two carbon atoms are bonded is that they are, in sp^2 hybridisation, able to form two different types of bond called σ and π bonds. The σ bond between the carbon atoms is formed from overlap of two sp^2 orbitals whilst the overlap of two p_z allows for a π bond. A single C-C bond will have one σ bond whereas a double C=C bond will have one σ bond and one π bond. We can also see from the energy diagram in (b) that the π bond dominates the highest filled and lowest unfilled

molecular orbital. This can be rationalised by considering that the π electrons reside, on average, further from the atomic cores than the sigma electrons and are therefore more loosely bound. When a molecule consists of alternating double and single carbon bonds we call this conjugation, and the π electron density forms one continuous π-orbital across the structure. This means electrons are delocalised within the structure. The highest occupied molecular orbital (HOMO) is a π bonding state and the lowest unoccupied molecular orbital (LUMO) is a π^* anti-bonding state. The HOMO and LUMO can be thought of as analogous to the valence and conduction bands in traditional semiconductors. The band-gap of organic semiconductors can be approximated roughly as the difference between the HOMO and LUMO energies[1]. The band-gap typically varies between 1.5 and 3 eV in typical organic semiconductors and reduces with more extensive conjugation. Figure 2.3 shows a representative sample of commonly studied organic conjugated materials. Note that the conjugated structures formed by the network of carbon atoms in the sp^2 configuration tend to be flat. This reflects the trigonal geometry of the sp^2 σ bonds. One feature of conjugated materials is their rigidity: the π bonding makes it very difficult for the conjugated part of the molecule to twist out of the plane of conjugation because doing so would break the conjugation. At this point we introduce the concept of conjugation length which is the length over which a π bond exists. There are a few ways the conjugation length can be limited: by chemical structure, molecular conformation, and different kinds of defects. In small conjugated molecules of some some tens of atoms the π molecular orbitals are typically delocalised over the whole conjugated backbone and the conjugation length is approximately the size of the molecule. In a larger molecule or a polymer, twists within the molecule can differentiate the backbone into conjugated segments of different conjugation length; these may be referred to as chromophores. The conjugation length has a key impact on the electronic and optical behaviour of the material, specifically that longer conjugated segments present smaller band-gaps and smaller optical gaps than shorter segments. The variety of segment lengths present in a polymer sample leads to disorder in the electronic properties and broadens the optical response.

[1]There are in fact two concepts here: firstly, the fundamental gap, which is the difference between a molecule's ionisation potential and its electron affinity. It is the energy associated with *adding* an electron into the excited state. The other concept is that of the optical gap which corresponds with the energy needed to promote an electron, via an optical excitation into the excited state. Here we use band-gap to refer to the fundamental band-gap, rather than the optical band-gap.

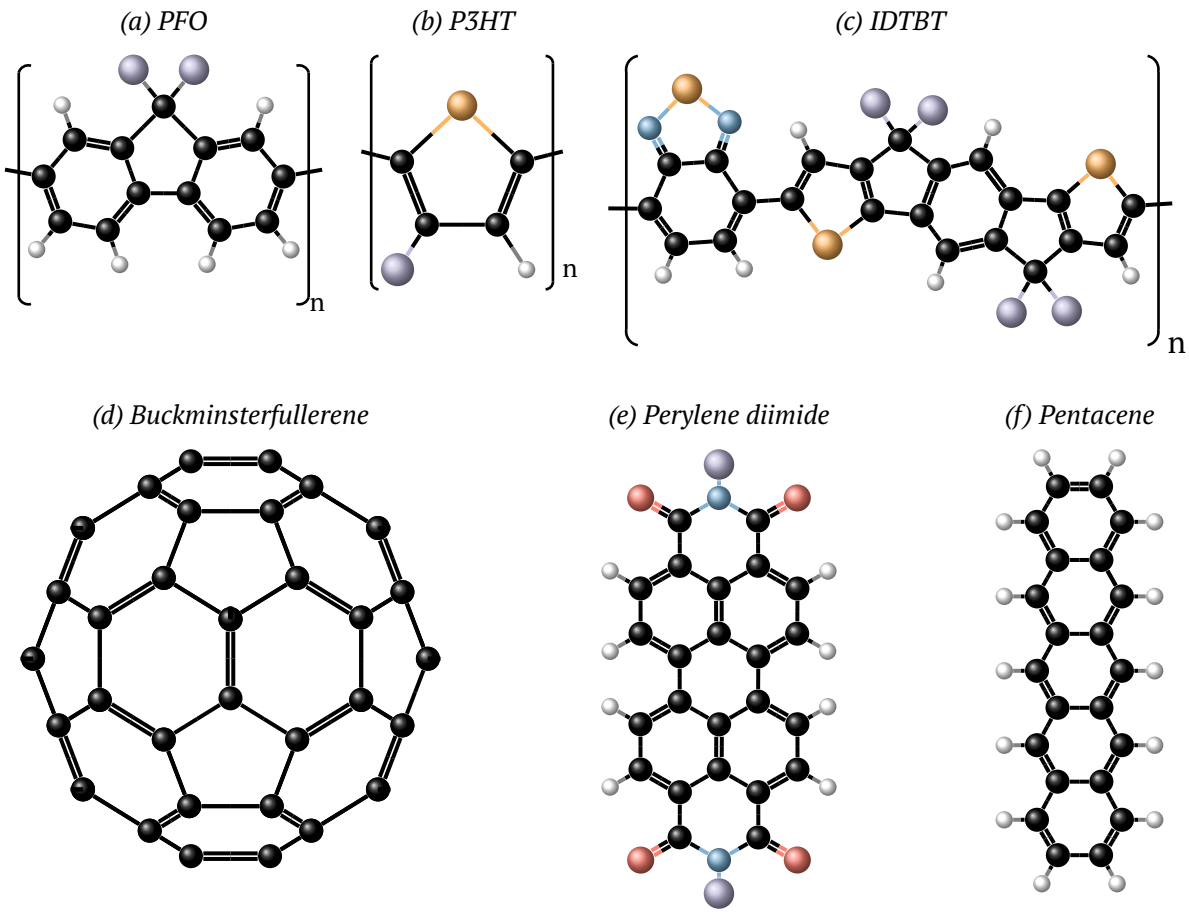


Figure 2.3: This figure shows a selection of commonly used and studied conjugated organic materials. (a) shows Polyfluorene (PFO) (b) shows Poly(3-hexylthiophene-2,5-diyl), P3HT, (c) shows indacenodithiophene-co-benzothiadiazole (IDTBT), (d) shows a C60 buckminsterfullerene, (e) shows Perylene diimide (f) shows Pentacene. (a), (b) and (c) are classified as polymers where as (d), (e), and (f) are classified as small molecules. Purple atoms show points for sidechains to be attached.

As well as the conjugated backbone, constructed mainly of carbon atoms in the sp2 configuration, organic semiconductors are synthesised with solubilising side chains that are necessary for dispersion of the polymer in solvents during processing. These side chains are typically made from alkyl chains based on carbon atoms in the sp^3 configuration, or other types of chain like ethylene glycol chains, which may be added for compatibility with polar solvents. Organic materials like those in Figure 2.3 are often grouped into categories: small molecules and polymers.

2.1.1 Polymers

Polymers are constructed from repeating units of base building blocks called monomers; Figures c, d and e of Figure 2.3 are of polymers. Polymers are usually longer than their conjugation length and as such have a number of weakly electronically coupled segments or chromophores. Polymers require a number of new concepts which we will outline here. In contrast to small molecules, a system of polymers contains a distribution of chains of varying lengths; to characterise this the concept of molecular weight is used. The molecular weight of a polymer is some average of the set of atomic weights associated with each polymer chain. There are two quantities that are studied and measured: the number average of molecular weights in the sample and the weight average molecular weight. The ratio of these two quantities provides information on the spread of the distribution of molecular weights, called polydispersity. The synthesis of different polymers can lead to different molecular weights and it is an important measure of polymer quality and properties.

Another important concept in polymer physics is the concept of chain conformation. A conformation is a single shape the polymer chain can adopt, as the result of different rotations sampled by the molecule around the various degrees of freedom in the polymer chain. It is important to note that in polymers where the repeat unit is based upon aromatic rings or fused ring structures, such as PFO, P3HT and IDTBT in Figure 2.3, the bond joining monomers is largely of a single-bond character and the components on either side may twist relative to each other. In some cases they are forced to twist out of plane by steric hindrance effects, as for example where two phenyl groups are linked. The torsional potential is a function that describes the energy of the molecule as a function of the dihedral angle between the two linked conjugated units. It will have minima in the most energetically favourable positions but there will be a range of other torsions that are readily accessible at room temperature. With each monomer-monomer link sampling this range of accessible torsion values, the polymer can adopt a wide range of different shapes and in the case of polymers whose geometry means that consecutive units are not co-linear, the polymer may explore the three-dimensional space. Polymers (and sidechains) will thus have access to a lot of different conformations that are allowed by the chemical structure, and the environment in which they exist will bias the favourability of different conformations. For example, interactions between the polymer and its environment could influence the value of the torsional angle between monomers. Much of the work in understanding the structures

adopted by conjugated polymers involves studying the relationship between a polymer's conformation in the solution from which it is processed and the microstructure of the polymer in the final device.

As well as influencing conjugation length, polymer conformation influences the polymer's persistence length. Persistence length is defined as the length over which correlations in direction of monomers are lost. What this means is that monomers that are closer than a persistence length apart will behave like a flexible rod and if they are more than the persistence length apart they move statistically like a three-dimensional random walk. This property is a key measure of the stiffness of a polymer and is known to have an impact on the microstructure of a polymer film and both the charge transport properties[76] and the optical properties [77].

Solubility and aggregation effects in polymers are also very important for conformation and polymer behaviour and form an important part of the work in this thesis. Both solubility and aggregation can be controlled through the use of sidechains which can change the interactions between the polymer and different solvents but also the interactions between polymers (or between parts of the same polymer). An example of this is that it is common to add glycolated sidechains to increase the compatability of a polymer with water[78, 79, 80].

2.1.2 Electronic Structure of Organic Materials

Quantum mechanics represents the fundamental theory at the atomic scale. It is based primarily on experimental data that is so far from human-level perception that the results can often feel highly counter-intuitive. The theory of quantum phenomena could, and does, fill many volumes of text book and we shall restrict ourselves here to the bare basics we require to understand the methods we employ in this thesis. At the heart of quantum theory is the concept that a particle can be fully described by a wavefunction, often denoted $\psi(\mathbf{r}, t)$. Whilst not physically observable and therefore not unique the wavefunction can be considered as probability amplitude for the particles whereabouts. The wavefunction can most readily be understood from the Schrödinger Equation,

$$\hat{H}\psi(\mathbf{r}) = E\psi(\mathbf{r}), \tag{2.1}$$

where E represents the energy of a state and $\hat{H}$ is the hamiltonian (energy) operator. This is the governing equation for a single electron non-relativistic case where we have supressed the spin labels for brevity. This is for a static situation, where the system is evolving in time and the equation of state will be the time-dependent Schrödinger equation,

$$\hat{H}\psi(\mathbf{r},t) = i\hbar\frac{\partial}{\partial t}\psi(\mathbf{r},t). \tag{2.2}$$

So far we have just left the Hamiltonian unspecified; it is the energy operator and it encapsulates all the physical situation the particle experiences, for example an electron in an external potential, $V(\mathbf{r})$ would have a Hamiltonian of the form:

$$\hat{H} = -\frac{\hbar^2}{2m}\nabla^2 + V(\mathbf{r}). \tag{2.3}$$

So far we have only considered a system of a single particle, but unfortunately all of chemistry and physics takes place in situations with many particles. The principle is much the same but the wavefunction must become a many-body wavefunction depending on the positions of all the particles in the system. In addition the Hamiltonian gains a number of additional terms to account for the particle types (electron and nuclei) and for the interactions between different particles. In this case the time-independent Schrödinger equation can be written as:

$$\underbrace{-\sum_{e_i}\frac{\hbar^2}{2m_e}\nabla^2_{\mathbf{r}_{e_i}}\Psi}_{\text{Electron Kinetic Energy}} \underbrace{-\sum_{N_i}\frac{\hbar^2}{2m_{N_i}}\nabla^2_{\mathbf{r}_{N_i}}\Psi}_{\text{Nuclei Kinetic Energy}} + \underbrace{\sum_{e_i,e_j}^{i\neq j}\frac{e^2\Psi}{4\pi\varepsilon_0|\mathbf{r}_{e_i}-\mathbf{r}_{e_j}|}}_{\text{Electron-Electron interaction}} + \underbrace{\sum_{N_i,N_j}^{i\neq j}\frac{Z_iZ_j\Psi}{4\pi\varepsilon_0|\mathbf{r}_{N_i}-\mathbf{r}_{N_j}|}}_{\text{Nuclei-Nuclei interaction}} + \underbrace{\sum_{e_i,N_j}^{i\neq j}\frac{eZ_j\Psi}{4\pi\varepsilon_0|\mathbf{r}_{e_i}-\mathbf{r}_{N_j}|}}_{\text{Electron-Nuclei interaction}} = i\hbar\frac{\partial}{\partial t}\Psi, \tag{2.4}$$

where N_i is the i$^{\text{th}}$ nuclei, e_i is the i$^{\text{th}}$ electron, Z_i is the charge on the i$^{\text{th}}$ nuclei. This many-body molecular hamiltonian is very hard to solve but it is what nature solves to determine the behaviour of our systems. We discuss methods employed in how to tackle this feat in Section 3.1. Considering the terms though we can elucidate and understand elements of our systems. The interaction between the electronic and nuclear degrees of freedom are relatively strong compared to a case of an inorganic crystal. The consequence of this is that the electronic state is a strong function of the nuclear coordinates. Often we consider that the nuclear coordinates are moving much more slowly than electronic coordinates and thus separate these degrees of freedom (more on this in Section 3.1.1). These many-electron wavefunctions are often represented as combinations of single electron wavefunctions. The ground state of a system or molecule is a particular arrangement of electrons and nuclei that minimises the Hamiltonian, that is the global minimum of the total energy of the system.

In a molecular orbital picture, as we have outlined here, we regard the ground state as the state where orbitals are filled up to the HOMO which is doubly occupied (one with each spin). We will be concerned with several types of excited states of the system, particularly the neutral excited state or exciton, where additional energy is given to the electrons and in a molecular orbital picture at least one electron has been excited to a higher energy orbital, typically from the HOMO to the LUMO. The exciton has a total spin of zero (singlet exciton) or one (triplet exciton) depending on the alignment of the two unpaired spins i.e. whether antiparallel (singlet) or parallel (triplet).

We are also concerned with the singly charged excited states of the molecule, the negatively charged and positively charged state which can be regarded as the situation where the LUMO is singly occupied and the HOMO is full, and that when the HOMO is singly occupied and the LUMO is empty, respectively. We show the different types of excitation and how the energy levels might look in Figure 2.4

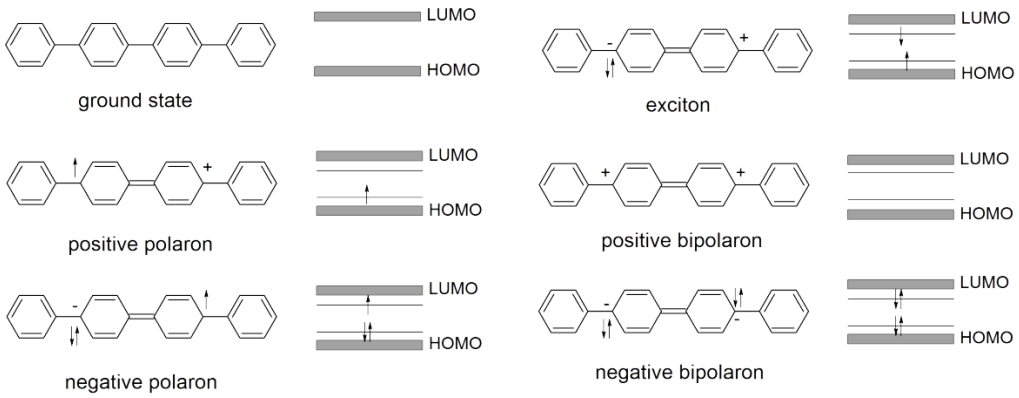


Figure 2.4: This figure shows the different type of excitation in organic materials: (a) shows excitons, (b) shows polarons, and (c) shows bi-polarons. As shown polarons (and bi-polarons) exist for both positive and negative charge. From [1].

Due to the strong electronic-nuclear interaction, any change in electron distribution, such as in a neutral exciton or a polaron relative to the ground state means that the nuclear coordinates corresponding to the minimum energy configuration of the exciton or polaron are in general different to those in the ground state. The dependence of state energy on nuclear coordinates can be represented using configuration coordinate diagrams where a curve (potential energy

surface) shows how the ground state or excited state energy varies with nuclear coordinates. (See Figure 2.5).

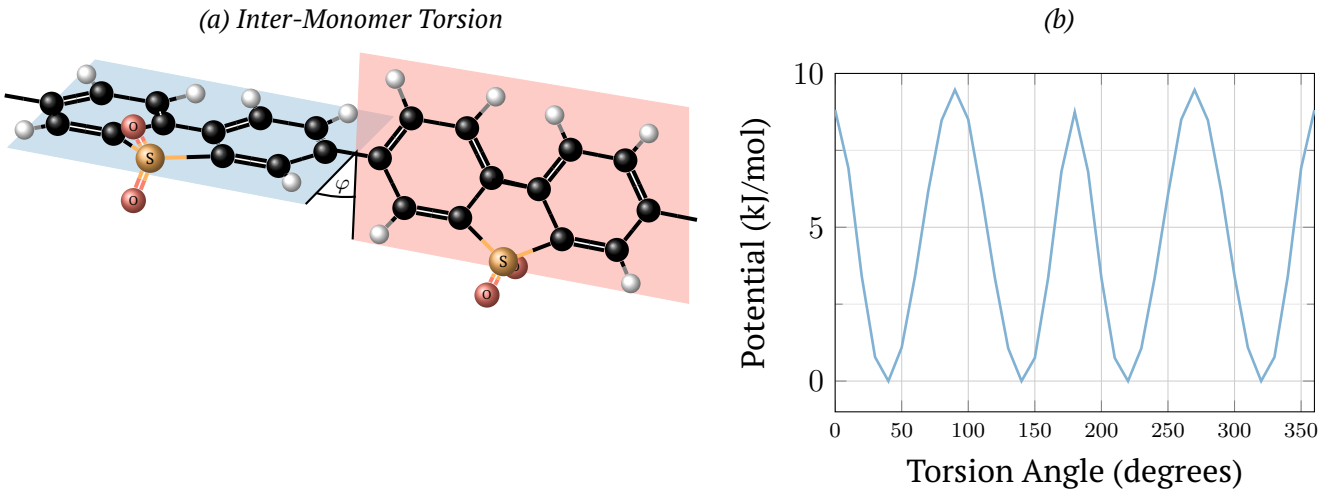


Figure 2.5: A figure showing how the ground state total energy of a system varies as a nuclear coordinate is changed, in this case the inter-monomer torsion. The nuclear coordinate is shown in (a) and the potential energy surface in (b).

The change in minimum energy configuration upon excitation results in a distortion of the local nuclear positions around an excitation and tends to localise the excited state in space. The exciton or polaron becomes stabilised by the local rearrangement of the nuclear and dielectric environment such that energy is required to release the excitation. We refer to this stabilisation energy as the exciton binding energy or polaron binding energy, in the case of an exciton and a polaron, respectively. In the case of the neutral exciton the binding energy is comparatively large (few tenths of an eV) because the low dielectric constant allows a strong Coulombic interaction between the promoted electron and the hole.

2.1.3 Generation and Recombination of Excitations

The excitons shown in Figure 2.4 are of key importance to the behaviour of the polymer's charge transport and optical properties. A neutral singlet exciton can be formed by the absorption of a photon. The rate of that optical transition from an initial state ψ_i to a set of final states ψ_f of energy E_f can be calculated by using Fermi's golden rule,

$$\Gamma_{\psi_i \to \psi_f} = \frac{2\pi}{\hbar} \left| \left\langle \psi_f \left| \hat{H}' \right| \psi_i \right\rangle \right|^2 \rho(E_f) \tag{2.5}$$

where $\hat{H}'$ is a perturbation, in this case an electromagnetic field, to the Hamiltonian of the system that results in the final state, $\rho(E_f)$ is the density of the states with an energy of E_f sometimes referred to as the degeneracy of the final state. In the dipole approximation (assuming

the wavelength of light is a lot longer than the atomic scale) this becomes

$$\Gamma_{\psi_i \to \psi_f} = \frac{2\pi}{\hbar} \left| \langle \psi_f \left| er \right| \psi_i \rangle \right|^2 \rho(E_f). \tag{2.6}$$

When ψ is expressed as a product of its electronic (ϕ), nuclear (χ) and spin (S) parts, $\psi = \phi\chi S$, the matrix element, $M_{if} = \langle \psi_f \left| er \right| \psi_i \rangle|$, therefore contains the overlap of the nuclear wavefunction, overlap of the spin wavefunctions and the electronic part which retains the position operator. Since the ground state of most molecules is a singlet, the requirement for the spin wavefunction overlap to be non-zero means that the final state must also be a singlet. This is an example of what a selection rule is: a result that if there is no overlap in any part of the final and initial state then the rate of that transition happening drops to zero. In addition there is an additional selection rule that always applies, because the operator is odd, and this imposes that the final and initial states must have opposite parity. The selection rules will depend on the molecule in question and in particular its symmetry[81].

Neutral excitons may also be formed by the combination of independent electron and hole polarons. In this case, triplets can be formed and are in the simplest approximation three times as likely as singlets to be formed. Positive and negative polarons can be generated from a neutral exciton that splits into charges or from charge injection from an electrode connected to an external circuit. As mentioned above, the excess of charge on the polymer causes the deformation of the equilibrium geometry of the polymer; a polaron then is a quasi-particle of the charge plus the distortion field that it creates. The distortion field tends to help localise the charge as it adds energetic cost to movement, but polarons can move in both an inter-chain and intra-chain fashion.

Although not a major feature in this work there is another type of excitation that plays a large role in the physics of organic donor/acceptor devices and that is the charge transfer (CT) state. A CT state is one that can form energetically in between the exciton energy and the charge separated state. It occurs at the interface and thus is a very important state in devices designed to generate charge such as OPVs[82, 83].

Excitations can then decay back to the ground state by recombination. There are several types of recombination that have distinctive behaviour:

- An excited state that stems from photoexcitation can decay radiatively by the electron returning to the ground state via spontaneous emission and giving off the energy as a photon; this process is known as photoluminescence.

- An excited state that arises from the combination of electrically injected positive and negative polarons to form a singlet exciton that then radiatively recombines is known as electroluminescence.

- The excited state can return to the ground state non-radiatively by releasing the excess energy through vibrations.

- The excited state can undergo a charge separation process to form a pair of oppositely charged polarons.

Luminescence can be categorised into two forms: Fluorescence and Phosphorescence. Fluorescence is where emitted light comes from an excited singlet state to the ground (singlet) state. Phosphorescence is a slower process where the excited state first undergoes what is known as an intersystem crossing, where the excited singlet state transfers its energy to an excited triplet state before emitting a photon through a triplet-singlet transition. Typically Fluorescence occurs on the order of nanoseconds after the absorption of a photon whereas phosphorescence takes place between milliseconds and seconds. These states and processes are often represented in a Jablonski diagram, similar to the example shown in Figure 2.6.

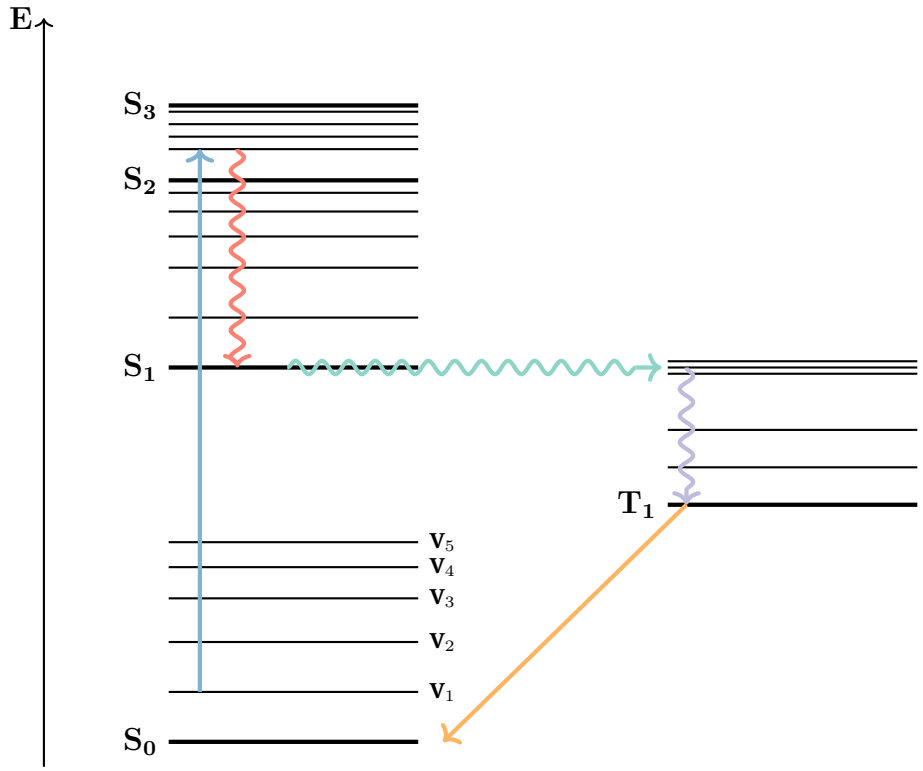


Figure 2.6: This diagram shows a Jablonski diagram. It shows the ground state, a singlet state labelled S_0, the first and second singlet excited states, S_1 and S_2, and the first triplet excited state T_1. For each state there exists a number of closely ($\backsim 0.1eV$) spaced energy levels corresponding to different vibrational modes. Different types of radiative and non radiative decays are shown.

2.1.4 Microstructure of Polymer systems

We have discussed the conformation of polymer chains and how that can be influenced by the shape of the monomer, the inter-monomer torsion, the position and type of sidechain and the interactions between polymers with the surrounding medium. In solid films this conformational freedom gives rise to a variety of solid state microstructures, including crystalline, amorphous, and liquid crystalline phases, and mixtures of all of these in different proportions. The packing the polymer adopts will be very important to the transport behaviour of excitons and polarons through the polymer film.

Chain packing is primarily controlled by weak Van der Waals interactions between the molecules mediated by steric interactions due to sidechains or hindrance that causes the chains to twist. Good electronic transport properties are associated with strong electronic coupling between conjugated units (chromophores). This can be acheived by packing the conjugated cores of

neighbouring chains closely together cofacially (referred to as "π-π" stacking). Strong electronic coupling between monomers in a polymer is also linked with good electronic transport. Thus we can conclude that good inter-chain and intra-chain coupling are both important for good electronic transport.

Achieving good coupling is limited by another constraint we have: to make the films, we require the polymers to be processable and in practice this means the addition of flexible sidechains. Sidechains do not assist in electronic transport and can disrupt the packing of the conjugated cores. Determining where to place the sidechains and what the sidechains are is a key part of the optimisation of the transport of a conjugated polymer system[84]. In this section we discuss the role of microstructure in the properties of polymer systems. As we have discussed, polymer systems possess a wide degree of both chemical and conformational flexibility and thus they can give rise to a myriad of different microstructures depending on how the films are processed and treated. In Figure 2.7 we show different polymer films with different degrees of ordering.

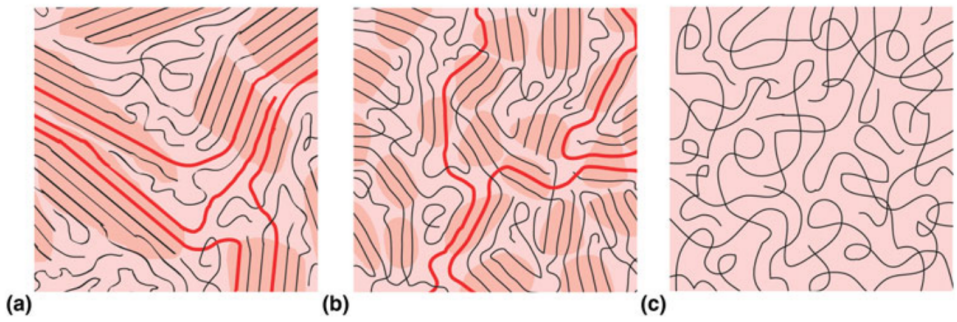


Figure 2.7: This figure, from [2], shows different microstructures for semiconducting polymer systems with (a) semi-crystalline, (b) weakly ordered and (c) completely amorphous character. Large scale crystallinity is not vital for charge transport but a minimal amount of aggregation is. Transport pathways are highlighted in red.

As a result of studying the transport properties of a range of conjugated polymer systems, certain design rules have emerged to generate polymer systems with high mobilities:

- Large conjugated cores[85, 86]
- Reducing π'-π stacking distance[84, 87]
- Minimising backbone torsion[60, 88, 86]
- Ensuring the electronic structure is resilient to disorder[2, 89]

- Films of both ordered and disordered phases[90]
- Increase molecular weight[91, 92]

Despite so much research having taken place looking at the effect of microstructure on properties and how things like annealing can restructure the microstructure, there is relatively little work that focuses on the question of to what degree the phase space, particularly conformation, in the liquid phase affects the developed microstructure in the final device.

2.1.5 Polyfluroene

Of particular interest to the study of organic materials, and in particular for this work, are derivatives of polyfluorene, often abbreivated to PFO. PFO has been widely studied in the literature; it has a number of desirable properties such as photoluminescene and electroluminescence in the blue[93, 94, 95], it has higher charge mobilities than a lot of other polymer systems[96, 97] and is highly processable in a variety of commonly used organic solvents[93, 94, 95]. As a result of these properties PFO has found itself being investigated for a wide range of applications such as LEDs[98, 99]. It is known that PFO can be processed in the solid state to adopt a range of microstructures including glassy, crystalline, liquid-crystalline and the so-called β phase, and this in turn leads to a range of observed optical and electronic properties[100, 101, 102]. Of particular note is the β-phase conformation which is characterised by a planarised backbone. It is of note due to the fact that this microstructural motif results in a distinct spectral signature. This means that different experimental set-ups can be tested to see what influences the development of β-phase. The question of β-phase formation has been a research focus for some time and factors that are known to affect its development include solvent[94, 103], sidechain[104] and molecular weight[105]. β-phase is known to impede charge transport in PFO films by acting as a trap[97, 106]. In this work, in Chapter 5, we study the formation of β-phase in solution using molecular dynamics.

2.2 Photocatalyic Water Splitting

2.2.1 Fundamentals of Water Splitting

Much of this work will focus on a relatively new field, that of organic materials being used as photocatalysts for the splitting of water into hydrogen and oxygen. Before we turn to discuss this recent development we first discuss the basic principles of water splitting and briefly

overview water splitting with non-organic materials. The basic process of photocatalytic water splitting can be described as follows:

1. A photocatalyst is immersed in water or mixtures of water with solvents.
2. A photocatalyst absorbs light placing it in an excited state.
3. An exciton must either undergo charge separation or migrate to the surface of the photocatalyst[2].
4. The exciton must undergo charge separation when it reaches the surface.
5. The charges must ultimately transfer to the water facilitating a reduction and an oxidation reaction producing hydrogen and oxygen.

In Figure 2.8 we show some of the ideal systems that a photocatalyst or set of photocatalysts would be in to perform overall water splitting. It shows a single device system in which a photocatalyst and co-catalyst are performing both halves of the redox reaction and dual-cell system where each cell performs half of the reaction and are joined by a film or a membrane that allows for the transfer of H^+ ions but not the O^2 molecules.

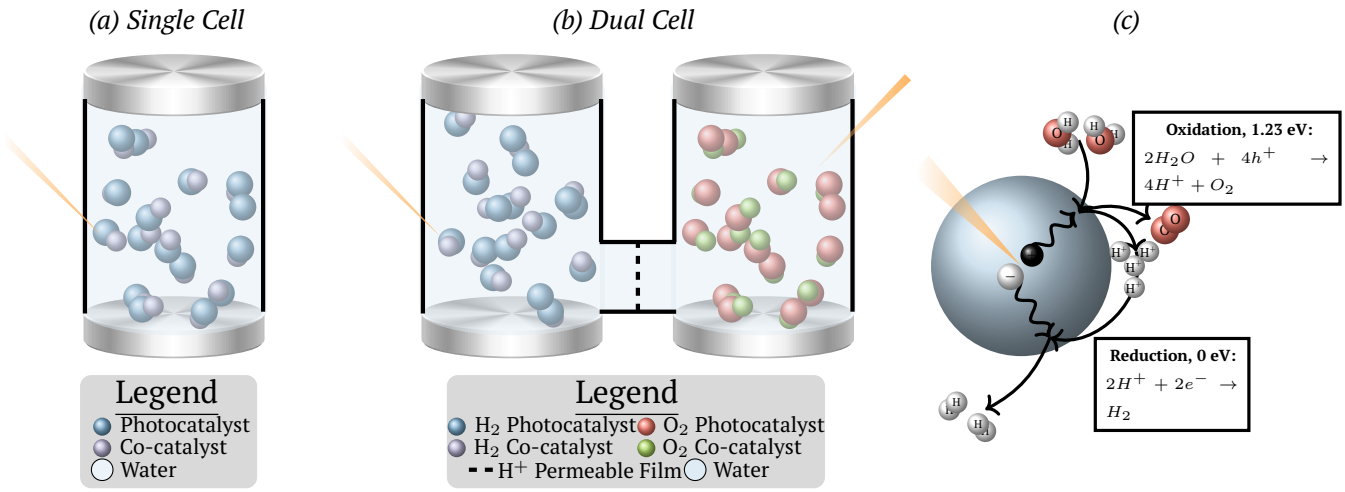


Figure 2.8: This figure shows the ideal experimental set-up of a single system in (a) and two system in (b) with a photocatalyst (and most likely a co-catatlyst) immersed in water and overall water splitting occuring. (c) shows a basic schematic of the reaction that would be taking place in the absence of a co-catalyst; when a co-catalyst is used the oxidation and/or the reduction occurs at the surface of it with the main catalyst acting as the photo-absorber.

[2]The binding energy of an exciton in organic materials is high and thus in the systems we consider charge separation will occur at the interface.

The reduction and oxygen reactions are outlined in Equations 2.7 and 2.8.

$$2H_2O + h^+ \rightarrow 4H^+O_2 \tag{2.7}$$

$$2H^+ + 2e^- \rightarrow H_2 \tag{2.8}$$

The whole reaction requires 2.46eV per molecule. This represents the minimum energy, as in real systems kinetic barriers must be overcome as well as additional forms of loss, such as recombination. A standard energy scale (Standard or Reversible Hydrogen Electron, SHE/RHE) is used in the field under which hydrogen reduction occurs at 0V and oxidation occurs at +1.23V. It is worth noting as well that Equations 2.7 and 2.8 provide no information about the actual mechanism for water splitting, just the products and the final reactants. There are several different mechanisms proposed for different systems[63] but that discussion is beyond the scope of this work. It is also worth noting that the systems studied can be incredibly complicated, and combined with the fact that the reaction itself is a four-hole reaction make obtaining meaningful data very difficult. To approach this, most work studies the reduction and oxidation reactions independently with the intention that either the gained understanding would be sufficient to design devices[63] or that the final device would consist of a reduction cell and oxidation cell and a membrane to exchange the necessary components[107]. This has the advantage of ensuring that the hydrogen and oxygen could be extracted safely without recombining. This work focuses on the hydrogen evolution side[14]. Whilst metal oxides have been demonstrated to split water directly[108], lots of work, particularly in recent organic work, uses a Sacrificial Electron Donor (SED) with a simpler or more understood mechanism[109]. This means that the experimental system that is closest to the majority of work in this field looks less like Figure 2.8 and more like that depicted in Figure 2.9. Figure 2.9 shows the case for the reduction reaction using Triethylamine as the SED. The exact reaction pathway in this case depends on the SED used. There have been a variety of SEDs used in the literature: the most common one used is triethanolamine[110, 111, 112, 113] but there is also triethylamine[13, 114], diethylamine[115], sodium sulfites[116], methanol[113, 114] and ascorbic acid[117]. Despite the key role SEDs play in the reaction and their potential to produce hydrogen themselves, they are rarely discussed or systematically investigated[109]. In Chapter 7 we discuss at length the role of the SED.

2.2.1.1 Measuring Device Performance

Photocatalysts are complex systems, espcially with the addition of SEDs, and as such finding metrics to compare and constrast performance between systems can be difficult. Work in the

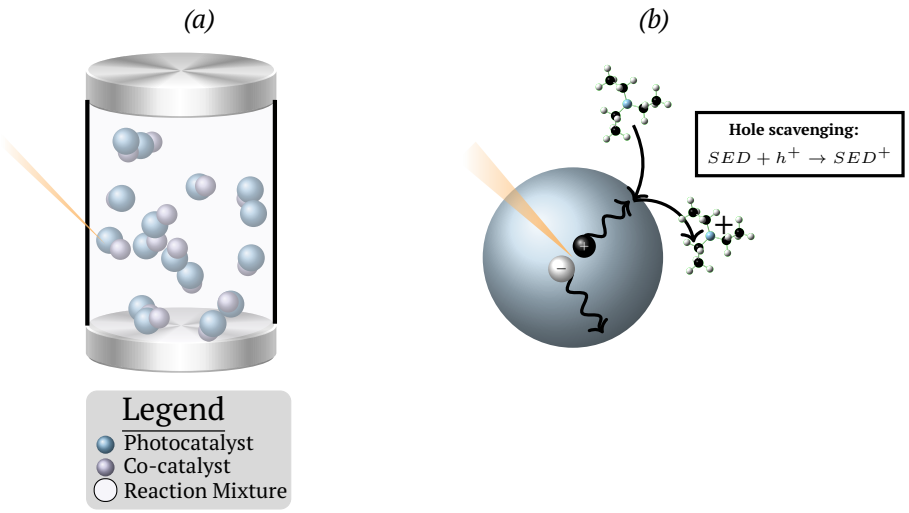


Figure 2.9: This figure shows the experimental set-up when hydrogen evolution is investigated using a Sacrificial Electron Donor that absorbs the charge and goes on to break down into products. One key difference is that the reaction occurs in a mixture of water and SED (and sometimes additional mixing agents) which will affect the Ph and polarity.

literature uses two commonly; Hydrogen Evolution Rate (HER) and the Apparent Quantum Efficiency (AQE). Hydrogen Evolution Rate is a simple metric: put the photocatalyst into the system and shine light on it, measure the amount of moles of hydrogen produced and divide it by the mass of photocatalyst used. For systems that are quite similar this can give a measure of comparison. There are however a few issues: if the light source changes then the data will not be comparable. In addition a polymer that absorbs slightly more coherently to the light source will appear to perform better without any mechanistic improvement in the catalysis. Apparent Quantum Efficiency provides a further step forward by calculating the amount of absorbed photons and determining the amount of them to generate hydrogen[3] expressed as a percentage.

2.2.2 Metal Oxide Systems

Inorganic photocatalysts remain the most studied and most effective for hydrogen evolution. Metal oxides have been known to induce photocatalytic oxidation of organic compounds for a long time but their application to water splitting stems from seminal work in 1972 by Fujishima and Honda [107]. This work demonstrated water splitting using TiO_2, in UV light and Pt within a photoelectrolytic cell. Since then a large body of work has sprung up considering metal oxide photocatalysts, primarily TiO_2 but also a variety of others such as ZnO,Fe_2O_3,WO_3, CdSe, and

[3]Since it takes two photon excitations for TEA as the SED it must be half the number of absorbed photons per hydrogen molecule.

GaAs[118]. TiO_2 has been particularly studied owing to a number of advantages: it is highly stable, nontoxic and can often be abundant[119, 120]. They can be limited by poor photoconversion efficiency due to exciton recombination and fast reverse reactions. One of their biggest limitations rests on the fact that the bandgap lies in the UV region of the light spectrum which means that only 4% of the solar spectrum can go on to generate hydrogen[119, 120, 118]. There have been a number of studies that attempt to address this issue by:

1. Doping the Metal Oxide with e.g. N [121].
2. Noble Metal loading. This is a common technique of adding noble metals grafted onto the metal oxide to make use of plasmonic effects[122].
3. Carbon-TiO_2 Composites. This works on the principle of combining carbon structures and the metal oxides[123].

We will not discuss further the ongoing work on metal oxides but we will note that overall water splitting using metal oxide photocatalyst systems have acheived up to 56% AQE in the UV and 30% AQE in the visible with ~1% solar-to-hydrogen (STH) efficiency. This translates to Hydrogen Evolutions rates maximum of 647,000 $\mu\text{mol}_{H_2}\text{h}^{-1}\text{g}^{-1}$ under visible light illumination for a Gold-Titanium Oxide nanohybrid system[124]. It is estimated that STH efficiency needs to be in excess of 10% to be practical for industrial roll-out of the technology[125].

2.2.3 Organic Photocatalyst Systems

2.2.3.1 Carbon Nitride Systems

In recent work, focus has moved to consider organic systems as potential photocatalysts. They are considered desirable as the wide chemical phase-space that exists opens up the potential of tuning the band gap to best match the solar spectrum. Initial work has focused on carbon nitrides when a study found both H_2 and O_2 evolution over the nitrides using a Sacrificial Electron Donor[126]. Carbon nitrides present some potential advantages to metal oxides; most notably, the absence of metal presents the possibility of increased sustainability[127]. Lots of work has been undertaken on carbon-nitrides, likely in part due to the flexibiltiy of synthesis that allows for many different nanostructured systems[128] in order to optimise separation of charge carriers or maximising surface area. A typical AQE of a carbon nitride based system has STH efficiency of 0.12%[129]. In a recent review of carbon-nitride systems they find an average of 3223 μmol_{H_2} g^{-1} of hydrogen evolution[128] with the best performing system being g-C3N4 nanorod system yielding 115180μmol_{H_2} g^{-1}[130].

2.2.3.2 Other Organic Systems

There have been a number of other photocatalyst systems that have emerged and been studied such as covalent organic frameworks[131] and triazine based frameworks[132], but this focuses on work that demonstrated the viability of certain conjugated microporous polymers[133]. These consist of conjugated polymers which have been extensively explored in other applications such as OPV and OLED but as yet remain largely unexplored for their potential as photocatalysts[134, 13]. Their synthesis has been shown to have fine control of some photophysical properties, in particular the optical gap. One consequence of this advantage is also an additional challenge: how to search within such a wide chemical phase space in order to optimise performance in a system that is poorly understood and where a variety of factors and polymer properties will affect final device performance. Whilst serious study of linear conjugater polymers as photocatalysts has only recently begun, the first demonstrations took place between 1985 and 1991 for a poly-p-pheneylene[135] and poly(pyradine-2,5diyl)[136]. These both experienced poor quantum efficiencies and hence low hydrogen evolution. Conjugated polymers were not studied again in this context until 2011 where poly(3-hexylthiophene) (P3HT) was considered as part of a study looking to enhance carbon-nitride's performance[137]. They found that whilst a combination of platinum, carbon nitride and P3HT exhibited hydrogen evolution, P3HT alone and with a platinum co-catalyst exibited very little (5μmol$_{H_2}$ g^{-1} with Pt co-catalyst).

The first conjugated polymers that exhibited perfomances of note were synthesised by the Cooper group in 2015 which observed a maximum of 117 μmol$_{H_2}$ g^{-1}[134]. Three linear polymers were studied that were analogous with a series of conjugated microporous structures, whilst for the peaks found with carbon nitrides or even metal oxides it suggested that linear polymers might be worth further study. This prompted a number of studies where a wide series of linear polymers were synthesised including phenylene, flourene and pyradine derivatives. The best performing polymer was a dibenzothiophene-phenylene polymer, named P7, which yielded 1492μmol$_{H_2}$ g^{-1} and an AQE of 7.2$\pm$0.3%. This performance, whilst not rivalling the best performing system of carbon nitride systems, is of the same magnitude as many of those systems. It is at this point in the story that this work begins, studying P7 and a derivative which was synthesised with no phenylene co-polymer, which was named P10. It was not immediately clear why either P7 or P10 would evolve hydrogen where others did not and this question is at the heart of the work in Chapter 6 and 7. The work on this was published[14] and since then

further studies have looked at close chemical analogues of P7 and P10[138]. It is worth at this point explaining that the exact choice of SED has often been seen as unnecessary of study; and where it has been studied, it has often been a case of trial and error and reporting the HER for the best performing case. As such, direct comparisons between reported HERs should be taken with a large amount of caution.

There is another element to experiments, particularly non-metal oxide photocatalysts, and that is the presence of heavy metals that act as a co-catalyst. This can either be present as a residual of the synthesis processor or can be added deliberately[14]. Recently a study systematically varied the concentration of a palladium co-catalyst to show that when it was removed from the system entirely the activity stopped[139]. As the concentration increased, the evolution quickly plateaued. Thus, it seems to be clear that it plays a key role in the hydrogen evolution, the exact nature of which remains an open research question. It should be noted that the illumination is beyond the heavy metals' ability to absorb the light and as such we can rule out that the heavy metals are playing the sole role in the hydrogen evolution.

3

Methods of Computational Materials

As previously discussed, the nature of investigating materials and their properties with an application focus involves understanding the physics and chemistry at many different scales. As such, this work has drawn on a number of different methods, often combining them to access the necessary understanding. In this chapter we outline how all of the different methods used in this thesis work. We will begin with the methods that are the most accurate and operate at the smallest scales, so called ab-initio methods, before moving on to discuss molecular dynamics and coarse-grained molecular dynamics. It is important to note that the methods outlined in this chapter are very far from a complete list of methods available to the computational materials scientist. I will do my best to point out other options that are often used in the literature.

3.1 *Ab initio* Methods

Ab initio methods refer to the principle that the method solves the calculation using only the physical constants as input, without relying on any empirical parameters. In practice most material properties are the result of quantum physics. We will first recall the fundamentals of quantum theory before discussing how different methods attempt to solve physical systems.

3.1.1 Quantum Theory

We have discussed how quantum theory states that behaviour of the system is embodied in solving the many-body Schrödinger equation:

$$\underbrace{-\sum_{e_i}\frac{\hbar^2}{2m_e}\nabla^2_{\mathbf{r}_{e_i}}\Psi}_{\text{Electron Kinetic Energy}}\underbrace{-\sum_{N_i}\frac{\hbar^2}{2m_{N_i}}\nabla^2_{\mathbf{r}_{N_i}}\Psi}_{\text{Nuclei Kinetic Energy}}+\underbrace{\sum_{e_i,e_j}^{i\neq j}\frac{e^2\Psi}{4\pi\varepsilon_0|\mathbf{r}_{e_i}-\mathbf{r}_{e_j}|}}_{\text{Electron-Electron interaction}}+\underbrace{\sum_{N_i,N_j}^{i\neq j}\frac{Z_iZ_j\Psi}{4\pi\varepsilon_0|\mathbf{r}_{N_i}-\mathbf{r}_{N_j}|}}_{\text{Nuclei-Nuclei interaction}}+\underbrace{\sum_{e_i,N_j}^{i\neq j}\frac{eZ_j\Psi}{4\pi\varepsilon_0|\mathbf{r}_{e_i}-\mathbf{r}_{N_j}|}}_{\text{Electron-Nuclei interaction}}=i\hbar\frac{\partial}{\partial t}\Psi, \tag{3.1}$$

where N_i is the i$^{\text{th}}$ nuclei, e_i is the i$^{\text{th}}$ electron, Z_i is the charge on the i$^{\text{th}}$ nuclei. This equation is not very tractable and making it so is the key to obtaining the behaviour of materials. It is

at this point that we use a physical approximation, known as the Born-Oppenheimer approximation. The Born-Oppenheimer approximation assumes that the motion of atomic nuclei and electrons can be decoupled. This means that the electronic states are well separated and that the nuclear degrees of freedom do not drive transitions between electronic states. This is sometimes rationalised by noting the fact that nuclei are much (~1800 times) heavier than electrons and thus will move much slower. The mathematical consquence of this approximation is that we can search only for wavefunctions of the form:

$$\Psi(\mathbf{r}_{e_1}, ..., \mathbf{r}_{e_N}, \mathbf{r}_{N_1}, ..., \mathbf{r}_{N_1}) = \psi_e(\mathbf{r}_{e_1}, ..., \mathbf{r}_{e_N})\psi_N(\mathbf{r}_{N_1}, ..., \mathbf{r}_{N_N}). \tag{3.2}$$

This means that the impact of nuclei can be incorporated into a potential term in the many-body electronic Schrödinger Equation which is given by:

$$-\sum_{e_i} \frac{\hbar^2}{2m_e} \nabla^2_{\mathbf{r}_{e_i}} \Psi_e + \sum_{e_i,e_j}^{i\neq j} \frac{e^2\Psi_e}{4\pi\varepsilon_0|\mathbf{r}_{e_i} - \mathbf{r}_{e_j}|} + \sum_{e_i} V(\mathbf{r}_{e_i})\Psi_e = i\hbar\frac{\partial}{\partial t}\Psi_e, \tag{3.3}$$

where V is the potential formed by the nuclei which are stationary from the perspective of the Born-Oppenheimer approximation. It is within this approximation that the two methods for solving this equation for reasonable atomic systems arise: Hartree-Fock based methods and Density Functional Theory. We shall now outline both of these in the next two sections.

3.1.2 Hartree-Fock

Hartree-Fock theory begins with the many-body electronic Schrödinger Equation, Equation 3.3. We attempt to solve this using normal methods for partial differential equations and some physical intuition. This intuition involves us identifying a form for the electronic wavefunction, Ψ_e. Slater[140] offered the following approach: assume the wavefunction can be written as the determinant of a matrix of single-electron particle wavefunctions ψ_i:

$$\Psi_e^{\text{HF}} = \frac{1}{\sqrt{N!}} \begin{vmatrix} \psi_1(\mathbf{r}_1) & \psi_2(\mathbf{r}_1) & \dots & \psi_N(\mathbf{r}_1) \\ \psi_1(\mathbf{r}_2) & \psi_2(\mathbf{r}_2) & \dots & \psi_N(\mathbf{r}_2) \\ \psi_1(\mathbf{r}_3) & \psi_2(\mathbf{r}_3) & \dots & \psi_N(\mathbf{r}_3) \\ \vdots & \vdots & \ddots & \vdots \\ \psi_1(\mathbf{r}_N) & \psi_2(\mathbf{r}_N) & \dots & \psi_N(\mathbf{r}_N) \end{vmatrix}. \tag{3.4}$$

This is known as a Slater determinant. For clarity we have suppressed the spin part of the wavefunction. The advantage of this approach is that it makes Ψ_e^{HF} antisymmetric in line with the fermionic behaviour of electrons by construction. This ansatz of a wavefunction is then used to find the expectation value of the Hamiltonian operator (which is the total electronic energy of the system). Calculus of variations is then used to find equations that each of the

single particle wavefunctions must obey:

$$\left[-\frac{\hbar^2}{2m_e}\nabla_i^2 + V\right]\psi_i(\mathbf{r}) + \frac{e^2}{4\pi\varepsilon_0}\left(\int \frac{\rho(\mathbf{r}') - \rho_i(\mathbf{r}')}{|\mathbf{r}-\mathbf{r}'|}d\mathbf{r}'\right)\psi_i - \frac{e^2}{4\pi\varepsilon_0}\sum_{j\neq i}\left(\psi_j \int \frac{\psi_j\psi_i}{|\mathbf{r}-\mathbf{r}'|}d\mathbf{r}'\right) = \epsilon_i\psi_i(\mathbf{r}), \tag{3.5}$$

where $\rho(\mathbf{r})$ and $\rho_i(\mathbf{r})$ is the total system and single electron density respectively. They can be related to the wavefunctions as:

$$\rho_i(\mathbf{r}) = |\psi_i|^2 \tag{3.6}$$

$$\rho(\mathbf{r}) = |\Psi_e|^2 = \sum_i^N |\psi_i|^2 \tag{3.7}$$

We can see from this why the Hartree approach is called a mean field approach as we have accounted for the interactions between electrons by having each electron interact with the average electron cloud before subtracting the part it contributes (and the electron doesn't interact with itself). The third term in Equation 3.5 is often called the Hartree potential. It describes Coulomb interaction of an electron with all the other electrons in the mean-field. The last term in Equation 3.5 has no classical parallel as it arises from the asymmetry requirement of fermionic behaviour. It represents the energy associated with exchanging two electrons and as such is called the exchange (or Fock) term. We can reframe the Fock term by interchanging the integration and summation, and then a small trick as follows:

$$-\frac{e^2}{4\pi\varepsilon_0}\sum_{j\neq i}\psi_j\int\left(\frac{\psi_j\psi_i}{|\mathbf{r}-\mathbf{r}'|}\right)d\mathbf{r}' = -\frac{e^2}{4\pi\varepsilon_0}\int\left(\sum_{j\neq i}\frac{\psi_j\psi_i}{|\mathbf{r}-\mathbf{r}'|}\psi_j\right)d\mathbf{r}' \tag{3.8}$$

$$= -\frac{e^2}{4\pi\varepsilon_0}\int\left(\sum_{j\neq i}\frac{\psi_j(\mathbf{r}')\psi_i(\mathbf{r}')}{|\mathbf{r}-\mathbf{r}'|}\frac{|\psi_i(\mathbf{r})|^2}{|\psi_i(\mathbf{r})|^2}\psi_j\right)d\mathbf{r}' \tag{3.9}$$

$$= -\frac{e^2}{4\pi\varepsilon_0}\psi_i(\mathbf{r})\int\left(\frac{\rho^X(\mathbf{r},\mathbf{r}') - \rho_i(\mathbf{r}')}{|\mathbf{r}-\mathbf{r}'|}\right)d\mathbf{r}' \tag{3.10}$$

where $\rho^X(\mathbf{r},\mathbf{r}') = \sum_{i=1}^{N}\frac{\psi_j^*(\mathbf{r}')\psi_i(\mathbf{r}')\psi_j(\mathbf{r})}{\psi_i(\mathbf{r})}$ and is a non-local charge density. It is this term that is difficult to deal with since it is orbital dependent (depends on i). Finally then we have our Hartree-Fock equation:

$$\left[-\frac{\hbar^2}{2m_e}\nabla_i^2 + V + \frac{e^2}{4\pi\varepsilon_0}\left(\int\frac{\rho(\mathbf{r}') - \rho_i(\mathbf{r}')}{|\mathbf{r}-\mathbf{r}'|}d\mathbf{r}'\right) - \frac{e^2}{4\pi\varepsilon_0}\int\left(\frac{\rho^X(\mathbf{r},\mathbf{r}') - \rho_i(\mathbf{r}')}{|\mathbf{r}-\mathbf{r}'|}\right)d\mathbf{r}'\right]\psi_i(\mathbf{r}) = \epsilon_i\psi_i(\mathbf{r}). \tag{3.11}$$

We can see from this that the self interaction terms cancel each other out leaving us with:

$$\left[-\frac{\hbar^2}{2m_e}\nabla_i^2 + V + \frac{e^2}{4\pi\varepsilon_0}\int\frac{\rho(\mathbf{r}')}{|\mathbf{r}-\mathbf{r}'|}d\mathbf{r}' - \frac{e^2}{4\pi\varepsilon_0}\int\frac{\rho^X(\mathbf{r},\mathbf{r}')}{|\mathbf{r}-\mathbf{r}'|}d\mathbf{r}'\right]\psi_i(\mathbf{r}) = \epsilon_i\psi_i(\mathbf{r}) \tag{3.12}$$

This cancellation of errors is one key reason why post Hartree-Fock methods are still used despite being computationally more expensive than DFT, which we will discuss in the next section. We know that the Hartree-Fock energy will be an upper bound for the real ground state

energy. The difference between the real ground-state energy and the Hartree-Fock energy is called the correlation energy. This name arises from the fact that the difference originates in how contrasting the real system is from a mean-field. There are a number of post Hartree-Fock developments that attempt to bring this difference down but at increasing computational cost. We do not use Hartree-Fock directly in this thesis (nor post Hartree-Fock). Hartree-Fock nominally scales as N^4 for system size however in practice approximations can be used to achieve linear scaling [141]. Post Hartree-Fock formally scales between N^5 and N^7 but methods have been employed to obtain linear and near linear scaling for both perturbation (MP2, MP4 etc) and coupled cluster methods[142, 143, 144, 145].

3.1.3 Density Functional Theory

Density Functional Theory (DFT) makes use of a similar train of thought to Hartree-Fock but alongside the idea that fully solving the Schrödinger Equation provides more information than we are actually interested in. Namely, we do not really need to know where each individual electron is; all that really matters is the electron density. Thus, DFT takes the approach of reframing the Hamiltonian and the wavefunction in terms of this electron density. The electron density can be defined as:

$$\rho(\mathbf{r}) = \int |\Psi(\mathbf{r}_1, ..., \mathbf{r}_N)|^2 \left(\sum_{i=1}^{N} \delta(\mathbf{r} - \mathbf{r}_i) \right) d\mathbf{r}_1 ... d\mathbf{r}_N. \tag{3.13}$$

It is not immediately clear why this would help us. However, Kohn, Sham and Hohenberg provided two theorems and a practical system that in fact make this approach useful[146, 147] which have since been rigourously generalised[148, 149]. They are:

1. The electron-nuclei interaction operator, the third term in Equation 3.3, is a unique (up to a constant) functional of the ground state electron density. Thus for a given set of nuclei that gives rise to an external potential on the electrons there is a single ground state electron density function.

2. The energy functional produces the lowest energy if and only if the ground state density is the true ground state density. This theorem in itself does not tackle how to represent the potential and so a more useful proof can be found in [148] which also solves the V-representability problem.

We shall not outline the proofs here as they are well covered elsewhere[150, 151, 152]. Determining the functional has been a focus of ongoing work ever since the formulation of DFT and it remains an unsolved problem[153]. We know that it must contain a term that accounts

for the kinetic energy of the electrons and a term accounting for the electron-electron interaction. Functional theories like this existed long before Kohn and Sham but tended to have poor results[154, 155, 156]. The kinetic energy of the electrons is a large component of the total energy and tended to be poorly mapped in this approach. Kohn and Sham's approach was to introduce a fictitious set of non-interacting orbitals ϕ_i, called Kohn-Sham orbitals. These orbitals are such that the electron density can be written as:

$$n(\mathbf{r}) = \sum_{i=1}^{N} |\phi_i(\mathbf{r})|^2. \tag{3.14}$$

Due to these particles being non-interacting we can use the Slater Determinant we outlined in the previous section. Doing so allows us to write the kinetic energy of the system as:

$$T[n(\mathbf{r})] = \sum_i \left\langle \phi_i \left| -\frac{\hbar^2}{2m_e}\nabla^2 \right| \psi_i \right\rangle. \tag{3.15}$$

The electron-electron interaction is slightly more tricky as there are terms we can easily calculate and terms that are less clear. The clearer term is the Hartree term, the electron cloud's interaction with itself, which will include some erroneous self-interaction. The other part is called the Exchange-Correlation term due to the behaviour it must account for, namely the exchange property dictated by the fermionic behaviour (exchange) and from coloumbic repulsion that is not accounted for in the Hartree term (correlation). The exact form of this Exchange-Correlation term is unknown and is a very active topic of research [153]. It has to tackle three things:

1. Account for deviations due to the approximation of the kinetic energy in Equation 3.15.
2. Cancel out the self-interaction error introduced by the Hartree term.
3. Account for Exchange-Correlation effects.

3.1.3.1 Exchange-Correlation Approximations

Just because the exact form remains unknown however does not mean that we can't make some approximations, and in fact many of the approximations produce results that are not too inaccurate. Working on new functional forms for the exchange-correlation remains a very active research field[157, 158].

Local Density Approximation (LDA)

We know from Hartree-Fock that in a uniform system the exchange contribution to total energy can be written as $E_x = \frac{3}{4}\frac{e^2}{\pi}k_f N$ where k_F is the Fermi level momentum. We use this in what is

known as the local density approximation (LDA) because it is based on the assumption that, locally, the system has the same energy as a uniform electron gas. This allows us to write an exchange functional term as:

$$E_x[n] = -\frac{3}{4}\left(\frac{3}{\pi}\right)^{\frac{1}{3}} e^2 \int n(\mathbf{r})^{\frac{4}{3}} d\mathbf{r} = \int \epsilon_X^{LDA} n(\mathbf{r}) d\mathbf{r} \tag{3.16}$$

In the LDA XC approach we then make a similar choice for the correlation part, that it will follow the same functional form as the exchange part, namely that the correlation of the whole system can be made by integrating the correlation component of a uniform electron gas[159].

$$E_{xc}[n] = \int \epsilon_{xc}^{LDA} n(\mathbf{r}) d\mathbf{r} \tag{3.17}$$

There are a number of different functional forms of the LDA and the most commonly used is the one formulated by Perdew and Zunger[160]:

$$E_{xc}[n] = \frac{1}{2}\int\int \frac{n(\mathbf{r}) g(\mathbf{r}, \mathbf{r}')}{|\mathbf{r} - \mathbf{r}'|} d\mathbf{r}' d\mathbf{r} \tag{3.18}$$

where $g(\mathbf{r}, \mathbf{r}')$ is the density of the hole around an electron at $\mathbf{r}$ at $\mathbf{r}'$[159]. We summarise the LDA below:

- The LDA fails to fully cancel out self-interaction. This leads to energy gaps that are structurally underestimated by DFT.
- The LDA is inherently local and as such doesn't capture physical phenomena that are inherently non-local, such as the Van der Waals interactions.
- The LDA has assumed that the density is slowly varying across all space and this is in general very unlikely to be true. As it happens as a result of spherical averaging this approximation turns out to be surprisingly successful[161].

Generalised Gradient Expansions (GGA)

The next approximation we will consider is the Generalised Gradient Expansions (GGA). This approach is designed to tackle the short-coming of the local nature of the LDA. As we have discussed, the LDA does not account well for quickly changing electron densities. One way of dealing with this is to consider the LDA as the zereoth order of an expansion and consider extra terms which include the gradient of the electron density, so:

$$E_{xc}^{\text{GGA}}[n] = \int \epsilon_{xc} \left(n(\mathbf{r}, \nabla n(\mathbf{r})\right) d\mathbf{r} \tag{3.19}$$

This extra freedom in the form of the exchange-correlation function can be parameterised in a number of ways and the best form is still a matter of some debate[162]. Two common and important GGA functionals are BLYP[163] and PBE[164]. PBE differs from BLYP in that no empirical paramaterisation is employed and as such has wide applicability and, unlike BLYP, is still commonly used.

meta-Generalised Gradient Expansions: meta-GGA

The next logical extension is to allow the functional to be not just a function of the electron density and its gradient (as in the GGA approach) but also of the kinetic energy density $T = \sum_i \frac{1}{2}|\nabla\phi_i|^2$. So we have:

$$E_{xc}^{\text{GGA}}[n] = \int \epsilon_{xc}\left(n(\mathbf{r}, \nabla n(\mathbf{r}), T\right) d\mathbf{r}. \tag{3.20}$$

It is worth noting that this is the second order expansion as the kinetic energy is a function of the second-order gradient of the density. Such meta-GGA functions are considered to be a step up in accuracy and are considered to be the most accurate of the pure DFT methods. Functionals of this type include M06-L[165] and TPSS[166].

Hybrid Functionals

At this stage in the development of these methods it was noted that Hartree-Fock (HF) methods have the opposite errors to DFT, with HF tending to under-bind atoms and predict gaps that are too large, whereas DFT tends to over-bind atoms and underestimate band gaps. Thus on a simplistic level a functional that is able to combine the two approaches in some way could in principle provide a cancellation of errors. There is no systematic way of knowing how much (if at all) different amounts of HF being included will improve the performance overall. One of the more common functionals, particularly in organic chemistry, is B3LYP[167, 163, 168, 169]. B3LYP uses the DFT approach from BLYP as we discussed above whilst adding 20% of HF. Another important class of hybrid is a range-separated functional, one where DFT is used fully for long range parts. One we use in this work is ωB97XD[170, 171] which has good performance, in particular for charge transfer processes and for including some of the Van der Waals interaction[172]. In addition, hybrids can also be built up from a meta-GGA basis and the Minnesota functions are a commonly used example of this with good performance records[173, 174, 175, 176].

Basis Sets

One thing all methods require, including Hartree-Fock, is a set of orbitals to use as a basis-set for the calculation. There are a variety of different approaches for the choice of basis-set:

- Orbitals based on Slater functions (STOs). These provide long and short range behaviour and are quite accurate, although the computation is intensive.

- Gaussians centered on the nuclei (sometimes abbreviated to GTOs). Gaussian based basis-sets are very commonly used by quantum chemists. They have the advantage of the Gaussian product theorum which makes them very easy to compute. However, they are less accurate than STOs.

- A linear combination of enough GTOs to emulate the behaviour of an STO.

In addition to these, which represent the different forms the orbitals take, we also have the choice of how many to select. In a minimal case we use one basis function for each atomic orbital that there is, but this usually is not sufficient for reasonable accuracy. Moving up in complexity we could use two basis functions for every atomic orbital; this is referred to as the double-ζ level, and in addition we can keep adding functions per atomic orbital to give the triple-ζ and so on levels of basis-set size. In addition to this there is also the split-valence approach which uses the fact that the core orbitals can be more accurately represented by a single function. This approach has one function for every core atomic orbital and more than one for valence atomic orbitals. We can also ensure that some of the functions have wider ranges; these are referred to as diffuse functions and are particularly necessary when we are dealing with anions. In this work we use two basis-set types: the Pople basis sets[177] and the Dunning correlation-consistent basis sets[178]. Specifically, in the Pople set, we use 6-311G and 6-311+G which are split-valence triple-ζ basis sets with and without the addition of diffuse functions respectively. In the Dunning correlation-consistent basis set we use cc-pVDZ and aug-cc-pVDZ which is a polarised valence double-ζ basis set with and without diffuse functions respectively. The advantage of the latter is that they are designed to converge systematically as we move towards a complete basis set and as such extrapolation to the infinite basis set level is possible[178]. They can, however, sometimes find it hard to reach convergence and so often require geometry optimisations at different levels of theory first.

Summary of accuracy consideration DFT approaches

In this section we have outlined the full complexity of DFT (and HF) methods and how the results depend on a wide array of factors that are often highly system dependent. One way of visualising this, based on Perdew's DFT Jacob's Ladder [3] is shown in Figure 3.1. It is important to note that, especially nearer the top of the ladder, it becomes hazy and very situation-dependent as to what level is more accurate[179, 180]. For example, will it improve the accuracy of our systems to choose a larger basis set or to rely on functionals with long-range corrections? The calculations we perform in this work all start at the fourth "rung" up the ladder. We choose to do this in part because we are calculating differences between calculated energies, and this requires a higher level of accuracy.

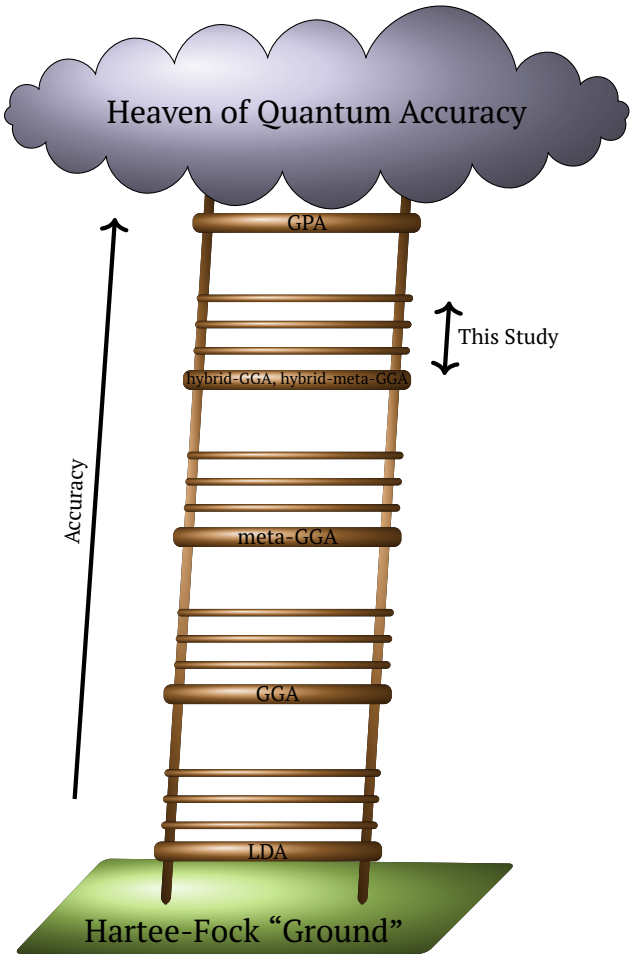


Figure 3.1: This depicts the chemical understanding of levels of theory, based on that of Perdew [3], and its relation to the ideal "heaven" of chemical accuracy. Larger rungs represent different levels of DFT. We carry out our entire study around the fourth main rung and do this because of the complex nature of what we want to investigate. Smaller rungs represent improvements within that DFT treatment such as more complete basis sets or functionals that contain long-range corrections.

3.1.4 Limitations

DFT can be very powerful but has a few key drawbacks:

- It is expensive and therefore limited to smaller systems.
- It provides limited information on non-absolute zero (kinetics) behaviour [1].
- It treats long-range non-covalent interactions poorly.
- The lack of the "true" exchange-correlation functional means treatment of free negative charge is poor but can be compensated somewhat by use of hybrid functionals.
- DFT can only really provide information on trends given that it reproduces exact energies of band gaps poorly.[153]

3.2 Atomistic Molecular Dynamics

We have seen from the previous section on quantum chemical methods the options available for obtaining information about molecules, but we have also seen the limitations that the computational cost causes on system size and the difficulty of using it to research processes where kinetics are important. In addition to this we also note that whilst quantum mechanics is necessary to explain some of the phenomenon we see on the macroscale, it is also sometimes not necessary at all. In this space a new method is called for, and it is in this space that molecular dynamics sits. Unlike quantum chemical methods, molecular dynamics (MD) does not explicitly represent the electrons at all, subsuming them as partial charges focused on each atom. Each atom is treated classically as spherical objects that interact with each other according to interaction potentials or, equivalently, forces. They move according to Newtonian mechanics. There are a few different kinds of MD that differ in where they source the interaction forces from and in what they consider a single bead or object. These are shown in Table 3.1.

[1] As we make use of in this work, one can use frequency calculations to determine the vibrational modes and then occupy them up to $k_B T$ to provide some information, but it will not be as accurate as other methods such as MD.

MD type	Bead	Forces from	Formal Scaling
Ab Initio	Atoms	DFT, HF or post-HF each timestep	$\mathcal{O}(N^4)$-$\mathcal{O}(N^7)$
Atomistic	Atoms	Experimental & computational parameterisation	$\mathcal{O}(N\log N)$
United Atom	$CH/CH^2/CH^3$ groups	Experimental & computational parameterisation	$\mathcal{O}(N_{\text{Non-H}}\log N_{\text{Non-H}})$
Coarse-Grained	Atom Groups	Atomistic MD or Macroscopic Properties	$\mathcal{O}(N_{\text{groups}}\log N_{\text{groups}}$

Table 3.1: This table shows the different types of MD, outlining the minimal unit of each, how the forces are derived and consquently how that type formally scales computationally. It should be noted that, as discussed previously, linear scaling of ab initio *methods is available and thus in practice ab initio MD can be performed with $\mathcal{O}(N\log N)$. It is worth also noting that the overall cost of* ab initio *MD is much higher even if the scaling behaviour can be similar to Atomistic MD.*

Table 3.1 shows the different types of MD in order of decreasing accuracy and computational expense. At the most computationally intense end we have *ab initio* molecular dynamics which evolves the atoms according to MD but at every time step recalculates the forces on the atoms using an *ab initio* method, usually Hartree-Fock. This scales at about the same level as DFT but adds the ability to study the kinetics of the system. One way of understanding it is as a next step of the Born-Oppenheimer approximation which separates the behaviour of the nuclei and the electrons, and in *ab initio* MD the nuclei behaviour is abstracted again to be considered as classical. At the next level up we have the most commonly used type of MD: fully atomistic MD. The forces at this level arise from a complex paramaterisation that involves reproducing experimental properties and on occasion *ab initio* calculations about basic behaviours (such as the torsional potential). This type of MD allows much larger systems sizes than *ab initio* methods and is the primary method we use throughout this thesis. The next two levels are types of coarse-graining where the beads are groups of atoms that are parameterised either from atomistic MD (so called bottom-up approaches) or from macroscopic/microscopic thermodynamic properties (so called top-down approaches). In this section we explain how MD works, including the force-fields, but before doing so we briefly recap some concepts from statistical mechanics which are fundamental to MD.

3.2.1 Nuts and Bolts of MD

We now outline the fundamental mechanics of a MD system. We start with a system of N particles. Each particle interacts with each other particle via an interaction potential, $V(\mathbf{r}_1, \mathbf{r}_2, \ldots, \mathbf{r}_N)$. For simplicity MD usually considers the interactions as a sum of pairwise-potentials, meaning elements that involve more than two atoms. This gives the total potential on particle i as

$V_i(\mathbf{r}_1, \mathbf{r}_2, \ldots, \mathbf{r}_N) = \sum_{i=1} V_{ij}(\mathbf{r}_i^{N, i \neq j}, \mathbf{r}_j)$. Newton's equations of motion can be written using this potential for particle i as

$$-\nabla_{\mathbf{r}_i} V_i(\mathbf{r}_1, \mathbf{r}_2, \ldots, \mathbf{r}_N) = m \frac{d^2 \mathbf{r}}{dt^2}. \tag{3.21}$$

Naturally we have N such coupled equations. The potential interaction must account for all types of interaction between atoms including Van der Waals, Bonds, Angle and Dihedral as well as electrostatic interactions, demonstrated visually in Figure 3.2.

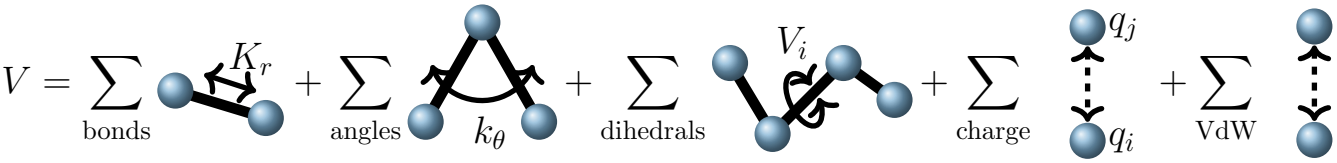


Figure 3.2: A diagrammatic representation of the atom-atom interactions in MD that must be specified in what is known as a force field.

As we have discussed in *ab initio* MD this interaction is calculated at each time step using an *ab initio* calculation, but in atomistic MD we need to have outlined every interaction before the simulation. The set of all these interactions with different atoms in different chemical contexts is referred to as a force field. It should be noted at this stage that because the force field is on the whole fixed for the duration of the simulation, any physical phenomenon that involves changes in the chemistry (such as deprotonation, or conformation dependence of charge distributions) cannot be easily modelled using MD. Some work does add force fields that allow for deprotonation-like events but they are a minority[181, 182].

3.2.2 Force Field Design and Optimisation

We have seen that to perform atomistic MD we require a force field that describes how every atom in the system interacts with every other atom. Considerable work has been undertaken in this area and there are a number of force field systems that have been developed. A selection of the force fields commonly used for the study of macromolecules in the literature are:

1. Optimised Potential for Liquid Simulations (OPLS) developed by Jorgensen and colleagues[183, 7]. It has been used on a wide array of systems and as such parameters for many molecules already exist in the literature.

2. Assisted Model Building with Energy Refinement (AMBER) developed by Kollman and colleagues[184]. Commonly employed for the study of proteins and DNA molecules.

3. Groningen Molecular Simulation (GROMOS). Originally developed alongside the Gromacs molecular dynamics code and used primarily for biomolecules[185].

4. Chemistry at Harvard Macromolecular Mechanics (CHARMM) which was originally developed in Harvard by Karplus and colleagues[186, 187, 188]. Initially developed for macromolecules but includes small molecule parameterisations.

This list is far from exhaustive and many, many more force fields exist, but outside of these four they are often either very system specific[189], polarisable[190, 191], include reactivity[192, 193], or are coarse-grained[194, 195]. For practicality, all of these force fields make a key simplification: Van der Waals parameters are considered properties of a particular atom type and not an interaction. What this means is that rather than having a list of parameters of every type of atom with every other type of atom, it instead includes only a single parameter set that specifies the interaction of the atom type with itself. In order to determine the parameters for interaction with non-alike atoms a scheme is needed, called a mixing rule. Each of these force fields use different mixing rules and for this reason force fields for a particular molecule should not be used in conjunction with a different force field system. In this thesis we exclusively use the OPLS force field because they were, as we will momentarily discuss, optimised to reproduce liquid properties.

3.2.2.1 OPLS

The functional form of OPLS is given as

$$V = V_{\text{bonds}} + V_{\text{angles}} + V_{\text{prop.dihedrals}} + V_{\text{imp.dihedrals}} + V_{\text{nonbonded}} \tag{3.22}$$

with,

$$V_{\text{bonds}} = \sum_{\text{bonds}} K_r (r - r_0)^2 \tag{3.23}$$

$$V_{\text{angles}} = \sum_{\text{angles}} k_\theta (\theta - \theta_0)^2 \tag{3.24}$$

$$V_{\text{prop.dihedrals}} = \frac{V_1}{2}\left[1 + \cos(\phi - \phi_0)\right] + \frac{V_2}{2}\left[1 - \cos 2(\phi - \phi_0)\right] + \frac{V_3}{2}\left[1 + \cos 3(\phi - \phi_0)\right] + \frac{V_4}{2}\left[1 - \cos 4(\phi - \phi_0)\right] \tag{3.25}$$

$$V_{\text{imp.dihedrals}} = \sum_{\text{imp.dihedrals}} \frac{1}{2} k_i (\phi - \phi_0)^2 \tag{3.26}$$

$$V_{\text{nonbonded}} = \sum_{i>j} f_{ij} \left(\frac{A_{ij}}{r_{ij}^{12}} - \frac{C_{ij}}{r_{ij}^{6}} + \frac{q_i q_j e^2}{4\pi\varepsilon_0 r_{ij}} \right) \tag{3.27}$$

where r_{ij} is the distance between atom i and atom j. The parameters K_r, k_θ and V_i represent the effective spring constants for bond stretching, angle changing and dihedral movement. Whilst

A_{ij} and C_{ij} represent the strength of Van der Waals interactions and q_i and q_j are partial charges. A_{ij} and C_{ij} can be linked to traditional Lennard-Jones parameters as:

$$A_{ij} = 4E_{ij}\sigma_{ij}^{12} \tag{3.28}$$

$$C_{ij} = 4E_{ij}\sigma_{ij}^{6} \tag{3.29}$$

The mixing rules for OPLS are:

$$A_{ij} = \sqrt{A_{ii}A_{jj}} \tag{3.30}$$

$$C_{ij} = \sqrt{C_{ii}C_{jj}}, \tag{3.31}$$

or equivalently

$$\sigma_{ij} = \sqrt{\sigma_{ii}\sigma_{jj}} \tag{3.32}$$

$$E_{ij} = \sqrt{E_{ii}E_{jj}}. \tag{3.33}$$

Non-bonded interactions are only included if the atoms in question are not joined by one or two bonds. In addition, non-bonded interactions are multiplied by a "fudge factor" of 0.5 if they are the first and last atom in a dihedral interaction. This fudge factor is meant to account for the interactions and behaviours which cannot be represented using pair-wise potentials[183]. Improper dihedrals are those that are added to atoms that are not bonded; they are added in order to apply additional contraints on conformation to match physical intuition, such as ensuring the planarised nature of conjugated systems.

The parameters in the OPLS force field are found via an initial set of scans using Hartree-Fock calculations with a 6-31G* basis set for bonded interactions. Non-bonded parameters were then fitted to ensure the force field optimally matched liquid experimental data[7, 183]. Over the years this approach has been reproduced for a number of molecules and there now exists a large number of parameters that can be chosen from.

3.2.2.2 Ensembles

An important aspect of molecular dynamics is ensembles. Ensembles are different possible states that can occur in statistical mechanics when certain macroscopic properties are held constant. In molecular dynamics there are three ensembles that are primarily used:

- Microcanonical Ensemble, also known as the NVE ensemble. It holds the number of particles, the volume and the total energy constant. It is an adiabatic process with no heat exchanged in or out of the system.

- Canonical Ensemble, sometimes known as the NVT ensemble. It holds the number of particles, the volume and the temperature constant.
- Gibbs or the Isobaric-Isothermal Ensemble. This holds the number of particles, the pressure in the system and the temperature constant. It is the ensemble that most closely represents the experimental "flask" conditions.

It is worth noting here that temperature is actually a macroscopic statistical property and thus holding it constant means in practice ensuring that the distribution of particle speeds matches what would be expected for a given temperature, which is that

$$\frac{1}{2}n_f k_B T = \sum_{i=1}^{N} \frac{1}{2} m_i |\mathbf{v}_i|^2 \tag{3.34}$$

where n_f is the number of degrees of freedom. The exact computational details of how this equivalence is maintained in simulations is dealt with in Section 3.2.3.5.

3.2.3 Computational Implementation

We have, in principle, outlined all we need to know physically about a molecular dynamics simulation. However, there are a number of details arising from the computational implementation that have important consquences for the quality and interpretation of the results. We shall discuss these here.

3.2.3.1 Periodic Boundary Conditions

Molecular dynamics simulations are finite boxes of a finite number of atoms: they can behave quite differently to bulk systems which may contain many orders of magnitude more atoms and molecules. One method to help alleviate these finite size effects in an MD simulation is to introduce a periodic boundary condition. This involves connecting the boxes' edges to each other such that if an atom goes too far it reappears at the other side of the box. Another way of conceptualising this is if we enforce that the box is really a hypersurface. The advantage of doing this is that because the atomic interactions decay quickly (and as we shall discuss shortly, a cut-off is often used for algorithmic efficiency), if the box is of a large enough size then any given atom or molecule will never see an edge or feel any self-interactions and as such will behave more closely to the bulk situation. This is, of course, more accurate the more homogeneous the system is. In some systems it might make physical sense based on the symmetry to use periodic boundary conditions in just two directions, for example if there is a wall or surface in one direction, whereas in some other systems, such as vacuum NVT calculations, one might not use periodic boundary conditions at all.

3.2.3.2 Interaction Cut-Offs

As we briefly touched on, implementations of MD often utilise a cut-off distance in the interaction distance. The reason for doing this is entirely one of computational efficiency; it allows the algorithm to not calculate the size of the potential when it will be very small and make little impact to the final result. So in the case of a Van der Waals interaction the potential could be mapped as follows:

$$V_{ij} = \frac{A_{ij}}{r_{ij}^{12}} - \frac{C_{ij}}{r_{ij}^{6}} \rightarrow \begin{cases} \frac{A_{ij}}{r_{ij}^{12}} - \frac{C_{ij}}{r_{ij}^{6}} & \text{for } r_{ij} \leq r_c \\ 0 & \text{for } r_{ij} > r_c \end{cases} \tag{3.35}$$

This is often not used as it contains a discontinuity at r_c, so in order to avoid this the whole potential is shifted by the potential at r_c as follows:

$$V_{ij} = \frac{A_{ij}}{r_{ij}^{12}} - \frac{C_{ij}}{r_{ij}^{6}} \rightarrow \begin{cases} \left(\frac{A_{ij}}{r_{ij}^{12}} - \frac{C_{ij}}{r_{ij}^{6}}\right) - \left(\frac{A_{ij}}{r_{c}^{12}} - \frac{C_{ij}}{r_{c}^{6}}\right) & \text{for } r_{ij} \leq r_c \\ 0 & \text{for } r_{ij} > r_c \end{cases} \tag{3.36}$$

This could in turn be applied to Coulombic interactions, however, because these are longer-ranged a cut-off of this kind leads to neglecting effects that can have significant impact on the physics of a system. Of course this could be remedied by taking a much longer cut-off for these interactions, but instead a more sophisticated approach is often used.

When long-range interactions are deemed to be important a cut-off radius is still used and every interaction that occurs before that cut-off value is calculated directly, as before. Calculating the interactions beyond the cut-off value uses a different approach, the most common of which involves Fourier transformations into k-space. It works only for cases where periodic boundary conditions have been employed. The exact details and derivation of this approach shall be omitted but can be found in [196].

The choice of cut-off is decided in order to ensure it is large enough not to impact the physical behaviour, with a typical value between 1 and 1.5nm. Particular forcefields have been parameterised with a particular cut-off and too much deviation from that can lead to unpredictable behaviour.

3.2.3.3 Numerical Integrator

As we have discussed, MD is the process of evolving a system according to Newtonian mechanics and as such we require an algorithm that solves Newton's equations of motions in an efficient way. The most popular algorithm of choice is the velocity Verlet algorithm[197]. The algorithm works as follows: We know the position, velocity and acceleration at a time t ($\mathbf{r}(t)$,$\mathbf{v}(t)$,$\mathbf{a}(t)$) and we require these at a time $t + \Delta t$ where Δt is the time step. First we calculate the velocity at a time $t + \frac{1}{2}\Delta t$ as

$$\mathbf{v}\left(t + \frac{1}{2}\Delta t\right) = \mathbf{v}(t) + \frac{1}{2}\mathbf{a}(t)\Delta t. \tag{3.37}$$

If we now look at the expression for the position at time $t + \Delta t$

$$\mathbf{r}(t + \Delta t) = \mathbf{r}(t) + \mathbf{v}(t)\Delta t + \frac{1}{2}\mathbf{a}(t)\Delta t^2, \tag{3.38}$$

which we can immediately recognise as related to Equation 3.37, such that:

$$\mathbf{r}(t + \Delta t) = \mathbf{r}(t) + \mathbf{v}\left(t + \frac{1}{2}\Delta t\right)\Delta t. \tag{3.39}$$

The next step is to use the updated position to determine the updated acceleration via the potential.

$$\mathbf{a}(t + \Delta t) = -\frac{1}{m}\nabla V(\mathbf{r}(t + \Delta t)). \tag{3.40}$$

This step ensures that the interactions are accounted for. Finally then the algorithm uses all the previous steps to advance the velocity:

$$\mathbf{v}(t + \Delta t) = \mathbf{v}\left(t + \frac{1}{2}\Delta t\right) + \frac{1}{2}\mathbf{a}(t + \Delta)\Delta t. \tag{3.41}$$

This algorithm ensures that energy is conserved throughout and offers a good balance between speed and accuracy and as such is the most commonly used. The Runge-Kutta method is a much more intensive and more accurate method[198]. This work uses the velocity Verlet algorithm throughout.

There is an important element to this, and any numerical integrator: the time step. Choosing the time step is key, as too large and the errors will cascade, and too small and the simulations become too computationally intensive to be practical. The time step then should be chosen to accurately resolve the fastest of forces which in most cases are those involved in hydrogen bonds as they possess very short vibrational modes[199]. Sometimes, if it is deemed that it will

not affect the physics of interest, the hydrogen bonds are frozen in order to allow for a higher time step. In this work we use a time step of 1fs throughout.

3.2.3.4 Constraints

At different points within this work we also utilise constraints. Constraints are where certain coordinates are held in place, and these can include:

- Positions coordinates. We use this to aid for speedy equilibriation of oligomers in solution. By freezing the coordinates we can allow the solvent to equilibriate first.
- Bond constraints. As we have discussed it may useful to freeze the movement of hydrogen bonds in order to use higher time steps.
- Angle constraints. We use this to constrain PFO into a planarised conformation in Chapter 5.

3.2.3.5 Thermostats and Barostats

Thermostats and barostats algorithms are the names given to the algorithms that enforce a constant temperature and pressure respectively. There are a number of different types of thermostat and barostat that we will outline; they have different advantages and disadvantages and must be carefully considered.

Thermostat: Velocity rescaling

The most basic system for controlling the temperature of an MD system is the velocity rescaling system. This procedure involves explicitly modifying the velocities of the atoms at a given time step if the instantaneous system temperature deviates too much from the desired temperature. In this system the system temperature is calculated every N time steps. The velocities are all rescaled by a factor λ which is given by:

$$\lambda = \sqrt{1 - \frac{\alpha}{T_t}}. \tag{3.42}$$

where T_t is the thermostat's target temperature and α is how close to the desired temperature the rescaling should get. For exact matches, α would be one. This procedure is the simplest algorithmically that one could decide on in order to keep the temperature constant, however, it has some limitations in that it is considered to introduce a number of unphysical effects. This

stems from the fact that the velocities of all atoms are scaled in the same way and thus thermal fluctuations are intrinsically non-Boltzmann in their distribution. This severely limits the physical accuracy of the dynamics of the particles. For this reason velocity rescaling is rarely used.

Thermostat: Berendsen

One of the more commonly used thermostats is the Berendsen thermostat[200]. The Berendsen thermostat operates in a very similar way to the velocity rescale algorithm but attempts to reduce the "harshness" of the process in order to minimise the impact of the unphysical rescaling. The rescaling takes place exponentially via a relation:

$$\frac{dT}{dt} = \frac{T_t - T(t)}{\tau} \tag{3.43}$$

where τ is a parameter which sets the severity of the coupling between the system and the heat bath. The scaling factor for the velocity is then given by:

$$\lambda = \sqrt{1 + \frac{\Delta t}{\tau}\left(\frac{T_t}{T(t)} - 1\right)} \tag{3.44}$$

It is worth noting that setting the coupling to be the same as the time step reproduces the velocity rescaling algorithm, and if we take $\tau \to \infty$ then we will turn off thermostat behaviour altogether. Berendsen is a fast, efficient algorithm that reproduces the ensemble average accurately but will not manage to reproduce thermal fluctuations accurately.

Thermostat: Nosé-Hoover

One of the more common thermostats used for higher accuracy calculations (where more than average quantities are needed) is the Nosé-Hoover thermostat[201]. The Nosé-Hoover thermostat works by introducing a heat bath, as in the case of the Berendsen thermostat, but with a different coupling mechanism. The heat bath confers an extra degree of freedom on the Hamiltonian. This extra degree of freedom is a fictional dynamical variable, let's call it η, which physically is a kind of friction. This "friction" slows or accelerates particles until the particles on average meet the required temperature. The equations of motion (c.f. Eq 3.21) of the particles then become:

$$m_i \frac{d^2\mathbf{r}_i}{dt^2} = -\nabla V_i - \eta m_i \mathbf{v}_i \tag{3.45}$$

and we gain an additional equation of motion for the friction coefficient as

$$\frac{d\eta}{dt} = \frac{1}{Q}\left[\sum_{i=1}^{N}\frac{1}{2}m_i\mathbf{v}_i - \frac{1}{2}(3N+1)k_BT_t\right] \tag{3.46}$$

where Q is a parameter which controls the severity of coupling, i.e. how fast the relaxations to the temperature should be. The Nosé-Hoover algorithm requires a slight adjustment to the Verlet algorithm[202]. The Nosé-Hoover algorithm can be slightly unstable for systems far away from equilibrium and as such systems are sometimes equilibriated with either velocity rescaling or the Berendsen thermostat first. If a system has more than one conservation law in the real system then this approach will break down. In order to effectively use this system a "chain" of thermostats are used. What this means is that rather than a single additional parameter Q and a single new equation of motion, a set of M paramaters and M new equations of motion are introduced. Nosé-Hoover thermostats have long thermalisations and as such should be used on systems close to equilibrium. In this work, with simulations where only general conformation information is needed the Berendsen thermostat is used, but in cases where the energy of change is needed (see Free Energy calculations in Section 3.2.4.3) we use the Nosé-Hoover thermostat for the production run.

Barostat: Berendsen

A commonly used barostat is the Berendsen barostat[200]. It works analogously with the Berendsen thermostat. A macroscopic system maintains constant pressure by adjusting its volume. The Clausius virial theorem that links instantaneous pressure with microscopic quantities can be considered as:

$$P = \frac{2}{3V}\left(\sum_{i=0}^{N}\frac{1}{2}m_iv_i^2\right) - \frac{1}{2}\sum_{i<j}\mathbf{r}_{ij}\cdot\mathbf{F}_{ij}(\mathbf{r}_{ij}) \tag{3.47}$$

where $\mathbf{F}_{ij}$ is the force between i and j at r_{ij}. The Berendsen barostat works by adjusting the volume of the MD box at N time steps when the pressure is too high or too low. As such each cell length is scaled by a factor λ_P given by

$$\lambda_P = 1 - \frac{\gamma\Delta t}{\tau_P}\left(P_b - P(t)\right) \tag{3.48}$$

where γ is the isothermal compressability of the system usually taken to be that of water. The exact physical value is not of critical importance as it is modified by our choice of τ_p which is the barostat's relaxation time which governs how suddenly the barostat acts to redirect the pressure. P_b is the pressure the barostat is aiming for.

Barostat: Parrinello-Rahman

Another commonly used barostat is the Parrinello-Rahman barostat[203, 204]. This barostat does not rely on cubic cells, which is of particular interest to solid-state simulations (though in our work only the liquid state is considered). If the cell vectors are given by $\mathbf{a}, \mathbf{b}, \mathbf{c}$ then the volume of the box is given by

$$V = \det \mathbf{H} = \mathbf{a} \cdot (\mathbf{b} \times \mathbf{c}) \tag{3.49}$$

where $\mathbf{H}$ is a three by three matrix made of $\mathbf{a}, \mathbf{b}$ and $\mathbf{c}$. The equations of motion are then given by

$$\frac{d\mathbf{H}}{dt^2} = \frac{1}{Q}\left((\mathbf{P} - P_b\mathbf{I})V(\mathbf{H}^{-1})^T\right). \tag{3.50}$$

If fully accurate statistical ensembles are required then a mixture of Nosé-Hoover for the thermostat and Parrinello-Rahman for the barostat should be used.

3.2.4 Analysis Tools

Of course the importance of any simulation or computational work is the outputs, in order to confirm what physical information you can obtain from it. In this section we outline some of the common tools of analysis used on MD trajectories, ones that we make use of in this work.

3.2.4.1 Radial Distribution Function

A radial distribution function ($\rho(r)$) is the probability of finding an atom at a distance r relative to a completely uniform distribution. It can be considered as the ratio of the local number density $\rho(r)$ to the uniform (average) density ρ. It is averaged over all times in order to provide a statistically valid way of extracting the structure of the system. It is worth noting that the sharper the peaks the more ordered the system is. Liquids possess local ordering which means they tend to have a number of well-defined peaks. All radial distributions should tend to one as r tends to infinity (or in a finite MD system to the box size). In addition, rather than using atoms as the reference one can use the centre of masses of molecules. This can also be used to calculate a cumulative radial distribution function which counts the average number of atoms or molecules at a distance of r. We later make use of this to calculate the local volume fraction around an oligomer in a mixed solution.

3.2.4.2 Radius of Gyration

Another important quantity we consider in this work is that of the radius of gyration, r_g. The radius of gyration is a measure of how spread out the mass of an object is. It can be found by the root mean square of the distance of each atom from the centre of mass, all averaged over the simulation trajectory. A small r_g would symbolise that a polymer might be curled up tightly in a ball whereas a higher one would represent a stretched out conformation. This approach can also be readily applied to sidechains.

3.2.4.3 Free Energy Calculations

One of the key procedures we use in this work is to calculate the change in free energy as the result of some perturbation of the system. There are two cases we consider:

- Free Energy of Solvation: This involves perturbing the system by turning off interactions between the solute and solvent. It can be measured experimentally and gives us a measure of how much a solute prefers (or otherwise) being in the solvent relative to being in a gas. By comparing these quantities in different solvents it can also indicate where the solute might migrate to in systems of multiple solvents.

- Free Energy of Dihedral Restraints (or Planarisation). This work involves studying β-phase in PFO and as such planarisation plays a key role. By applying restraints that force the intermonomer dihedral to be planar and turning this restraint on and off we can get a value for the free energy cost (or gain) of planarising in different situations.

Both of these situations rely on the same procedure. We simulate a series of cases where the parameter of interest is scaled and then we perform a thermodynamic integration to obtain the total change in energy of the transition. This allows us to make meaningful quantitative statements about the situations of study but comes at a high computational cost. A large number of simulations need to be performed to ensure that there is adequate spacing between the 'off' case and the 'on' case.

3.2.5 Procedures

As we have discussed, for a trajectory to be meaningful it needs to have been properly equilibriated and have been run for enough time. In order to be consistent we keep to the same procedure for all the MD simulations we do. In this section we outline the two procedures: one for situations of just solvents, and one for oligomer-solvent systems. Figure 3.3 demonstrates

the procedure undertaken for systems of solvents in (a) and for systems of oligomer and solvents in (b).

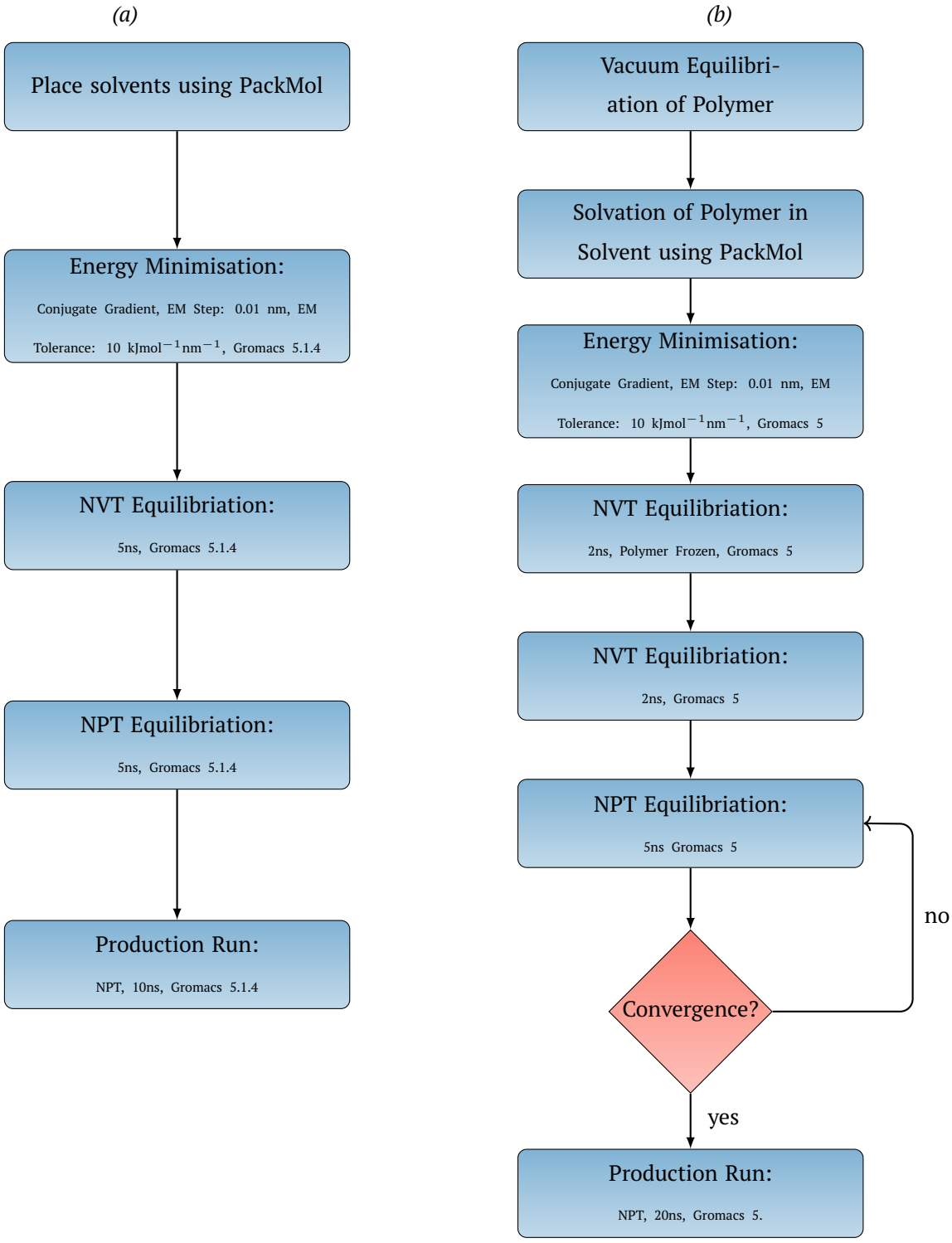


Figure 3.3: This schematic shows the procedure for generating production molecular dynamics trajectories for (a) systems of solvents only and (b) systems of oligomers and solvents. In (b) a convergence test is used to ensure that energy is conserved and the dihedral autocorrelations have reduced to zero. In some simulations, particularly persistence length calculations, would typically need longer than 5ns of equilibriation (~15-20ns).

3.2.6 Limitations

Molecular dynamics is an incredibly powerful tool but any use of it must keep in mind where it is likely to fail to produce physical results. We outline some of these limitations here:

- Many physical processes take place on time-scales that are inaccessible to MD. Improving the ability for MD to probe longer time and length scales is a highly active research area and can be categorised as follows: attempts to provide algorithm improvements to MD to improve the system size scaling behaviour[205]; improving the ability to make use of more or different hardware (through parallel processing or utilising GPUs)[206]; by using coarse-graining techniques to preserve only the interactions that are important to the physics of study. Some work in addition also looks at coarse-graining where a section of the system is treated atomistically but particles can cross over to be coarse-grained[207, 208, 209].

- Molecular dynamics follow the age old computer slogan "Garbage in, Garbage out". That is, the results that come out are only as good as the force field the user enters. There is considerable work that goes on into refining force fields and attempting to automate and streamline the search for a force field of a particular chemical structure. Force field development is at current a very labour-intensive approach and therefore makes MD hard to use for the screening of different molecules[210].

- The structure is fixed and determined by the force fields at the start of the simulation and as such bonds cannot be broken or formed. If the physics of interest involves this it can be hard to use MD as a tool. However, some work gets around this through either use of clever potentials that allow for a bond to break[192] or simply by simulating either side of the chemical reaction and thus not getting any information on the likelihood of reaction[211].

3.3 Summary

In this section we have outlined the two primary methods we use in this work: DFT and molecular dynamics. There are, of course, a number of other methods employed in materials modelling and we have chosen these because they provide the opportunity to study the systems effectively and efficiently. As can be seen from this chapter, each of the methods we use are optimised to produce different information and only by combining them can we effectively study the systems and physics of interest. One innovative way in which we combine data from both of these methods is seen in Chapter 7 where we use DFT to parameterise MD force fields of polymers, and use

MD to obtain information about the likely environment of the polymers before using that information in DFT calculations to obtain information about chemical reactions. This provides information that neither method alone would have been able to yield.

4

Molecular Dynamics of Multi-Phasic Systems of Solvents

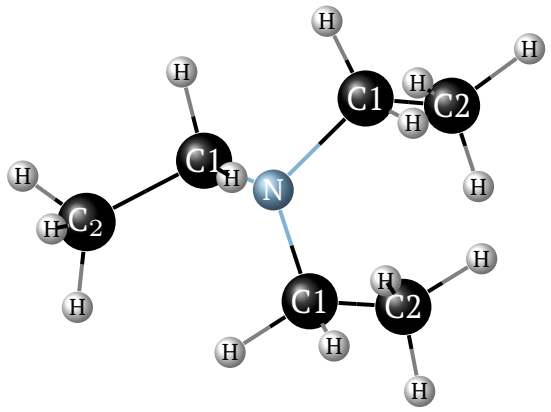
4.1 Introduction

In this Chapter we study solvents using the methods we come to use throughout this thesis. Solvents play a key role in many processes that involve organic polymers; they play a crucial role in the processing of films, and changes to the solvation environment can lead to significant microstructural variation and therefore performance of devices. We look in this chapter primarily at developing MD force fields for some organic solvents as well as water. We then study how well these force fields reproduce single-phase properties such as density and multi-phase properties such as free energies of solvation and mixing properties. We discuss the force field development in Section 4.2, before studying single-phase properties of the solvents in Section 4.3, two-phase solution systems in Section 4.4, and an important three-solvent mixture in Section 4.5.

4.2 Force Field Choice and Development

We have five solvents: Chloroform, Decalin, Water, TEA and Methanol. All of these have OPLS based force fields used in the literature except decalin. For water we choose the TIP4P model[5]. Triethylamine has been parameterised using MD with the OPLS force field before[4], and work has investigated its interactions with TIP4P OPLS water[212], thus we choose this force field. For methanol we use the OPLS force field which has been applied in many situations[6]. The models are shown and outlined in Figures 4.1, 4.2, 4.3, 4.4, 4.5 and 4.6 for TEA, Water, Methanol, Chloroform and Decalin (cis and trans) respectively.

(a)



(b)

Atom	q (e)	σ (nm)	ε (kJ/mol)
N	-0.63	0.33	0.711
C1	0.09	0.35	0.276
C2	-0.18	0.35	0.276
H	0.06	0.25	0.126
Overall	0.00	N/A	N/A

(c)

Bond	r_0(nm)	k_r (kJ/mol/nm^2)
N—C1	0.1448	159830
C1—C2	0.1529	112130
C1—H	0.109	142256
C2—H	0.109	142256

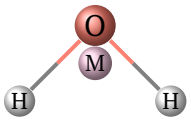
(d)

Angle	θ_0(deg)	k_θ (kJ/mol/rad^2)
N—C1—C2	109.47	235.14
C1—N—C1	107.20	216.73
N—C1—H	109.50	146.44
C2—C1—H	110.70	37.50
C1—C2—H	110.70	37.50
H—C1—H	107.80	138.10
H—C2—H	107.80	138.10

Dih. Angle	V_1(kJ/mol)	V_2(kJ/mol)	V_3(kJ/mol)
N—C1—C2—H	-4.238	-2.966	1.979
C1—N—C1—C2	1.741	-0.536	2.908
C1—N—C1—H	0.000	0.000	2.343
H—C2—C1—H	0.000	0.000	1.331

Figure 4.1: This figure outlines the force field used, from [4], for Triethylamine. a) shows the labelling scheme used, b) the partial charges, q, and Van der Waals parameters (σ, ε) for each atom, c) the bond equilibrium distance r_0 and spring constant k_r and d) the equilibrium angle (θ_0) and spring constant (k_θ) and dihedral Fourier parameters (V_1,V_2,V_3).

(a)



(b)

Atom	q (e)	σ (nm)	ε (kJ/mol)
O	0.00	0.315	0.649
H	0.52	0.00	0.00
M	-1.04	0.00	0.00
Overall	0.00	N/A	N/A

(c)

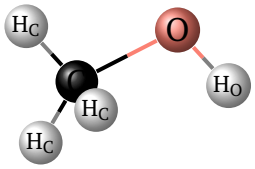
Bond	r_0(nm)	k_r (kJ/mol/nm^2)
O—H	0.096	502416
O—M	0.015	Virtual Site

(d)

Angle	θ_0(deg)	k_θ (kJ/mol/rad^2)
H—O—H	104.52	628.02

Figure 4.2: This figure outlines the TIP4P OPLS forcefield[5]. a) shows the labelling scheme used, b) the partial charges, q, and Van der Waals parameters (σ, ε) for each atom, c) the bond equilibrium distance r_0 and spring constant k_r and d) the equilibrium angle (θ_0) and spring constant (k_θ) and dihedral Fourier parameters (V_1,V_2,V_3). M is a virtual site whose position is held constant at 0.015nm away from the oxygen atom in the same direction as the two hydrogens.

(a)



(b)

Atom	q (e)	σ (nm)	ε (kJ/mol)
C	0.145	0.350	0.276
O	-0.683	0.312	0.711
H_C	0.040	0.250	0.126
H_O	0.418	0.00	0.00
Overall	0.00	N/A	N/A

(c)

Bond	r_0(nm)	k_r (kJ/mol/nm^2)
O—C	0.141	267776
O—H_O	0.095	462750
C—H_C	0.109	142256

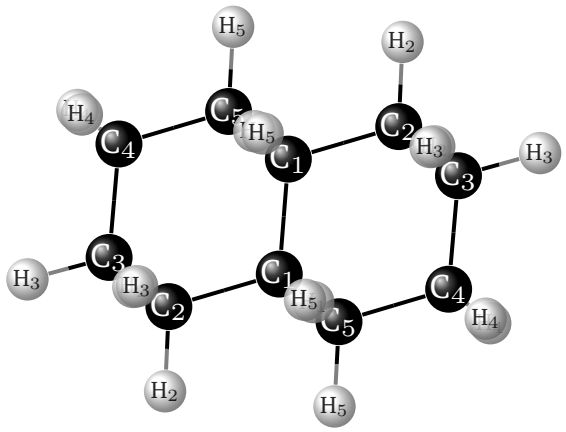
(d)

Angle	θ_0(deg)	k_θ (kJ/mol/rad^2)
O—C— H_C	109.5	292.88
C—O— H_O	108.5	460.24
H_C—C— H_C	107.8	276.144

Dih. Angle	V_1(kJ/mol)	V_2(kJ/mol)	V_4(kJ/mol)
HC—CT—OH—HO	0.941	2.824	-3.766

Figure 4.3: This figure outlines the force field used, from [6], for methanol. a) shows the labelling scheme used, b) the partial charges, q, and Van der Waals parameters (σ, ε) for each atom, c) the bond equilibrium distance r_0 and spring constant k_r and d) the equilibrium angle (θ_0) and spring constant (k_θ) and dihedral Fourier parameters (V_1,V_2,V_3).

(a)



(b)

Atom	q (e)	σ (nm)	ε (kJ/mol)
C1	0.240	0.355	0.293
C2	-0.156	0.350	0.277
C3	0.084	0.350	0.277
C4	-0.027	0.350	0.277
C5	-0.042	0.350	0.277
H1	-0.082	0.242	0.126
H2	0.016	0.242	0.126
H3	-0.024	0.242	0.126
H4	-0.002	0.242	0.126
H5	0.001	0.242	0.126
Overall	0.00	N/A	N/A

(c)

Bond	r_0(nm)	k_r (kJ/mol/nm^2)
C1—C1	0.1535	392459
C1—C2, C2—C3, C3—C4, C4—C5, C5—C1	0.1529	224262
All C—H	0.109	307106

(d)

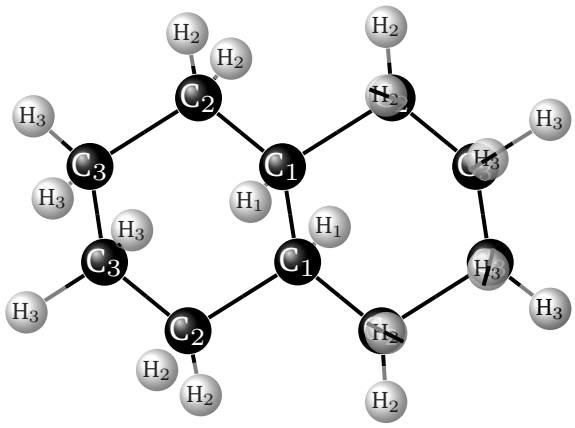
Angle	θ_0(deg)	k_θ (kJ/mol/rad^2)
C1—C1—$C_{2/5}$	111.00	527.184
C5—C1—C2	112.00	488.273
C2—C3—C4, C3—C4—C5	112.70	488.273
$C_{2/5}$ —C1—H, C1—C1 —H	107.00	292.880
C1—$C_{2/5}$—H	109.00	298.880
H—$C_{2/3/4/5}$—H	107.80	138.10

(e)

Dih. Angle	V_1(kJ/mol)	V_2(kJ/mol)	V_3(kJ/mol)	V_4(kJ/mol)	V_5(kJ/mol)	V_6(kJ/mol)
C2—C3—C4—C5, C2—C1—C1—C5, C5—C1—C1—C5, C2—C1—C1—C2	30.334	0.000	-30.334	0.000	0.000	0.000
C5—C1—C2—C3, C2—C1—C5—C4	2.929	-1.464	0.209	-1.674	0.000	0.000

Figure 4.4: This figure outlines the OPLS force field for cis-decalin. a) shows the labelling scheme used, b) the partial charges, q, and Van der Waals parameters (σ, ε) for each atom, c) the bond equilibrium distance r_0 and spring constant k_r and d) the equilibrium angle (θ_0) and spring constant (k_θ) and (e) dihedral Fourier parameters (V_1,V_2,V_3).

(a)



(b)

Atom	q (e)	σ (nm)	ε (kJ/mol)
C1	0.221	0.355	0.293
C2	-0.090	0.350	0.277
C3	0.028	0.350	0.277
H1	-0.063	0.242	0.126
H2	0.0015	0.242	0.126
H3	-0.010	0.242	0.126
Overall	0.00	N/A	N/A

(c)

Bond	r_0(nm)	k_r (kJ/mol/nm^2)
C1—C1	0.155	392459
C1—C2,	0.1529	224262
C2—C3,		
C3—C4,		
C4—C5,		
C5—C1		
All C—H	0.109	307106

(d)

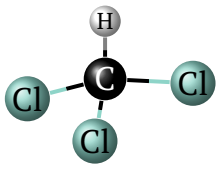
Angle	θ_0(deg)	k_θ (kJ/mol/rad^2)
C1—C1—C2	114.00	527.184
C2—C1—C2	112.70	488.273
C2—C3—C3	112.70	488.273
C2 —C1—H, C1-	107.00	292.880
—C1 —H		
C1—C2—H	110.00	298.880
H—$C_{2/3}$—H	107.80	138.10

(e)

Dih. Angle	V_1(kJ/mol)	V_2(kJ/mol)	V_3(kJ/mol)	V_4(kJ/mol)	V_5(kJ/mol)	V_6(kJ/mol)
C2—C3—C4—C5,	30.334	0.000	-30.334	0.000	0.000	0.000
C2—C1—C1—C5,						
C5—C1—C1—C5,						
C2—C1—C1—C2						
C5—C1—C2—C3, C2-	2.929	-1.464	0.209	-1.674	0.000	0.000
—C1—C5—C4						

Figure 4.5: This figure outlines the OPLS force field for trans-decalin. a) shows the labelling scheme used, b) the partial charges, q, and Van der Waals parameters (σ, ε) for each atom, c) the bond equilibrium distance r_0 and spring constant k_r and d) the equilibrium angle (θ_0) and spring constant (k_θ) and dihedral Fourier parameters (V_1,V_2,V_3).

(a)



(b)

Atom	q (e)	σ (nm)	ε (kJ/mol)
C	-0.3336	0.35	0.276
Cl	0.012	0.34	1.255
H	0.2976	0.250	0.126
Overall	0.00	N/A	N/A

(c)

Bond	r_0(nm)	k_r (kJ/mol/nm^2)
Cl—C	0.1781	205016
C—H	0.109	284512

(d)

Angle	θ_0(deg)	k_θ (kJ/mol/rad^2)
Cl—C—Cl	111.7	652.704
H—C—Cl	107.80	426.768

Figure 4.6: This figure outlines the OPLS force field for chloroform[7]. a) shows the labelling scheme used, b) the partial charges, q, and Van der Waals parameters (σ, ε) for each atom, c) the bond equilibrium distance r_0 and spring constant k_r and d) the equilibrium angle (θ_0) and spring constant (k_θ) and dihedral Fourier parameters (V_1,V_2,V_3).

As we discussed in Section 3.2.2, molecular dynamics is only as good as the force field chosen and as such must be validated in some way against experimental observables. All these force fields have been created and tested in the OPLS fashion but in this chapter we conduct some validation of our own, in tune with our specific needs. This means trying to ensure that the mixing behaviour of water, TEA and methanol is well modelled. In the next section we report tests on single phases, with comparisons to experimental data where it exists.

4.3 Single Phase Solvent Solutions

With the force fields in place we now simulate each of these solvents in isolation and select physical properties to help us validate them. This involves experimental data where we have access to it, and where we do not we use DFT.

4.3.1 Water

Water presents a particular challenge for MD owing to a particular sensitivity of the physical properties on small changes to how the interactions are modelled[213]. In addition, water ex-

hibits behaviours such as the fact that particular molecules are not stable and hydrogens will be routinely hopping between host molecules. As such there exist a large number of different models, each trying to reproduce different levels of these inter and intra molecular forces accurately, and which tend to achieve accuracy in reproducing different physical properties of water[214, 215]. We choose to use TIP4P, on account of it having previously been studied in conjunction with TEA[212]. As a first undertaking we simulate a box of TIP4P molecules in order to check the force field is performing as expected. In Table 4.1 we show molecular dynamics data for density, self-diffusion and free energy of solvations alongside DFT and experimental data.

	ρ_{298K}(kg/m^3)	Self-Diffusion (nm^2/ns)	ΔH_{Water}	ΔH_{TEA}
MD	991.0±0.3	3.27±0.09	-0.267±0.001	-0.106±0.001
Experiment	997.0[8]	2.57±0.022 [216]	-0.274[217]	N/A
DFT	N/A	N/A	-0.322	-0.142
% error exp	0.6	27.24	2.59	N/A
% error DFT	N/A	N/A	17.11	25.35

Table 4.1: This table shows results drawn from MD in comparisons with experimental data, where it is available, and DFT, performed using the infinite basis set approximation of the Dunning correlation consistent and the ωB97XD functional.

Figure 4.7 shows the RDFs compared with experimental data from [218, 8]. It should be noted that the RDF is not a directly measurable experimental quantity and as such the experimental data is likely to have broader peaks linked with the equipment's resolution.

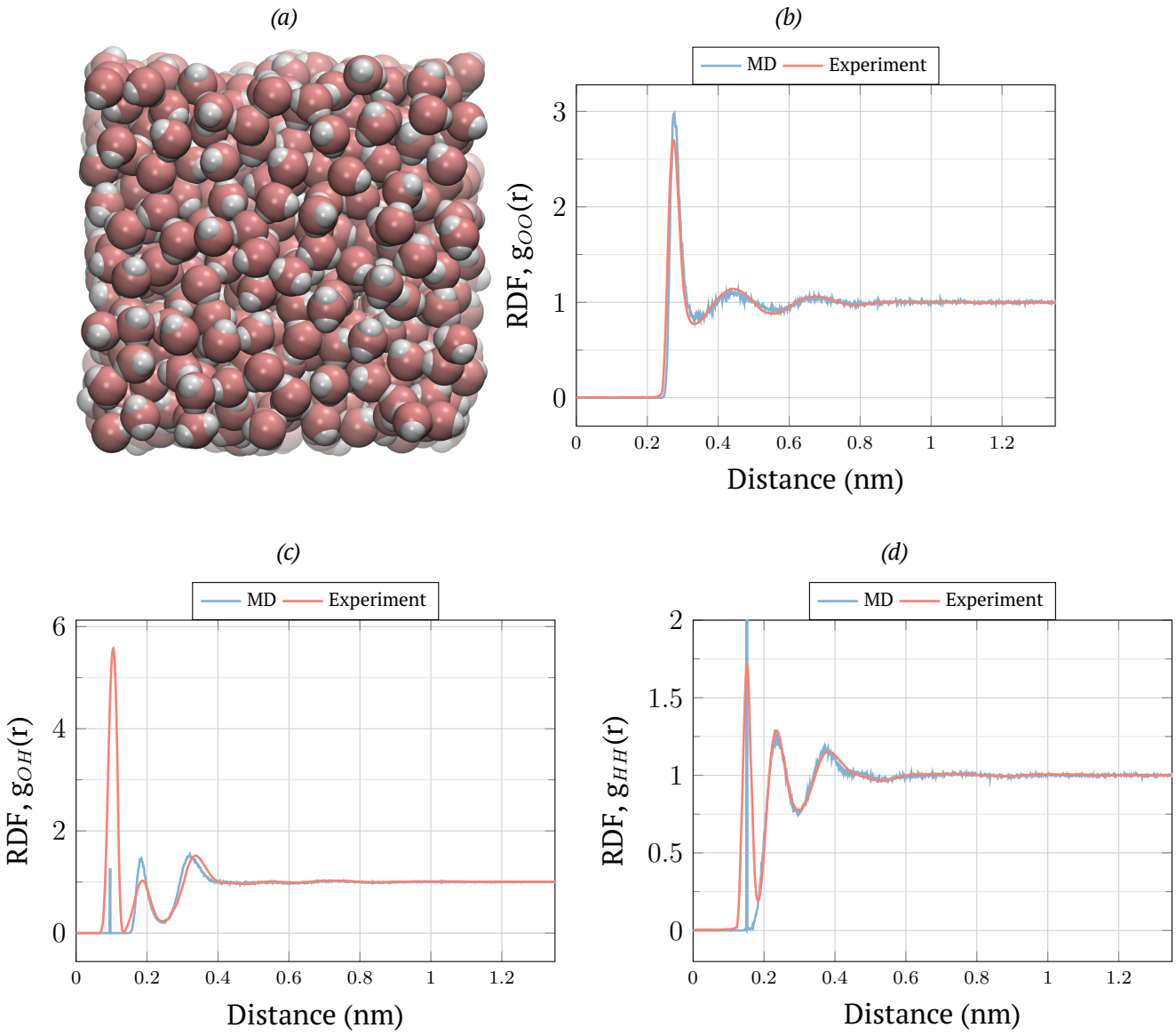


Figure 4.7: (a) shows the final state of the box of 686 water molecules, shown as Van der Waals Spheres, and a comparison between experimental RDFs[8] and MD RDFs for (b) oxygen-oxygen interactions, (c) oxygen-hydrogen interactions and (d) hydrogen-hydrogen interactions.

4.3.2 TEA

We simulate a box of 277 TEA molecules in order to examine its performance. There are several different physical quantities we could use to test the validity of the model. Since OPLS TEA has been extensively parameterised in order to maximise the accuracy of free energy calculations in other liquids we simply check that our implementation matches the literature[4] and DFT results. In addition we check the density of the liquid and the self-diffusion coefficient; all shown in Table 4.2. Figure 4.8 shows a snapshot of the box simulated alongside radial distribution functions, though unfortunately for TEA there are no experimental RDFs to compare to.

	ρ_{298K}(kg/m^3)	Self-Diffusion (10^5 cm^2/s)	ΔH_{Water}	ΔH_{TEA}
MD	740.97±0.05	1.65±0.12	-0.049±0.003	-0.190±0.004
Experiment	725.50[219]	1.24[219, 220]	-0.132[221]	-0.196[221]
DFT	N/A	N/A	-0.052	-0.141
% error exp	2.13	33.06	62.88	3.06
% error DFT	N/A	N/A	5.77	34.75

Table 4.2: This table shows some physical properties (density, self-diffusion, free energy of solvations) of TEA calculated using MD alongside experimental data where it exists and DFT calculations (performed with b3lyp/6-311g(d,p)). The average errors are shown.

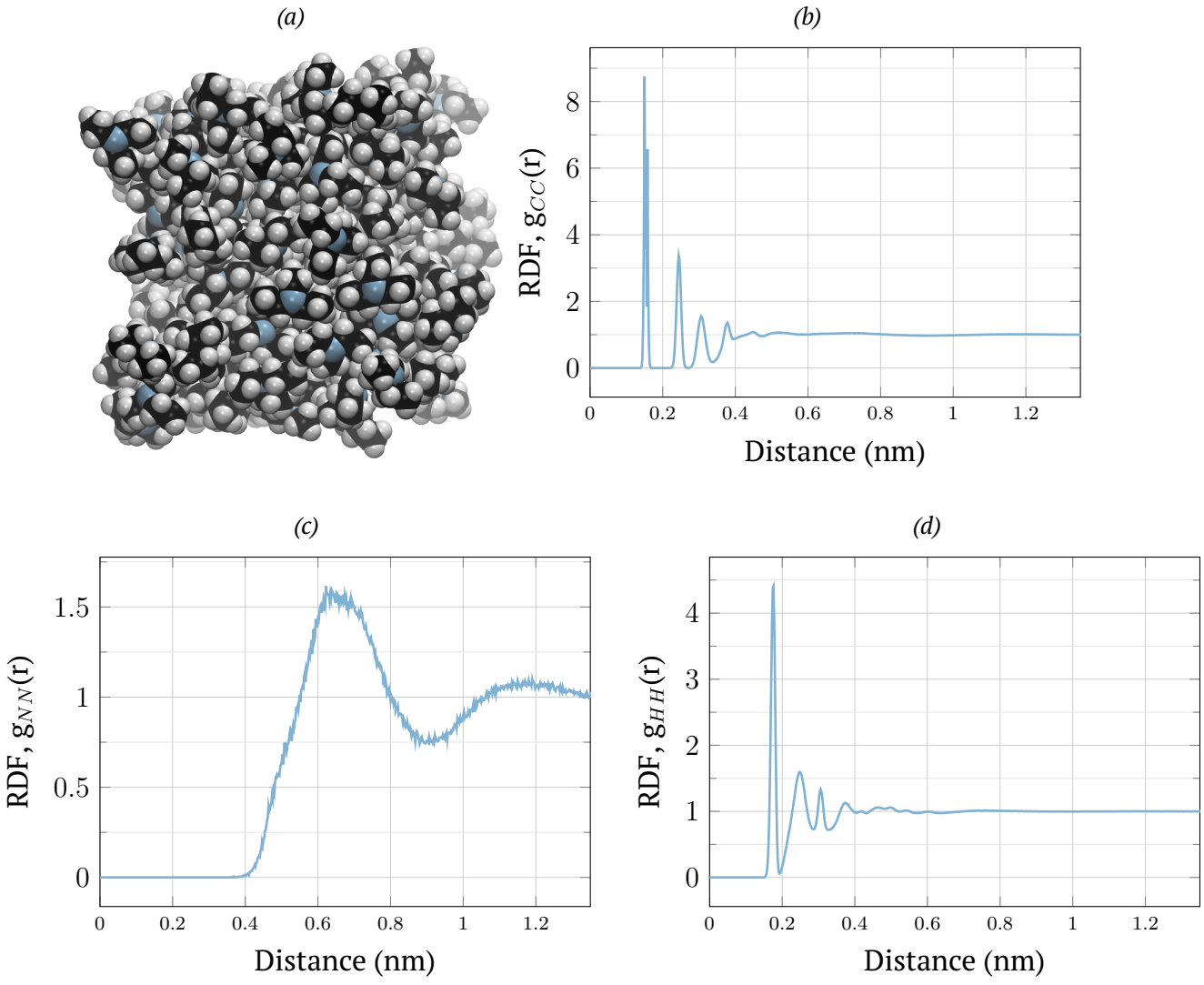


Figure 4.8: (a) shows the final state of the box of 277 TEA molecules, shown as Van der Waals Spheres and MD RDFs for (b) carbon-carbon interactions, (c) nitrogen-nitrogen interactions and (d) hydrogen-hydrogen interactions.

4.3.3 Methanol

We simulate a box of 402 methanol molecules in order to test the OPLS force field. As for the previous solvents we check some basic physical properties against experimental and DFT data, namely, the free energy of solvation properties, the density, and the self-diffusion coefficient, shown in Table 4.3.

	ρ_{298K}	Self-Diffusion(10^5 cm^2/s)	ΔH_{Water}(eV)	ΔH_{TEA}(eV)
MD	779.0	N/A	-0.193 $\pm$0.002	-0.062 $\pm$0.002
Experiment	792.0[222]	2.32$\pm$0.01[222]	-0.221[223]	N/A
DFT	N/A	N/A	-0.194	-0.088
% error exp	1.64	N/A	12.67%	N/A
% error DFT	N/A	N/A	0.52%	29.5%

Table 4.3: This table shows data used to check the validity of the force field for methanol compared with experimental data where it exists and DFT (b3lyp/6-311g(d,p)) where it does not.

We see from Table 4.3 that the force field reproduces the measures we have quite well and we can proceed on the assumption that methanol's interactions with water and TEA are well modelled. Figure 4.9 shows a snapshot alongside comparisons of the RDFs with experimental data from [9] to compare with. We can see from this that the peaks are reproduced in the right places, with one key difference being that there is stronger ordering in oxygen-oxygen interactions.

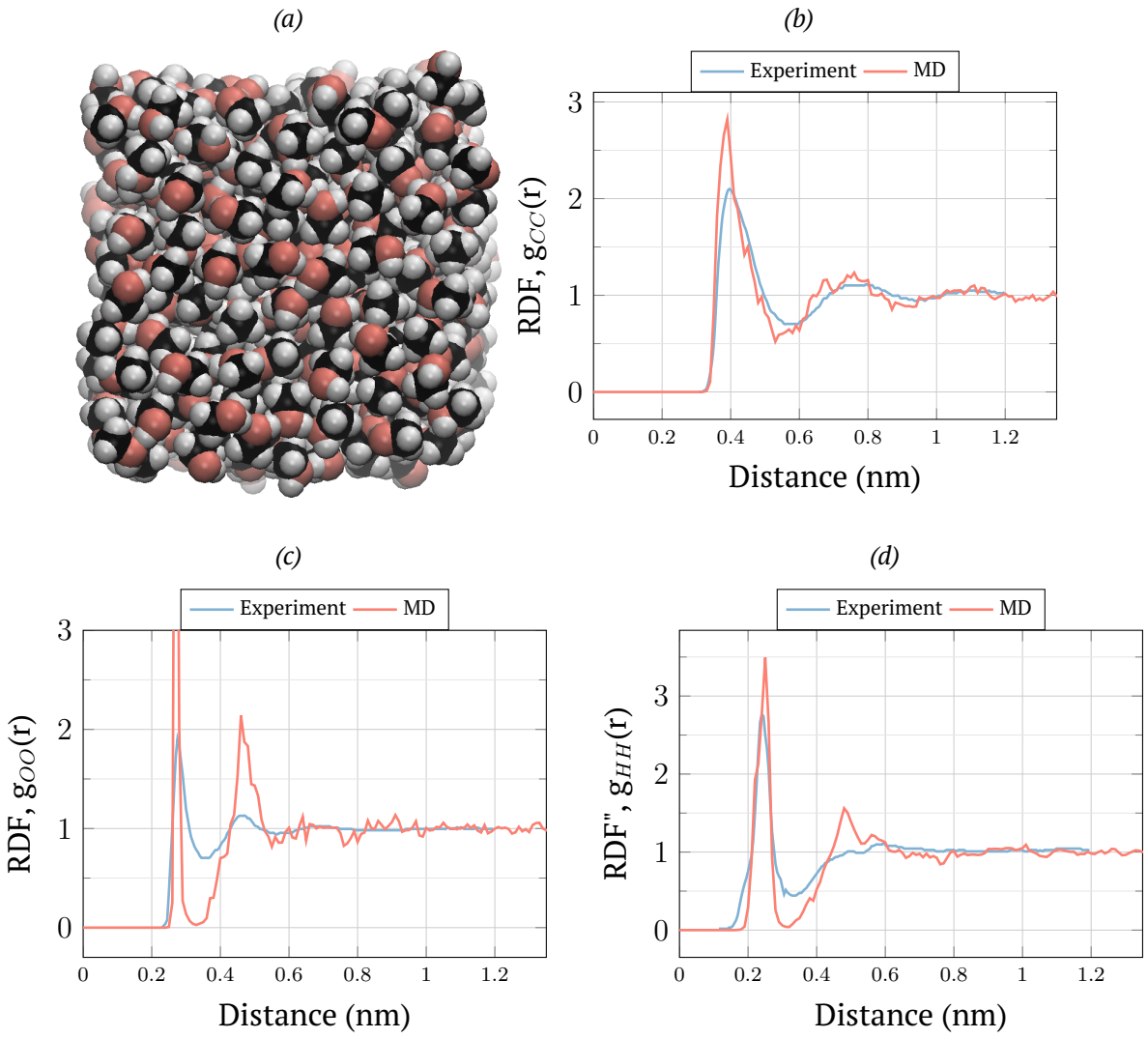


Figure 4.9: (a) shows the final state of the box of 402 methanol molecules, shown as Van der Waals Spheres, and a comparison between experimental RDFs[9] and MD RDFs for (b) carbon-carbon interactions, (c) oxygen-oxygen interactions and (d) non-methyl-hydrogen-non-methyl-hydrogen interactions.

4.3.4 Chloroform

Trichloromethane, more commonly known as chloroform, is a commonly used organic solvent, particularly used in NMR spectroscopy[224]. Chloroform is also well studied computationally and there exists an OPLS force field[7] which has been used and studied in a number of phenomenon[225, 226]. We consider it here primarily due to its use in NMR spectroscopy. Table 4.4 shows the MD results for density, self-diffusion and free energy of solvation in water.

	ρ_{298K}	Self-Diffusion(10^5 cm^2/s)	ΔH_{Water}
MD	1471.5±1.2	2.50±0.35	N/A
Experiment	1490	2.35[227]	N/A
DFT	N/A	N/A	-0.063
% error exp	1.24	6.38	N/A
% error DFT	N/A	N/A	N/A

Table 4.4: This table shows data used to check the validity of the force field for chloroform compared with experiment where it exists and DFT (b3lyp/6-311g(d,p)) where it does not.

In Figure 4.10 we show a snapshot from a MD simulation of a box of 203 chloroform molecules, alongside RDFs, from experiment[10] and MD, of chloroform-chloroform interactions.

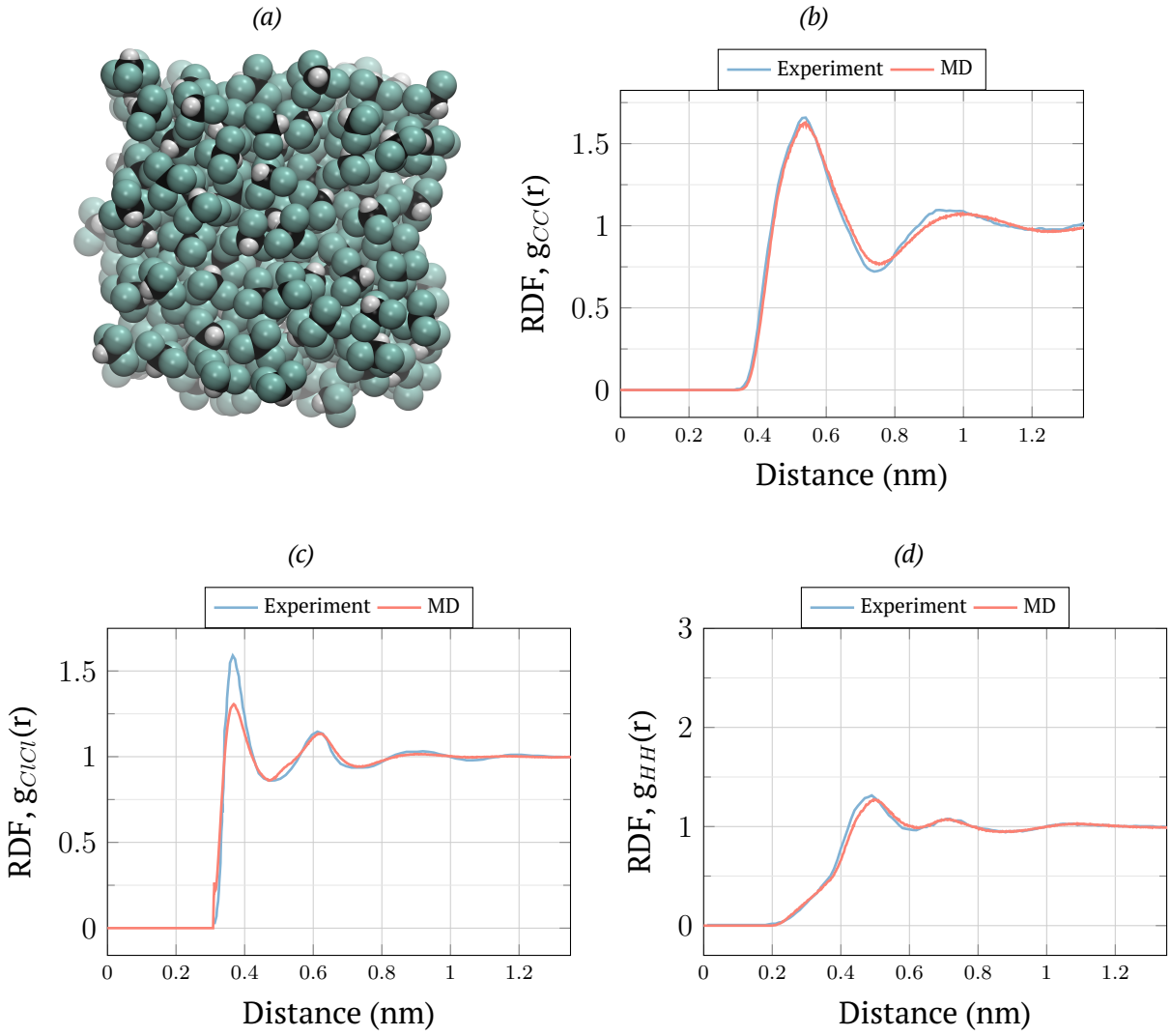


Figure 4.10: (a) shows the final state of the box of 203 chloroform molecules, shown as Van der Waals Spheres, and a comparison between experimental RDFs[10] and MD RDFs for (b) carbon-carbon interactions, (c) chlorine-chlorine interactions and (d) hydrogen-hydrogen interactions.

We see from Figure 4.10 that the RDFs from the OPLS force field for chloroform that we are using match experimental RDFs well.

4.3.5 Decalin

Decahydronaphthalene, more commonly known as decalin, is an organic solvent that is commonly used as a solvent for organic molecules and polymers. It is known to be fully miscible with chloroform, to be soluble with methanol, and to be insoluble in water. Unlike the other solvents in this chapter decalin is unique in that it has two common isomers, called cis-decalin and trans-decalin. The structures of both of these isomers are shown in Figures 4.4 and 4.5. Trans-decalin has much more steric hindrance and is thus the more stable of the two. It is

known that cis- and trans-decalin are miscible with each other. Figure 4.11 shows the snapshot of the MD simulation of 50:50 cis-/trans-decalin showing atoms coloured by element and by whether they belong to cis or trans molecules. In addition RDFs are plotted from MD.

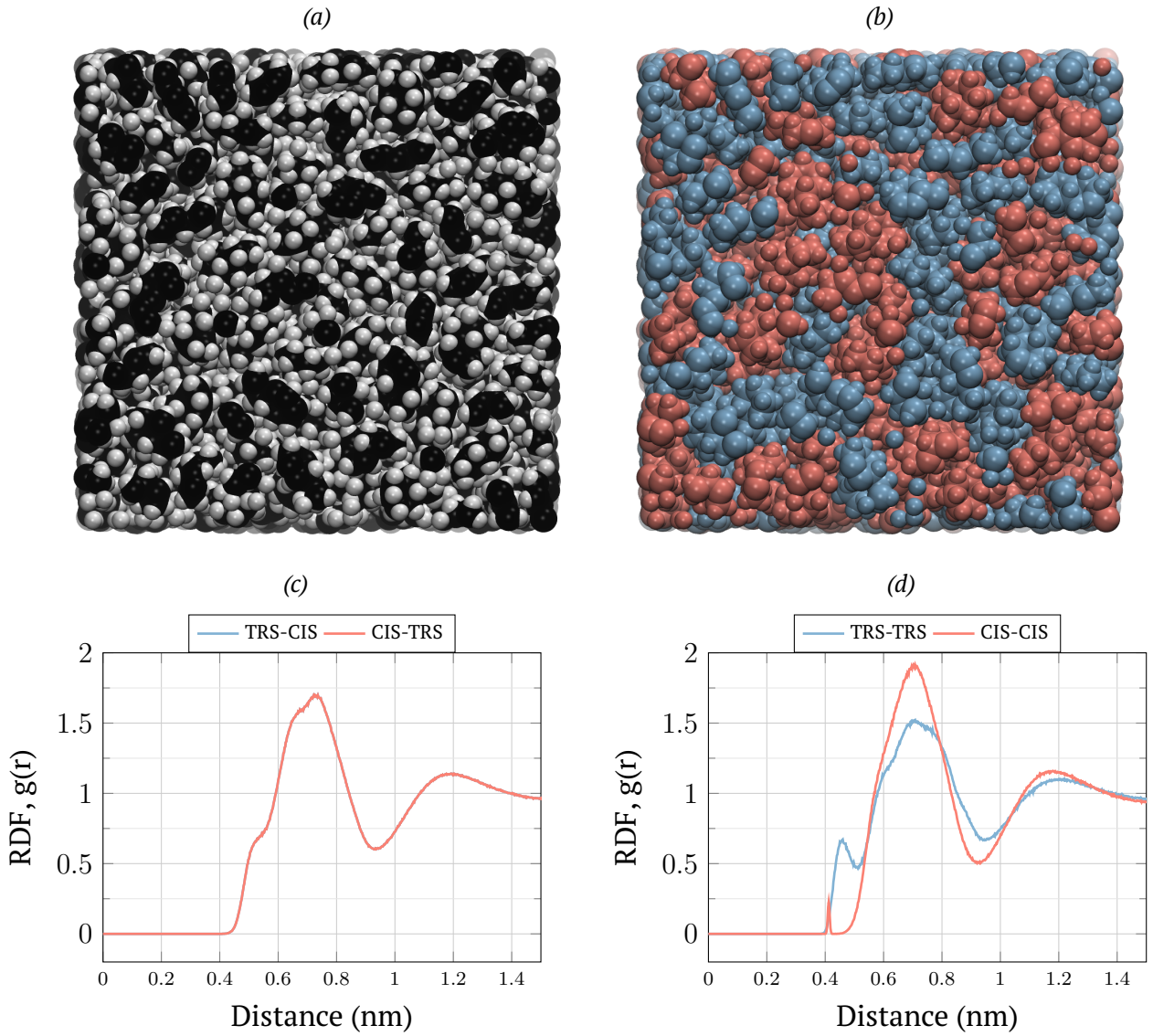


Figure 4.11: This figure shows the final state of the box of 402 decalin molecules, shown as Van der Waals Spheres coloured by atom in (a) and according to whether it is cis or trans in (b), and MD RDFs for (c) trans-cis interactions and (d) cis-cis and trans-trans interactions.

We can see from Figure 4.11 that the OPLS force fields for cis- and trans-decalin are indeed fully miscible. As further validation we also look at the density self-diffusion coefficients, the results of which are summarised in Table 4.5.

	ρ_{MD} (kg/m^3)	ρ_{exp}(kg/m^3)	D_{MD} (m^2/s)	D_{exp} (m^2/s)
Cis-Decalin	907.29±0.08	892.85[228]	0.304±0.002	0.44[229]
Trans-Decalin	908.43±0.19	865.84[228]	0.38±0.04	0.70[229]
50/50 Mixture	912.30±0.24	879.28 [228]	0.124±0.001	N/A

Table 4.5: This table shows data used to check the validity of the force field for methanol compared with experimental data where it exists and DFT (b3lyp/6-311g(d,p) where it does not. It is shown separately for cis and trans conformers.

As an additional form of validation we also perform free energy of solvation calculations in chloroform, methanol and water in both MD and DFT. Whilst we do not have quantitative numbers to compare experimentally we can confirm the experimental order of solubilities. Table 4.6 shows MD and DFT calculations for the free energy of solvation.

	ΔG^{MD}_{CHF}	ΔG^{DFT}_{CHF}	ΔG^{MD}_{Met}	ΔG^{DFT}_{Met}	$\Delta G^{MD}_{H_2O}$	$\Delta G^{DFT}_{H_2O}$	AE (%)
Cis	-0.350±0.003	-0.284	-0.200±0.002	-0.223	+0.062± 0.005	+0.046	22.78%
Trans	-0.362±0.004	-0.287	N/A	-0.224	+0.067±0.002	+0.051	28.75%

Table 4.6: This table shows the computed free energy of solvation for cis- and trans-decalin in chloroform, methanol and water, in eV, computed using MD and using DFT, using b3lyp/6-311g(d,p). In the final column the average difference between DFT and MD is shown as a percentage.

The data in Table 4.6 shows us that our force field of choice for decalin not only matches appropriately with quantitative data from DFT but also we see that it reproduces the experimental qualitative observations. Namely that the relative solubility of decalin from best to worst is chloroform, methanol and water.

4.4 Two-phase Solvent Solutions

Having established the behaviour and validity of the force fields in isolation we now turn to study the behaviour of two-phase solutions, looking at how solvents mix (or don't mix) and how consistent the MD is with experimental data and observations.

4.4.1 Water-Methanol

Methanol is expected to be fully miscible in water which means we would expect no phase segregation at any concentration of temperature. We see that the force fields we are using do indeed display miscability. Figure 4.12 shows MD snapshots of Methanol at increasing concentrations in water alongside a cluster analysis at each concentration.

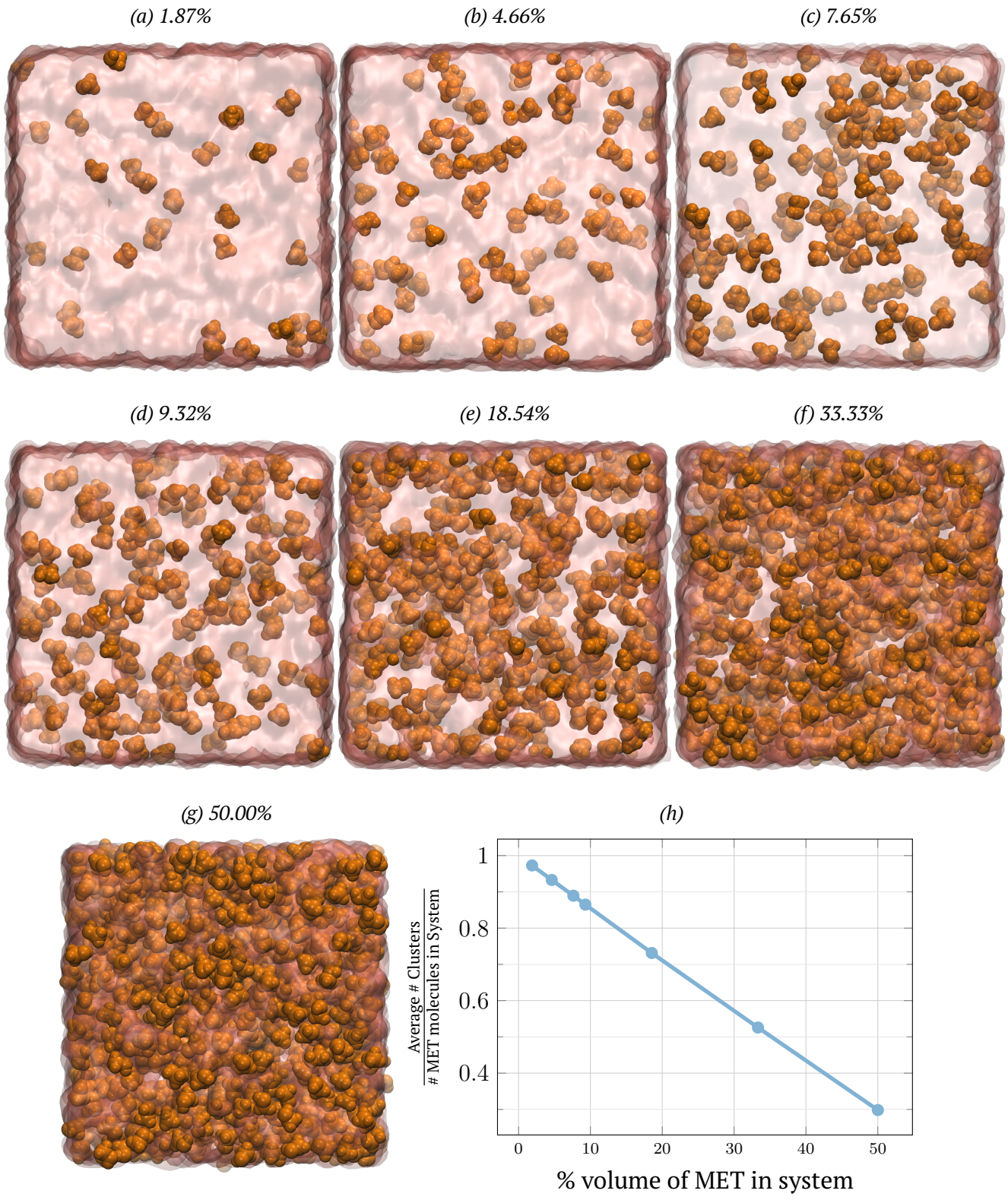


Figure 4.12: This figure shows snapshots of the MD simulations of water with methanol at (a) 1.87% (b) 4.66% (c) 7.65% (d) 9.32% (e) 18.54% (f) 33.33% (g) 50.00% by volume concentration in water. The average number of clusters per methanol molecule at each concentration is shown in (h).

We can see from Figure 4.12 that very little phase segregation is seen at all concentrations; the average number of clusters per methanol molecule is consistently high representing a high

likelihood of a given methanol molecule belonging to a cluster of just one. We now focus on the 50/50 concentration box and extract RDFs for the water-methanol interactions; this is shown in Figure 4.13.

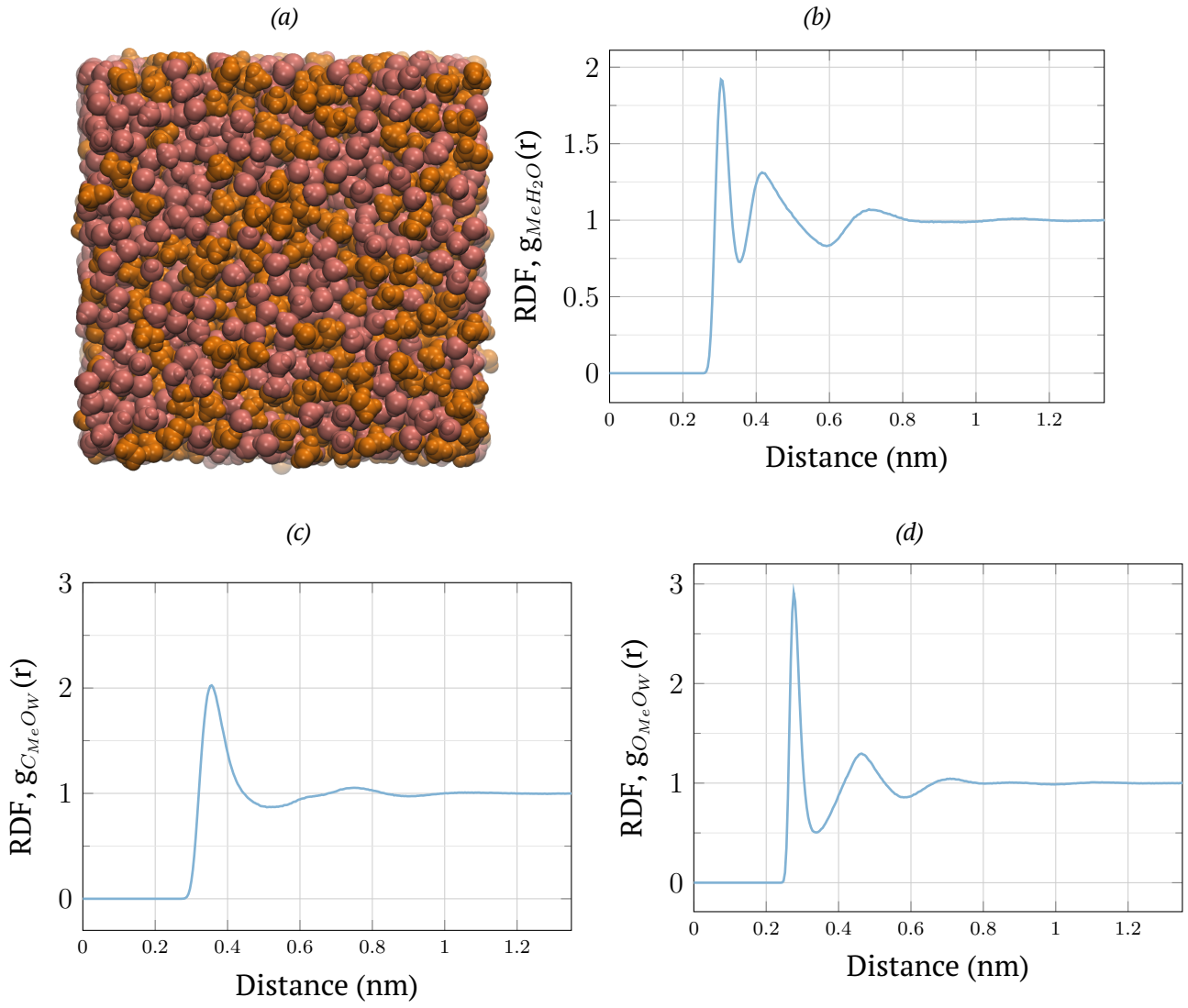


Figure 4.13: (a) shows the final state of the box with 1:1 water:methanol by volume, shown as Van der Waals Spheres, and MD RDFs for (b) methanol-water interactions, (c) carbon-oxygen interactions and (d) methyl-oxygen-water-oxygen interactions. Water is shown as red and methanol as orange.

Figure 4.13 shows a box simulated with equal volume water and methanol. We can see from the RDFs that methanol is nearly equally likely to have a water molecule nearby as it is a methanol.

We also perform a free energy of solvation calculation for methanol in water, which we can then compare with DFT and experimental values. We find it to be -0.193eV which compares favourably with -0.194eV obtained from DFT and -0.221eV found experimentally in the literature[230].

We can conclude that the interactions between water and methanol seem to match with experimental understanding to the extent that we can investigate it.

4.4.2 TEA-Methanol

We now turn to looking at the TEA/methanol two-phase system. There is not much detailed experimental work reported on mixtures of TEA and methanol, however it is reported that TEA, whilst not miscible in methanol, is expected to be soluble, which means anywhere in the region of up to 10 to 33% by volume of TEA to be fully solubilised into methanol. To investigate this we simulate an array of different concentrations of TEA in methanol and use the cluster analysis we used in the previous section to detect whether phase segregation is occurring. Snapshots of the different concentrations simulated, 1.87%, 4.66%, 7.65%, 9.32%, 18.54%, 33.33% and 50.00%, are shown in Figure 4.14 alongside the average cluster size as a fraction of all TEA molecules plotted against the concentration.

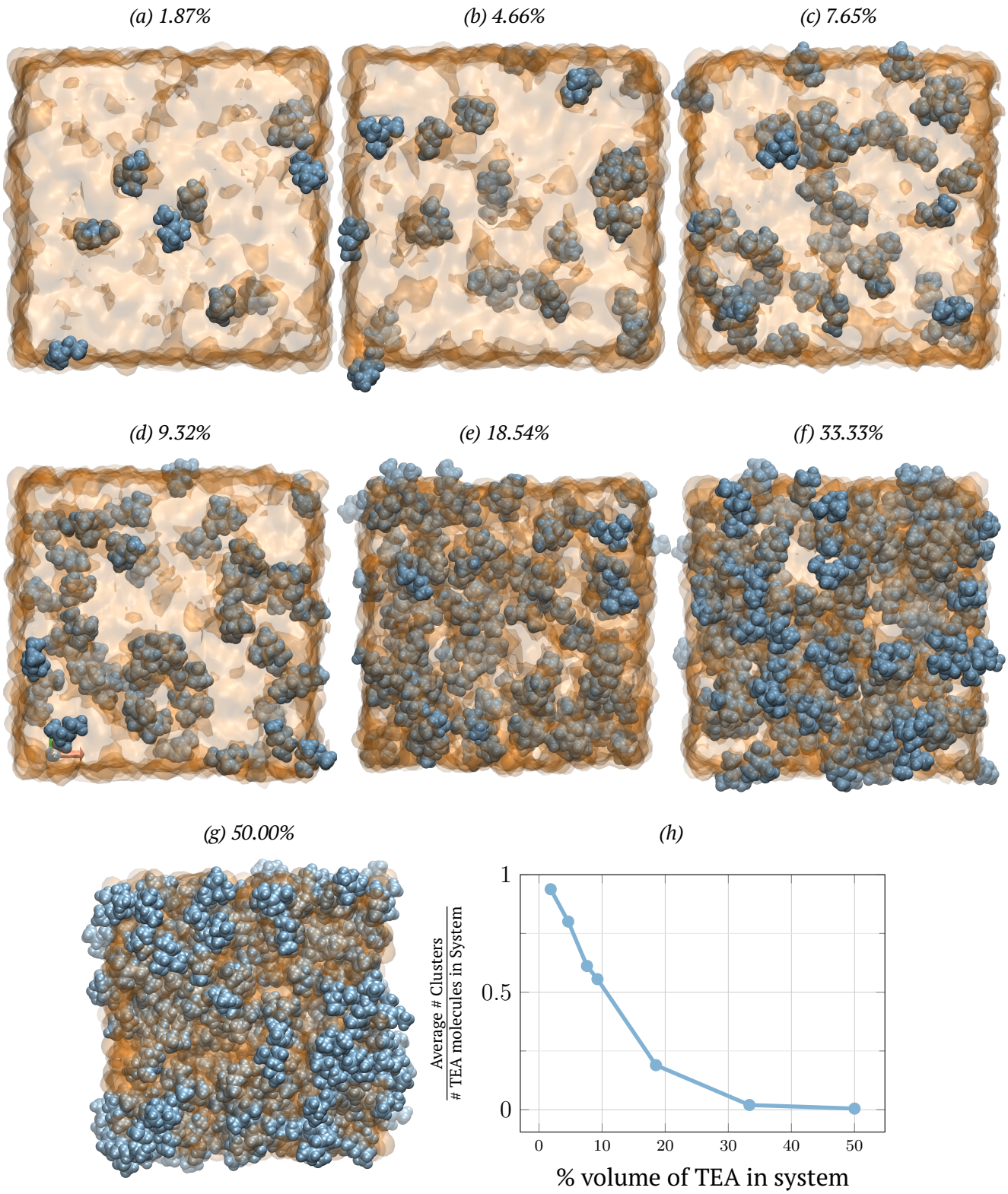


Figure 4.14: This figure shows snapshots of the MD simulations of TEA in methanol at (a) 1.87% (b) 4.66% (c) 7.65% (d) 9.32%(e) 18.54% (f) 33.33% (g) 50.00% by volume concentration in water. The average number of clusters per methanol molecule at each concentration is shown in (h).

The concentration study shows that TEA is largely soluble in methanol as expected from the literature and we do begin to see the signs of a weaker solubility than methanol in water. We

can proceed in confidence that the modelled interactions between TEA and methanol seem to reasonably approximate the limited experimental data.

4.4.3 Water-TEA

This is an important combination of solvents as it will be our initial approximation model for the full reaction mixture of the photocatalyst system in Sections 6.4.3.1 and 7.4.4. As such, we pay particular attention to this system, exploring different concentrations. Experimental measurements determine the solubility of TEA in water to be at 7.6% by volume (0.5435M). We simulate a series of concentrations of TEA in water, 4.66%, 7.65%, 9.32%, 18.54%, 33.33% and 50.00%. Snapshots of each of these are shown in Figure 4.15.

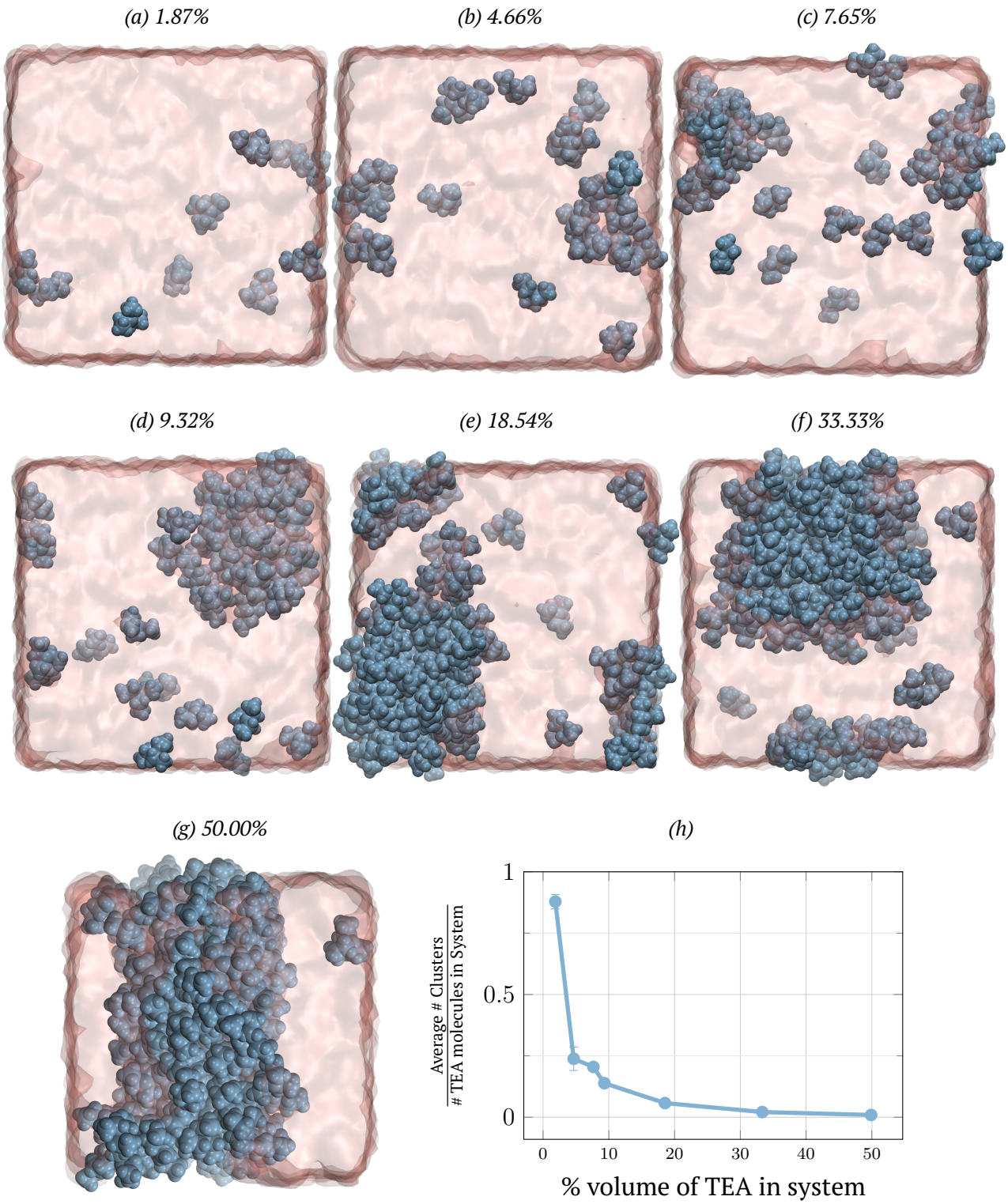


Figure 4.15: This figure shows snapshots of the MD simulations of TEA in water at (a) 1.87% (b) 4.66% (c) 7.65% (d) 9.32% (e) 18.54% (f) 33.33% (g) 50.00% by volume concentration in water. The average number of clusters per TEA molecule at each concentration is shown in (h).

From Figure 4.15 we can see that TEA does indeed seem to have poor solubility in water, with near complete drop off between 1.87 and 7.65% by volume concentration, broadly in line with experimental data. We now focus on the Water-TEA 50:50 mix in detail, and Figure 4.16 plots

RDFs of each solvent with each other solvent. These RDFs are constructed from centre-of-mass to centre-of-mass.

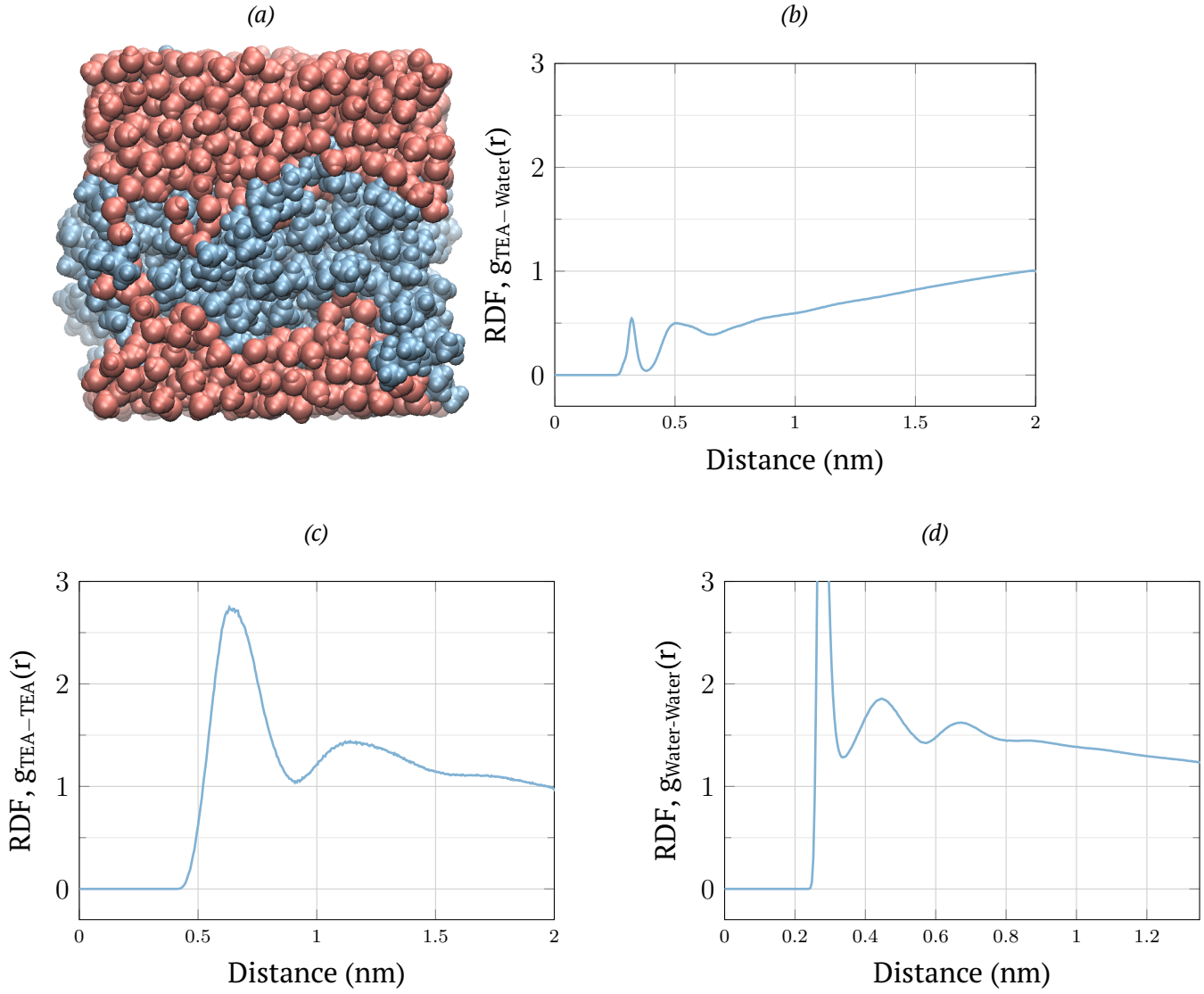


Figure 4.16: This figure shows the molecular dynamics simulation of a box of water and TEA with 1:1 concentration by volume, a snapshot of the final system is shown in (a), and radial distribution functions between the centre of masses of (b) TEA and water (c) TEA and TEA (d) water and water are shown.

This reinforces what we see from the cluster analysis that at 50:50 the TEA has completely segregated (TEA-water RDFs are weaker than TEA-TEA RDFs). This contrasts well with the previous section which explored the solubility of TEA in methanol and we can see that TEA in water is much less soluble then TEA in methanol, very much in line with experimental observations. In Chapter 6 we will use this as a simplification of the full experimental three-phase solvent mixture as the phase segregation allows us to focus more deeply on the interactions between the oligomer and both water and TEA.

4.4.4 Conclusions: Metrics of Solubility in MD

To summarise this Section it is worth noting that in examining three different two-phase systems we have also seen three different types of behaviour: complete miscibility, good solubility, and poor solubility. We thus have an insight into the metrics of solubility we can obtain from MD. We have seen that by slowly increasing the concentration of the solute we can identify at what point, if any, the solute phase-segregates. To show this more clearly, Figure 4.17 shows each of the cases we have studied on the same graph.

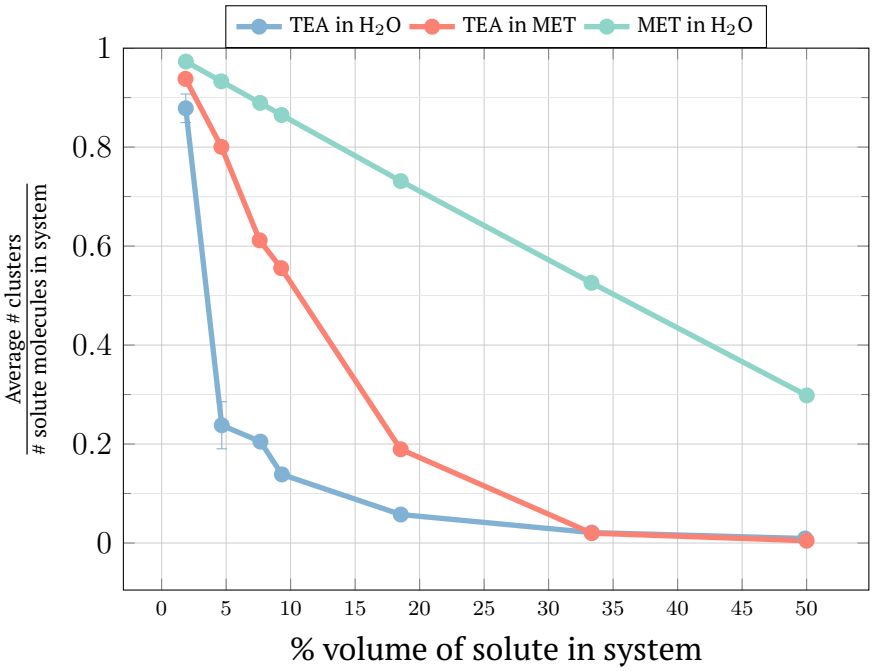


Figure 4.17: This figure shows the very different behaviour of three binary mixtures: TEA in water (blue), TEA in methanol (red) and methanol in water (cyan) which are understood to have limited solubility, good solubility and full miscibility respectively.

We see from Figure 4.17 the stark difference that solubility makes on this metric which is a measure of phase segregation. Using the cluster analysis on a system to work out the average number of clusters per molecule seems to be a good method of extracting the amount of phase segregation from a MD simulation.

4.5 Three-phase Solvent Solutions: Reaction Mixture

As we have previously discussed, the photocatalytic experiments we study in Chapters 6 and 7 take place in 1:1:1 by volume of water, TEA and methanol. As such we now study this system of solvents. We see a snapshot, coloured by solvent type, in Figure 4.18, alongside RDFs of TEA with each of the other solvents.

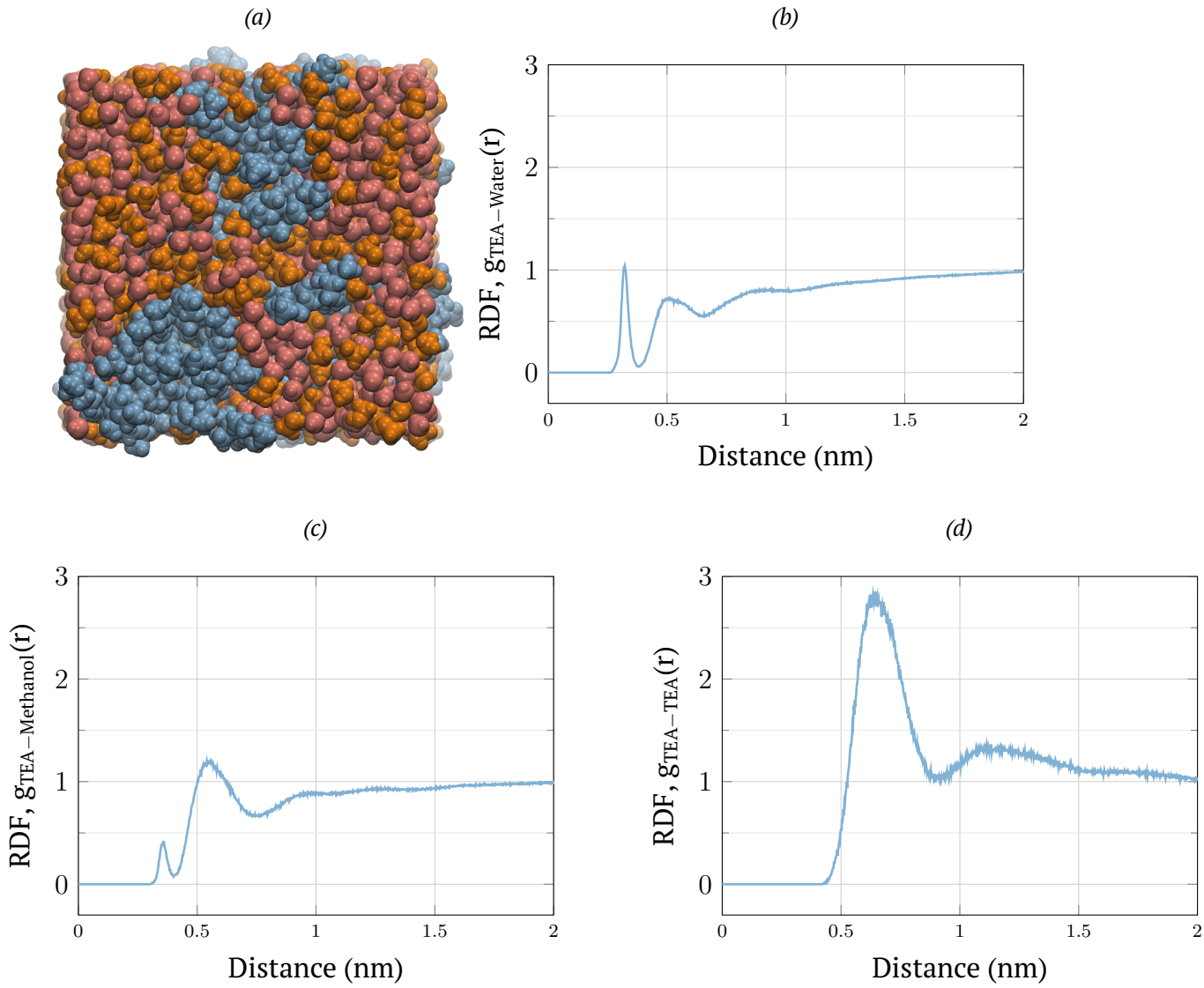


Figure 4.18: This figure shows (a) a snapshot of the MD simulation of a ternary mixture of water (red), methanol (orange) and TEA (blue) at equal volumes, and RDFs from the centre of mass of TEA to the centre of mass of (b) water (c) methanol and (d) TEA.

From Figure 4.18 we see that there appears to be some phase separation between TEA and non-TEA phases. We can see this also in the relative strength of the TEA-TEA RDF compared with the TEA-water and TEA-methanol RDFs. Experimental understanding of this solvent mixture suggest that this mixture should be less phase-segregated than a mixture of just water and TEA. To study this more thoroughly we, in Figure 4.19, plot the RDFs of TEA with water in the three-phase mixture against two two-phase TEA:water mixtures, 50.00% TEA by volume and 33.33% TEA by volume.

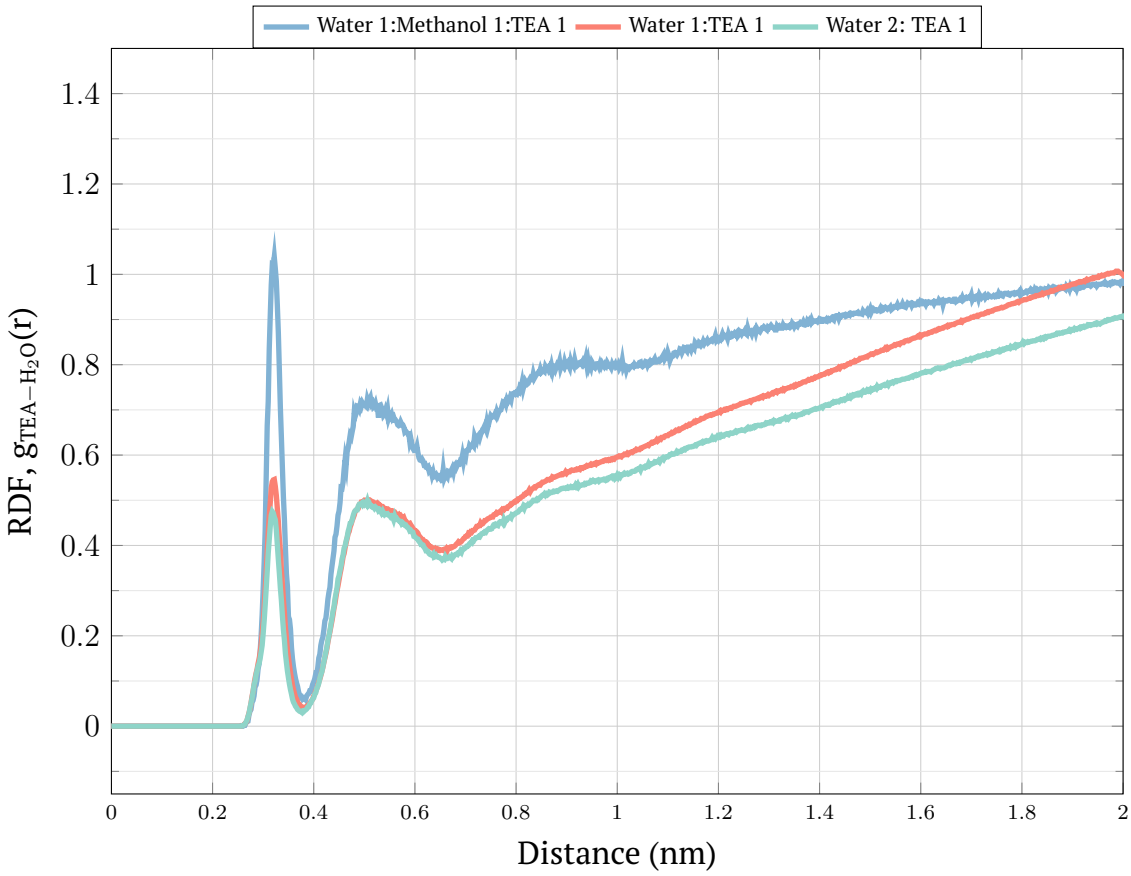


Figure 4.19: This shows a comparison of the RDFs between water and TEA between the systems with and without methanol and at two concentrations of TEA in water to make comparisons easier to see.

Figure 4.19 shows that methanol in the simulations, as observed in experiments[14, 134], serves to help bring a higher volume of water closer to TEA and aid mixing. In addition, we can also compare the average cluster of TEA molecules in this mixture with the value obtained in just water at the same TEA concentration. We find in the three-phase mixture that the average number of clusters of TEA molecules is 4.29±0.06 compared with 3.80±0.02 from the 33.33% TEA by volume water:TEA. From all of these sections we see that the qualitative behaviour of the solvents, as best as we can compare them, is reproduced by the MD force fields we have chosen. We proceed in the next section to build up force fields for the oligomers of consideration.

4.6 Conclusions

In this section we have investigated a range of solvents by choosing and/or developing force fields for their study in MD. We selected a force field, OPLS, to use for all of them to allow us to study the solvents as mixtures, since MD force fields do not behave well when mixed-and-matched. This has allowed us to use a variety of methods to validate them, namely by:

- comparing basic physical properties such as density and RDFs to experiment.

- comparing self-diffusion with experiment where possible.
- comparing the mixing of different solvents by looking at phase segregation at different concentrations, and at free energy of solvations, comparing them with DFT and experiment where available.

This work allows us to proceed with confidence in using any of these solvents to investigate oligomers in either single-phase solutions or multi-phase solutions. In addition, we have replicated a key physical observable, namely, that the addition of methanol in a water-TEA mixture helps to facilitate mixing. This is something observed experimentally and is key to the experiments that we study computationally in Chapter 6.

5

Insights into Polymer Behaviour through the Systematic Study of Oligomers in Solution

5.1 Introduction

As we have previously discussed, conjugated polymers are being developed for use in a number of applications and have the potential to either improve or replace inorganic semiconductors in a number of others[60, 70]. In this chapter we begin to investigate the role that molecular dynamics can play in understanding how polymers (modelled as shorter oligomers to make simulations tractable) interact. It is well understood that chain conformation, dynamics, stiffness and aggregation affect the charge transport properties[77, 76, 78] and thus, understanding these elements of organic conjugated polymers is of great importance to the resultant devices' performance. There is only a very small body of work that has looked at the impact of conformation in solution on the final microstructure and hence on electronic properties, and this is what motivates the present work.

In this chapter, we look at the case of Polyfluorene (PFO) which is known experimentally to exist in two phases in the solid-state: alpha phase, and a metastable state called β-phase. β-phase is characterised by the PFO chains existing in a higher energy, planarised conformation. It is observed when the polymer is processed in a variety of different solvents. What is known is that the sidechain will affect the ability to form β-phase: a branched sidechain like ethylhexyl would inhibit β-phase formation. What is not known is the process of β-phase formation and its relationship with aggregation. Do individual chains aggregate and, once aggregated, β-phase planarisation is stabilised, or does it happen the other way around?

In addition to investigating side-chain dependence on planarisation, we also study another important measure of conformations of polymers in solution: that of the persistence length. The persistence length is a measure of how able the polymer is to fold. To do this we utilise the work we have already done with PFO and in addition study Indacenodithiophene-co-benzothiadiazole (IDTBT)[77]. We choose these two because solution and solid phase transport data are available for both and present an interesting contrast. In particular IDTBT is much stiffer as a result of the monomer shape.

5.1.1 Experimental Context

Conjugated polymers enable the production of flexible semiconductor devices, made from earth abundant materials, that can be processed from solution at low temperatures and as such offer the potential for more sustainable devices. They have already seen commercial success in OLEDs but their use in Photovoltaics and OFETs has been hindered, at least in part, by their relatively poor charge transport properties. This is likely down to microstructural properties that are affected by the conditions in which the polymers are processed, however the exact relationship is unknown and difficult to study. This chapter focuses on two polymers that have been studied: PFO and IDTBT. Their chemical strucures are shown in Figure 5.1.

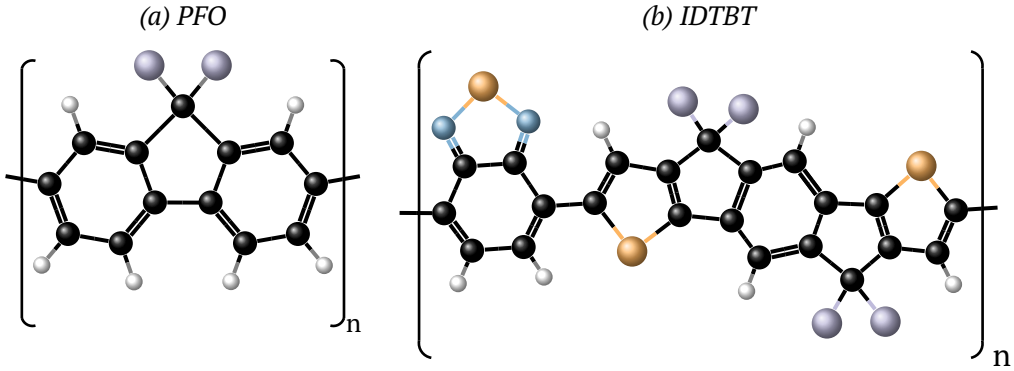


Figure 5.1: This figure displays the backbone structure of the polymers we consider in this chapter, namely (a) PFO and (b) IDTBT. Purple Atoms represent positions where sidechains are added.

PFO in particular has been extensively studied, in part because it possesses a meta-stable state, called β-phase; this phase is a solid state where the backbone of the polymer is planarised rather than adopting the lowest energy, torsionally twisted conformation. β-phase is linked to superior charge transport in isolated chains[93] but acts as a trap state when present as a minority component in solid films. One thing that makes β-phase unique and facilitates study

is that PFO α-phase and β-phase possess different photoluminescence signatures, as seen in Figure 5.2.

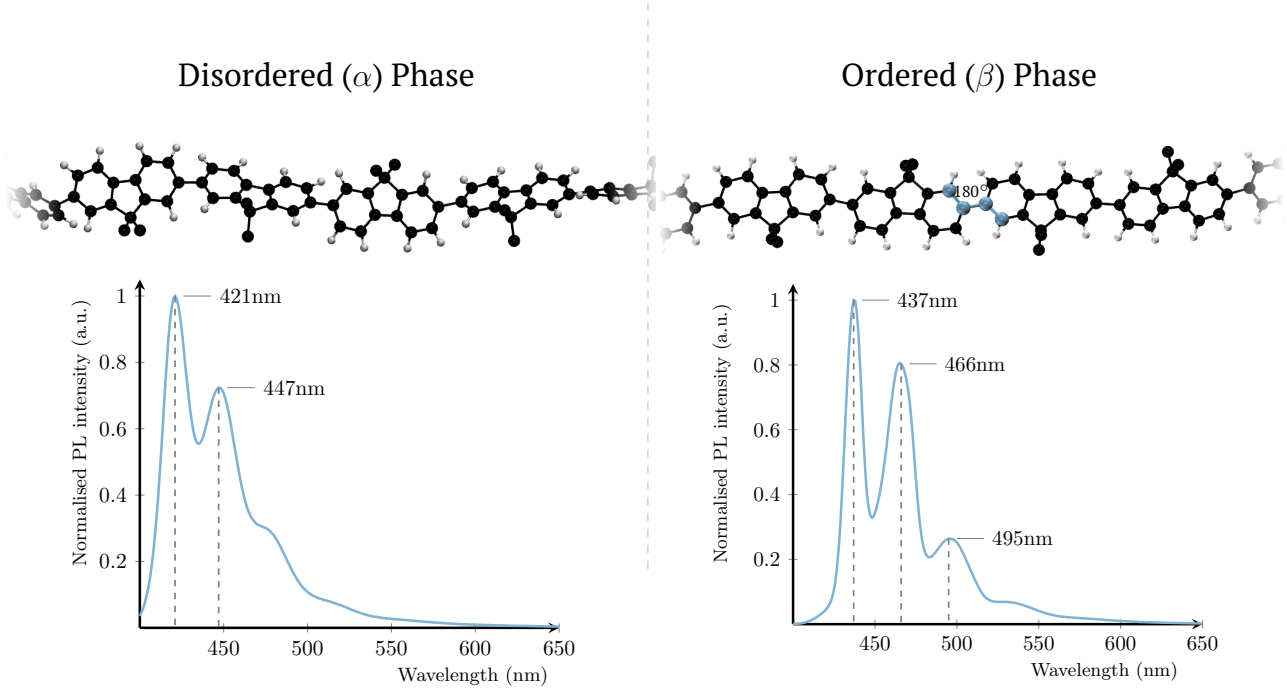


Figure 5.2: Two different conformations of the PFO chain, α and β-phase. Taken as snapshots from MD simulations. The relevant dihedral is highlighted (blue) showing it must be $180°$ in the β-phase. Sidechains are not shown. Below each are absorption (PL) measurements of the different phases showing the experimentally probe-able conformational markers[11].

The existence of an experimental, spectroscopic measure of conformation, Figure 5.2, allows one to trial different experimental set-ups to see which elements promote β-phase formation and which seem to inhibit it. From experimental work we see that several factors affect the development of β-phase:

- It forms in the presence of a variety of different solvents, such as chloroform, toluene, decalin and other organic solvents[231, 232].
- It forms when the polymer possesses sidechains like octyl (C_8H_{17}) or nonyl (C_9H_{19}) but not with longer sidechains like hexadecyl ($C_{16}H_{33}$) or branched sidechains like ethylhexyl ($C_2H_7(C_6H_{13})$)[104].
- It can be stimulated by the use of additives such as paraffin oil[233],
- It is affected by co-polymerisation[234]
- The incidence of β-phase in a solid film is affected by molecular weight[235]

Over the years of study a model for the mechanism of β-phase formation has been proposed: the sidechain-sidechain interactions provide sufficient chemical energy to overcome the barrier to planarisation[235]. This means that the choice of sidechain is very sensitive as it must have strong enough interactions to counter the steric hindrance of the backbone. The optimal sidechain length appears to be an octyl sidechain[104]. Beyond this the precise mechanism of formation of β-phase is unknown; for example, does planarisation occur in solution in an isolated polymer, changing the barrier of planarisation for other polymers upon aggregation, or does planarisation require the chains to already be aggregated? See Figure 5.3 for a schematic showing these options.

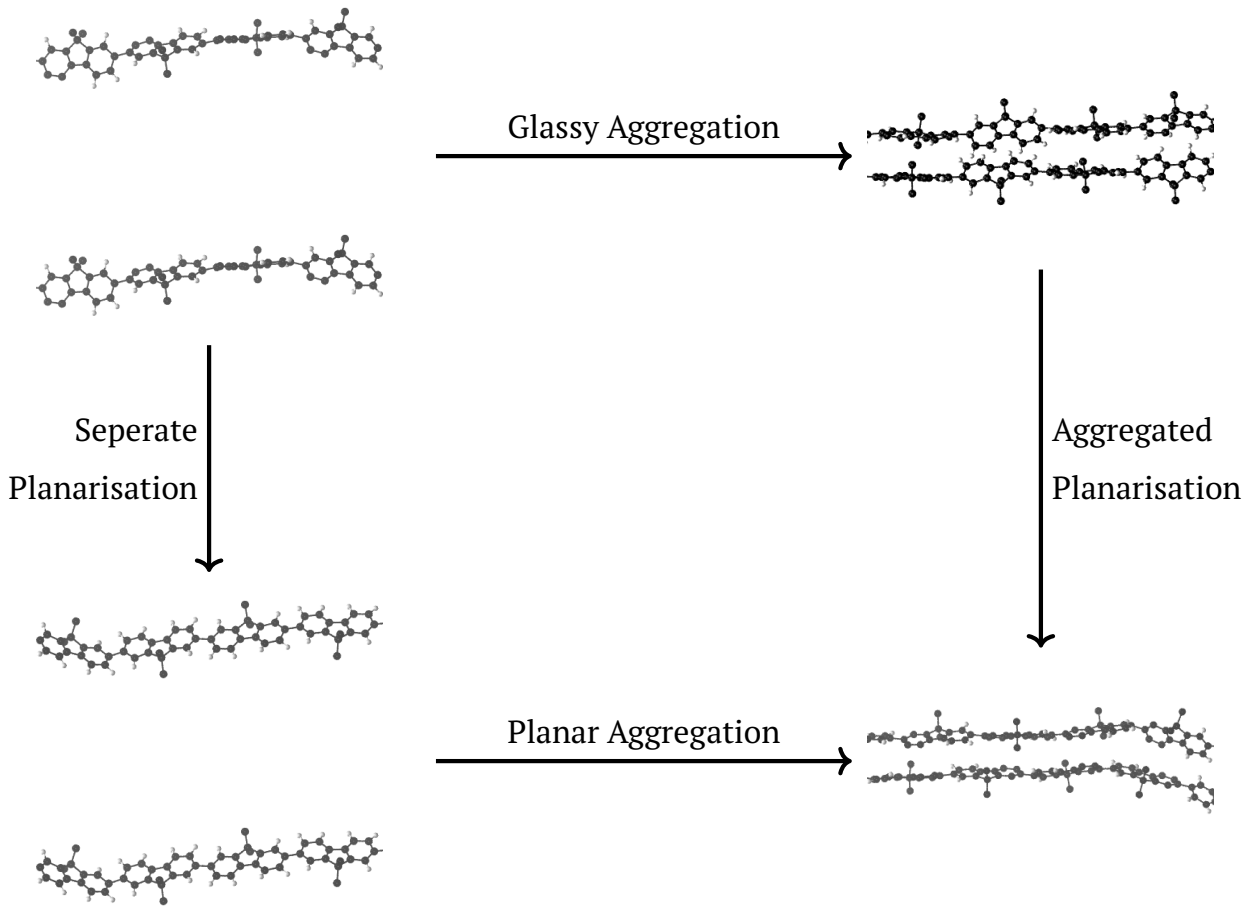


Figure 5.3: This figure shows the different parts of β-phase formation and the two paths in solution that can be taken depending on whether aggregation or planarisation occurs first. How these factors influence each other is a source of much discussion.

The second polymer selected for this study is IDTBT, also shown in Figure 5.1[77]. IDTBT provides another interesting case study that will be useful to study in contrast to PFO. It has been found to have high mobilities despite not having a high crystalline order. It is worth noting that IDTBT has a much higher degree of stiffness than PFO and is planar in its ground state

conformation and thus we suppose that the planarisation may be a factor that assists charge transport.

The experimental observations suggest that molecular conformation plays a vital role in the polymers' electronic performance, and understanding the polymer behaviour in solution opens the potential of producing consistent, good performance devices such as OFETs from solution using conjugated polymers. The scale of interest (firmly in the tens of nanometers and tens of nanoseconds) and the importance of thermal effects and solvents make it clear that the best tool for the study of this problem is molecular dynamics. In the next section we outline the development of the force fields necessary for the study of this problem.

5.2 Force field Development

As we have discussed, in order to study anything in molecular dynamics one must first develop force fields for the molecules being studied. Unlike *ab initio* methods MD force fields need to be developed for each molecule. Force field data usually come from a mixture of sources, from experimental parameterisation to ab-inito calculations, and as such it is vital that any force field is carefully chosen and validated. In this section, we outline the development and validation undertaken for the organic molecules we study in this chapter, the solvent molecules having been discussed more fully in Chapter 4.

5.2.1 Solvents

In this chapter we use several solvents. We use two organic solvents: chloroform and decalin, and water. We choose these solvents as different examples of reasonably "good" solvents (chloroform and decalin) for which there exist experimental data (chloroform for IDTBT and decalin for PFO) and water as an example of a "bad" solvent that should display signficantly different behaviour. In line with Chapter 4 we use the OPLS force fields we validated for decalin and chloroform, and the OPLS TIP4P model for water.

5.2.2 Polyfluorene

As we have chosen OPLS for the solvent molecules we must proceed to choose and refine an OPLS model for all the molecules and polymers of study as, as explained in Section 3.2.2, base-

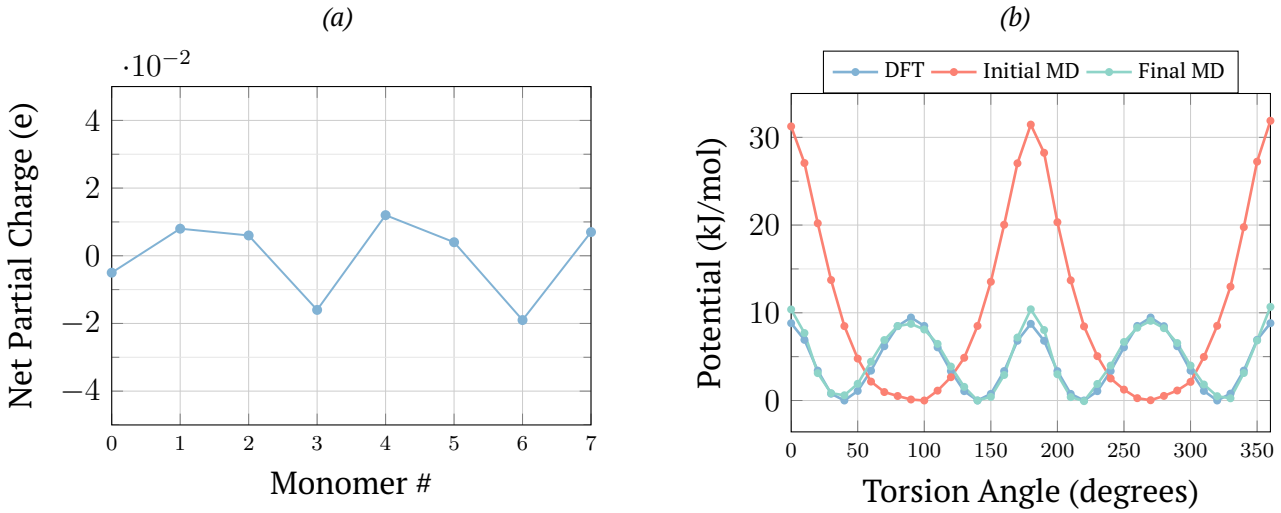


Figure 5.4: Figure showing a) charges, b) inter-monomer torsion

level force field types are not mix-and-matchable. We follow our standard methodology for force field development of a polymer/oligomer, but steps for these polymers are summarised as follows.

1. We identify OPLS atom types based on the chemical context, these are shown in (a) of Figures 5.5 for the backbone and Figures 5.6 and 5.7 for the sidechains.

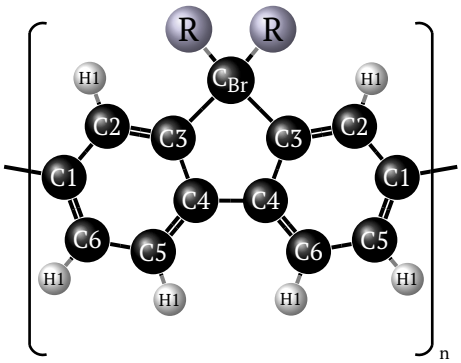
2. As all the atoms have corresponding atom types in OPLS the bond and angle properties also come from the OPLS database. The parameters are shown in (b) of Figures 5.5 for the backbone and Figures 5.6 and 5.7 for the sidechains.

3. We take the charges from DFT scans, symmetrising and averaging. The DFT population calculation is performed using CHELPG method with b3lyp/6-311g(d,p) on an n-mer. The resulting partial charges are shown in (b) of Figures 5.5 for the backbones and Figures 5.6 and 5.7 for the sidechains.

4. The DFT scans for the inter-monomer dihedral are performed with b3lyp/6-311g(d,p) for a dimer, with the sidechains cut off, and the results alongside the MD scan before and after the parameterisation is shown in Figure 5.4. Dihedrals along the sidechain are set to zero to allow free movement of the sidechain.

5. Improper dihedrals are added to ensure the backbone is flat, as OPLS does not reproduce this quality of conjugated polymers naturally. The scans are shown in Figure 5.4.

(a)



(b)

Atom	q (e)	σ (nm)	ε (kJ/mol)	OPLS name
C1	0.215	0.355	0.293	OPLS 145
C2	-0.160	0.355	0.293	OPLS 145
C3	-0.125	0.355	0.293	OPLS 145
C4	0.070	0.355	0.293	OPLS 145
C5	-0.135	0.355	0.293	OPLS 145
C6	-0.215	0.355	0.293	OPLS 145
H1	0.115	0.242	0.126	OPLS 146
C_{Br}	0.360	0.355	0.293	OPLS 145

(c)

Bond	r_0(nm)	k_r (kJ/mol/nm^2)	Angle	θ_0(deg)	k_θ(kJ/mol/rad^2)
C1-C1	0.146	322168	CX-CY-HZ	120.00	292.88
C1-C2, C3-C4, C4-C5, C6-C1	0.137	456893	C1-C2-C3, C2-C3-C4, C5-C6-C1, C6-C1-C2, C_{Br}-C3-C4,C_{Br}-C3-C2,C3-C4-C4	120.00	527.184
C_2-H_1,C_5-H_1,C_6-H_1	0.108	307106	C5-C1-C2, C4-C4-C2, C4-C4-C3, C1-C1-C2,		
C4-C4, C3-C_{Br}	0.146	322168	C1-C1-C5, C4-C3-C_{Br},		
C2-C3, C4-C5 ,C_6-C_1	0.140	392459	C2-C3-C_{Br}, C2-C_{Br}-C3		

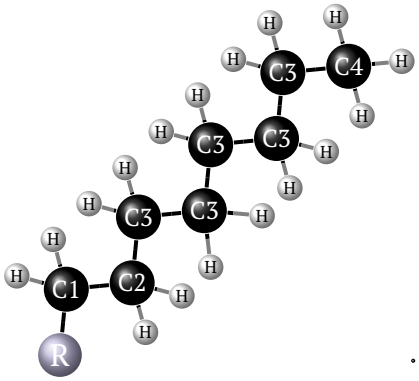
Dih. Angle	V_1(kJ/mol)	V_2(kJ/mol)	V_3(kJ/mol)	V_4(kJ/mol)	V_5(kJ/mol)	V_6(kJ/mol)
Ci-Cj-Ck-Cl, Ci-Cj-Cl-Hl, C6-C1-C1-$C_{2,6}$	30.334	0.000	-30.334	0.000	0.000	0.000
C1-C2-C2-C1	8.2514	0.1505	-27.4849	-0.7389	2.30775	0.6923

(d)

Improper Dihedral Angle	θ_0(deg)	k_θ (kJ/mol/rad^2)
C3—C4—C3—C4, C4—C3—C3—C_{Br}, C4—C4—C3—C_{Br}, C4—C4—C_{Br}—C3, C3—C4—C_{Br}—C3	180.0	391.47
C4—C3—$C_{2,5}$—H1, C1—C3—$C_{2,5}$—H1, C4—C6—$C_{2,5}$—H1, C1—$C_{2,5}$—C6—H1	180.0	311.812
C1—$C_{2,5}$—C4—C3, $C_{2,5}$—C3—$C_{2,5}$—C4, C3—C4—C6—$C_{2,5}$, C6—C1—C3—$C_{2,5}$, C4—$C_{2,5}$—C1—C6, C1—$C_{2,5}$—C6—$C_{2,5}$	180.0	188.781
$C_{2,5}$—C6—C1—C1	180.0	280.445

Figure 5.5: PFO backbone force field. a) nomenclature used. b) atom types, partial charges and Van der Waals parameters. c) shows bond, angle and proper dihedral parameters where X,Y,Z represent all C-C-H angles. i,j,k,l represent all intra-monomer C-C-C-H/C-C-C-C angles. d) shows the improper dihedrals which are added to account for planar stiffness due to conjugation. R represents the sidechain of choice and the parameters are outlined separately in Figures 5.6 and 5.7.

(a)



(b)

Atom	q (e)	σ (nm)	ε (kJ/mol)	OPLS name
C1	-0.355	0.350	0.347	OPLS 139
C2	-0.060	0.350	0.347	OPLS 139
C3	-0.120	0.350	0.347	OPLS 139
C4	-0.180	0.350	0.347	OPLS 139
H	0.060	0.250	0.126	OPLS 140

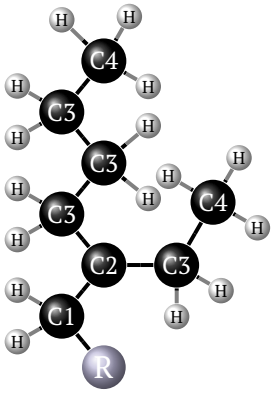
(c)

Bond	r_0(nm)	k_r (kJ/mol/nm^2)	Angle	θ_0(deg)	k_θ(kJ/mol/rad^2)
R-C1	0.154	218095	CX-CY-HZ	110.70	313.80
C1-C2, C2-C3, C3-C4	0.153	224262	R-C1-C2	114.00	527.184
C1-H, C2-H, C3-H, C4-H	0.109	284512	R-C1-H	109.50	292.880
			C1-C2-C3, C2-C3-C3,C3-C3-C4	112.70	488.273

Dih. Angle	V_1(kJ/mol)	V_2(kJ/mol)	V_3(kJ/mol)	V_4(kJ/mol)	V_5(kJ/mol)	V_6(kJ/mol)
C2-C3-C3-C3, C3-C3-C3-$C_{3,4}$,	2.929	-1.464	0.209	-1.674	0.0	0.0
Ci-Cj-Ck-Hl	0.6276	1.8828	0.0	-2.5104	0.0	0.0

Figure 5.6: Octyl (and 16 by extending the number of C3s) sidechain force field. a) nomenclature used. b) atom types, partial charges and Van der Waals parameters. c) shows bond, angle and proper dihedral parameters where X,Y,Z represent all C-C-H angles. i,j,k,l represent all intra-monomer C-C-C-H angles.

(a)



(b)

Atom	q (e)	σ (nm)	ε (kJ/mol)	OPLS name
C1	-0.355	0.350	0.347	OPLS 139
C2	0.000	0.350	0.347	OPLS 139
C3	-0.120	0.350	0.347	OPLS 139
C4	-0.180	0.350	0.347	OPLS 139
H	0.060	0.250	0.126	OPLS 140

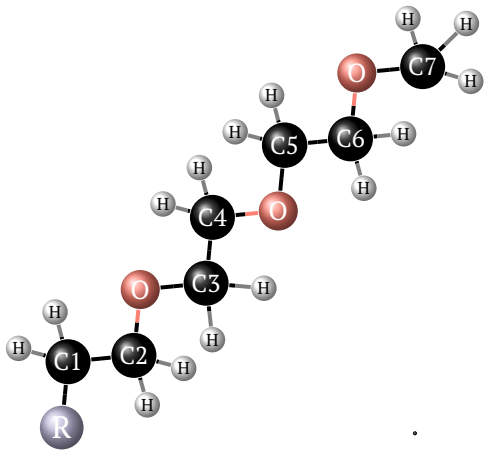
(c)

Bond	r_0(nm)	k_r (kJ/mol/nm^2)	Angle	θ_0(deg)	k_θ(kJ/mol/rad^2)
R-C1	0.154	218095	CX-CY-HZ	110.70	313.80
C1-C2, C2-C3, C3-C4	0.153	224262	R-C1-C2	114.00	527.184
C1-H, C2-H, C3-H, C4-H	0.109	284512	R-C1-H	109.50	292.880
			C1-C2-C3, C3-C2-C3, C2-C3-C3,C3-C3-C4	112.70	488.273

Dih. Angle	V_1(kJ/mol)	V_2(kJ/mol)	V_3(kJ/mol)	V_4(kJ/mol)	V_5(kJ/mol)	V_6(kJ/mol)
C2-C3-C3-C3, C3-C3-C3-$C_{3,4}$,	2.929	-1.464	0.209	-1.674	0.0	0.0
Ci-Cj-Ck-Hl	0.6276	1.8828	0.0	-2.5104	0.0	0.0

Figure 5.7: Ethylhexyl sidechain force field. a) nomenclature used. b) atom types, partial charges and Van der Waals parameters. c) shows bond, angle and proper dihedral parameters where X,Y,Z represent all C-C-H angles. i,j,k,l represent all intra-monomer C-C-C-H/C-C-C-C angles. d) shows the improper dihedrals which are added to account for planar stiffness due to conjugation.

(a)



(b)

Atom	q (e)	σ (nm)	ε (kJ/mol)	OPLS name
C1	-0.246	0.350	0.347	OPLS 139
C2	0.013	0.350	0.347	OPLS 139
C3	0.005	0.350	0.347	OPLS 139
C4	0.009	0.350	0.347	OPLS 139
C5	0.009	0.350	0.347	OPLS 139
C6	0.002	0.350	0.347	OPLS 139
C7	-0.049	0.350	0.347	OPLS 139
O	-0.383	0.290	0.586	OPLS 179
H	0.060	0.250	0.126	OPLS 140

(c)

Bond	r_0(nm)	k_r (kJ/mol/nm^2)	Angle	θ_0(deg)	k_θ(kJ/mol/rad^2)
R-C1	0.154	218095	CX-CY-HZ	110.70	313.80
CX-CY	0.153	224262	R-C1-C2	114.00	527.184
CX-H	0.109	284512	R-C1-H, O-CX-H	109.50	292.880
CX- O	0.141	267776	CX-O-CY	109.50	502.08
			CX-CY-O	109.50	418.400

Dih. Angle	V_1(kJ/mol)	V_2(kJ/mol)	V_3(kJ/mol)	V_4(kJ/mol)	V_5(kJ/mol)	V_6(kJ/mol)
CX-CY-O-CZ	1.715	2.845	1.046	-5.607	-0.000	0.000
H-CX-CY-O	0.979	2.937	0.000	-3.916	-0.000	0.000
H-CX-CY-H	0.628	1.883	0.000	-2.510	0.000	0.000
H-CX-O-CY	1.590	4.770	0.000	-6.360	-0.000	0.000
O-CX-CY-O	-1.151	1.151	0.000	-0.000	-0.000	0.000

Figure 5.8: Polyethylene Glycol sidechain, commonly called PEG force field used in Section 7.4.4. a) nomenclature used. b) atom types, partial charges and Van der Waals parameters. c) shows bond, angle and proper dihedral parameters where X,Y,Z represent generic sequential carbons (e.g. 1,2,3 or 4,5,6).

5.2.3 IDTBT

In this section we outline the force field development for indacenodithiophene-benzothiadiazole (which we refer to as IDTBT). The same general procedure was applied to generate the force field, the full details of which can be seen in [12]. IDTBT has four sidechains per monomer, unlike PFO which only has two; we restrict ourselves to the more physically realisable situation where all the side chains are the same so, for example, C8-IDTBT, has four sidechains at positions R1, R2, R3 and R4 all being octyl sidechains.

The same procedure we use for PFO was used by a former visiting student and collaborator, Anders Skovbo Gertsen from the Technical University of Denmark, to develop a force field for IDTBT. The force field is reported in [12] but we highlight a few elements worthy of note: unlike PFO a three residue model was used. In addition, as in PFO, additional improper dihedrals were needed to ensure the stiffness that arises from the conjugation was well modelled. Full details about this force field and its parameterisation can be found in[12].

5.3 Conformational Behaviour of Isolated Oligomers

As we have discussed, the final device performance depends on the conformational properties of the final film, which will in turn depend on the nature of the solvent-polymer interactions in the solution that the film is produced from. In the first instance, we look at basic conformational properties of the polymers, with different sidechains. Snapshots of the MD simulations of PFO octamers in chloroform, decalin (a 50:50 mix of cis and trans conformers) and water can be seen for octyl sidechains in Figure 5.9, hexadecyl sidechains in Figure 5.10 and ethylhexyl sidechains in Figure 5.11.

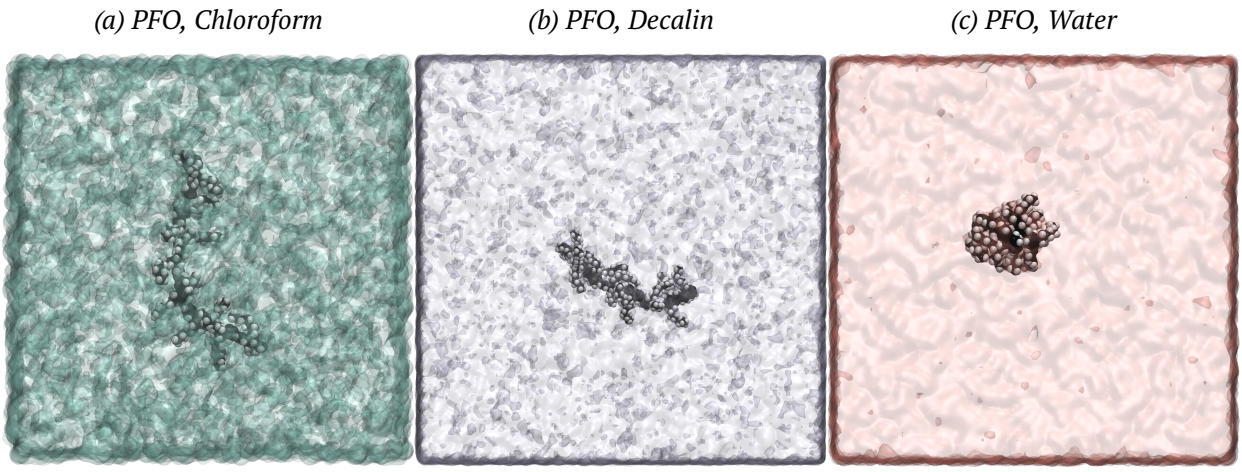


Figure 5.9: This figure shows snapshots of polyflourene with octyl (C_8H_{17}) sidechains in (a) chloroform, (b) a mixture of cis- and trans-decalin and (c) water.

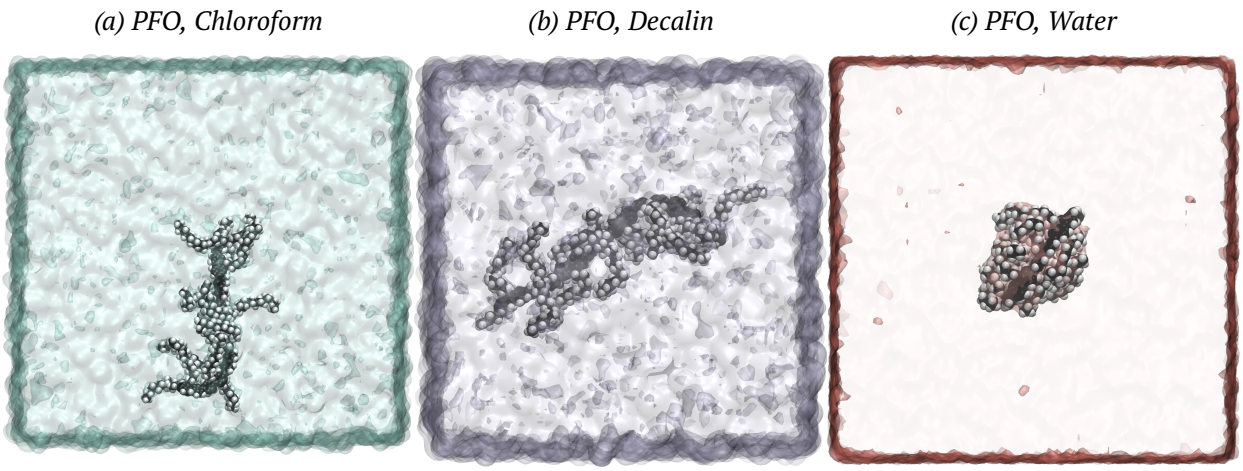


Figure 5.10: This figure shows snapshots of polyflourene with hexadecyl (C_16H_{33}) sidechains in (a) chloroform, (b) a mixture of cis- and trans-decalin and (c) water.

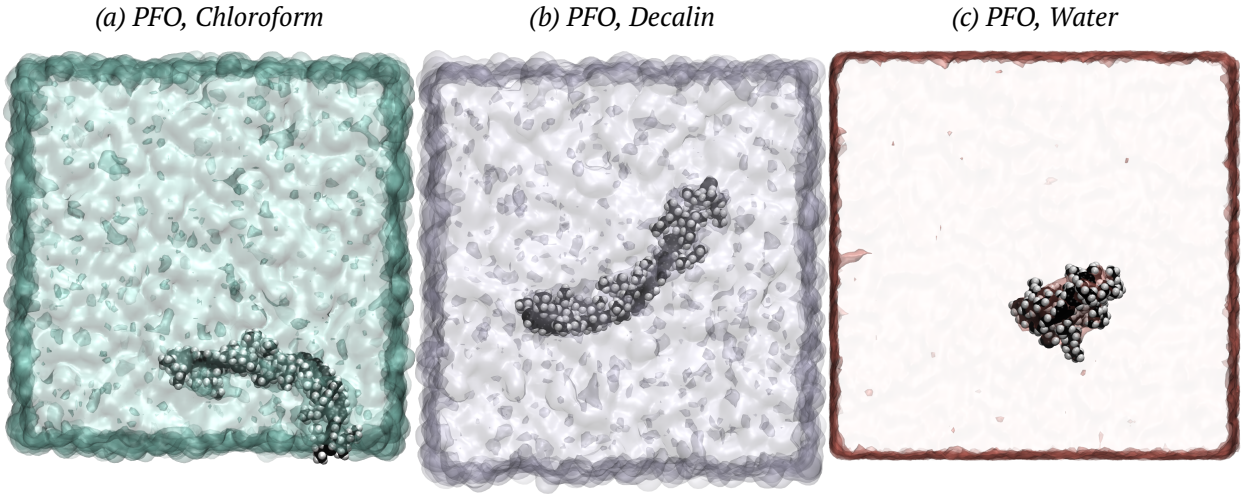


Figure 5.11: This figure shows snapshots of polyflourene with ethylhexyl ($C_2H_7(C_6H_{13})$) sidechains in (a) chloroform, (b) a mixture of cis- and trans-decalin and (c) water.

It is important to remember with molecular dynamics that no single timeframe or snapshot is physically meaningful, only quantities that are calculated over the whole trajectory and are then averaged. As such, whilst Figures 5.9-5.11 may provide some idea of where to begin looking, we must investigate this over the duration of a statistically significant simulated time. One feature that does leap out at us is that when a solvent is bad for the polymer (such as water) it attempts to "scrunch" up, making the surface area in contact with the solvent as small as possible compared with good solvents. We utilise the concept of radius of gyration, explained in Section 3.2.4.2, to determine the degree to which the oligomers curl up in each solvent. There are two different radiuses of gyration that are of interest to us; that of the backbone of the oligomer and that of the sidechains. If a sidechain or the backbone has a smaller radius of

gyration then it signifies that on average it is curled up more tightly. The radius of gyrations for the backbones and sidechains of PFO in chloroform, decalin and water and IDTBT in chloroform and water are shown in Table 5.1. It should be noted that these are taken as averages over one trajectory, and for a more reliable figure multiple configurations and trajectories should be used or alternatively a technique like the blocking method[17] to estimate the errors. For our purposes however it is enough to just note the comparitive results for the single trajectories. We can see from this that poor solvents for these polymers result in the radius of gyration of the backbone being much lower, implying that for PFO the best solvent is narrowly chloroform and the worst is water, and for IDTBT the best solvent is chloroform and the worst is once again water. These results match well with experimental observations.

Oligomer	Sidechain	Solvent	$r_{g\text{backbone}}(nm)$	$r_{g\text{sidechains}}(nm)$
PFO, 8mer	Octyl	Chloroform	1.7651	1.8136
PFO, 8mer	Hexadecyl	Chloroform	1.7944	2.0209
PFO, 8mer	EthylHexyl	Chloroform	1.7506	1.7427
PFO, 8mer	Octyl	Decalin	1.7936	1.8959
PFO, 8mer	Hexadecyl	Decalin	1.8656	2.143
PFO, 8mer	EthylHexyl	Decalin	1.8456	1.8724
PFO, 8mer	Octyl	Water	0.9443	0.7920
PFO, 8mer	Hexadecyl	Water	1.1146	0.9597
PFO, 8mer	EthylHexyl	Water	1.1079	0.9605
IDTBT, 12mer	Hexadecyl	Chloroform	5.4494	0.53580
IDTBT, 12mer	EthylHexyl	Chloroform	5.4314	0.25170
IDTBT, 12mer	Hexadecyl	Water	5.3637	0.5320
IDTBT, 12mer	EthylHexyl	Water	5.3591	0.25220

Table 5.1: This table shows the average radius of gyration for both the backbone and sidechains of PFO and IDTBT for a spectrum of solvents and sidechains. It is worth noting that these numbers represent a single sampling, and a more fuller picture would require multiple different starting configurations or through a technique like blocking[17] to properly represent the errors in these values.

We can confirm the link between the radius of gyration of the backbone and the quality of the solvent for that oligomer by performing free energy of solvation calculations, explained in Section 3.2.4.3, the results of which are also shown in Table 5.2.

Oligomer	Sidechain	Solvent	$\Delta F_{\text{sol}}(eV)$
PFO, 8mer	Octyl	Chloroform	-20.607±0.028
PFO, 8mer	Octyl	Decalin	-20.145±0.025
PFO, 8mer	Octyl	Water	-15.117±0.078

Table 5.2: This table shows the free energy of solvation of polyfluorene in three different solvents: chloroform, decalin and water, as calculated using molecular dynamics.

We show the limited number of data points we have between $r_{g_{\text{backbone}}}$ and $\Delta H_{\text{Solvation}}$ in Figure 5.12.

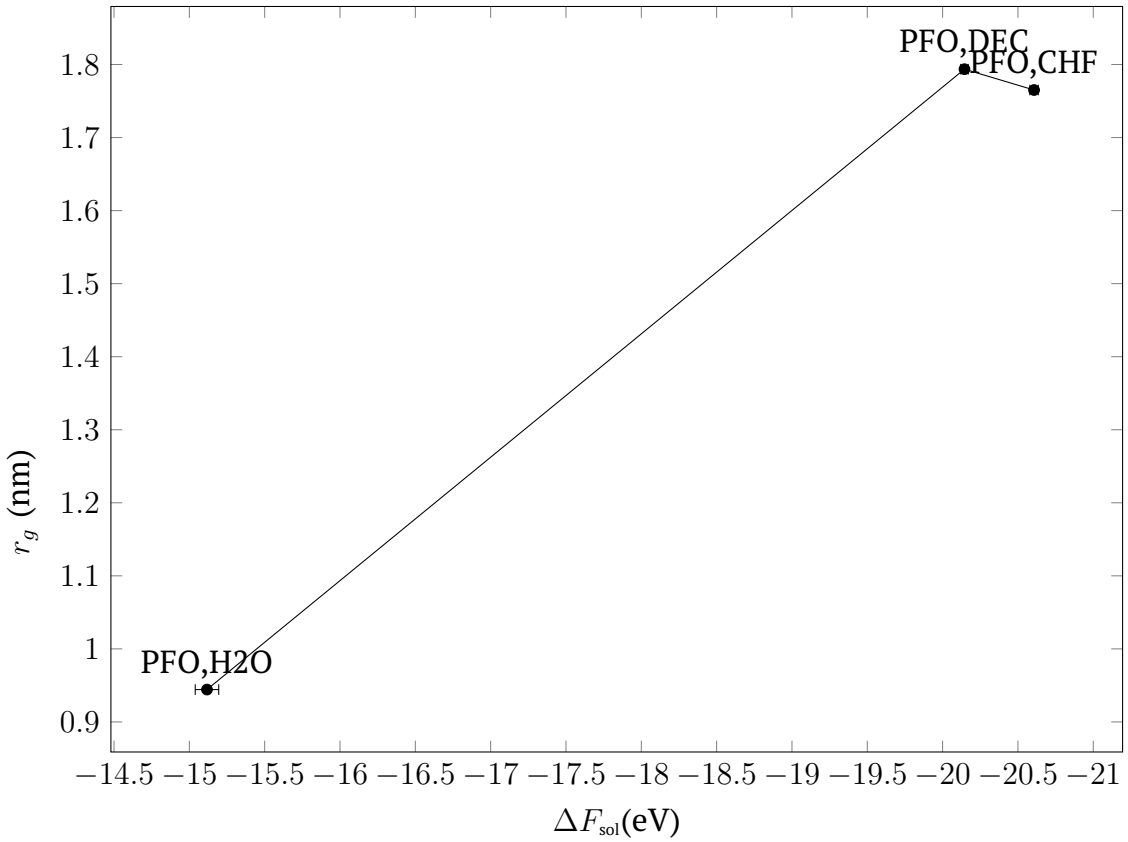


Figure 5.12: This plot shows the calculated free energy of solvation values for PFO in each of the solvents and how poor solvation corresponds with a decrease in the radius of gyration.

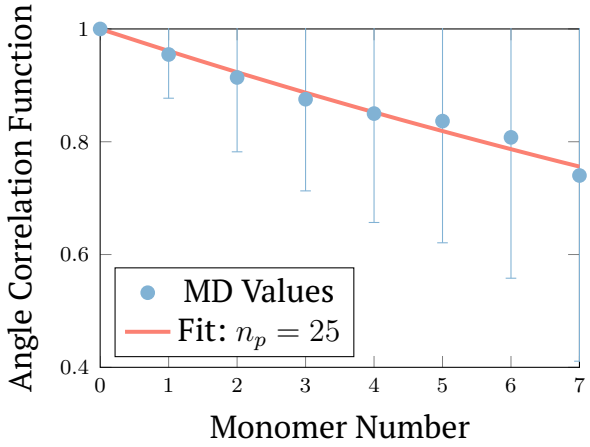
5.3.1 Persistence Length

We move on to consider a related property, the persistence length. The persistence length of a polymer is a measure of stiffness, and is defined as the length of a infinite polymer over which any correlations are lost. That is to say that there is no correlation between the direction of the tangent to the plane of the backbone of a monomer at the persistence length away from

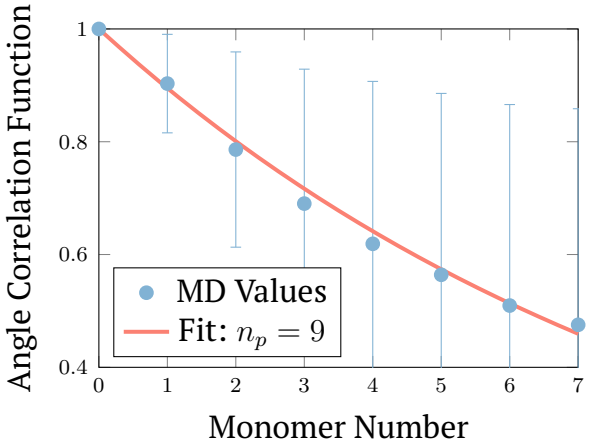
another monomer. There are different methods of determining this from experiment, such as small-angle neutron scattering and small-angle x-ray scattering, as well as chromatography based methods; however values of 8.5 nm (~8 monomers) exist for PFO in chloroform[236] and for IDTBT we know that the persistence length is much higher, though an exact number is not measured[77]. The relationship between the theoretical persistence length of an infinite polymer and the experimental measurement of a finite polymer is not clear.

We can also use molecular dynamics to obtain a measurement approximating the persistence length; we call this a stiffness measure to make it clear that the two concepts are not identical. To do this we calculate the cosine of the angle between the tangents of a monomer with monomers that are n monomers away from it, and then average it over all the monomers. This gives us the correlation as a function of monomer index (n), and if we restrict ourselves to dealing with n values that are smaller than the persistence length then the MD stiffness measure length can be estimated by fitting the correlation function to the form $C \propto e^{-\frac{n}{n_p}}$ where n_p is the stiffness measure expressed in a number of repeat units. Given there is more confidence in the persistence length of PFO we can use this to investigate the validity of the method before using it to narrow down the realm of possibility from experimental work. For this study, we simulate 8mers of PFO and 12mers of IDTBT. The stiffness measures calculated from the correlation functions, shown in Figures 5.12 and 5.13, are shown in Table 5.3.

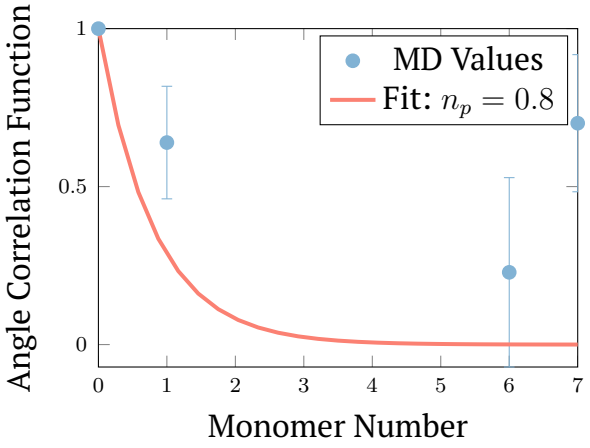
(a) PFO, Octyl, Decalin



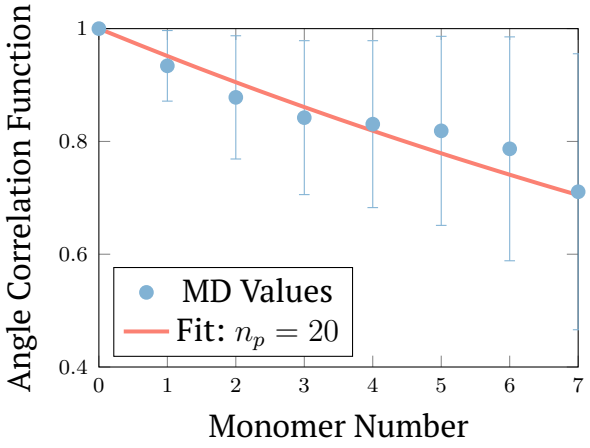
(b) PFO, Octyl, Chloroform



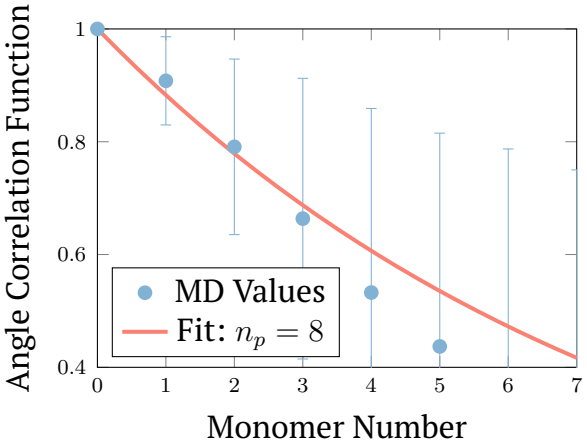
(c) PFO, Octyl, Water



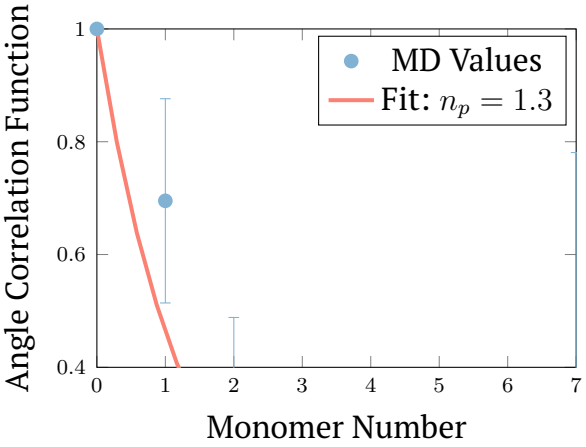
(d) PFO, Ethylhexyl, Decalin



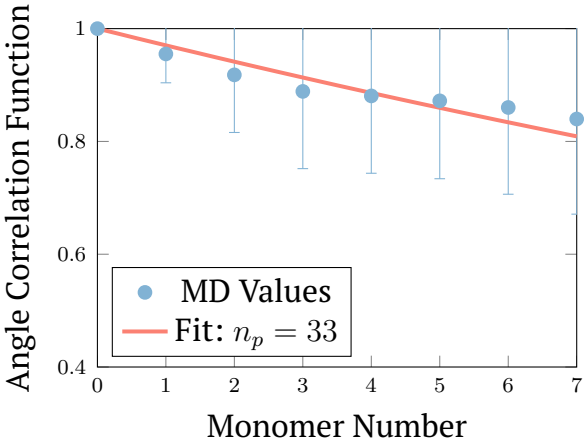
(e) PFO, Ethylhexyl, Chloroform



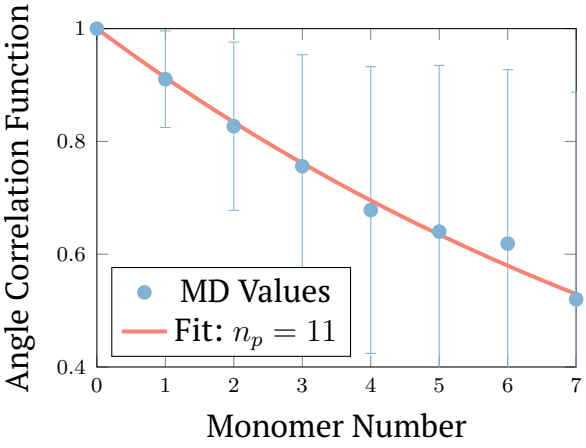
(f) PFO, Ethylhexyl, Water



(g) PFO, Hexadecyl, Decalin



(h) PFO, Hexadecyl, Chloroform



(i) PFO, Hexadecyl, Water

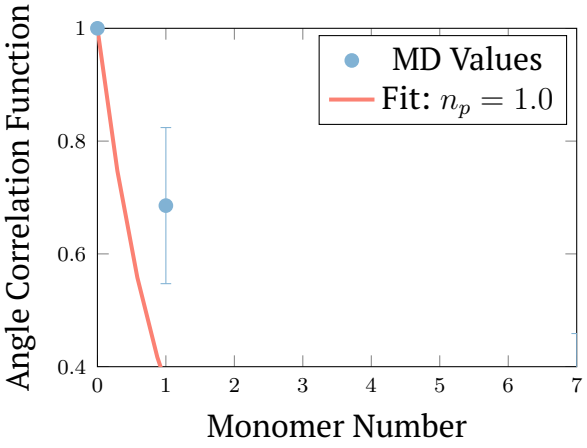
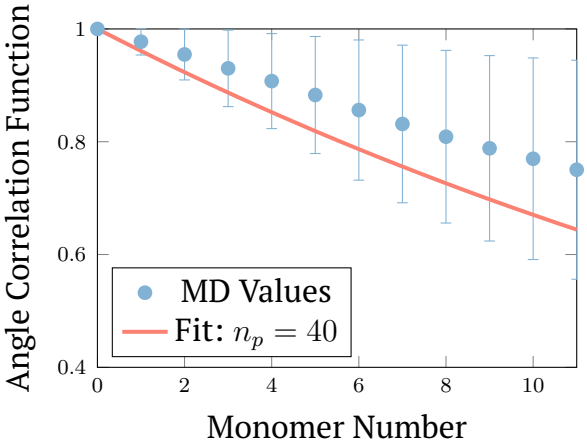
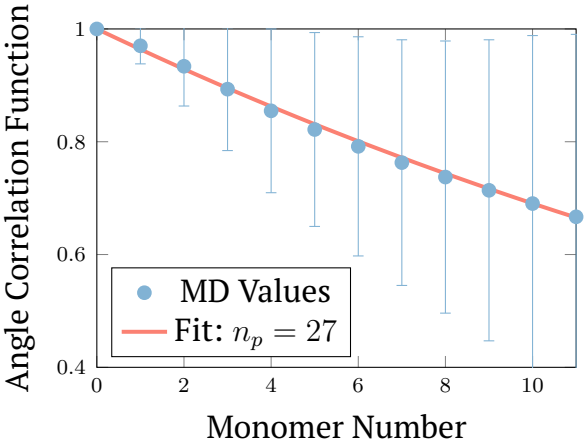


Figure 5.12: These plots show the results of the correlation function of monomer angles and the resultant fit used to determine the MD stiffness measure for PFO with (a), (b), (c): octyl sidechains, (d), (e), (f): ethylhexyl sidechains and (g), (h), (i): hexadecyl sidechains in (a), (d), (g): decalin, (b), (e), (h): chloroform and (c), (f) and (i): water.

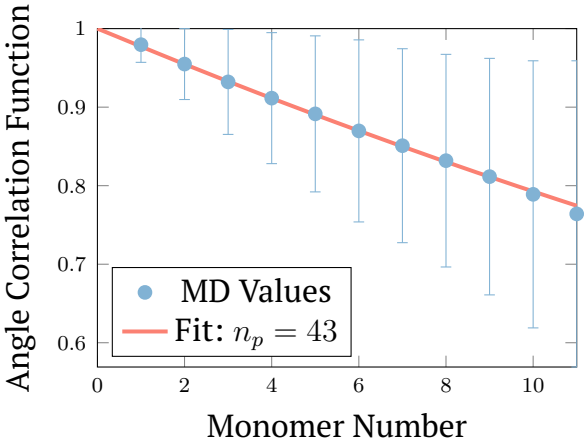
(j) IDTBT, Ethylhexyl, Chloroform



(k) IDTBT, Ethylhexyl, Water



(l) IDTBT, Hexadecyl, Chloroform



(m) IDTBT, Hexadecyl, Water

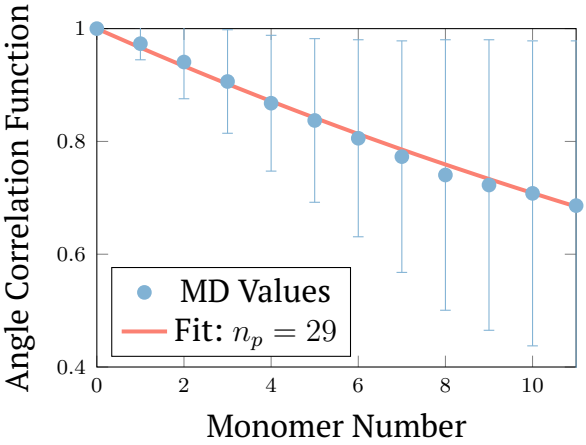


Figure 5.13: These plots show the results of the correlation function of monomer angles and the resultant fit used to determine the MD stiffness measure for IDTBT, from [12] with (a), (b): ethylhexyl sidechains and (c), (d): hexadecyl sidechains in (a), (c): chloroform and (b), (d): water

Oligomer	Sidechain	Length	Solvent	n_p(monomers)
PFO	Hexadecyl	8mer	Chloroform	11±4
PFO	Octyl	8mer	Chloroform	9±3
PFO	EthylHexyl	8mer	Chloroform	8±3
PFO	Hexadecyl	8mer	Decalin	33±16
PFO	Octyl	8mer	Decalin	25± 14
PFO	EthylHexyl	8mer	Decalin	20±8
PFO	Hexadecyl	8mer	Water	1.0±0.3
PFO	Octyl	8mer	Water	0.8±0.4
PFO	EthylHexyl	8mer	Water	1.3±0.6
IDTBT,	Hexadecyl	12mer	Chloroform	43± 12
IDTBT	EthylHexyl	12mer	Chloroform	40±11
IDTBT,	Hexadecyl	12mer	Water	29±9
IDTBT	EthylHexyl	12mer	Water	27±9

Table 5.3: This table shows the results of the correlation function fit obtaining the MD stiffness measure, with IDTBT values taken from [12] with permission. The errors given represent only the fitting error which we note is not a good representation of all sources of error.

We can see from this that for IDTBT the choice of sidechain seems to have a limited impact on the stiffness, but that the solvent drastically reduces it, an effect we also see in PFO. However, we see more of an impact of sidechain on the stiffness measure, where ethylhexyl seems to slightly reduce the IDTBT stiffness, than on the r_g metric, which was similar for both sidechain types. This may in part be to do with the locations of the sidechains allowing for a blocking effect to be more significant. We see for PFO that the stiffness is also impacted by being in a poor solvent like water. In general we can see that this approach is able to find values of the stiffness measure that seem to qualitatively agree with the experimentally measured values of persistence length. We can also see that the method begins to fail for really poor solvents (like water), and in general the method needs a longer simulation time to reduce the size of the error and ideally for different preparations or the blocking method to be used to better estimate the size of the errors. It should also be noted that thick chains are not expected to have exponential decaying autocorrelation functions and this can be seen clearly in PFO in water. Simulating longer chains may help resolve this.

5.4 Using Molecular Dynamics to understand Beta Phase in PFO

As we have outlined in the Introduction, the formation of a phase in PFO, called β-phase, characterised by planarisation of the backbone and different optical and electronic properties is important but a clear understanding of the mechanism of β-phase formation is lacking. To study this we use the force field developed to study the energy cost in solution of planarisation in different systems. We can study the factors that are known in the literature, such as the effect of sidechain length[104], branching of sidechains[237] and solvent effects[231, 232] in molecular dynamics to see if we can reproduce them as well as understand the reasons why.

5.4.1 Beta Phase Simulations

We first simulate single oligomers in solution with the oligomer backbones constrained to be planar and then examine changes in behaviour. Snapshots of octamers with and without restraints in the planar (β) phase are shown in Figure 5.14

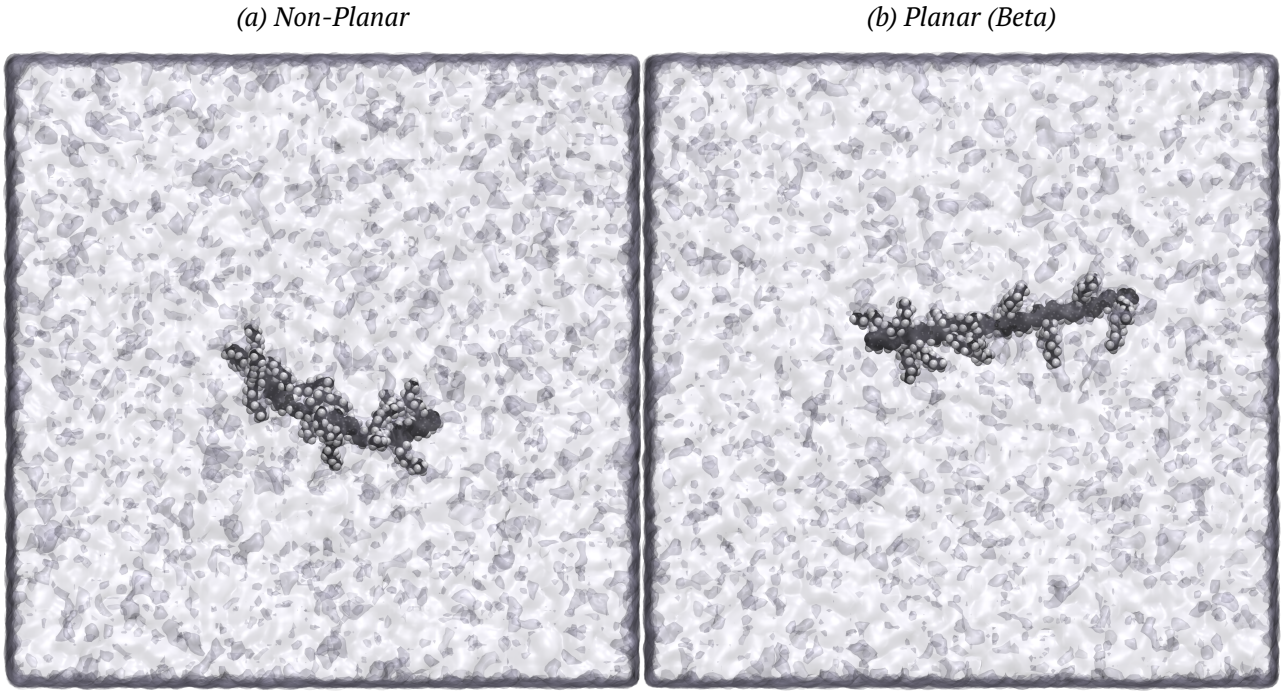


Figure 5.14: This figure shows snapshots from MD where PFO has been simulated in decalin with (a) no intermonomer dihedral restraints and (b) dihedral restraints that force PFO to planarise its backbone in a manner similar to the solid state beta-phase conformation.

We can see from this that, by eye, there seems to be a discernible change in the radius of gyra-

tion of the polymer itself upon β phase formation. We can't see any obvious changes with the sidechains. We now use the same methods as before to see if these passing observations stand up to statistical scrutiny. As we have outlined, beta-phase is characterised by the backbones of PFO being planarised, and as such it is clear that we must know if a backbone is planarised. To do this we analyse the time-averaged probability function of the dihedral angles. Examples for planarised and non-planararised oligomers are shown in Figure 5.15. When the restraint on the backbone is released the polymer adopts the lower energy, non-planar conformation, indicating that the interaction with the solvent is not enough to maintain planar conformation for an isolated chain in any of the solvents studied.

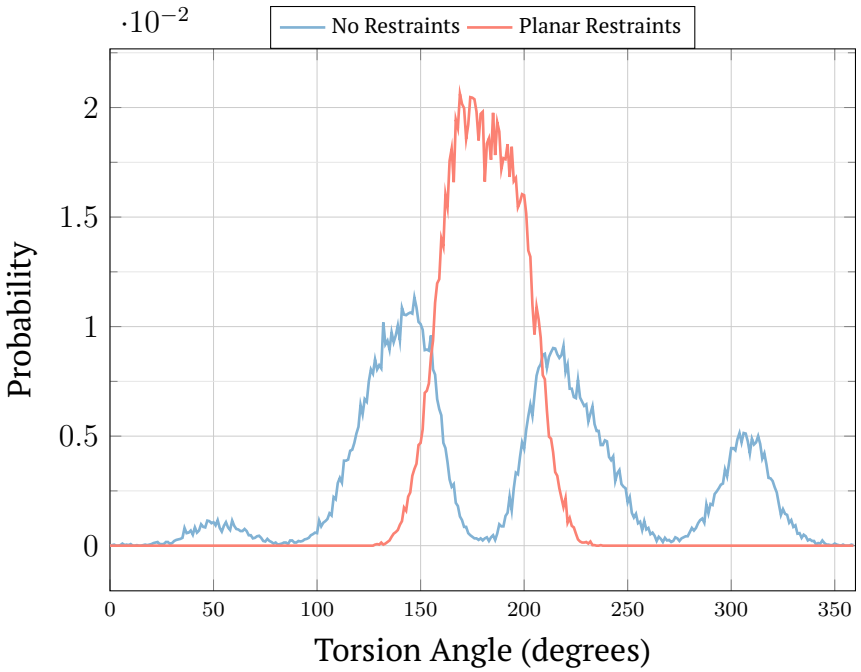


Figure 5.15: This figure shows representative angle probability distributions of the intermonomer dihedral of an octomer in chloroform. We can see that when not forced to be planar it samples the minima of the torsional potential.

We can, of course, control the width of the planar distribution by varying the strength of the potential holding it into planar formation.

5.4.2 Free Energy of Planarisation

As we discussed in Section 5.1.1 there are a few different pathways of producing beta-phase and it is not clear which is the physical pathway. In Figure 5.3 we see that there are two processes at work: aggregation and planarisation, and which occurs first is the key research question. Both of these mechanisms could, in principle, be studied using molecular dynamics. Aggregation could be investigated through the use of a technique called the potential of mean force (PMF)

which is where the distance between two oligomers is varied through a number of simulations (but held constant within one simulation) and then intergrated to obtain a potential profile for disaggregation. This is beyond the scope of the current work however. We instead investigate the differences in the free energy cost of planarisation (FEP) using a free energy calculation in MD. This follows a similar understanding but the strength of the planar constraint is varied instead of the distance; see Section 3.2.4.3 for more details of free energy calculations. The restraining potentials themselves will add to the total energy and a correction can be deduced by thermodynamically integrating the analytical expression for the restraining potential. Finally this gives a value that represents the free energy of the planarisation in those conditions.

In this section we study a number of different sidechains and solvents as well as systems of pairs of 'aggregated' oligomers. Doing this we hope to be able to reproduce the experimental observations from the literature that we outlined in Section 5.1.1, namely, that C8 sidechains should have the lowest FEP and for solvents water should have the highest FEP. Finally, we do not as yet have experimental guidance on whether the FEP should be bigger for isolated oligomers or for pairs. Table 5.4 shows the results of the FEP calculations for the different situations.

Oligomer	Sidechain	Solvent	Number	FEP(eV)
PFO, 8mer	Octyl	Chloroform	Single	+1.06±0.07
PFO, 8mer	EthylHexyl	Chloroform	Single	+1.73±0.14

Table 5.4: This table shows calculated free energy of planarisation for PFO oligomers with different sidechains and different solvents.

From Table 5.4 we see that ethylhexyl PFO is significantly harder to planarise but both cases have relatively large energy costs. This suggests that, at least for isolated short monomers, planarising is unlikely to be stable in a good solvent like chloroform and this is indeed as the experimental work suggests.

5.5 Conclusions

In this chapter we have used molecular dynamics to investigate the conformational properties of polymers in solution. In particular we have looked at metrics of determining a polymer's

stiffness, namely the radius of gyration and the persistence length. In both these cases we looked at the impact of solvent and of sidechains. We found that sidechains played a minimal role in the persistence length whereas the quality of the solvent made a significant difference. It should be noted however that in the situation in our simulations the oligomers are already dissolved and in reality the sidechain will have a solubising effect. This work suggests however that the structural impact of the sidechain is less significant than the solubilising impact of the sidechains.

We have also investigated the phenomenon of β-phase in PFO. By using restraints to force the oligomer to adopt a conformation akin to its solid state β-phase conformation, we have calculated the free energy cost of the process. This gives us an idea of the favourability of planarising, and we have used this to reproduce a well known experimental result that branched sidechains do not readily adopt β-phase.

6

Using Molecular Dynamics Simulations to Understand Local Microstructure of Conjugated Polymers for Water Splitting

6.1 Introduction: Differential Hydrogen Evolution

As previously discussed in Section 1.1 photocatalytic water splitting has been considered a way of generating a low-carbon renewable fuel that can be used to supply energy for technologies that can not readily be electrified, or as a form of energy storage. Approximately ~56% of all light (at sea-level) has enough energy (1.23eV) to perform the water splitting reaction. The process is strongly kinetically limited, however, by the reactions' complexity, involving a four-hole process for water oxidation. Whilst there are some photocatalysts that have been able to complete overall water splitting, mostly metal oxides[238], most work separates the reaction into two half-reactions: hydrogen reduction and oxidation. By focusing on these two reactions independently we hope either to one day use the knowledge in order to aid in the materials design of a system that can do both parts, or a hypothetical system of two cells, each doing one half of the reactions, that could together perform the whole reaction. In this work we focus on the hydrogen evolution side of the work. This usually involves the use of a Sacrificial Electron Donor (SED) which facilitates the hydrogen evolution reaction.

Whilst metal oxide photocatalysts have been the most extensively studied, recent work has begun to focus on organic materials, which are desirable for a variety of reasons including low toxicity, band gap tuneability, control of microstructure, and the earth abundance of the materials. The huge variability of options for organic materials provides great promise but also

leads to a large amount of complexity. Further, the ultimate final performance of the systems depends on a lot of different factors, including electronic structure, ability to disperse in the reaction mixture, solvation effects and the chosen SED.

6.2 Systems of Study

Experimental work (e.g. [134, 13]) has shown that photocatalytic activity varies with chemical structure. Since the activity is not related to the driving force calculated from IP*/EA we conclude it must relate to other properties or systems. The most pronounced effect noted in experimental work to date is from the inclusion of sulphone, therefore we focus our series using different fractions of sulphone. We select MD as our tool to study the effect of chemical structure on polymer morphology and the interaction with its (liquid) environment. We focus on a sub-class of organic materials, Figure 6.1, that have shown the best results: linear conjugated polymers. We focus on this particular work in an attempt to explore which of the many

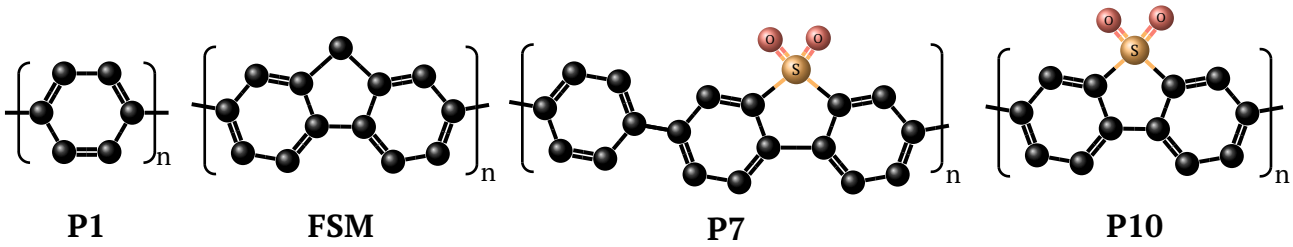


Figure 6.1: This figure shows the chemical structures of all the polymers considered experimentally, P1, P7, P10 and FSM. The latter was less well studied experimentally but is included for the computational study.

different properties could explain the differential hydrogen evolution. Much of the detail of what happens at the microscale of these systems is inaccessible through experiment. We know from experimental work[134, 13, 239] that small differences in electronic structure can lead to significant differences in performance at hydrogen evolution. In Figure 6.2 we present the key experimental insight into these systems, published in [14], by plotting results from Transient Absorption Spectroscopy (TAS) and the corresponding observed Hydrogen Evolution Rates (HERs).

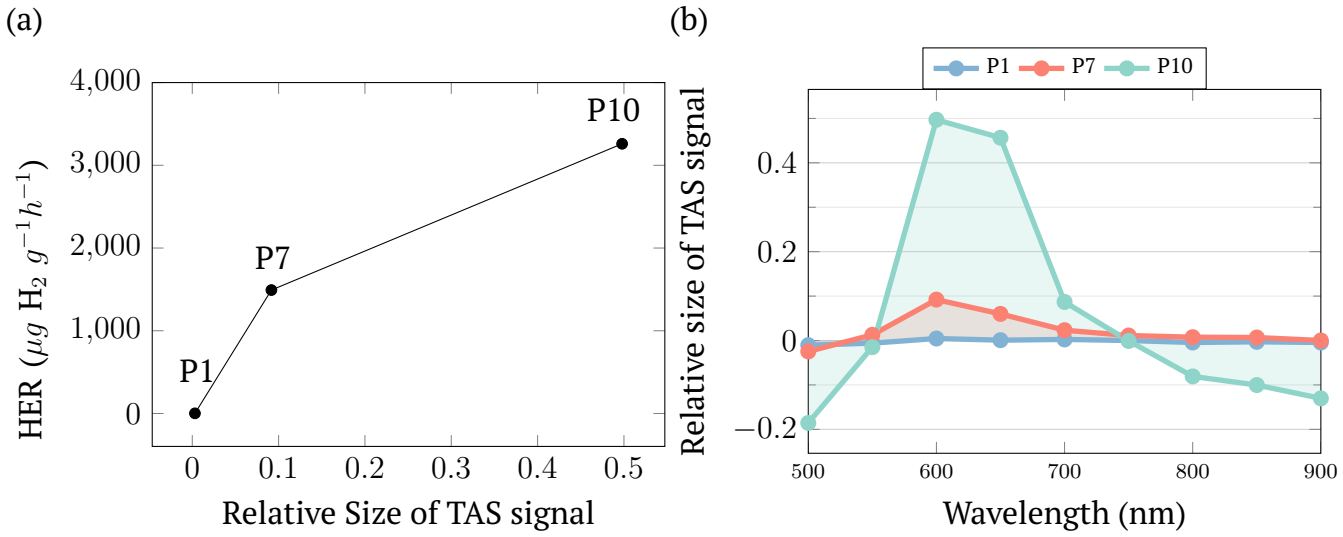


Figure 6.2: This figure summarises the experimental observations from [13] and [14], namely that (i) P7 and P10 evolve hydrogen whilst P1 does not and (ii) that this evolution correlates to a TAS signal, believed to be an electron polaron on the polymer. (a) Shows the relative TAS signal at 600nm after 100μs compared with the HER. (b) Shows the TAS spectrum at 100μs for P1, P7 and P10. Data reproduced from [14].

We see from Figure 6.2(b) that the experimental work[13, 14] shows that there is a long-lived species observable in Transient Absorption Spectroscopy (TAS) measurements. The signal of this long-lived species correlates with the polymers' observed hydrogen rates. As discussed there are a variety of reasons that HER might be different for different polymers. As such we must consider carefully the different possible reasons in turn, which are outlined below:

1. Different Electronic Structures

   How does the EA energy level (also sometimes used interchangeably with LUMO[1] of the polymer align with the redox potential for proton reduction. A bigger gap between these levels means the process is likely to be more driven and overcome kinetic and other barriers more readily.

2. Different exciton lifetimes

   If an exciton is longer lived it is more likely to have time to diffuse to the Polymer/Solvent interface and generate charge.

3. Different Absorption

   We do know that the solar photon flux spectrum at sea level reaches a peak in the near infrared,

[1]The EA and the LUMO are distinct things; in reality the electrons will rearrange and adjust the energy when accepting a new electron.

and if one polymer's energy levels lie closer to this region then they will absorb more photons and will likely have a higher apparent HER whilst not necessarily having a higher Quantum Efficiency.

4. Different amounts of residual metal co-catalysts.
   The synthesis process leaves a residual amount of platinum, or other heavy metal, which is known to have a significant effect on hydrogen evolution[139]. Higher performing polymers may just result from processes that leave more residual platinum.

5. Solvation effects.
   The polarity of the local medium will affect the EA level and thus how driven the reaction is.

6. Particle Size Effects.
   The only part of the particle volume that will contribute to HERs will lie between the surface and one exciton diffusion length deep. Therefore, if different polymers disperse differently in the reaction mixture, this can lead to different amounts of active material for the same concentration of polymer.

In the next sections I outline the theoretical tests I performed to evaluate most of these possible explanations, as well as the experimental work my collaborators undertook.

6.3 Investigating differential hydrogen evolution

In this section we outline the results from work using a mixture of computational methods and experimental work carried out by collaborators. This section is dedicated to ruling out the explanations that we found did not explain the observations. In the next section we outline the main body of work of this chapter that did seem to have some explanatory power, namely, local solvent effects.

6.3.1 Electronic Structure

In order to understand if well performing polymers have a larger "driving force" (difference between the EA and standard hydrogen evolution level, SHEL) we used DFT to calculate the EA level, corresponding to the reaction given by Equation 6.1:

$$P^- \rightarrow P + e^-. \tag{6.1}$$

The EA values found for FSM, P1, P7 and P10 are shown in Figure 6.3.

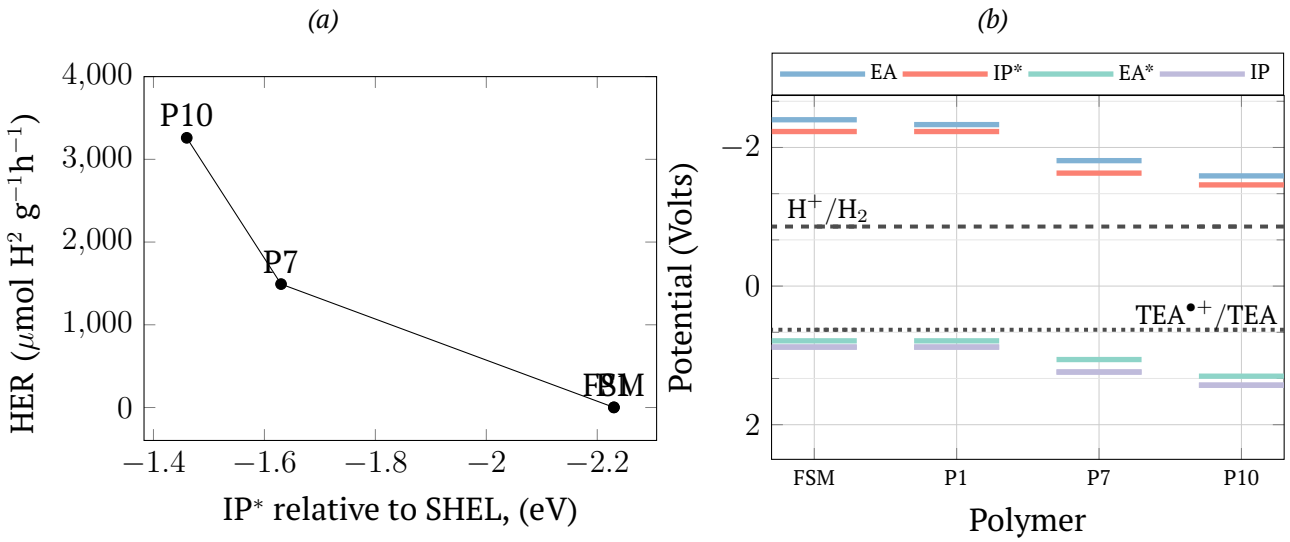


Figure 6.3: This figure shows a method from the literature of determining the likelihood of hydrogen evolution occuring. We determine the EA, IP, EA* and IP values relative to the SHEL. From this we can deduce a "driving force" by looking at the difference between IP* (some people approximate this using EA) and the hydrogen evolution potential. (a) plots the experimental HER versus the calculated driving force. (b) shows the levels relative to the SHEL.*

It shows that far from helping to explain differential HER performance, the trend shown is actually that higher performing polymers have weaker driving forces. Although all the driving forces would be considered strongly driven. We also compare electron density profiles between them in Figure 6.4, and we can see that the sulfone (SO_2) groups do not introduce significant changes in the spatial distribution of the LUMO and HOMO molecular orbitals.

One significant difference we can note from electronic structure calculations is the introduction of a large dipole moment in polymers containing sulfone groups, see Figure 6.5. This is likely to impact solvation effects as we shall see in the next section.

6.3.2 Exciton Lifetimes and Particle Sizes

In order to investigate whether the difference in hydrogen evolution was in fact down to differential amounts of active volume we need to investigate particle sizes in solution and their exciton lifetimes. This would allow us to calculate the active volume or mass. In order to do this my experimental collaborator, Sam Hillman, performed Dynamic Light Scattering (DLS) measurements to obtain values for the average particle size in dispersion of P1, P7 and P10. In addition, he calculated exciton lifetimes by fitting exponentials to the TAS kinetic data. The

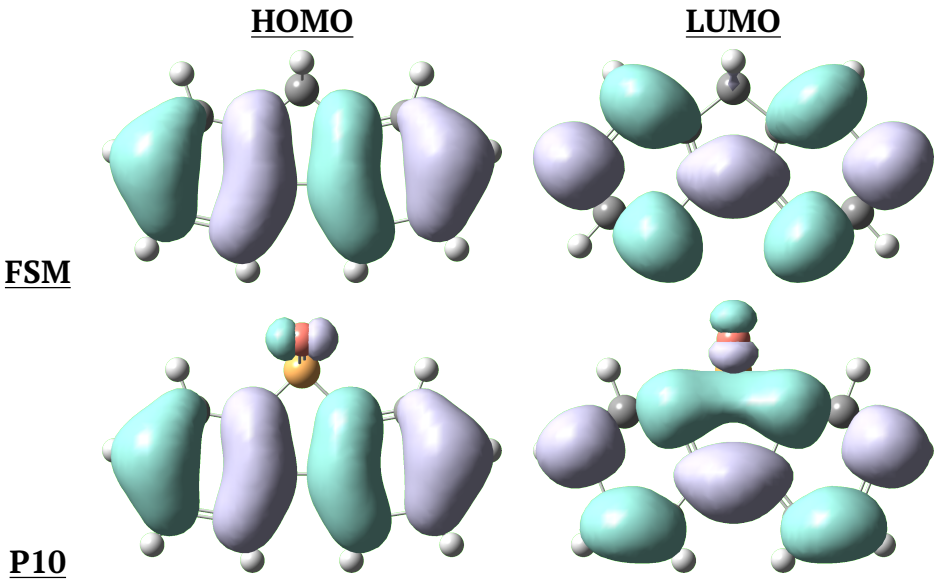


Figure 6.4: This figure shows the spatial distribution of the electron in the Kohn-Sham HOMO and LUMO states for FSM and for P10. These have been calculated using DFT with the ωB97XD functional and the aug-cc-pVDZ basis set.

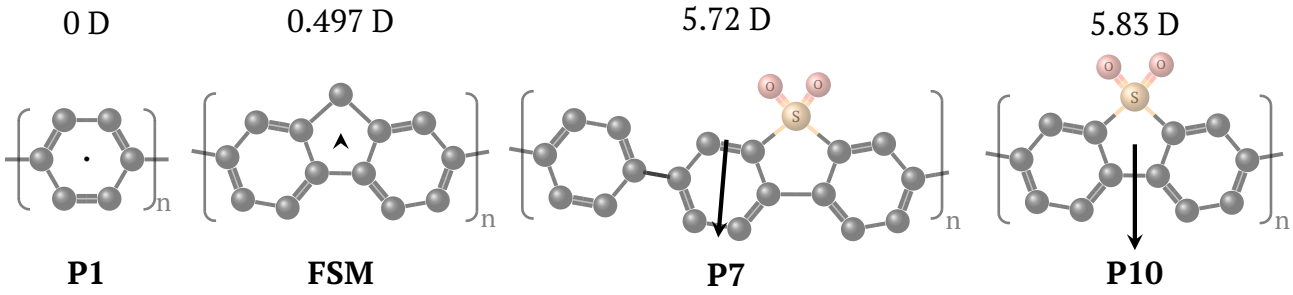


Figure 6.5: This figure shows the magnitude and direction of the dipole moments in Debeye found using the ωB97XD functional and the aug-cc-pVDZ basis set for monomers of P1, FSM, P7 and P10.

exponentials were of the form:

$$y(t) = A + \sum_i B_i \exp\left(-\frac{t}{\tau_i}\right), \tag{6.2}$$

where i runs over several exponentials in order to best fit the data. In this case, three are used. An average lifetime is then calculated by $\bar{\tau} = \sum_i B_i \tau_i$. In Figure 6.6 we plot these average lifetimes against the observed HERs.

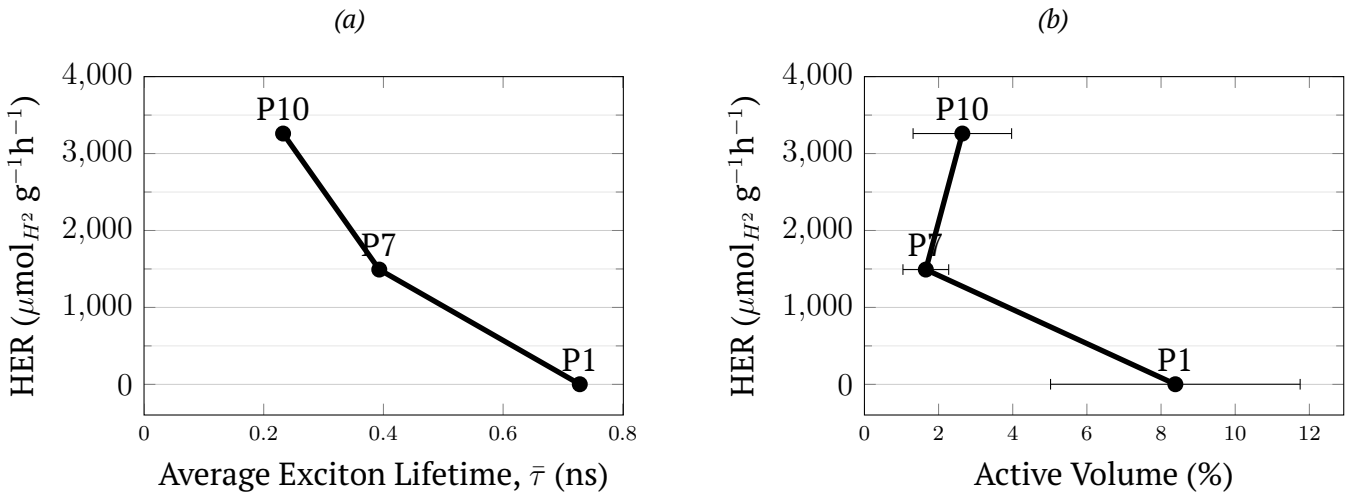


Figure 6.6: This figure shows the hydrogen evolution rates (HERs) for P1, P7 and P10 plotted against (a) average exciton lifetime from TAS data[14], (b) active volume, calculated from Equation 6.3 as a percentage.

From the data we see that, as for the electronic driving force, the trend is not what we would expect if exciton lifetime was the limiting factor. The largest lifetime belongs to P1 which also has the lowest HER. This suggests that all our systems are in a region where the exciton lifetime is not the limiting factor. We must be aware that particle size is going to be interlinked with lifetime. The exciton lifetime and diffusion will control how much of a particle is available for activity, see Figure 6.7.

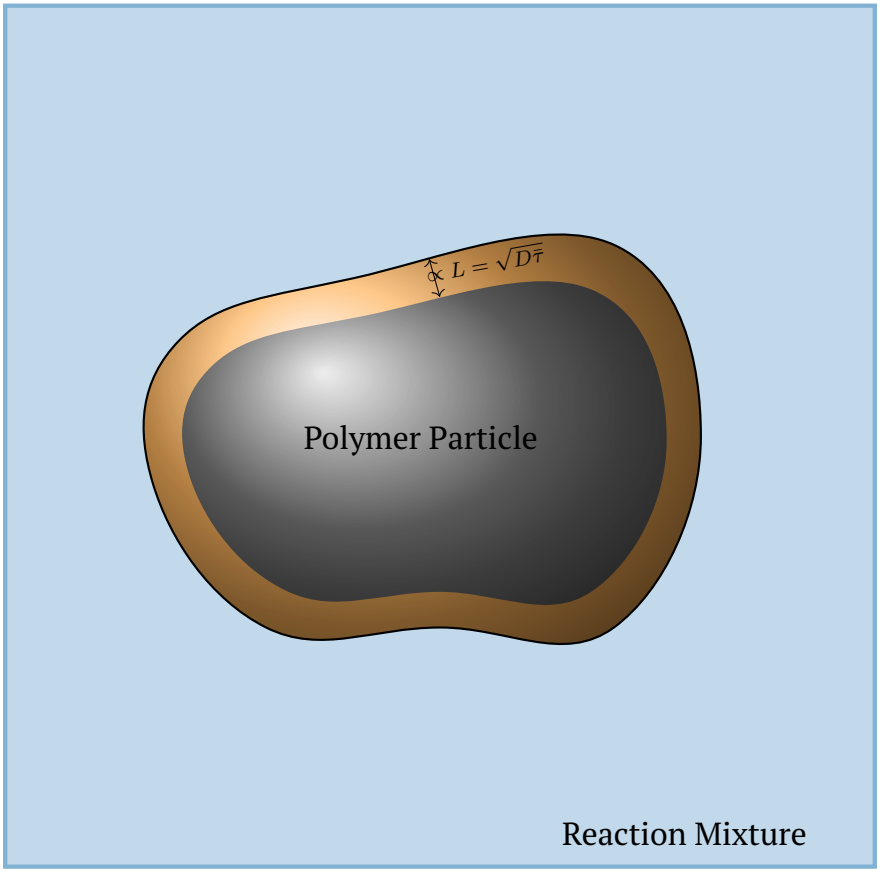


Figure 6.7: This figure shows how exciton lifetime and diffusion affect how much polymer in the material is active for contributing to hydrogen evolution. The active area is highlighted in orange, and represents the average length that excitons can travel within its given lifetime. Thus, excitons generated inside the orange region have the potential to generate hydrogen whilst those in the grey region do not. In the schematic we show a case where the diffusion length is much smaller than the particle size.

In order to understand this we need to examine these data comparatively with an understanding of the particle size. For this we highlight data collected by Sam Hillman [14] on the suspensions of these polymer particles measured using Dynamic Light Scattering (DLS) in water and reaction mixture. The measurements show that P1, P7 and P10 have average sizes of 535 ± 47nm, 915 ± 76nm and 648 ± 11nm in water and 421 ± 39nm, 2199 ± 103nm and 1507 ± 314nm in reaction mixture respectively. Using the exciton lifetimes we can estimate a diffusion length and in doing so estimate the percentage of the polymer that is active in each case. We do this by assuming the particle is a sphere with a radius of average particle size, and the active volume will be made by a shell of thickness L_d into this sphere, with L_d being the diffusion length which can be related to the exciton lifetime as $L_d = \sqrt{D\bar{\tau}}$ with D being the exciton diffusion coefficient. The diffusion coefficient adds some uncertainity into the calculation as these have not been measured for our systems. We do have this exciton lifetime data and if we combine this with

estimates of diffusion lengths for a similar class of materials calculated by a film thickness study we can obtain a reasonable range of values for the diffusion coefficient. This data suggests a diffusion length of 6 ± 2nm[240]. This would suggest the diffusion coefficients for this set of polymers could lie anywhere in the range of 20-300 nm^2/ns. We take the value of 150 nm^2/ns but we will factor this range into the errors of the calculation. The equation for the fraction of active volume is given by

$$f_a = 1 - \frac{(d_{\text{av}} - 2L_d)^3}{d_{\text{av}}^3}, \tag{6.3}$$

where f_a is the volume fraction of particle that is photocatalytically active, L_d is the diffusion length and d_{av} is the average particle size (which is a diameter). Figure 6.6 shows both the average exciton lifetime and the calculated active volume against the experimental HER values.

We can see from Figure 6.6 that it is not only exciton lifetimes and particle sizes that fail to explain the different amount of hydrogen evolution between these polymers, as neither does the expected active volume. It is also important to note that none of the polymers are near their total potential evolution of hydrogen. As such, it is clear that if we want to maximise the performance of a polymer we should investigate closely the ability of the polymer to disperse as fully as possible in reaction mixture.

6.3.3 Differential Co-catalyst amounts

In organic photocatalysts there are often co-catalysts which are known to impact on H_2 evolution. It is possible that the different performance observed is as a result of different amounts of co-catalyst being present. To understand this our experimental collaborators tested this effect and found that the only potential co-catalyst present was palladium which had previously been suggested as having a function as a co-catalyst[14]. More recently, extensive work has studied the impact of different concentrations of palladium on hydrogen performances of a different linear organic photocatalyst. Most of these studies suggest that increasing the concentration of palladium above between 0.015-0.03%wt ceases to have significant effects on the hydrogen evolution[139]. When the amount of palladium is measured in our systems it is found that P1, P7 and P10 have 0.33wt.%, 0.38wt.% and 0.4wt.% respectively. Whilst this trend is positively correlated with HER, all these numbers are beyond the reported saturation concentration so it suggests the differences are unlikley to be the cause of the different performances. We should move forward, however, with an awareness that the palladium content is likely to be a signifi-

cant contributing factor to reported HER values.

6.3.4 Absorption Spectra

In this section we discuss how different absorption could be responsible for different levels of hydrogen evolution. Any given polymer is likely to have different absorption spectra from another given polymer due to energy levels that differ. This consideration should be combined with the fact that the solar spectrum has different photon flux densities at different wavelengths. For example, a polymer that absorbs more strongly in the red region will absorb more photons than one that absorbs more in the blue. In order to examine this we employ both experimental measurements of the polymer dispersions, as well as TD-DFT calculations, to obtain the absorbance and the decadic optical density of the materials respectively. TD-DFT calculations are used to obtain the energy and oscillator strength of excited states, a guassian with a width of 0.333eV at half height to generate the ε. ε is the decadic extinction coefficient. We now need a way of relating these quantities to the expected absorptance. There are two possible regimes we could be in, low optical density and high optical density. The relationship between absorptance and absorbance can be written as,

$$A_t = 1 - 10^{-A_b}. \tag{6.4}$$

Which in the case of low optical density we can write as $A_t = \log(10)A_b$. DFT calculations can be converted to absorbance by multiplying the dedadic extinction coefficient found,ε, by the optical path length (which from experimental parameters we take to be 3cm) and the concentration (which the experimental setup has as 1.73mM).

Multiplying the polymers absorptance by the spectrum of the lamp used in the HER experiments (a 300W Newport Xe light source, Model 6258) yields the absorbed photon flux spectrum in the experiment. The lamp spectrum is plotted alongside the solar spectrum in Figure 6.8.

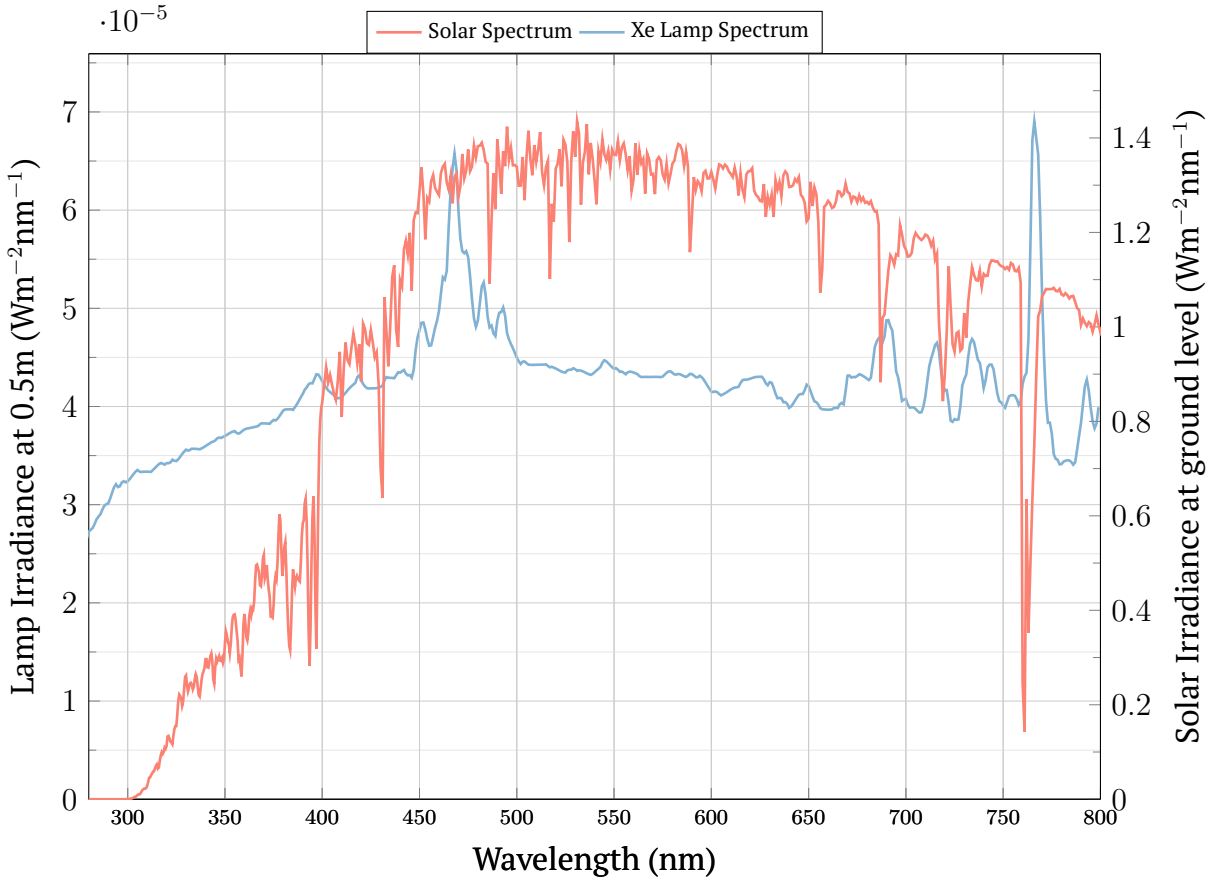


Figure 6.8: This figure shows the spectrum of the Xe lamp used (a Newport Model 6258) in the hydrogen evolution experiments. For reference the solar spectrum at sea-level is also plotted.

In Figure 6.9 we show the experimentally measured absorbance, from [14]. Alongside this we show the absorbed photon flux calculated using the experimental absorptance (assumed to be proportional to the absorbance).

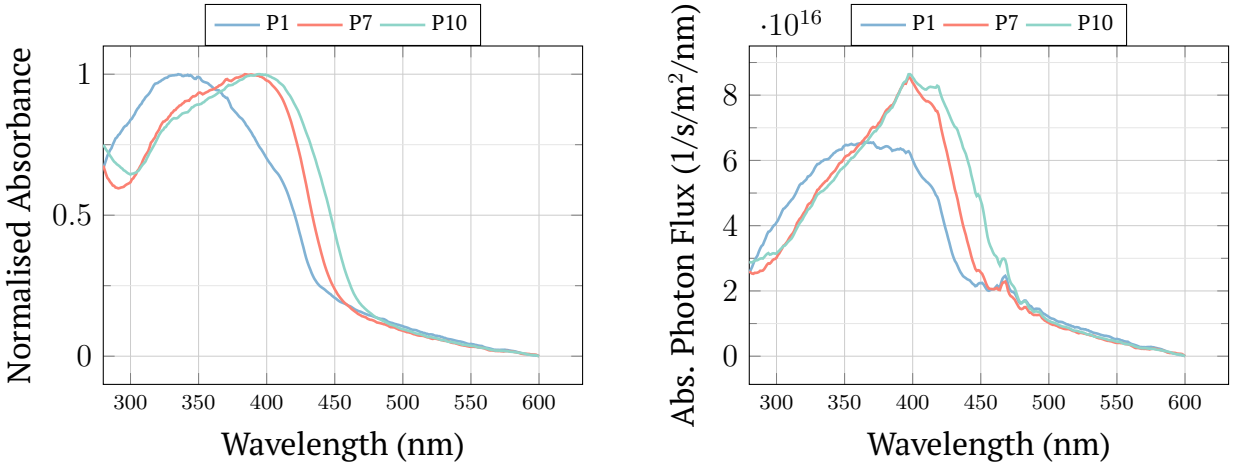


Figure 6.9: Normalised experimentally measured absorbance spectra are shown on the left. The right shows the absorbed photon flux by each polymer, based on the experimental absorption and spectrum of the lamp used in the HER experiments.

We now replicate Figure 6.9 but for theoretically derived absorbance, from TD-DFT. This is shown in Figure 6.10.

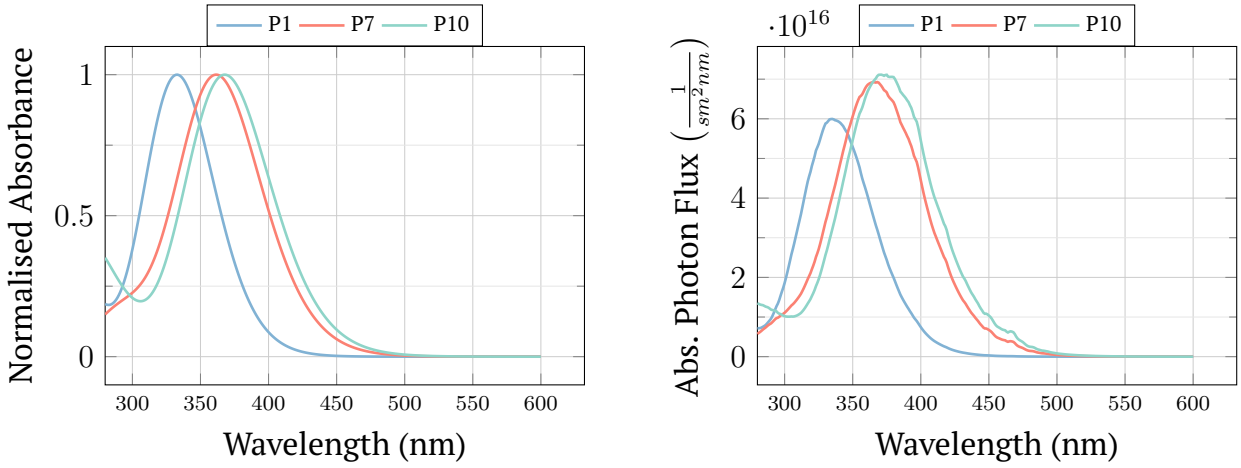


Figure 6.10: Absorption, predicted theoretically using TD-DFT calculations, is shown on the left. The right shows the absorbed photon flux by each polymer, based on the theoretically predicted absorption and lamp spectra of the lamp used in the HER experiments.

We see from both Figures 6.9 and 6.10 that the theoretical and the experimental absorbances line up well; the exact locations of the peaks are not identical but with TD-DFT this is not surprising. We now need to integrate the absorbed photon flux spectrum so we can get a total absorbed photon flux that tell us how many photons are absorbed in the HER experiments that could, in theory, go on to evolve hydrogen. In Figure 6.11 we show the correlation between HER and both the experimentally and theoretically derived total photon absorbance flux. From this we see that there is a trend between higher photon absorbance and HERs, but an examination of the numbers involved suggests this is not the primary cause of the increase in HER. The number of photons absorbed by P10 is only 1.16 times (1.57 times) the number absorbed in P1 using the experimental (theoretical) absorbance, compared with the P10 HER being 2026 times the P1 HER.

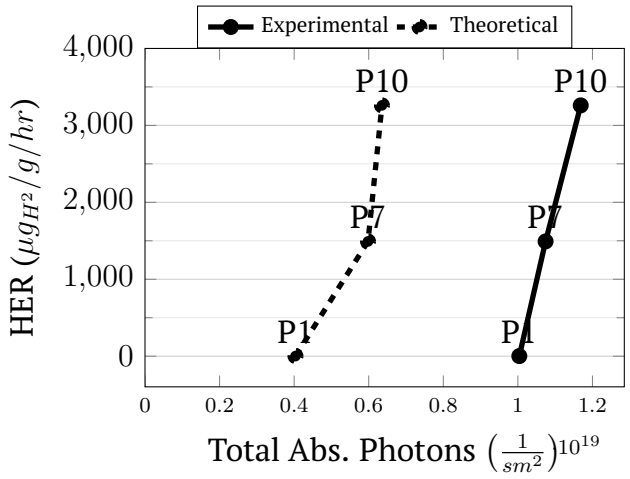


Figure 6.11: This figure shows both experimental (solid line) and theoretical (dashed) predicted total photon absorbance of P1, P7 and P10 compared with the experimental HERs. We see that increased number of photons is only 1.64 times going from P1 to P10 whereas the HER is 2026 times.

From this we conclude that both experiment and theory are in agreement that differences in absorption of the polymers is not sufficient to explain the differences in hydrogen evolution. As a result we continue examining the other potential options.

6.4 Molecular Dynamics of Solvation

6.4.1 Introduction and Choice of Method

The experimental set-up is quite complex, involving three solvents, residual palladium and a variety of sizes of particle. Information about how each of these components behave in the experimental set-up is difficult to obtain, particularly how solvents interact with each other and the polymers at the microscale. We know in principle that differing local environments will affect the favourability of the reactions involved either by affecting the energetics of the reaction (higher polarity environments are likely to stabilise charge separation reactions) or by affecting the kinetics (by affecting the availability of the reactants).

Since we don't have access to experiments able to provide information about the microscopic local environment[2] at equilibrium in such a complex system we turn to consider theoretical methods that may help us understand any differences in interactions between the solvents and

[2]There are a number of experimental techniques that could be used to gain some information about the system such as neutron scattering and SAXS/WAXS.

the polymers. The natural method of choice for this situation is molecular dynamics (MD), allowing us to simulate, with statistical validity, the equilibrium state of boxes of lengths up to ~50nm in reasonable times with reasonable amounts of computational resource dedicated to it. Experimental DLS measurements tell us that the nanoparticles are between 525nm and 915nm and thus to simulate it alongside a reasonable solvation shell, would need a box of 1μm which lies beyond the capability of atomistic MD. This gives us two options; consider a model that is tractable in MD, i.e. a subset of the system that will still give us some useful information on solvent interactions, or recourse to a coarse-grained model. As a coarse-grained model would need to be extensively parameterised and tested against an atomistic molecular dynamics model we first investigate a model of the full experimental set-up, extracting all useful information from it before returning and considering whether a coarse-grained model would yield useful extra information that we require. As a result, in the first instance, we simplify the system in three ways: considering short oligomers rather than polymers; considering only single, fully dispersed, oligomers rather than nanoparticles; and neglecting the palladium, as that would statistically be unlikely to be present in systems of our size.

6.4.2 Force Field Development of Polymers

6.4.2.1 Overview

In this subsection, we build the force fields for the polymers we have discussed in this chapter, FSM, P1, P7 and P10. We follow the general procedure for developing force fields for oligomers that we outline in Section 5.2. We now outline the procedure for this specific case.

1. OPLS contains parameters for atoms in the same or very similar chemical contexts. These are shown in (b) of Figures 6.17, 6.18, 6.19 and 6.20 for FSM, P1, P7 and P10 respectively.

2. Bond and Angle parameters were available directly from the OPLS database and thus no DFT calculations were required. The chosen parameters are shown in (c) of Figures 6.17, 6.18, 6.19 and 6.20 for FSM, P1, P7 and P10 respectively.

3. DFT calculations were performed to extract partial charges on each monomer[3]. This established that the single residue model was a good approximation. Figure 6.12 shows the results of these calculations. The partial charges are symmetrised and averaged and this gives the force fields' partial charges. The results of this are shown in (a) of Figures 6.17, 6.18, 6.19 and 6.20 for FSM, P1, P7 and P10 respectively.

[3]Partial charges are not a quantum observable and thus must be derived in some way. We use the CHELPG method which is most commonly used for accurate partial charges for MD.

4. The intermonomer torsion was fitted to DFT calculations, and these are shown in Figure 6.13. The final parameters found from this procedure are outlined in (c) of Figures 6.17, 6.18, 6.19 and 6.20 for FSM, P1, P7 and P10 respectively.

5. Finally, OPLS force fields do not reproduce well the backbone stiffness known to exist for conjugated polymers and as such we add improper dihedrals to the backbone. The DFT scans performed to do this are shown in Figures 6.14, 6.15, 6.16. The parameters derived are shown in (d) of Figures 6.17, 6.18, 6.19 and 6.20 for FSM, P1, P7 and P10 respectively[4].

Section 6.4.2.2 contains all the data obtained from DFT and used to parameterise the MD. Section 6.4.2.3 presents the complete force fields with all the parameters necessary to run the simulations.

6.4.2.2 Data for Force Fields

Partial Charges

In this section we plot, Figure 6.12, the net partial charge on monomers for oligomers of different sizes, as calculated using SCF with DFT.

[4]The accuracy of DFT, specifically the b3lyp functional we use here, is important to discuss. The barrier heights associated are known to be systemaically underestimated due to the fact the full exchange-correlation favours less localised charge which occurs when near the maxima of the potential energy surface (through, e.g., the hydrogens being forced closer together). Since MD, by it's very nature, samples regions of the phase space that are close (relative to k_BT) to the minima of the potential energy surface and the results show high barriers relative to k_BT we proceed in the knowledge that for the sampled region the DFT scans can be considered sufficiently accurate.

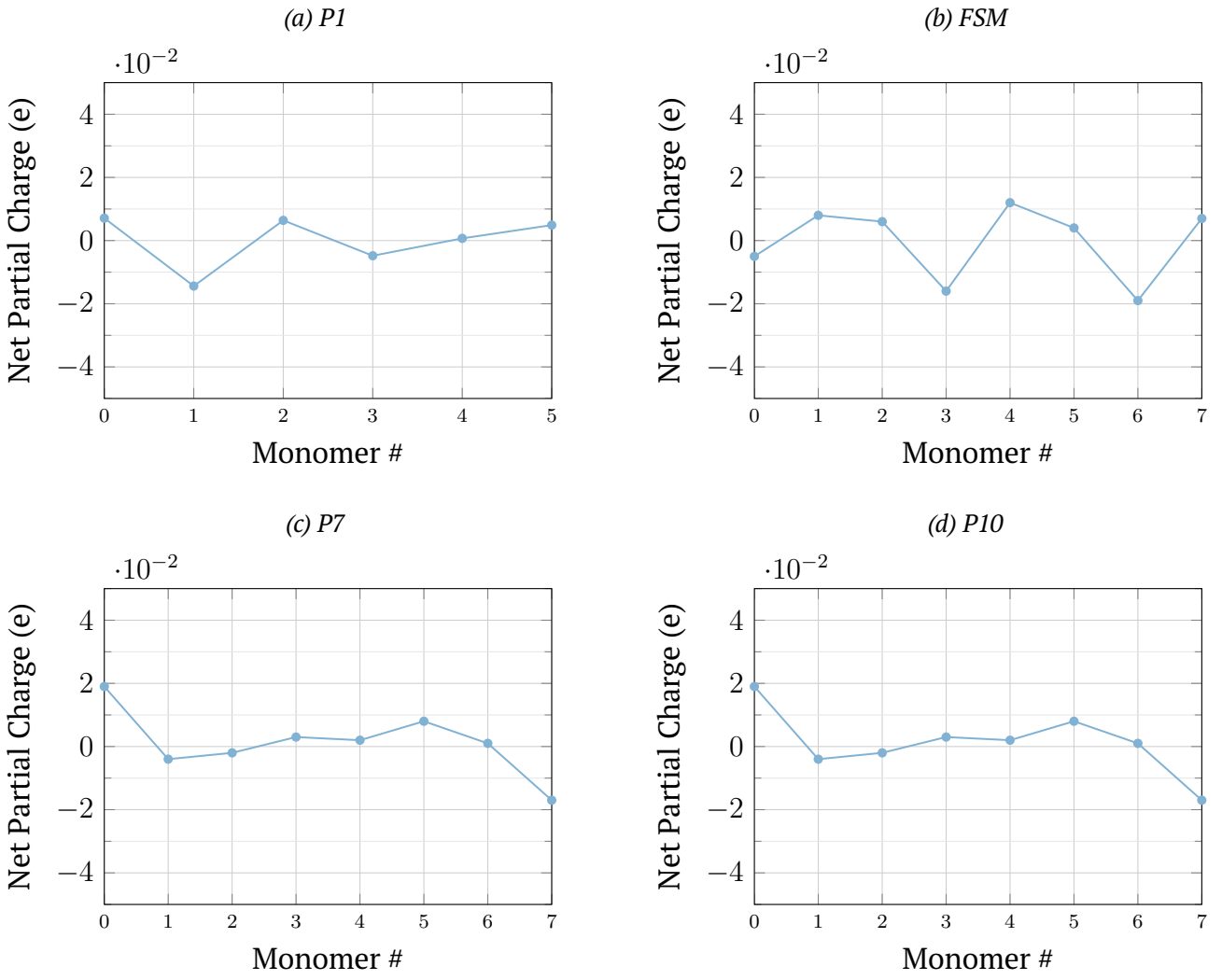


Figure 6.12: This figure shows the average partial charge on each monomer of a) a 6-mer of P1, b) 8-mer of FSM, c) 8-mer of P7 and d) 8-mer of P10. Whilst we notice some edge effects, we see that it is small (less than two hundreths of an electron charge) and thus neglect it in our model.

We see that for most polymers the profile of the oligomers becomes uniform to within 2% of an electron charge and in most cases much more uniform than that. This suggests that a single-residue model where we model each monomer of the polymer the same, irrespective of their position in the oligomer, should model our polymers well.

Inter-Monomer Torsion

In this section we fit the force field to DFT scans of the intermonomer torsion potential.

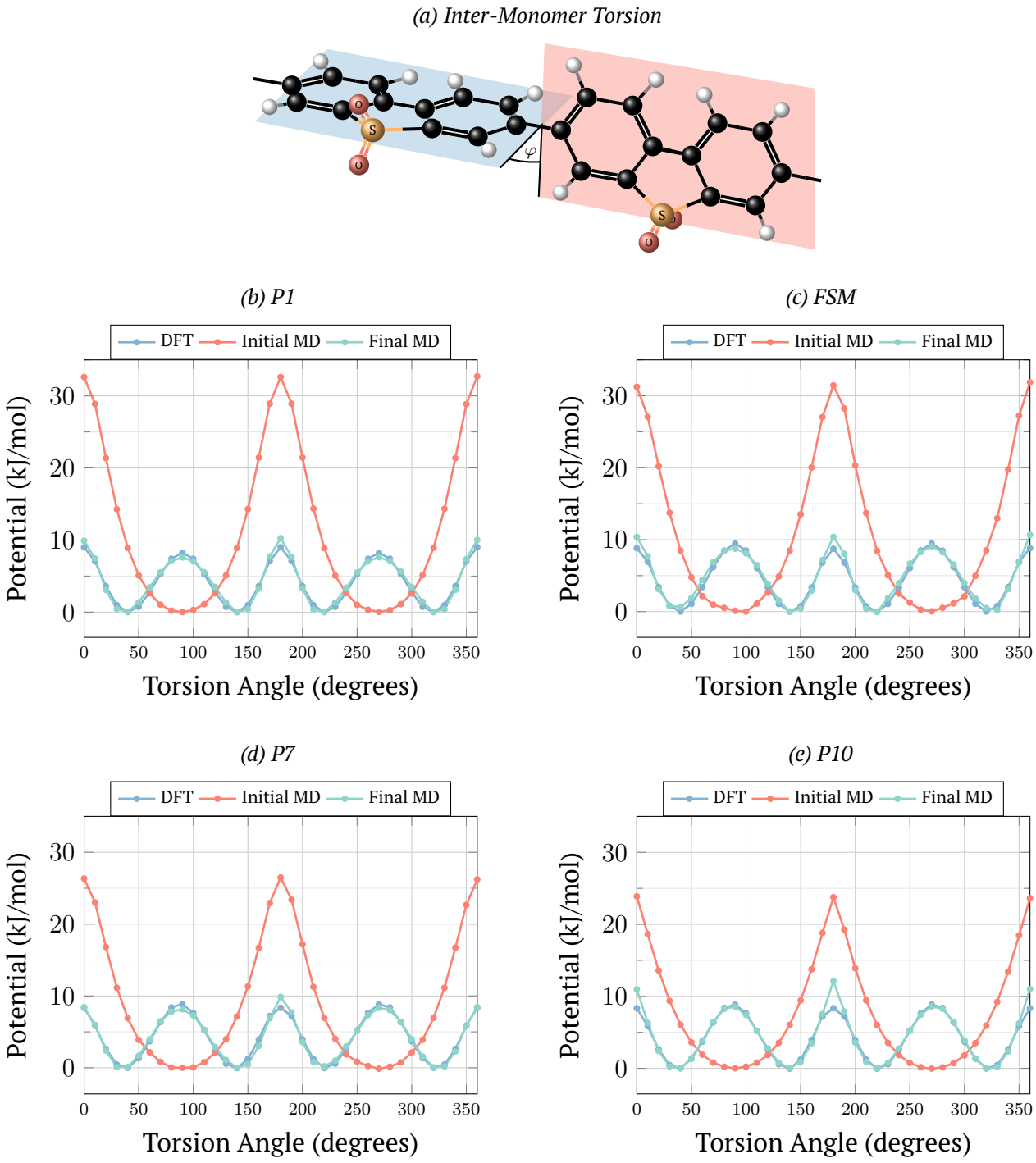


Figure 6.13: This figure shows the fitting of the intermonomer torsion from DFT for (a) P1, (b) FSM, (c) P7 and (d) P10.

Backbone Improper Dihedrals

This section shows the DFT and parameter fit for all the additional improper dihedrals added to ensure the backbone is as stiff as in nature.

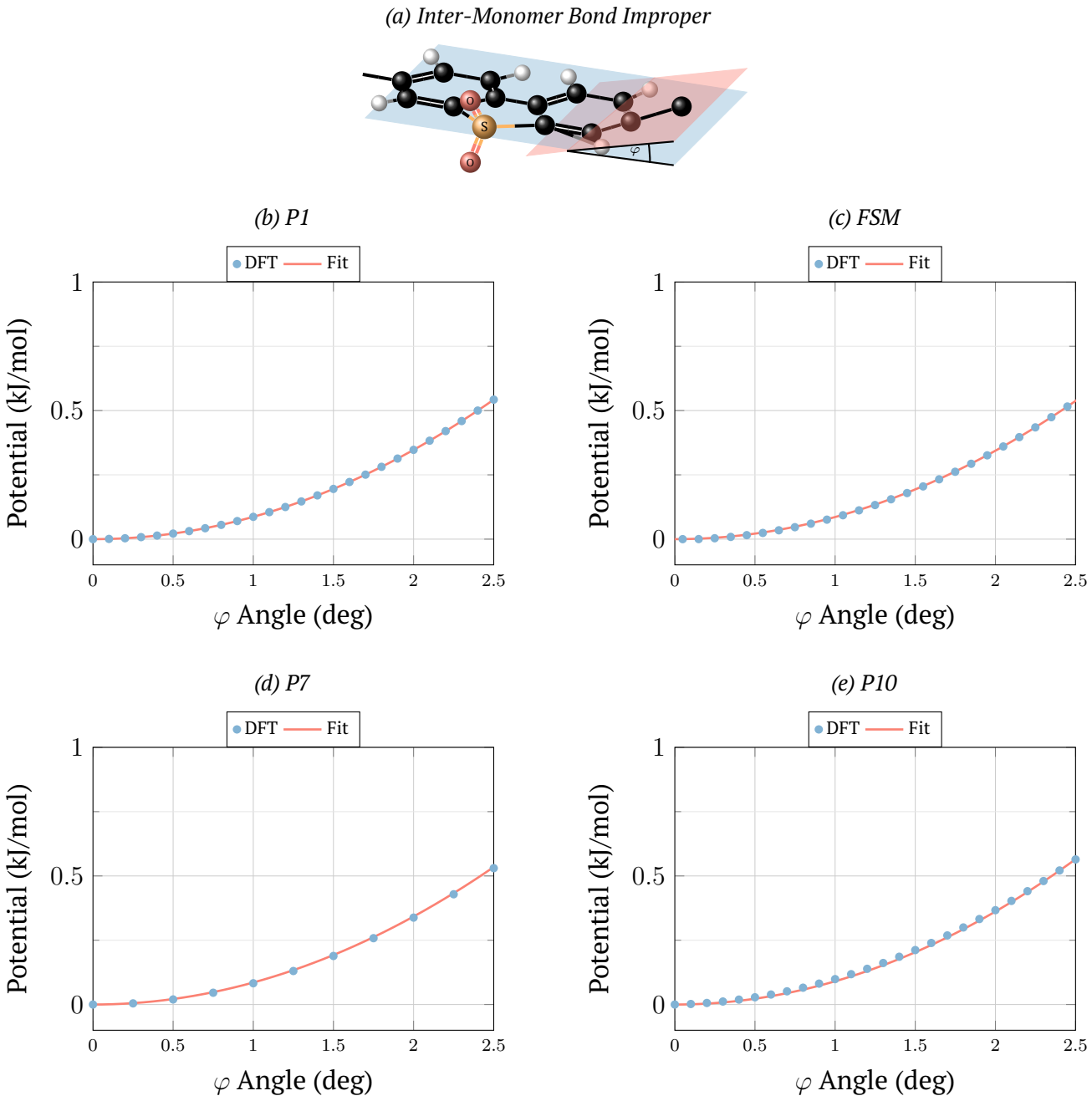


Figure 6.14: This figure shows the fitting of the intermonomer out-of-plane bond bending from DFT for (a) P1, (b) FSM, (c) P7 and (d) P10.

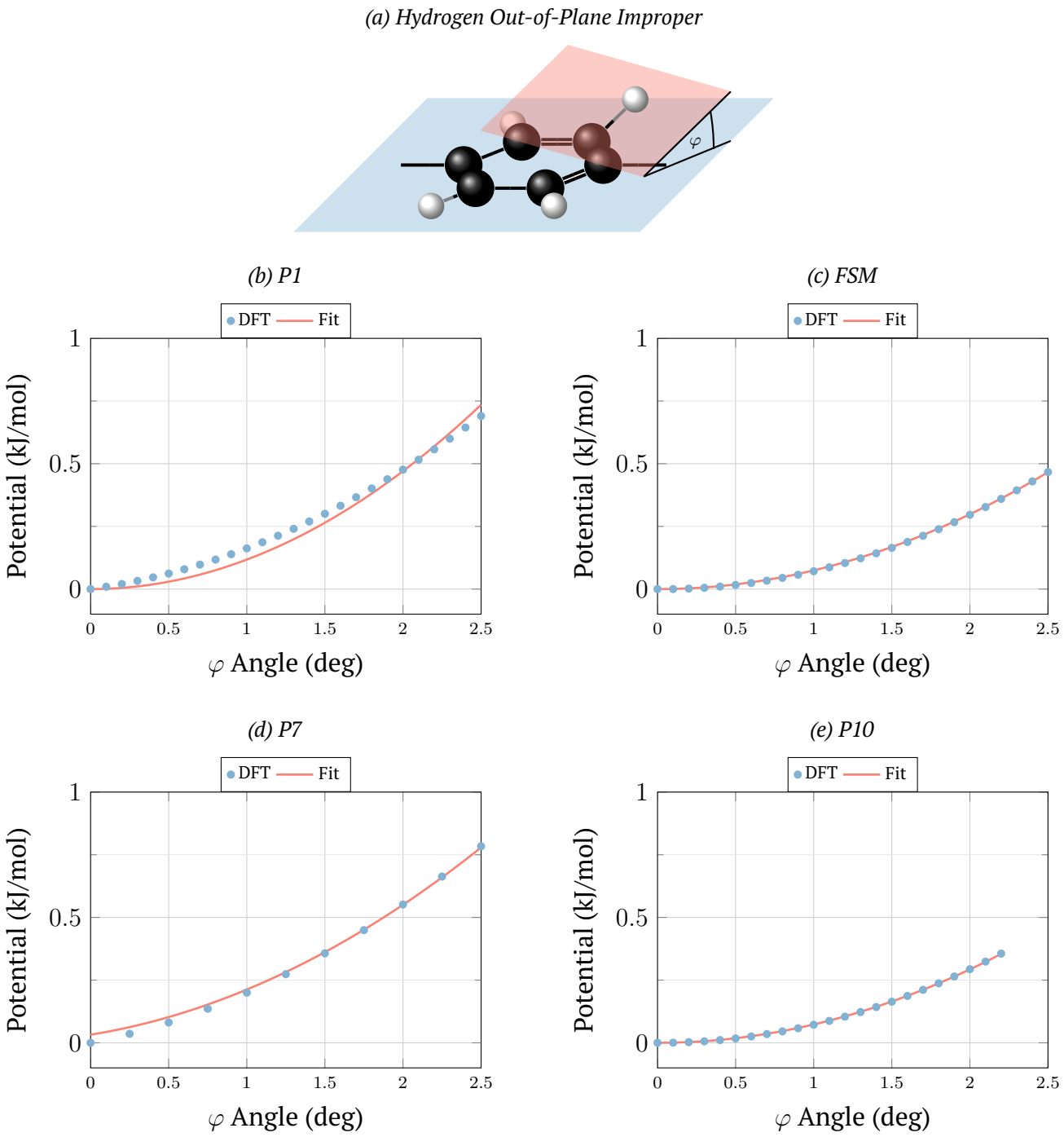


Figure 6.15: This figure shows the fitting of a hydrogen bond being bent out of the plane of conjugation from DFT for (a) P1, (b) FSM, (c) P7 and (d) P10.

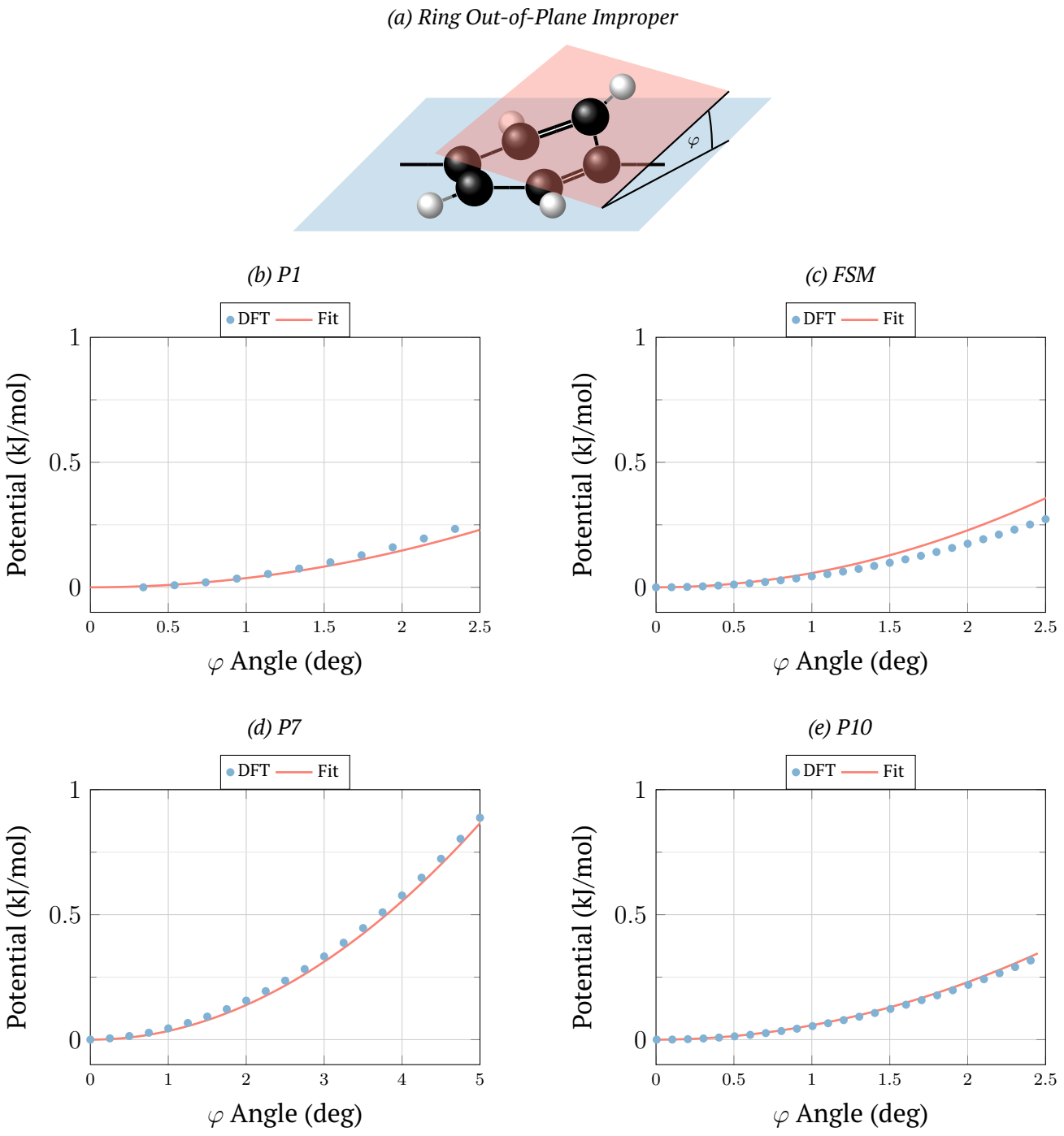
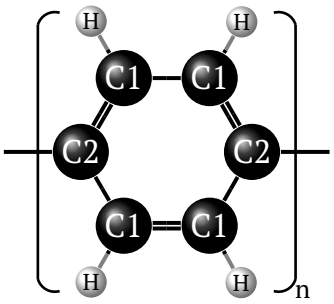


Figure 6.16: This figure shows the fitting of a carbon atom being bent out of the plane of conjugation from DFT for (a) P1, (b) FSM, (c) P7 and (d) P10.

6.4.2.3 Final Force Fields

We outline for each of P1, FSM, P7 and P10 the chosen parameters for each of these steps, in Figures 6.17, 6.18, 6.19 and 6.20.

(a)



(b)

Atom	q (e)	σ (nm)	ε (kJ/mol)	OPLS name
C1	-0.109	0.355	0.293	OPLS 145
C2	0.038	0.355	0.293	OPLS 145b
H	0.09	0.242	0.126	OPLS 146

(c)

Bond	r_0(nm)	k_r (kJ/mol/nm^2)	Angle	θ_0(deg)	k_θ (kJ/mol/rad^2)
C1—C1	0.14	392459	C1—C1—C2	120.0	527.184
C2—C2	0.14	392459	C1—C2—C1	120.0	527.184
C1—C2	0.14	392459	C1—C2—C2	120.0	527.184
C1—H	0.108	307106	C2—C1—H	120.0	527.184
			C1—C1—H	120.0	292.880

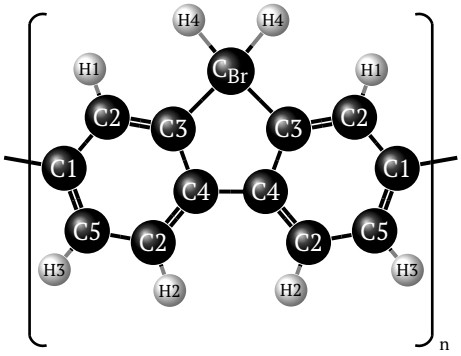
Dih. Angle	V_1(kJ/mol)	V_2(kJ/mol)	V_3(kJ/mol)	V_4(kJ/mol)	V_5(kJ/mol)	V_6(kJ/mol)
C1-C2-C1-C1	30.334	0.000	-30.334	0.000	0.000	0.000
C2-C1-C1-C1	30.334	0.000	-30.334	0.000	0.000	0.000
C2-C2-C1-C1	0.000	0.000	0.000	0.000	0.000	0.000
C1-C2-C2-C1	7.536	0.091	-25.685	-0.626	-4.436	0.675

(d)

Improper Dihedral Angle	θ_0(deg)	k_θ (kJ/mol/rad^2)
C2—C1—C2—C1	180.0	120.76
C2—C1—C1—C1	180.0	120.76
C1—C2—C2—C1	180.0	120.76
C2—C1—C1—H	180.0	386.00

Figure 6.17: P1 Force field. a) nomenclature used. b) atom types, partial charges and Van der Waals parameters. c) shows bond, angle and proper dihedral parameters where X,Y,Z represent all C-C-H angles. i,j,k,l represent all intra-monomer C-C-C-H/C-C-C-C angles. d) shows the improper dihedrals which are added to account for planar stiffness due to conjugation.

(a)



(b)

Atom	q (e)	σ (nm)	ε (kJ/mol)	OPLS name
C1	0.048	0.355	0.293	OPLS 145
C2	-0.154	0.355	0.293	OPLS 145
C3	-0.041	0.355	0.293	OPLS 145
C4	0.034	0.355	0.293	OPLS 145
C5	-0.118	0.355	0.293	OPLS 145
H1	0.093	0.242	0.126	OPLS 146
H2	0.109	0.242	0.126	OPLS 146
H3	0.087	0.242	0.126	OPLS 146
C_{Br}	0.192	0.355	0.293	OPLS 145
H4	-0.01	0.242	0.126	OPLS 140

(c)

Bond	r_0(nm)	k_r (kJ/mol/nm^2)	Angle	θ_0(deg)	k_θ(kJ/mol/rad^2)
C1-C1	0.146	322168	CX-CY-HZ	120.00	292.88
C1-C2, C3-C4, C4-C2, C5-C1	0.137	456893	C5-C2-C4, C2-C5-C1, C2-C4-C3, C1-C2-C3,	120.00	527.184
C_2-H_1, C_2-H_2, C_5-H_3	0.108	307106	C5-C1-C2, C4-C4-C2, C4-C4-C3, C1-C1-C2,		
C4-C4, C3-C_{Br}	0.146	322168	C1-C1-C5, C4-C3-C_{Br},		
C2-C3, C2-C5	0.140	392459	C2-C3-C_{Br}, C2-C_{Br}-C3		
C_{Br}-H_4	0.109	284512	C3-C_{Br}-H4	111.80	313.8

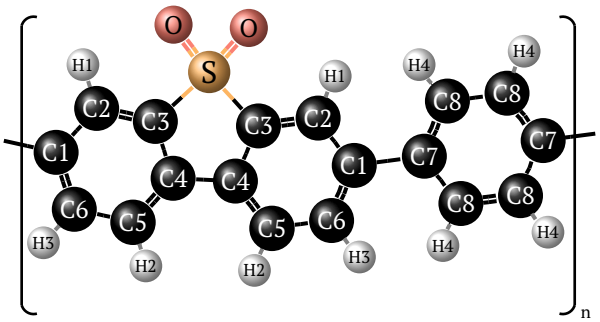
Dih. Angle	V_1(kJ/mol)	V_2(kJ/mol)	V_3(kJ/mol)	V_4(kJ/mol)	V_5(kJ/mol)	V_6(kJ/mol)
Ci-Cj-Ck-Cl, Ci-Cj-Cl-Hl, C5-C1-C1-$C_{2,5}$	30.334	0.000	-30.334	0.000	0.000	0.000
C1-C2-C2-C1	8.6760	-0.0629	-28.1615	-0.6410	-1.9118	0.7430

(d)

Improper Dihedral Angle	θ_0(deg)	k_θ (kJ/mol/rad^2)
C4—C2—C4—C3, C2—C4—C3—C_{Br}	180.0	233.202
C1—C2—C4—C3, C2—C3—C2—C4, C3—C4—C5—C2, C4—C2—C1—C5, C1—C2—C5—C2, C5—C1—C3—C2	180.0	188.781
C_{Br}—C3—C4—C4, C4—C4—C_{Br}—C3, C4—C3—C3—C_{Br}, C3—C_{Br}—C4—C3, C3—C4—C3—C4	180.0	391.47
C2—C5—C1—C1	180.0	280.445
C4—C3—C2—H2, C1—C3—C2—H2, C1—C3—C2—H1, C4—C5—C2—H2, C1—C2—C5—H3	180.0	311.812

Figure 6.18: FSM Force field. a) nomenclature used. b) atom types, partial charges and Van der Waals parameters. c) shows bond, angle and proper dihedral parameters where X,Y,Z represent all C-C-H angles. i,j,k,l represent all intra-monomer C-C-C-H/C-C-C-C angles. d) shows the improper dihedrals which are added to account for planar stiffness due to conjugation.

(a)



(b)

Atom	q (e)	σ (nm)	ε (kJ/mol)	OPLS name
C1	0.036	0.355	0.293	OPLS 145
C2	-0.041	0.355	0.293	OPLS 145
C3	-0.181	0.355	0.293	OPLS 145
C4	0.062	0.355	0.293	OPLS 145
C5	-0.139	0.355	0.293	OPLS 145
C6	-0.063	0.355	0.293	OPLS 145
H1	0.118	0.242	0.126	OPLS 146
H2	0.118	0.242	0.126	OPLS 146
H3	0.090	0.242	0.126	OPLS 146
S	1.174	0.355	1.046	OPLS 493
O	-0.600	0.296	0.711	OPLS 494
C7	0.025	0.355	0.293	OPLS 145
C8	-0.097	0.355	0.293	OPLS 145b
H4	0.091	0.242	0.126	OPLS 146

(c)

Bond	r_0(nm)	k_r (kJ/mol/nm^2)	Angle	θ_0(deg)	k_θ(kJ/mol/rad^2)
C1-C7, C4-C4	0.146	322168	CX-CY-HZ	120.00	292.88
C1-C2, C3-C4, C5-C6, C7-C8,	0.137	456893	C5-C2-C4, C2-C5-C1, C2-C4-C3, C1-C2-C3	120.00	527.184
C2-H1, C2-H2, C5-H2, C6-H3, C8-H4	0.108	307106	C5-C1-C2, C4-C4-C2, C4-C4-C3, C1-C1-C2, C1-C1-C6		
C2-C3, C4-C5, C6-C1, C8-C8	0.140	392459	C4-C3-S	110.90	259.408
S-O	0.147	230120	O-S-O	119.00	271.960
C3-S	0.181	243720	C2-C3-S	126.00	259.408

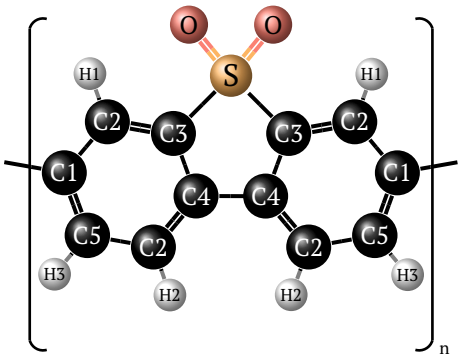
Dih. Angle	V_1(kJ/mol)	V_2(kJ/mol)	V_3(kJ/mol)	V_4(kJ/mol)	V_5(kJ/mol)	V_6(kJ/mol)
Ci-Cj-Ck-Cl	30.334	0.000	-30.334	0.000	0.000	0.000
Ci-Cj-Cl-Hl	30.334	0.000	-30.334	0.000	0.000	0.000
C2-C1-C7-C8	8.4225	-2.473	-27.7439	6.0258	2.3424	-3.0872

(d)

Improper Dihedral Angle	θ_0(deg)	k_θ (kJ/mol/rad^2)
C3—C4—C4—S, C3—C4—C4—C3	180.0	230.106
C1—C3—C2—C5, C2—C4—C3—C6, C3—C5—C4—C1, C4—C6—C5—C2, C5—C1—C6—C3, C6—C2—C1—C	180.0	113.69
C7—C8—C8—H4	180.0	386.00
C7—C8—C8—C8, C8—C7—C8—C8, C8—C8—C7—C7	180.0	130.16
C2—C6—C1—C7, C8—C8—C7—C1	180.0	276.44

Figure 6.19: P7 Force field. a) nomenclature used. b) atom types, partial charges and Van der Waals parameters. c) shows bond, angle and proper dihedral parameters where X,Y,Z represent all C-C-H angles. i,j,k,l represent all intra-monomer C-C-C-H/C-C-C-C angles. d) shows the improper dihedrals which are added to account for planar stiffness due to conjugation.

(a)



(b)

Atom	q (e)	σ (nm)	ε (kJ/mol)	OPLS name
C1	0.036	0.355	0.293	OPLS 145
C2	-0.041	0.355	0.293	OPLS 145
C3	-0.181	0.355	0.293	OPLS 145
C4	0.062	0.355	0.293	OPLS 145
C5	-0.139	0.355	0.293	OPLS 145
C6	-0.063	0.355	0.293	OPLS 145
H1	0.118	0.242	0.126	OPLS 146
H2	0.118	0.242	0.126	OPLS 146
H3	0.090	0.242	0.126	OPLS 146
S	1.174	0.355	1.046	OPLS 493
O	-0.600	0.296	0.711	OPLS 494

(c)

Bond	r_0(nm)	k_r (kJ/mol/nm^2)	Angle	θ_0(deg)	k_θ(kJ/mol/rad^2)
C1-C1, C4-C4	0.146	322168	CX-CY-HZ	120.00	292.88
C1-C2, C3-C4, C5-C6	0.137	456893	C5-C2-C4, C2-C5-C1, C2-C4-C3, C1-C2-C3	120.00	527.184
C1-H1, C2-H2, C5-H2, C6-H3	0.108	307106	C5-C1-C2, C4-C4-C2, C4-C4-C3, C1-C1-C2, C1-C1-C6		
C2-C3, C4-C5, C6-C1	0.140	392459	C4-C3-S	110.90	259.408
S-O	0.147	230120	O-S-O	119.00	271.960
C3-S	0.181	243720	C2-C3-S	126.00	259.408

Dih. Angle	V_1(kJ/mol)	V_2(kJ/mol)	V_3(kJ/mol)	V_4(kJ/mol)	V_5(kJ/mol)	V_6(kJ/mol)
Ci-Cj-Ck-Cl	30.334	0.000	-30.334	0.000	0.000	0.000
Ci-Cj-Cl-Hl	30.334	0.000	-30.334	0.000	0.000	0.000
C2-C1-C1-C2	8.188	-1.110	-28.523	0.620	-2.490	0.443

(d)

Improper Dihedral Angle	θ_0(deg)	k_θ (kJ/mol/rad^2)
C3—C4—C4—S, C3—C4—C4—C3	180.0	230.106
C1—C3—C2—C5, C2—C4—C3—C6, C3—C5—C4—C1, C4—C6—C5—C2, C5—C1—C6—C3, C6—C2—C1—C4	180.0	113.69
C2—C6—C1—C1	180.0	276.44

Figure 6.20: P10 Force field. a) nomenclature used. b) atom types, partial charges and Van der Waals parameters. c) shows bond, angle and proper dihedral parameters where X,Y,Z represent all C-C-H angles. i,j,k,l represent all intra-monomer C-C-C-H/C-C-C-C angles. d) shows the improper dihedrals which are added to account for planar stiffness due to conjugation.

6.4.3 Results: Single Oligomers in Solution

With the confidence in our choice and parameterisation of our force fields we can now proceed to investigate the system of study that we are using to model the experimental set-up. We simulate the equivalent length of six benzene rings, which is a hexamer of P1, a trimer of FSM and P10 and a dimer of P7. As we have previously discussed the whole system is complex and in order to ensure we fully understand the different interactions we are going to simulate the oligomers in a 1:1 water:TEA mixture before proceeding with the full experimental reaction mixture (1:1:1 water:TEA:methanol). This allows us to isolate the impact of the interaction between polymer, water and TEA without the complexity of the full reaction mixture.

6.4.3.1 Water-TEA

Our first clue to the different behaviour of these different polymers in simulation comes from the introduction of our initial model for the reaction mixture, a 50:50 mixture by volume of water and TEA. We start here with this bi-phasic system rather than the full experimental reaction mixture as methanol is largely understood to be a mixing agent inert in reaction. As we know from Section 4.5 the TEA/water mixture segregates more than the full reaction mixture and this might lead to different effects than in the experimental setup, but we will be able to see the nature of interactions between the polymers, TEA and water. Figure 6.21 shows snapshots of the final simulation box, a close up of the environment around the oligomer and RDFs of the oligomer with each of the solvents.

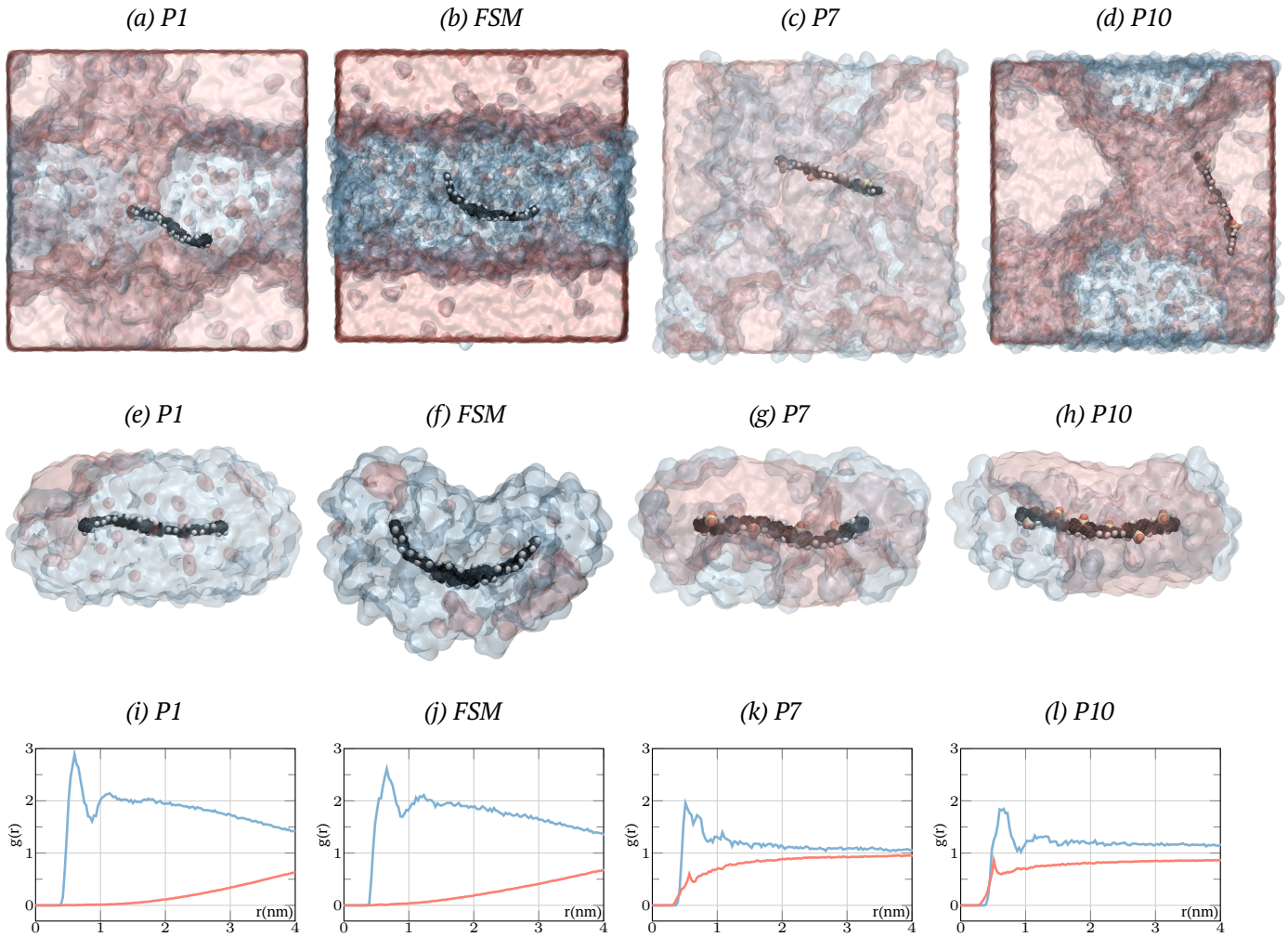


Figure 6.21: This figure shows the results of MD of P1, FSM, P7 and P10 in a 50:50 mixture of water and TEA. It shows snapshots of the final state in (a)-(d) with close ups of the local environments in (e)-(h) and finally the centre-of-mass RDFs of the oligomers to the solvents are shown in (i)-(l). In all cases red represents water and blue represents TEA.

It is worth noting that these snapshots are single time frames with a particular starting configuration, however choosing different starting configurations (or different time points) does not meaningfully change the solvation shell or the average conformational properties of the oligomer. The simulations have also been allowed to equilibriate, in line with our methodology outlined in Section 3.2.5. We see from the RDFs and snapshots in Figure 6.21 that there seems to be a trend in that better performing polymers bring more water nearby. To make this more clear we calculate the percentage volume occupied by each of the solvents at distances away from the oligomers, and we do this using the volume occupied by a molecule of solvent on average. The environment of each of the polymers as a function of distance is shown in Figure 6.22.

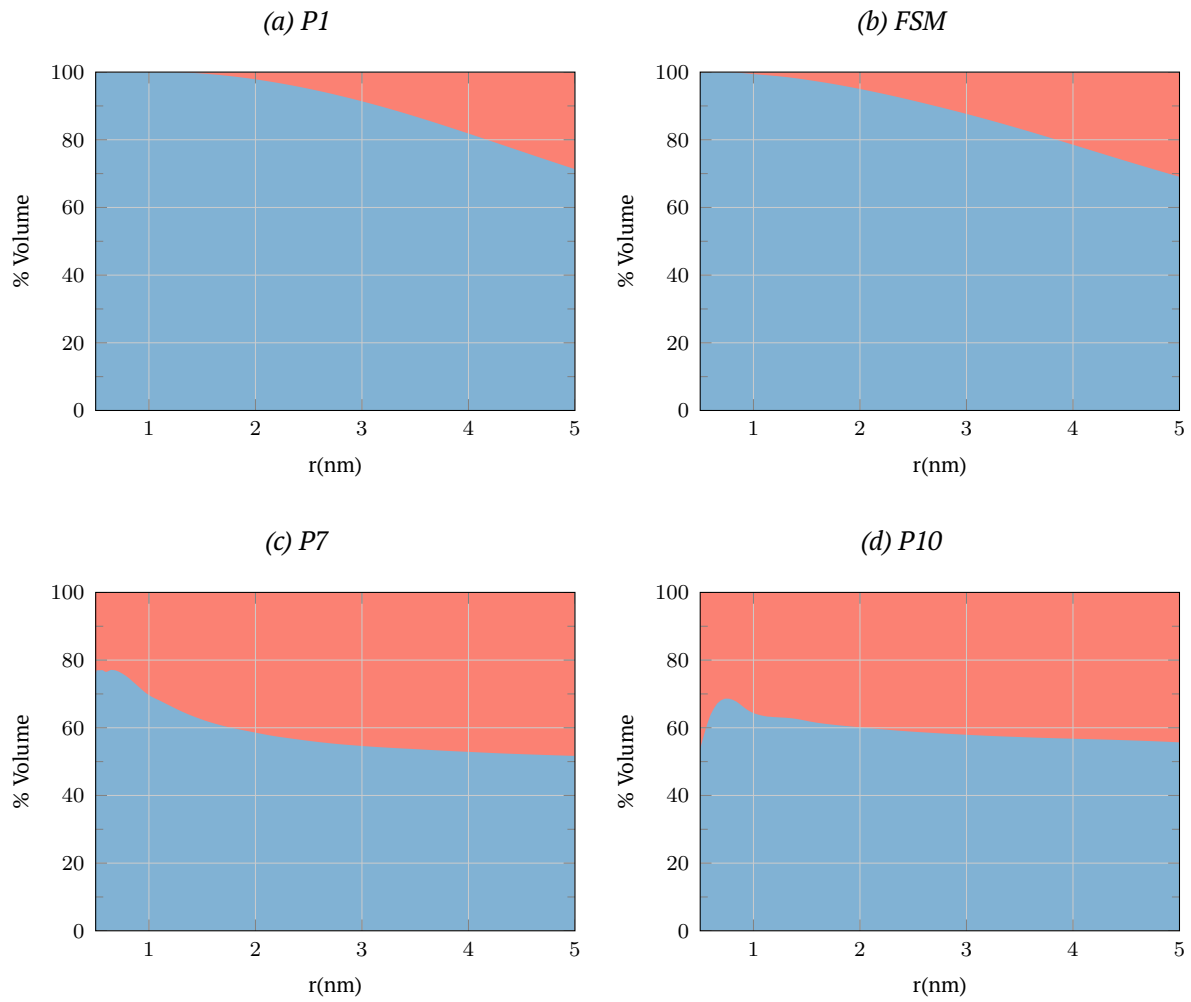


Figure 6.22: This figure shows local environments by volume of each of the oligomers, which are calculated through the cumulative RDF and the molar volumes of each of the components. Red and blue represent water and TEA respectively.

Figure 6.22 shows quite clearly the stark difference in the local environments of the active polymers and the inactive ones. We now turn to test the robustness of this observation upon the inclusion of methanol in the system.

6.4.3.2 Reaction Mixture

We have seen that there seems to be significant interaction differences between performing polymers (P7 and P10) and non-performing polymers (FSM and P1) when they are solvated in a TEA/water mixture. This is highly suggestive that the performance correlates with an increased amount of water or decreased amount of TEA nearby. However, since in the experimental set-up we have a mixture of water:TEA:methanol we must be careful not to draw conclusions from a water:TEA system about the experimental system. We know from Section 4.5 that the addition of methanol disrupts phase segregation and helps water to mix, and so it is possible that the

effect illustrated in Figure 6.22 is not seen in the full reaction mixture. As such we turn to simulate the full reaction mixture for each oligomer. Figure 6.23 shows snapshots of the end of the simulation for FSM, P1, P7 and P10 in reaction mixture alongside RDFs of the oligomer with each of the solvents.

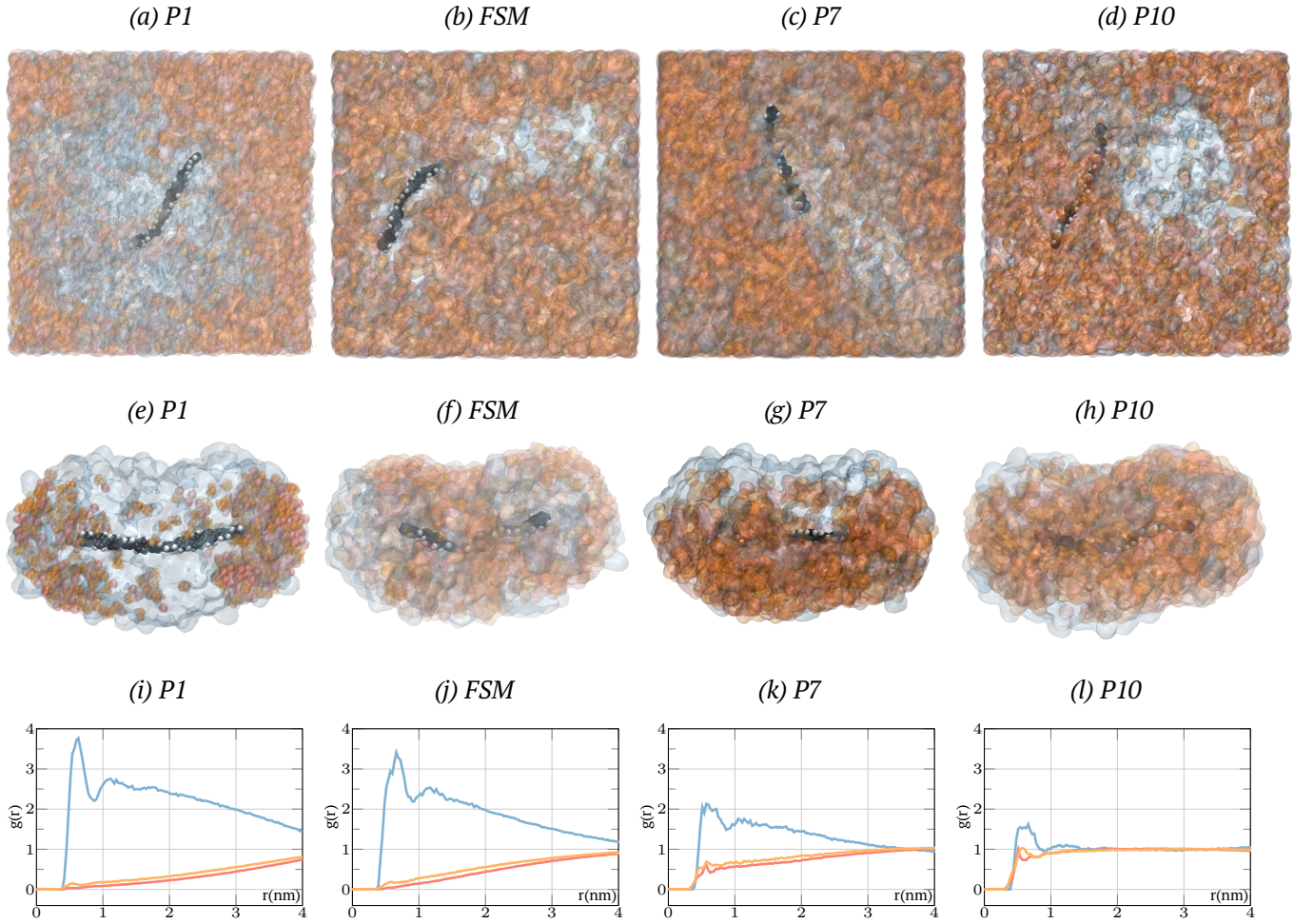


Figure 6.23: This figure shows the results of MD of single oligomers of FSM, P1, P7 and P10 in a 1:1:1 mixture of water, methanol and TEA. It shows snapshots of the final state in (a)-(d) with close-ups of the local environments in (e)-(h) and finally the centre-of-mass RDFs of the oligomers to the solvents are shown in (i)-(l). In all cases red represents water, blue represents TEA and orange represents methanol.

We, as in the previous section, convert RDFs into the percentage of volume occupied by each solvent as a function of distance away from the polymer. This allows us to see the different local environments the polymer creates around it.

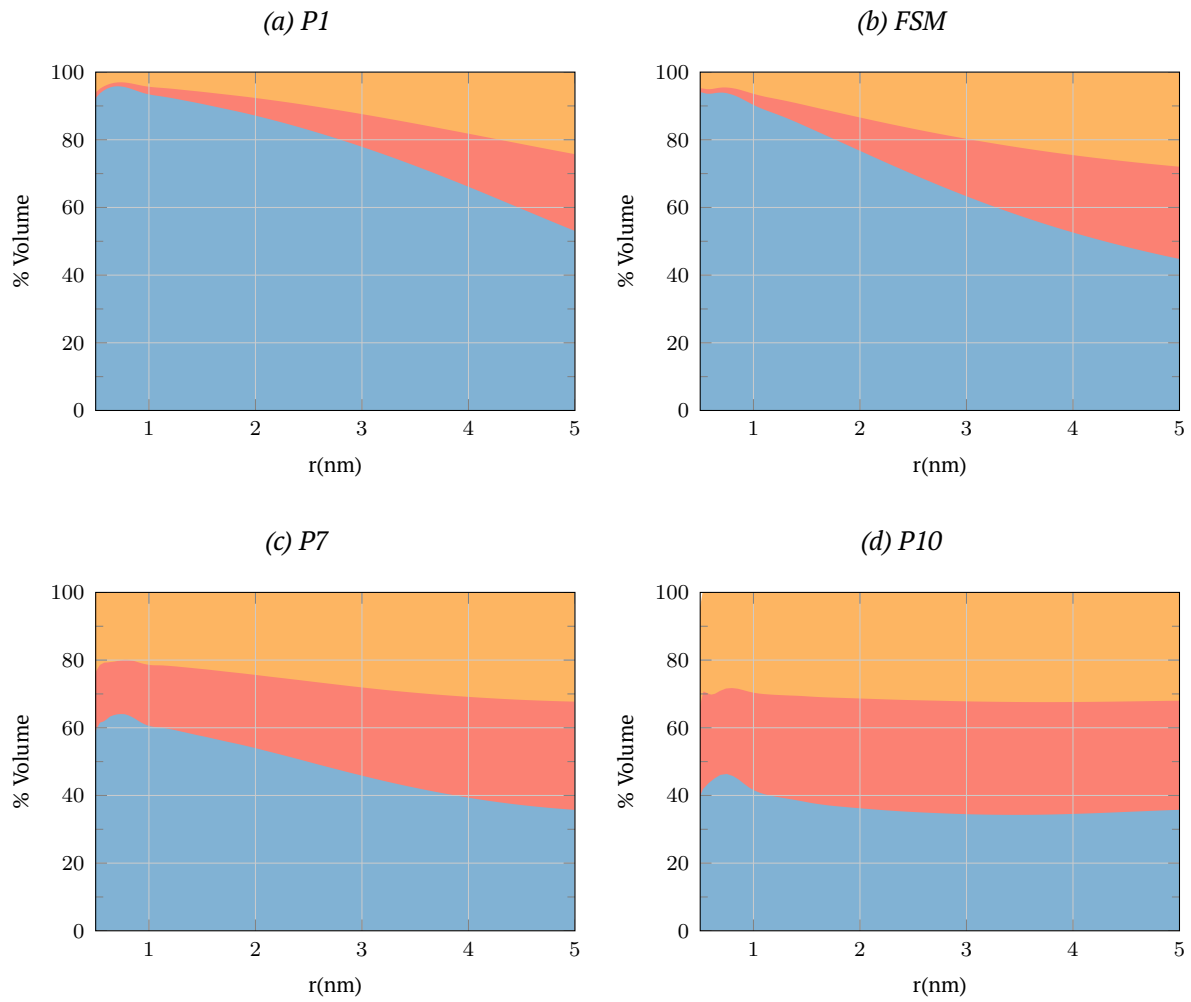


Figure 6.24: This figure shows local environments in a 1:1:1 water:TEA:methanol mixture, by volume, of each of the oligomers, which are calculated through the cumulative RDF and the molar volumes of each of the components. Orange, red and blue represent methanol, water And TEA respectively.

From this we can see that the effect observed in just water:TEA still holds. The sulfone group brings more water and methanol alongside the oligomer, excluding TEA as a result and this behaviour seems to correlate with the higher performing polymers. It is not immediately clear why higher amounts of water would help the reaction that involves mostly TEA. We will investigate this behaviour in the next chapter. For now it is sufficient to note that polymers that have higher amounts of water in their local environment evolve more hydrogen in experiments than ones that don't[5]. We now turn to increase the concentration of oligomer in solution to see the impact.

[5]A signature of water could be experimentally measured by the use of, for instance using neutron scattering or x-ray scattering technique to obtain a radial distribution function by species.

6.5 Towards Aggregates: Multiple Oligomers in Solution

6.5.1 Introduction

We have worked towards simulations that, as close as possible, match experimental conditions. There are a few significant differences remaining between my simulations and the experimental set-up: in the experiment a co-catalyst is present, polymers are used rather than oligomers, and the polymers are introduced as an aggregate, not as isolated polymers in solution. In this chapter we attempt to test the robustness of the findings by investigating how the behaviour changes as we move towards aggregates in solution. Simulating meso-scale particles along with sufficient solvent and sufficient time to obtain valid statistics is beyond the practical scope of atomistic MD. However, we can do simulations to move in the direction of aggregates and assess the impact. There are two main ways we could use our atomistic MD to investigate the likelihood to disaggregate, in order of increasing complexity of calculation:

- Assessing the difference in solvation environments between single oligomers and 'aggregates' of two oligomers.
- Performing a potential of mean force (PMF) calculations to calculate the potential surface of disaggregation in the different solvent environments.

In this chapter we perform only the former of these on account of PMF calculations being particularly computationally expensive. In addition, PMFs are best suited to consider the research question of how to improve performance of a particular polymer by controlling aggregations (e.g. through sidechains) and as we discussed in Section 6.3.2 the experimental data suggests that this question is not key to explaining the reason why some polymers evolve hydrogen and others do not.

6.5.2 Solvation Environments of Bi-Oligomer Aggregates

One way we can examine aggregation effects on the nanoscale that is accessible by atomistic MD is to 'aggregate' two oligomers together in vacuum before solvating them in the different solvents. This approach allows us to see two things: whether the oligomers remain aggregated together or disperse and, if they do remain aggregated, whether that has an impact on the solvation properties. It is clear that any results from this sort of calculation must be taken with caution, as the forces of this pair will likely be quite different than nanoparticles of polymers. We can envision situations where the aggregated system solvates very differently if, for example, certain groups are more likely to present themselves at the interface, something a pair

has limited opportunity to optimise. The pair aggregates are shown in a water-TEA mixture in Figure 6.25 and in the full reaction mixture in Figure 6.26.

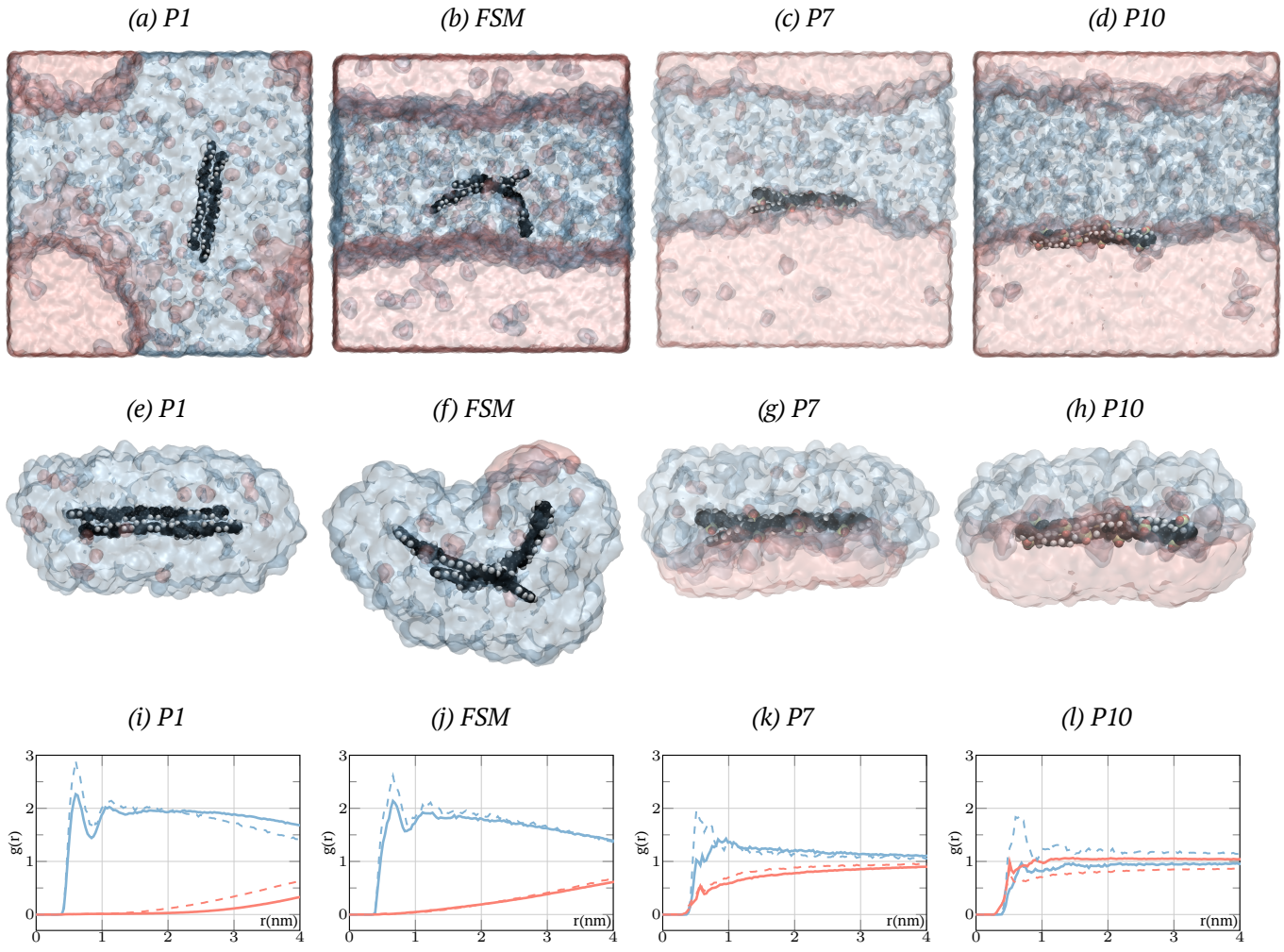


Figure 6.25: This figure shows the results of MD of an aggregated pair of P1, FSM, P7 and P10 in a 1:1 mixture of water and TEA. It shows snapshots of the final state in (a)-(d) with close-ups of the local environments in (e)-(h) and finally the centre-of-mass RDFs of the oligomers to the solvents are shown in (i)-(l). In all cases red represents water, blue represents TEA.

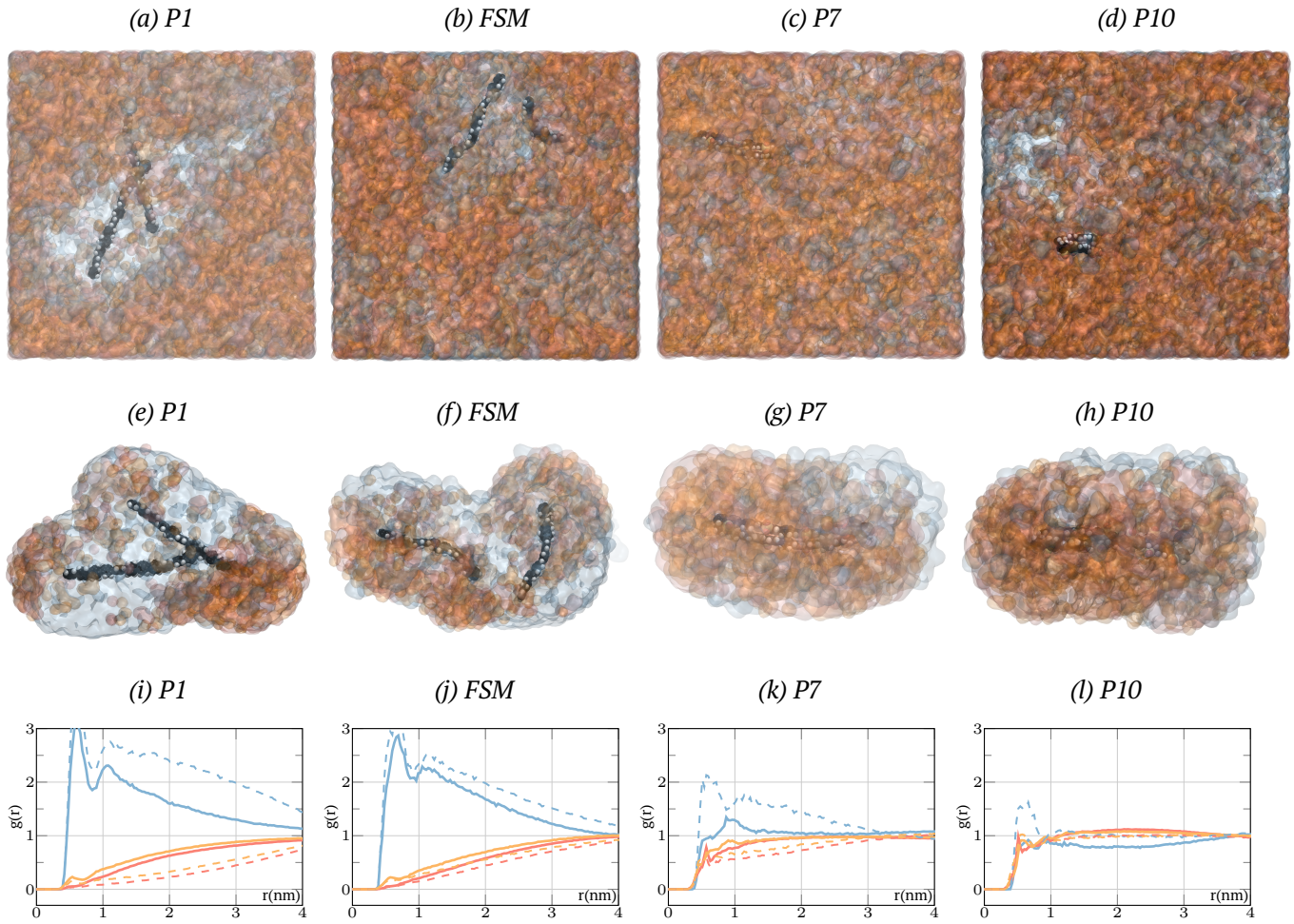


Figure 6.26: This figure shows the results of MD of aggregated pairs of P1, FSM, P7 and P10 in a 1:1:1 mixture of water, methanol and TEA. It shows snapshots of the final state in (a)-(d) with close-ups of the local environments in (e)-(h) and finally the centre-of-mass RDFs of the oligomers to the solvents are shown in (i)-(l). In all cases red represents water, blue represents TEA and orange represents methanol.

We see from Figures 6.25 and 6.26 that the aggregates on the whole match the behaviour we see for single isolated oligomers, with P1 and FSM residing in TEA and P7 and P10 sticking to the interface. We can also see the polymers with strong dipoles remain aggregated in all cases. We also repeat the local environment calculations to see if their pairing has introduced significant quantitative differences. This is shown in Figure 6.27 for water:TEA and in Figure 6.28 for water:TEA:methanol.

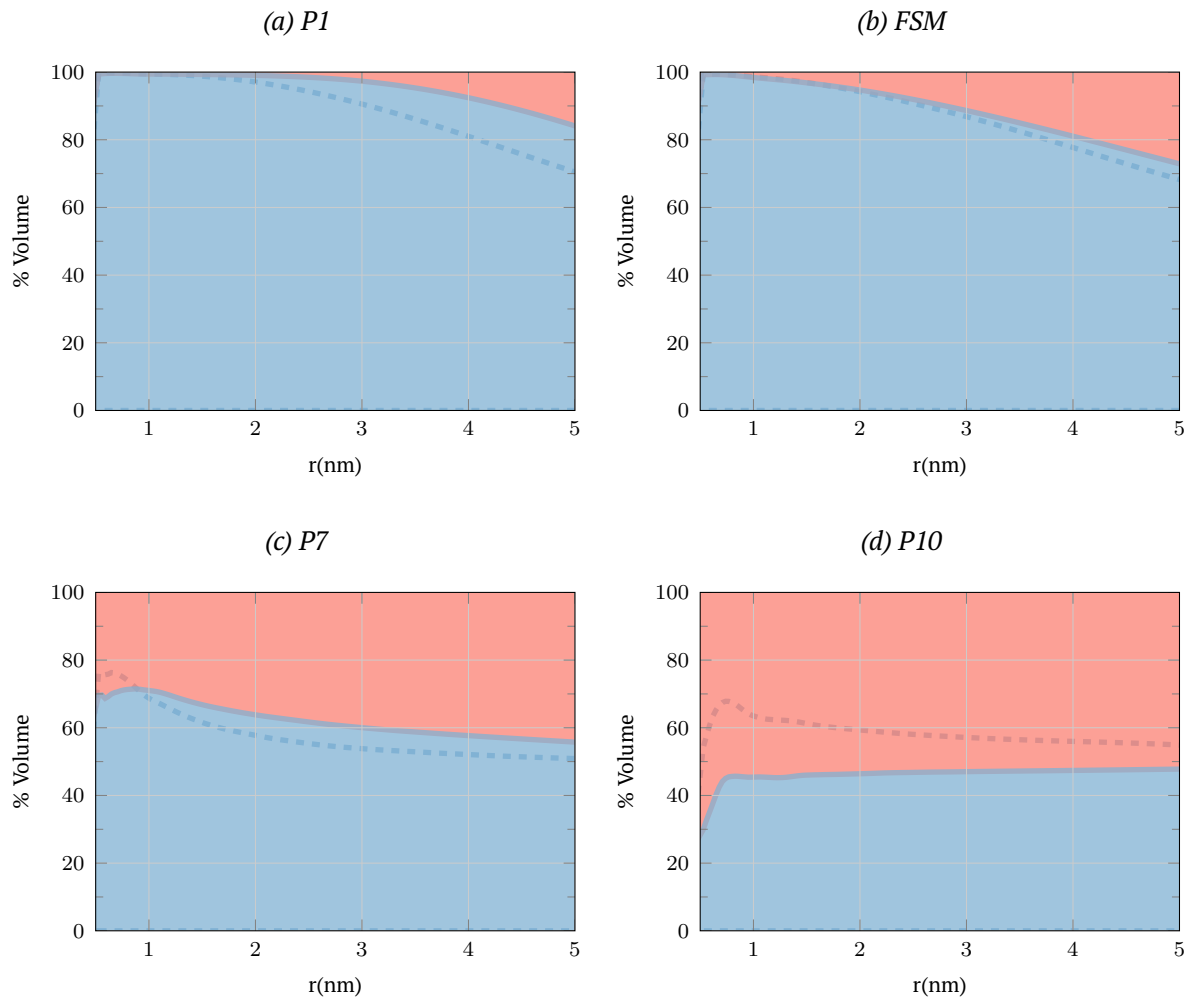


Figure 6.27: This figure shows the calculated average local environment for aggregated pairs of oligomer in a 1:1 mixture of water and TEA. The dashed line shows the equivalent TEA line for the single oligomers. Blue and red represent TEA and water respectively.

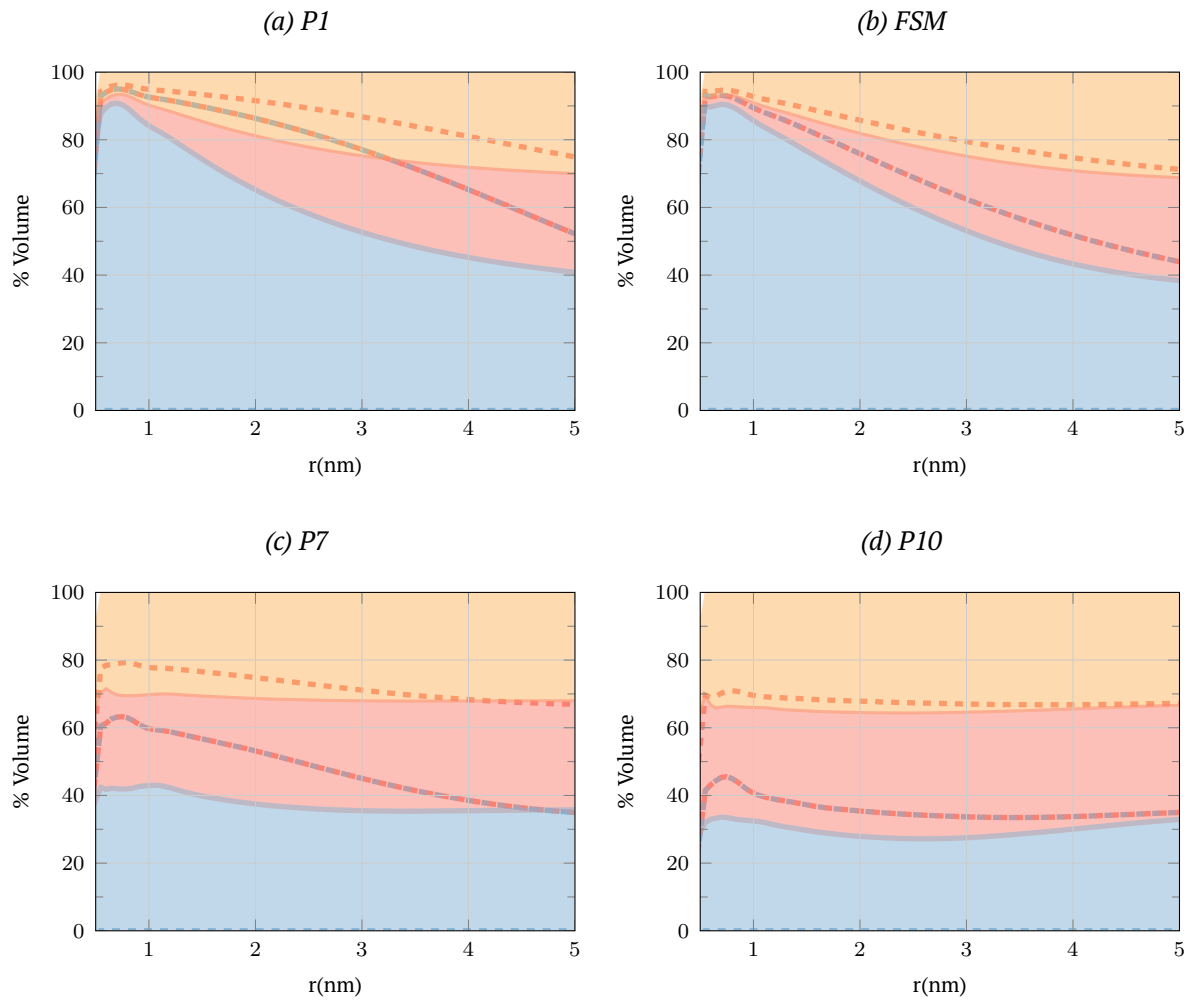


Figure 6.28: This figure shows the calculated average local environment for aggregated pairs of oligomer in a 1:1:1 mixture of water, methanol and TEA. Above the orange dashed line lies the methanol phase for a single oligomer, between the orange and red dashed lines lies the water phase for a single oligomer, and below the red dashed line lies the TEA phase for a single oligomer. Blue, red and orange represent TEA, water and methanol respectively.

From Figures 6.25 to 6.28 we see that the aggregate does have some differences in solvation behaviour to the isolated oligomer but that the trend for higher performing polymers to bring in much more water (and methanol when present) than non-performing polymers still holds. We also see an additional factor; P1 and FSM both disaggregate whereas the oligomer-oligomer interactions for P7 and P10, likely due to dipole-dipole interactions, hold the aggregate together. This model does not help us compare directly with DLS measurements as it only tells us whether oligomers are likely to break away from each other or not. Oligomers that do break away are likely to lead to smaller particle sizes in dispersion than oligomers that do not. This trend agrees with the observed effects in the experimental DLS measurements with P1 producing the smallest particles in the reaction mixture.

6.6 Conclusions

In this chapter we introduced the problem of organic photocatalyst polymers and the unexplained performance differences between them. We investigated each possible theoretical explanation and through a mixture of experimental results, DFT and MD have ruled out all but one likely explanation: better solvation with water correlates with better hydrogen evolution. Our findings can be summarised as follows:

- More water in the local environment correlates with higher hydrogen evolution.
- Whilst not tractable to simulate meaningful sizes of aggregate we have shown that trends still hold as we move toward aggregates by introducing pairs. The nature of a surface of a particle is still unknown. A mean force profile is not computed in this work but would be a logical next step.
- Particle sizes are different for the polymers but all are much above the diffusion length associated with the measured exciton lifetimes. Thus, any future work could also look at additions that would help disaggregation as that would likely improve performance.
- A co-catalyst is present in all systems but is at a concentration where all of the performance difference is likely to be saturated. The role of the co-catalyst is as yet poorly understood.
- Molecular dynamics presents a workable method to investigate local nano-scale environments of organic photocatalysts which have helped to understand the consequent hydrogen evolution rates observed experimentally.

We also see quite clearly where there are some open questions:

- It is not immediately clear why higher water concentration would help a reaction that primarily involves TEA. Reasons for this could be that a bottle neck could be the one step involving water molecules, or that the higher polarity of the water could stabalise the reaction.
- If we wish to understand the meso-scale nature of polymer aggregates we would need to use coarse-grained MD to access the scales. This could help us see if surface effects change the solvation environment or play a key role in aggregation.
- Introducing a co-catalyst into the simulation and investigating the interactions and behaviour it has with the oligomers.

The first of these we tackle at length in the next chapter.

7

Unpacking the mechanism of Hydrogen Evolution in Conjugated Photocatalyst Polymers and Development of an Effective Screening Method

7.1 Introduction

In the last chapter, we introduced systems using dispersed conjugated photocatalysts and Sacrificial Electron Donors (SEDs) in order to evolve hydrogen via the harvesting of energy from light. Using molecular dynamics at the nanoscale on model systems we showed that modifying the chemical structure of the photocatalyst can lead to vastly different local environments. These changes in local environment, namely different proportions of water, led to discernible differences in the amount of evolved hydrogen found in experiment. The hydrogen evolution reaction, and the system, are complex and in this chapter we attempt to investigate it in greater depth in order to attempt to understand this connection between water and the SED hydrogen evolution reaction. We then go on to attempt to outline a procedure for screening potential polymers expected to perform well. In order to properly develop this method we extend our set to a wider array of polymers for which there are experimental observations. In addition, we test the method against a different but similar SED, namely Triethanolamine (TEOA). This allows us to attempt to predict differences in performance by relying on the extensive knowledge of the evolution pathway we have developed.

7.2 Triethylamine: Hydrogen evolution pathway

As previously discussed in Section 2.2.1, with the exception of metal oxide photocatalysts all hydrogen evolution experiments use a Sacrificial Electron Donor (SED). Very little work however has been performed on the details of the SED's role and often different SEDs are trialled for each photocatalyst with the best performing reported. There is little understanding about why some SEDs perform better with some photocatalysts than others. In this section we examine the SED used in the previous chapter, namely Triethylamine (TEA). TEA has two known pathways of degradation that lead to the products we see (Diethylamine, abbreviated DEA, and Acetaldehyde, abbreviated ADH): aerobic[241] and anaerobic degradation[242, 243]. We focus on anaerobic degradation as our systems are degassed and thus oxygen should not be present. This reaction pathway is shown in Figure 7.1 and the chemical equations for each step are outlined in Equations 7.1 through 7.6. The intermediate steps for TEA radical where one hydrogen has been stripped is abbreviated as TEAR and the proton-TEA adduct is abbreviated as $TEAH^+$.

Step 0: $$P \xrightarrow{h\nu} P^* \tag{7.1}$$

Step 1: $$TEA + P^* \rightarrow TEA^{\bullet +} + P^- \tag{7.2}$$

Step 2: $$TEA^{\bullet +} + TEA \rightarrow TEAR^{\bullet} + TEAH^+ \tag{7.3}$$

Step 3: $$TEAR^{\bullet} + P^* \rightarrow TEAR^{\bullet +} + P^- \tag{7.4}$$

Step 4: $$TEAR^{\bullet +} + H_2O \rightarrow DEA + ADH + TEAH^+ \tag{7.5}$$

Step 5: $$2 \times TEAH^+ + 2 \times P^- \rightarrow 2 \times TEA + 2 \times P + H_2 \tag{7.6}$$

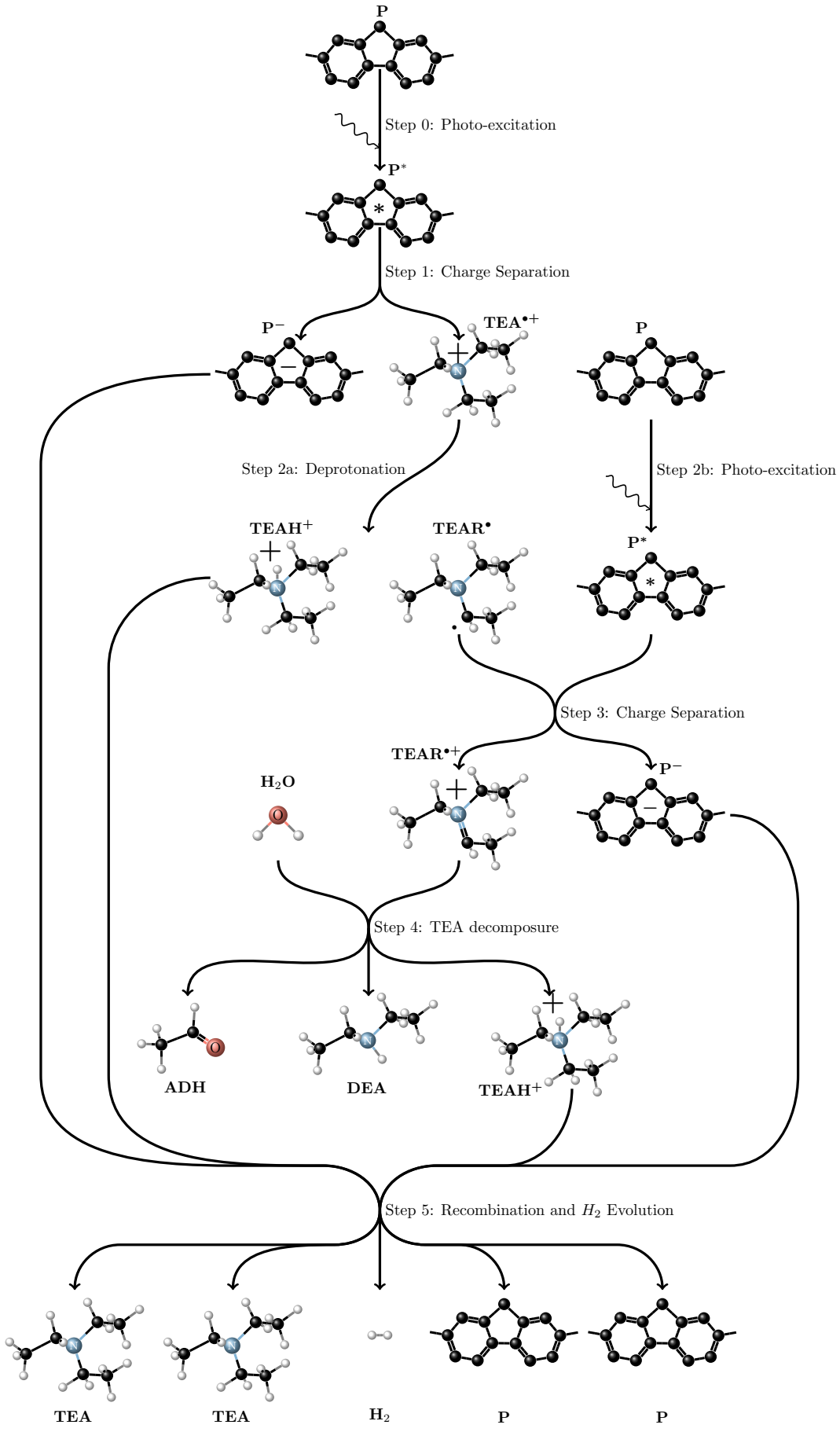


Figure 7.1: This figure shows part of the reaction that leads to the photo-induced decomposure of TEA into the products DEA, ADH and protons (which eventually recombine into hydrogen). The polymer (FSM) shown represents whichever polymer photocatalyst is present.

One key aspect of the process is the difference in free energy between the reactants and the final products[243]; this overall reaction is outlined in Equation 7.7.

$$\text{Overall Reaction:} \qquad \text{TEA} + \text{H}_2\text{O} \rightarrow \text{DEA} + \text{ADH} + \text{H}_2 \tag{7.7}$$

Looking at this reaction has some merits in comparing SEDs or the impact of solvation as it outlines the thermodynamic barrier this event has to overcome. However, it should be noted that it has no dependence on the photocatalyst[1] and therefore will not help us to understand differential performance of photocatalysts. As such, previous work[134] has also looked at a set of half-reactions; the half-reactions for TEA are outlined in Equations 7.8-7.12.

$$\text{TEAH}^+ + e^- \rightarrow \frac{1}{2}H_2 + \text{TEA} \tag{7.8}$$

$$\text{TEA}^{\bullet+} + e^- \rightarrow \text{TEA} \tag{7.9}$$

$$\text{TEAR} + \text{TEAH}^+ + e^- \rightarrow 2\text{TEA} \tag{7.10}$$

$$\text{DEA} + \text{ADH} + \text{TEAH}^+ + e^- \rightarrow \text{TEAR} + \text{TEA} + \text{H}_2\text{O} \tag{7.11}$$

$$\text{DEA} + \text{ADH} + 2\text{TEAH}^+ + 2e^- \rightarrow 3\text{TEA} + \text{TEA} + \text{H}_2\text{O} \tag{7.12}$$

The benefit of these is that they can be calculated and compared to the polymer potentials: electron affinity (EA), electron ionisation potential (IP), excitonic ionisation potential (IP*) and excitonic electron affinity (EA*), outlined in Equations 7.13-7.16. This will indicate whether a particular polymer is able to thermodynamically drive a particular reaction.

$$\text{EA:} \qquad P^- \rightarrow P + e^- \tag{7.13}$$

$$\text{IP*:} \qquad P^* \rightarrow P^+ + e^- \tag{7.14}$$

$$\text{EA*:} \qquad P^* \rightarrow P^- + h^+ \tag{7.15}$$

$$\text{IP:} \qquad P^+ \rightarrow P + h^+ \tag{7.16}$$

We can recognise EA* as directly related to Step 3 (Equation 7.4), with the difference being the assumption that the proton must form an adduct with TEA[2]. It should also be noted that there exists another, more energetically favourable, potential step to obtain TEAR$^{\bullet+}$, namely:

$$2 \times \text{TEA}^{\bullet+} \rightarrow \text{TEAR}^{\bullet+} + \text{TEA}^{\bullet+}. \tag{7.17}$$

This reaction, although more energetically favourable, requires two charged TEA molecules to find each other. This route is therefore unlikely to compete with the combination of Step 2 and 3 unless the light intensity is high enough.

[1] As we would expect for the full chemical reaction of something involving a catalyst!

[2] DFT calculations suggest that adducting to TEA as opposed to either water or methanol is always the energetically favoured option.

We see from this discussion, and particularly in Figure 7.1, that the hydrogen evolution process is complex and there are many stages that might act as bottlenecks or present obstacles to overcome, even if the overall reaction is favourable. We thus reach the conclusion that to properly understand the differential performance of different polymers we must study each of the intermediate steps of hydrogen evolution in turn. By also including the solvation effects in these calculations we can begin to determine which intermediate step or steps have strong solvation dependence, which will in turn explain the observed dependence of overall hydrogen evolution on the presence of water. It is not immediately clear why a high presence of water would aid a reaction which predominantly does not involve it. In a complex system, such as this, it is possible that the differences between polymers and the impact of solvation may lie outside of the energetics and be linked to the kinetics or to some mechanism limiting back-reactions. However, in the first instance, we proceed to examine the energetics of the system using DFT. We look at each of the steps, calculating the energy associated with each step in water and TEA (using a Polarisable Continuous Medium) and in vacuum.

7.2.1 DFT calculations of driving forces in TEA pathway

In this section we are trying to ascertain the change in energy of each step. To do this we use the following procedure:

- Perform an optimisation on each of the reactants and products[3]. We choose two different functionals and basis sets to ensure stability of the conclusions: we choose the B3LYP functional, commonly used in the literature, with the pople 6-311g(d,p) basis set alongside the newer ωB97XD functional with the cc-pVDZ basis set, which performs better at Van der Waals interactions.

- Perform an energy calculation on the optimised states of each.

- Subtract the total energy of the reactants from the products to obtain the change in energy of the step, which yields the change in *ethalpy*[4] of the step.

Results of these calculations are shown in Figure 7.2, for B3LYP and Figure 7.3, for ωB97XD.

[3]This means making the assumption that interactions between products and between reactants are not significant.

[4]Since we make no attempt to include the change in entropy at this stage, this calculation yields enthalpy not the more physically meaningful free energy. We will return to this in Section 7.3.

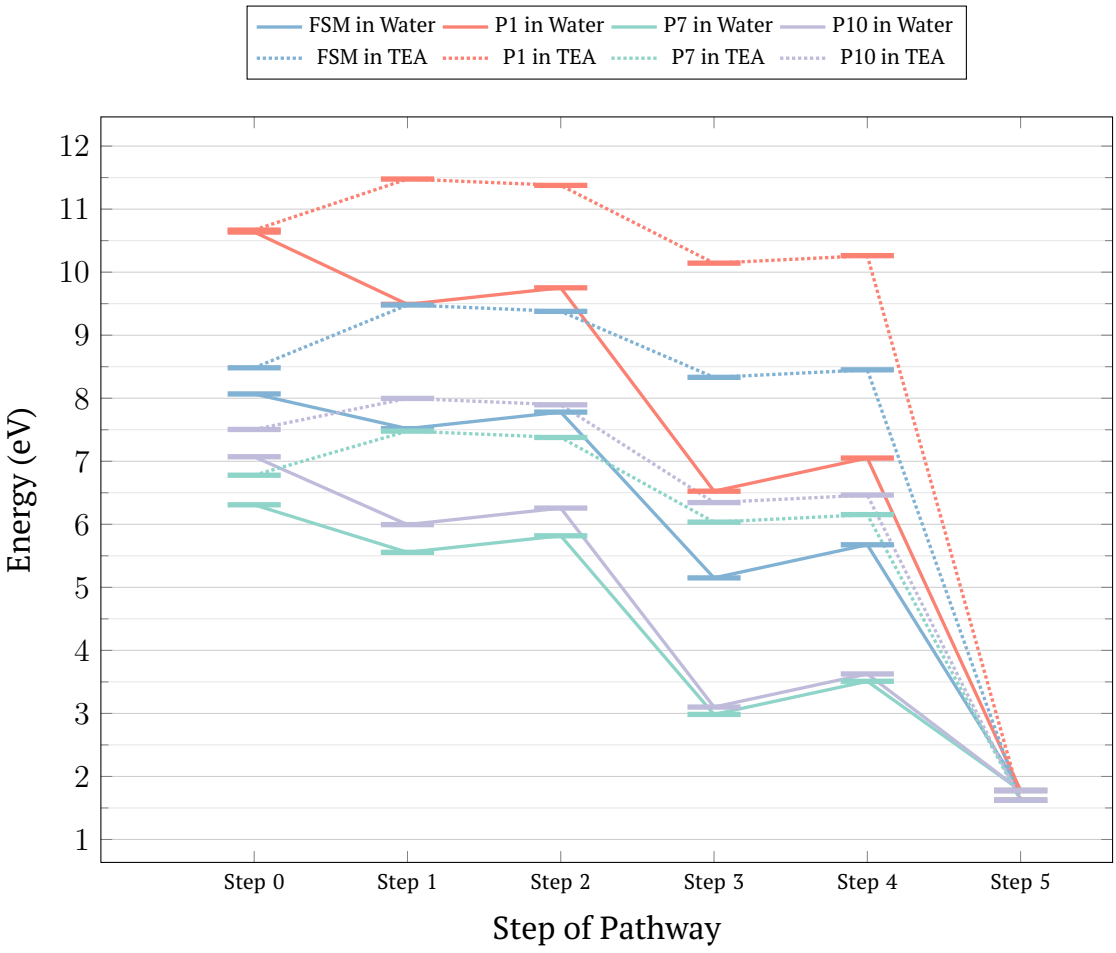


Figure 7.2: This figure shows two active polymers (P7 and P10) and two inactive polymers (FSM and P1) from the previous chapter. The total energy at each step in Figure 7.1 is shown in both TEA (dashed) and in water (full line). These calculations were performed using the ***b3lyp*** *functional and the* ***6-311g(d,p)*** *basis set. It can be seen from these that it appears to be solvation and not chemical structure that strongly affects the thermodynamics of these steps.*

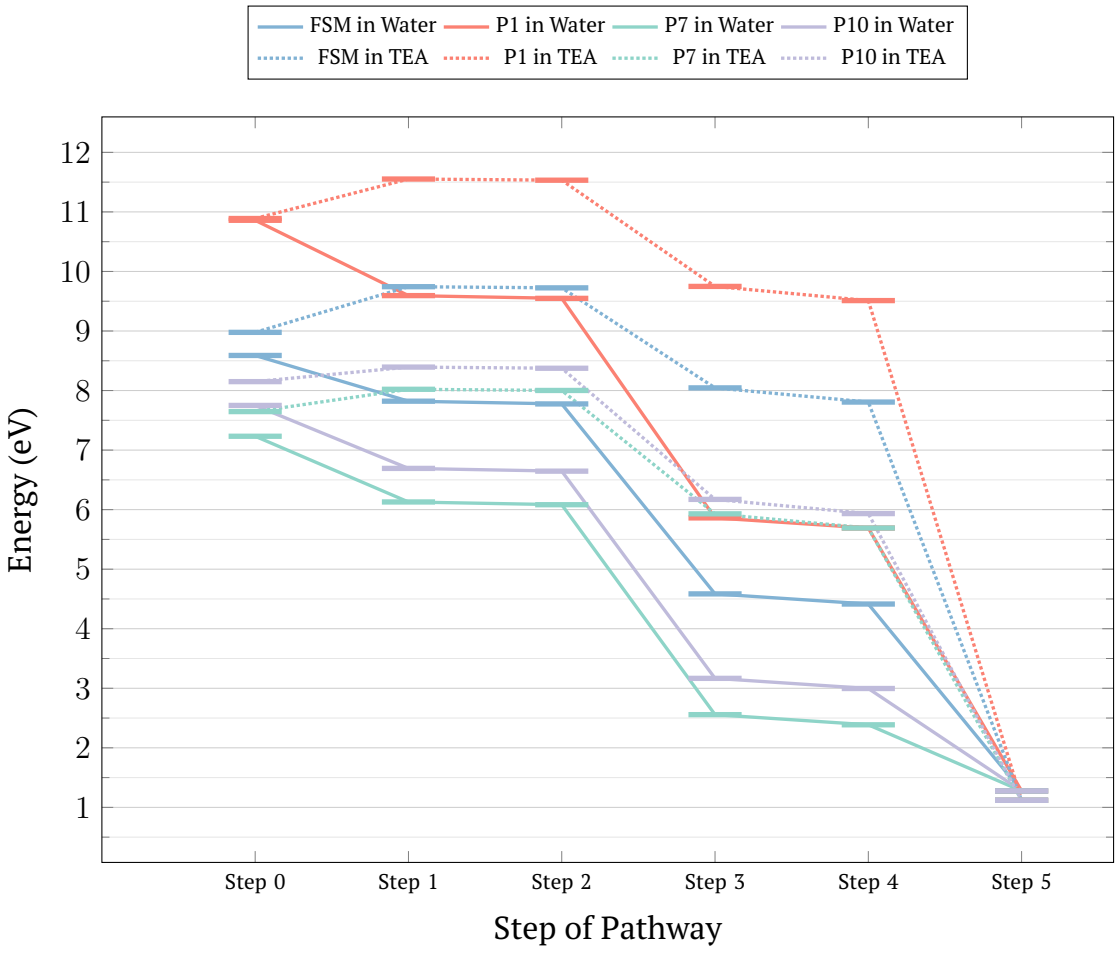


Figure 7.3: This figure shows two active polymers (P7 and P10) and two inactive polymers (FSM and P1) from the previous chapter. The total energy at each step in Figure 7.1 is shown in both TEA (dashed) and in water (full line). These calculations were performed using the ***wB97XD*** *functional and the* ***cc-pVDZ*** *basis set. It can be seen from these that it appears to be solvation and not chemical structure that strongly affects the thermodynamics of these steps.*

Each step in Figures 7.2-7.3 refers to the steps outlined in Figure 7.1 and Equations 7.1 to 7.6, with the exception of step 0. For clarity we have included two photo-excitations at the start (combining step 2b into step 0); this is to allow the start to contain all required external energy. Looking at these results we conclude some key observations:

- The overall reaction is thermodynamically favourable (after the excitations) in both solvents.
- Degradation steps (deprotonation in step 2 and decomposure into DEA and ADH in step 4) are comparitively flat, particularly in the ωB97XD case. Solvation does not seem to impact these steps very much.
- The second charge separation (Step 3) is 'downhill' regardless of solvation environment,

but water does make the reaction even more driven (although both are strongly driven and that is unlikely to explain why some polymers do not perform well).

- Solvation has the biggest impact on the first charge separation (Step 1) where it switches from an 'uphill' reaction in TEA to a 'downhill' one in the higher polarity water environment. This effect holds for both functional and basis sets.

- Choice of functional and basis-set makes a quantitative difference but little difference to trends. Some of the steps switch from being slightly thermodynamically favourable to being slightly unfavourable (e.g. Steps 2 and 4).

With these observations about the data we can move towards a tantalising conclusion by combining them with the knowledge from Chapter 6. We know from this chapter that the polymers performing well have more water in their local environment and from this work we can see that this is likely to have the effect of 'switching' the charge separation (Step 1) to be thermodynamically 'on'. There is some uncertainty here as the DFT uses an environment entirely composed of TEA or water and we know from the MD that the reality is likely to be somewhere in the middle. At this stage then we can be confident to qualitatively explain the experimental observations, but if we are to develop a model that is fully predictive we need one that we can rely on to be quantitatively correct as well. To do this we first need to more rigorously analyse our choice of methodology before attempting to account for multiphasic environments. To study the former, we use a wider set of polymers for which experimental data is available, and this will allow us to see the degree to which this approach is able to quantitatively predict the degree of hydrogen evolution.

It is worth dwelling on one key assumption we make in this approach before we proceed; we are looking at the change in enthalpy between the initial and final states of the reactions in equilibrium. As such, in between the "steps" of Figures 7.2 and 7.3 are energy barriers. In principle these energy barriers could be calculated for some of these transitions by choosing an appropriate reaction coordinate and calculating the energy at certain points along it. This is beyond the scope of this work but we acknowledge that different polymers might have different energy barriers which could explain differences in hydrogen evolutions.

7.3 Methodological dependence of driving forces and solvation properties

We have identified some very tantalising leads on what causes differential hydrogen evolution for a small subset of polymers that we know well, both experimentally and computationally. In this section we focus on testing the robustness of our findings when we relax different assumptions we have made, represented schematically in Figure 7.4. The tests we implement, each coming at higher computational cost, can be summarised as:

- Effect of different functionals.

  We know that different functionals can describe different elements with different degrees of accuracy. In order to ensure the results are robust we use three different functionals: B3LYP, which is very commonly used in the literature[167, 163, 168, 169]. ωB97XD, which is another hybrid functional with an additional dispersion correction to account for long range effects (which is better able to include Van der Waals effects)[170, 171]. Lastly we use M06HF, a hybrid functional based on meta-GGA, which includes a full Hartree-Fock term as that is more accurate for charge separation, due to the fact no self-interaction of a charge occurs[173, 175, 176].

- Effect of diffuse functions in the basis set.

  It is well known that basis sets with diffuse functions provide a better description on anions which are involved in the charge separation steps[151] and as such we explore the impact of this by using 6-311g(d,p) and cc-pVDZ basis sets for non-diffuse basis sets and 6-311+g(d,p) and aug-cc-pVDZ as the equivalent sets with diffuse functions.

- Effect of basis set size.

  The basis sets we chose were the Dunning correlation-consistent basis sets. These were chosen due to the fact they converge uniformally to a complete basis set limit and thus by performing the same calculation at three different sizes of a basis set allow us to extrapolate to a complete basis set approximation.

- Effect of using free energy (via a frequency calculation) instead of enthalpy.

  DFT calculations provide energies at 0°K and as such when a difference between two states is calculated the change in enthalpy is found. The physically meaningful quan-

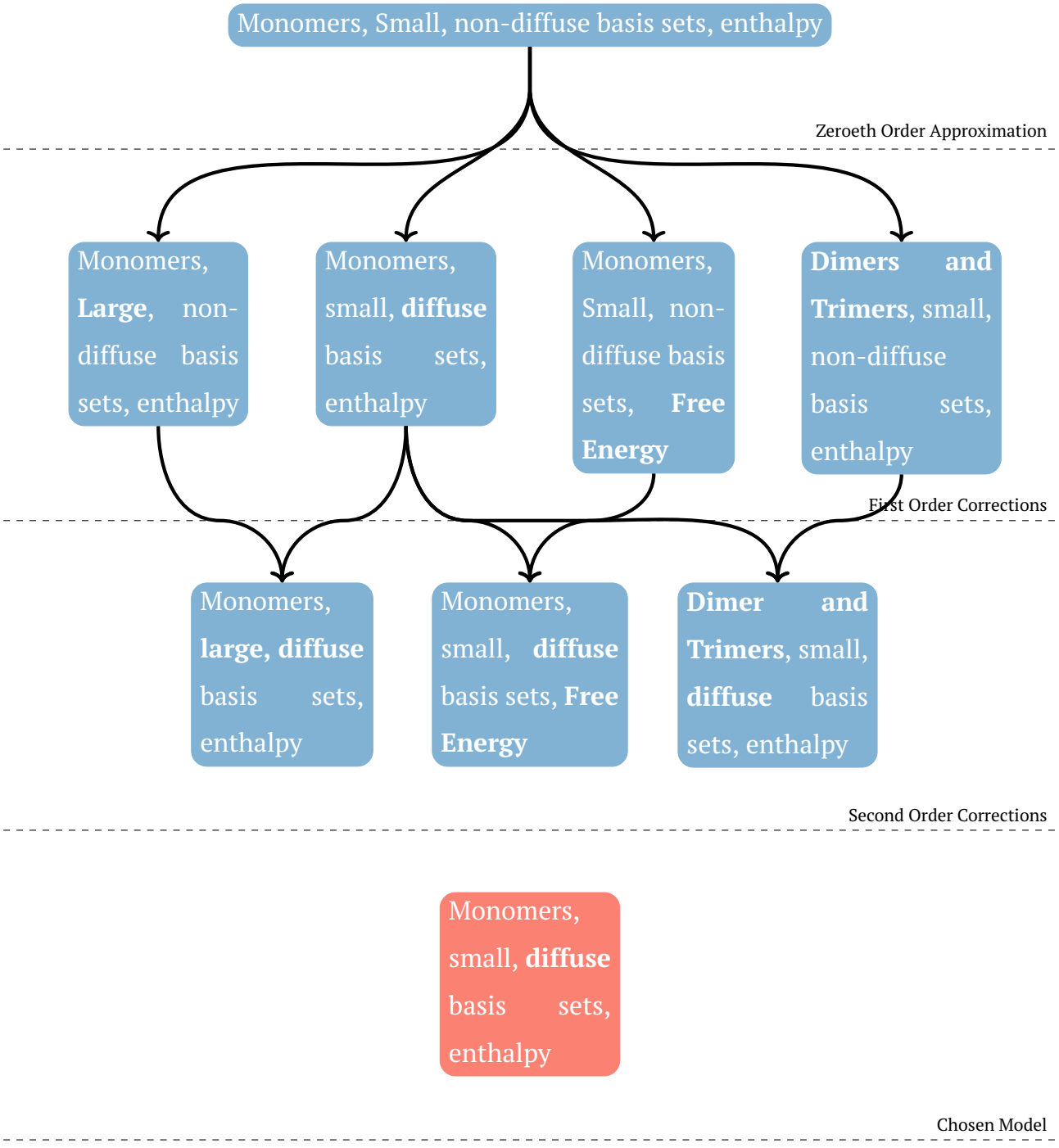


Figure 7.4: This schematic shows the ways of modelling the polymer and the different ways in which I have relaxed different assumptions in order to test the robustness of the approach. By examining each of these levels we isolate the minimal model that adequately explains the phenomenon in order to isolate a prospective screening method. Finally, in red the chosen model is shown.

tity is, of course, the change in free energy between the two states. To do this a frequency calculation is performed on the optimised system in order to obtain the density of states which can then be used to obtain the entropic contribution (via Boltzmann's equation). This is done under the harmonic approximation which assumes

that the nuclear motion (phonons) can be described as a set of independent quantum harmonic oscillators[5]. Previous work investigating this has had mixed results; some studies have looked at the impact of entropic terms and found the effect to be minimal [244, 245], however it is clear that this must be considered on a case-by-case basis.

- Effect of number of monomers modelled.

  We need to ensure that modelling the polymers as small molecules made of just a monomer of the polymer is justifiable. We expand this to dimers which dramatically expand the computational expense due to the increase in conformational phase space. As such we find suitable conformations before also extending to trimers.

It is not clear what impact any of these changes will make on the accuracy of our trends, so to answer this question for our systems we now painstakingly rerun the calculations from the last section, changing different properties at each time to study the impact. As we have identified the charge separation reaction as key, we focus in on this part and look at the impact of moving to these various different degrees of improved accuracy.

[5]This approach is expected to fail at high temperatures and in structures bonded by hydrogen bonds. As such I expect this to be a reasonable approximation for these systems.

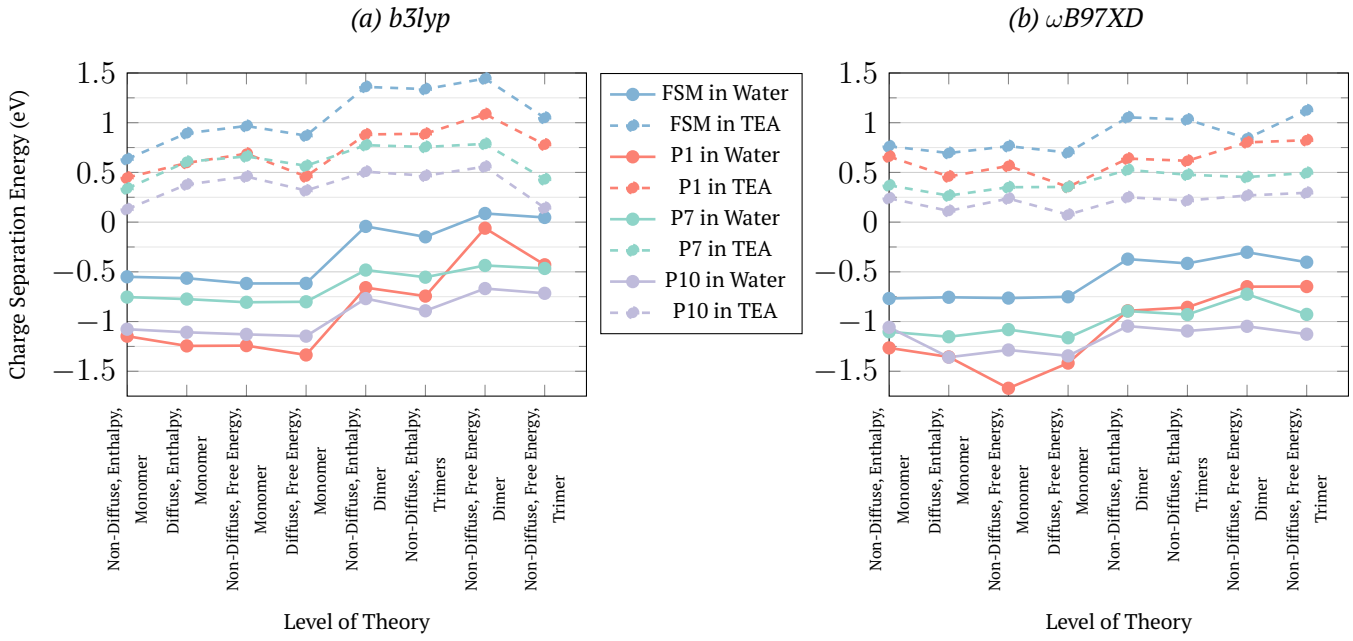


Figure 7.5: This figure shows the dependence of the energy of the charge separation step (Step 1) under some of the different situations shown in Figure 7.4 for (a) the b3lyp functional and pople basis set and (b) the ωB97XD functional with the Dunning correlation-consistent basis sets.

The results of these tests are demonstrated in Figure 7.5. We see that moving towards longer molecules tends to reduce the favourability of the charge separation, and using diffuse functions tends to slightly increase it[6], as does switching to free energy. We now choose a method offering the best balance, attempting to produce the most accurate results for the minimal computational cost[7]. At this stage all we can hope to reproduce is the trend that higher performing polymers both are more solvated in water than TEA, and that they have larger driving forces for the first charge separation reaction. We choose to stay with monomers and enthalpy but switch to basis-sets with diffuse functions as that is likely to be important for the charge separation step. Given we have performed calculations at higher levels we can conclude that the values we find will likely be over-estimates of the driving force, and if we wished for more accurate values we should attempt longer molecules before other ways of achieving higher accuracy.

[6]This makes sense since the diffuse functions will more accurately reproduce the free electron and the favourability arises from the medium effectively screening the free charge.

[7]Given DFT does not reproduce reality it is worth noting here that we ideally want a result that is accurate to the real performance but in this section we concern ourselves primarily with acheiving convergence to the DFT value for minimal computational cost.

7.4 Expanded trial set of polymers

7.4.1 Introduction

In order to test whether the trends observed in Figures 7.2 and 7.3 are universal we apply the same method to a wider set of linear polymers. Ideally this set would contain a variety of performances of polymers in order to test whether the size of Step 1 is predictive (and not just an on/off situation).

In order to ensure we are comparing like for like, to be included in the set a polymer needs to have been tested experimentally, satisfying the following three conditions:

- in the form of a dispersion of linear monomer units,
- using TEA as a SED,
- using the same reaction mixture (in this case an equal by volume mixture of water, TEA and methanol as a mixing agent).

Due to the complexity of the experiments, this limits us to work that has been performed in a very limited number of research groups for a relatively narrow set of chemical structures.

7.4.2 Outline of Set

In the previous section we drilled into the whole pathway for hydrogen evolution where TEA is the SED for the set of polymers from the previous chapter. We found that the defining difference between polymers that are observed to evolve hydrogen and those that do not was two-fold: a) molecular dynamics simulations suggest polymers should perform better in a more water-rich local environment and b) DFT calculations suggest that full immersion in water would make the charge separation step to being thermodynamically favourable, compared with being unfavourable in TEA. Thus, we adopt volume of water surrounding polymer and free enthalpy of the charge separation in water as metrics to study. In this section we attempt to stress-test this observation with a variety of different polymers that do not share as many chemical similarities of the previous set but have been investigated experimentally using the same set-ups. The set is made up of four subsets:

1. The full set of phenylene and flourene co-polymers investigated with chemical substitution from [239], with the addition of P10 from [14].

2. A set analogous to the previous set where the solubility is varied with side-chains and different co-polymerisation options[246, 247].

3. A set of phenylene-thiophene co-polymers investigated by systematic variation of thiophene concentration from [248].

4. A set of nitrogen-phenylene polymers and co-polymers investigating both nitrogen concentration and position of nitrogen substitution from [249].

The four subsets' chemical structures and nomenclature are shown in Figure 7.6.

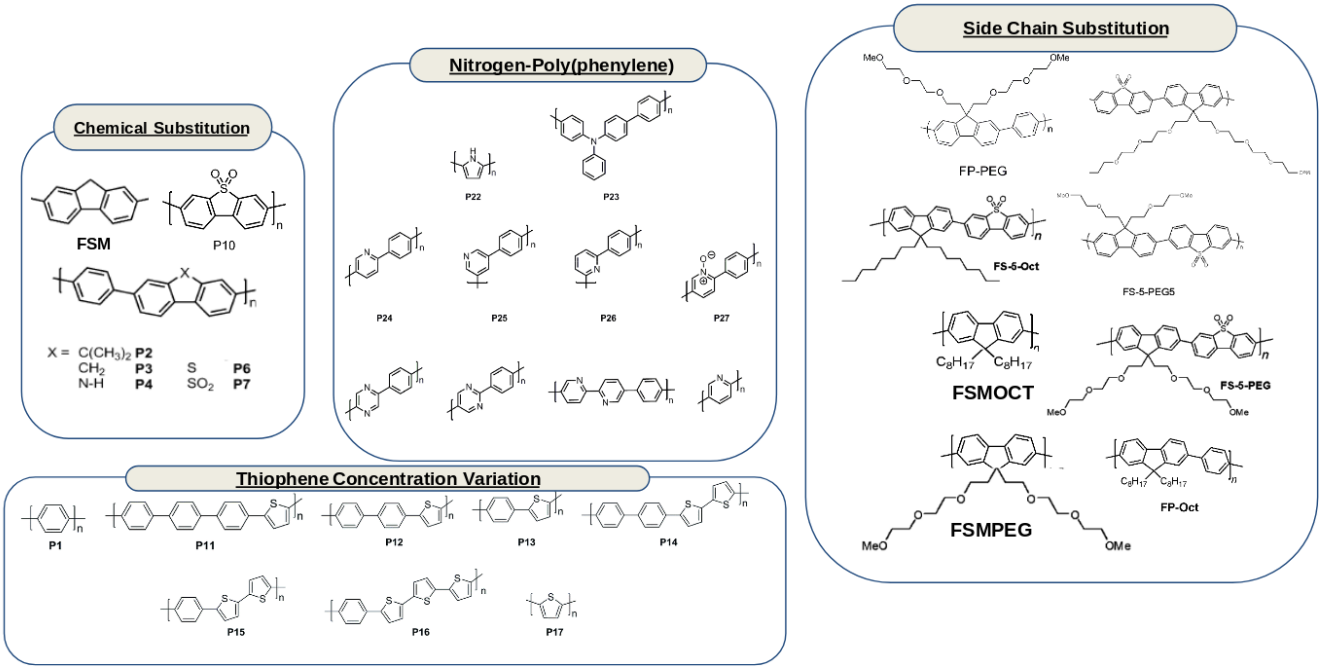


Figure 7.6: This figure shows the make up of the new set of polymers used to stress-test the theoretical connection we have isolated between solvation and hydrogen evolution.

7.4.3 Comparing DFT driving forces with HER performance

We use the methodology we have chosen in the previous sections to investigate to what extent we can explain the variability of the hydrogen evolution over this wider set. We look to see if either a) the charge separation change in energy or b) the difference in free energy of solvation in water and TEA predict hydrogen evolution performance. Both were understood to be important for hydrogen evolution in the last chapter, but in this chapter we are seeking to understand dif-

ferential levels of performance. In Figure 7.7 we plot the experimentally measured HER[8] against the difference between the free energy of solvation in water and TEA per monomer, calculated using DFT. In this way a negative value would signify that the free energy of solvation of the polymer in water is greater than in TEA, which would mean that the polymer preferentially wants to solvate in water. In Figure 7.8 we plot the weighted-HER against the calculated energy change for charge separation in different mediums (which we refer to as the driving force for charge separation).

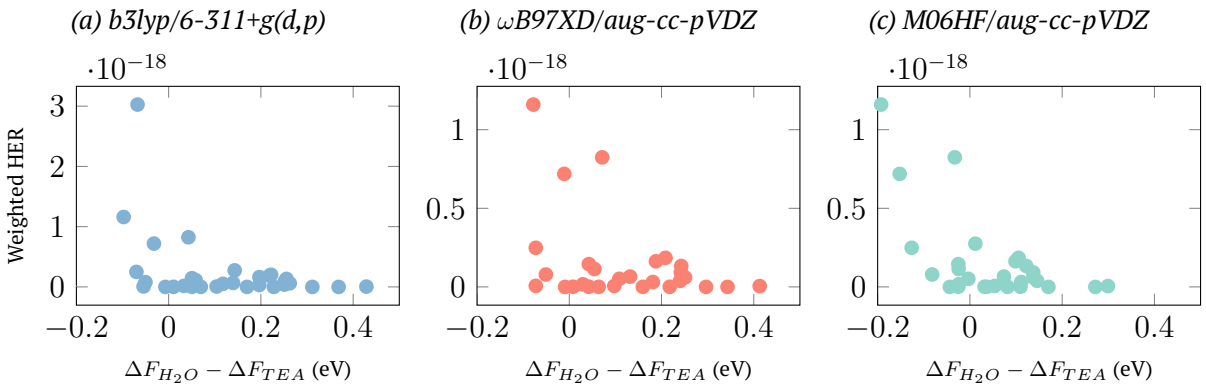


Figure 7.7: This figure shows how correlated the hydrogen evolution rate (in μg H_2/hr per monomer) is with the difference between a polymer's free energy of solvation in water and its free energy of solvation in TEA as calculated using b3lyp/6-311+g(d,p) in blue, ωB97XD/aug-cc-pVDZ in red and M06HF/aug-cc-pVDZ in cyan. Polymers that lie on the left of zero preferentially want to lie in water and this correlates strongly with performance.

[8]Weighted to amount of hydrogen per monomer of polymer, in order to help maximise the comparability of our measurements.

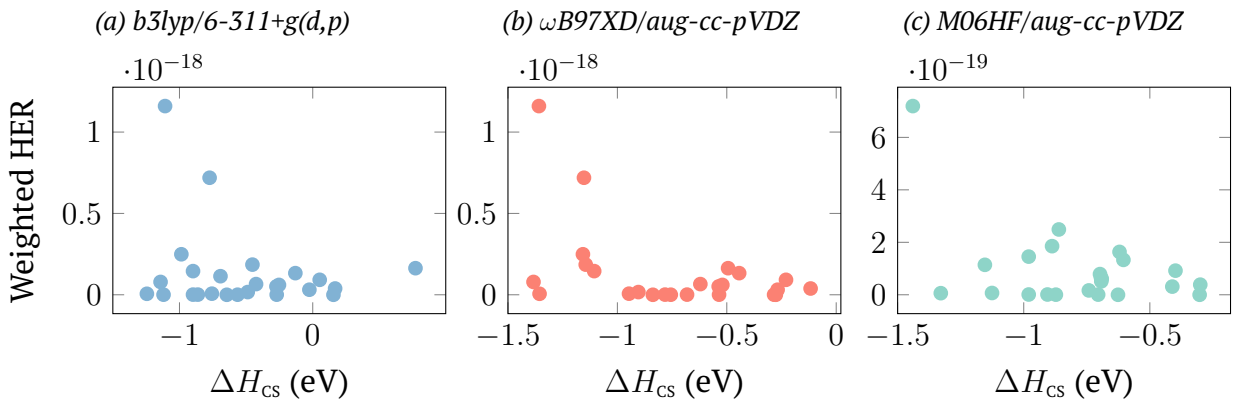


Figure 7.8: This figure shows how correlated the hydrogen evolution rate (in $\mu g\ H_2$/hr per monomer) is with the calculated charge separation "driving force" in water as calculated using b3lyp/6-311+g(d,p) in blue, ωB97XD/aug-cc-pVDZ in red and M06HF/aug-cc-pVDZ in cyan. We can see that there is no strong correlation.

We can see from Figure 7.7 that for this set DFT demonstrates that being solvated preferentially in water acts as a necessary if not a sufficient condition for a polymer to evolve hydrogen at a significant rate. If we look at the driving force for charge separation in different mediums (Figure 7.8) we can see that there is no correlation. Therefore the driving force for charge separation has no predictive power. This makes sense in the context that this approach, where all polymers are considered to be wholly in a particular medium, doesn't account for the medium the polymer is actually in[9]. In the next section we attempt to quantify the local environment of a small subset to see if we can utilise MD and DFT to obtain a more realistic "driving force" that could be more predictive of hydrogen evolution. It is clear from this that we haven't yet been able to isolate descriptors that could be used to potentially pre-screen for hydrogen evolution, if such a thing is possible. What we would need is a way of determining the driving force in the medium the conjugated polymer finds itself in as a result of the solvation properties.

7.4.4 Quantifying Local Environment with Molecular Dynamics

To begin to explore this we will return to molecular dynamics but this time exploring a larger set of phenylene and fluorene co-polymers (FSM, P1, P2, P3, P4, P6, P7, P10) alongside sidechain and co-polymer derivatives (FSMPEG, FSMOCT, FPPEG, FPOCT, FS5PEG and FS5OCT). The chemical structures of each of these polymers are shown in Figure 7.6. We will prepare the force

[9]It is, of course, possible that this is not the only thing missing. The factors involved in hydrogen evolution experiments are numerous and difficult to control. Notably, different polymers may have different rates of dispersion into the reaction mixture.

fields using the same methodology as outlined in Section 5.2 and used in Chapter 6. We need to quantify what the local environment of each polymer is; this is inaccessible by experiment and this is why MD is ideal. Figures 7.9 to 7.12 show molecular dynamics snapshots for each member of the set, including close ups which show only solvents within 2nm of the oligomer. Some differences can be observed by eye from these snapshots. One thing to note is that whilst polymers like FSM and P1 seem to disperse themselves entirely in TEA there are no polymers that do the reverse, situating themselves entirely in water. Such observations, however, must be validated by analysing and averaging over the whole simulation time.

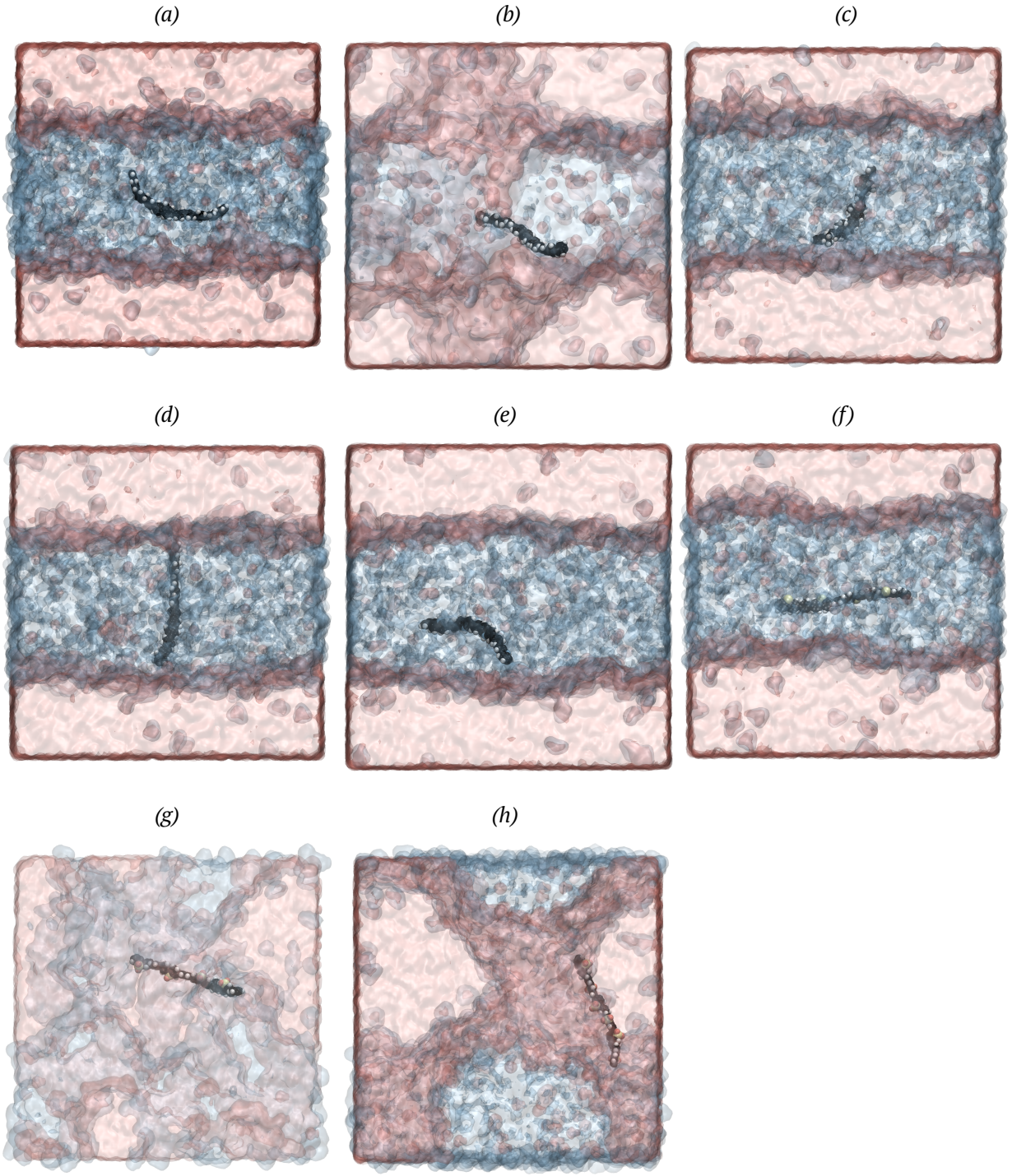


Figure 7.9: This figure shows the snapshots of a) FSM 6mer, b) P1 12mer, c) P2 4mer, d) P3 4mer, e) P4 4mer, f) P6 4mer, g) P7 4mer and h) P10 6mer surrounded by a 1:1 mixture of water and TEA at 300K.

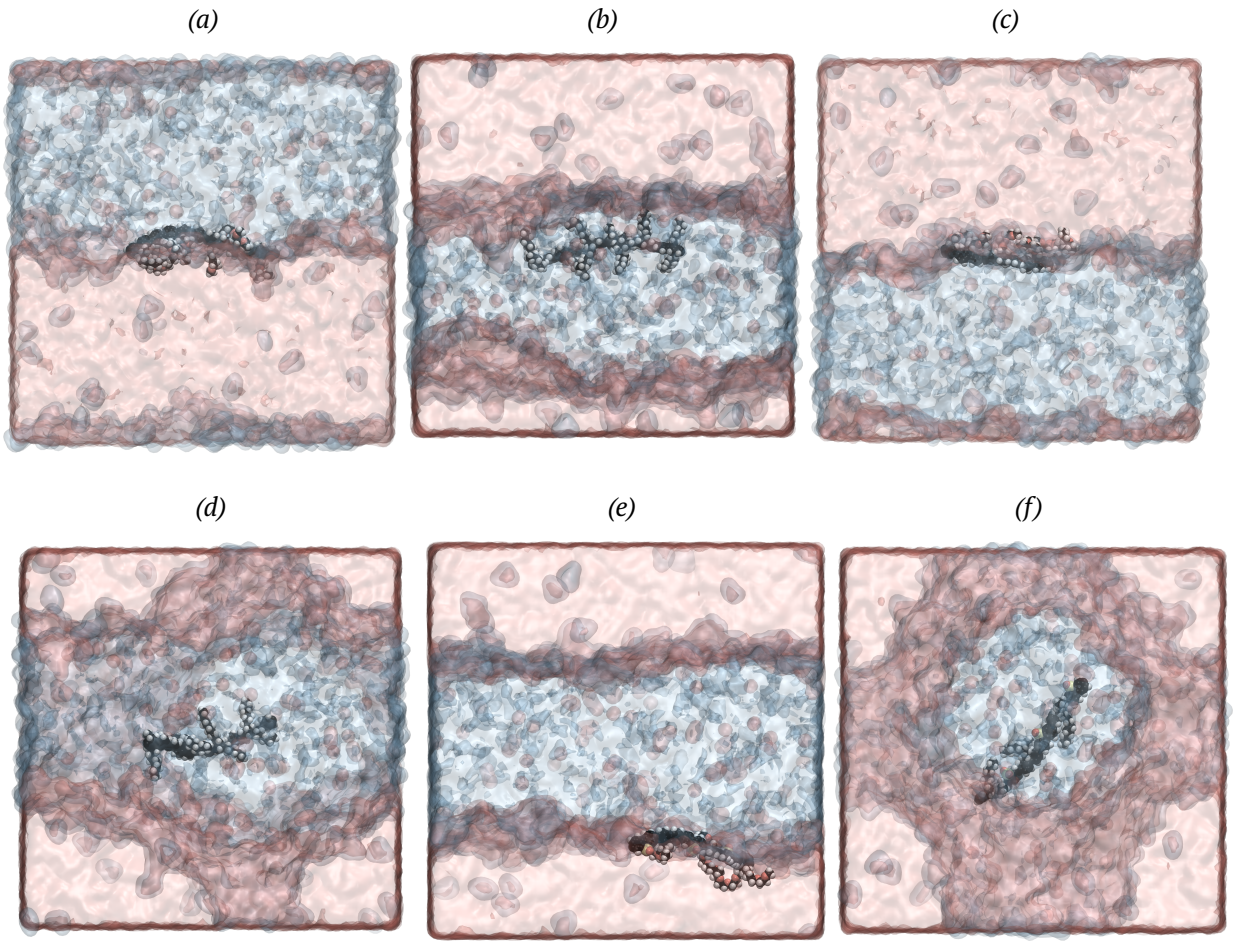


Figure 7.10: This figure shows the snapshots of a) FSMPEG, b) FSMOCT, c) FPPEG, d) FPOCT, e) FS5PEG and f) FS5OCT surrounded by a 1:1 mixture of Water and TEA at 300K.

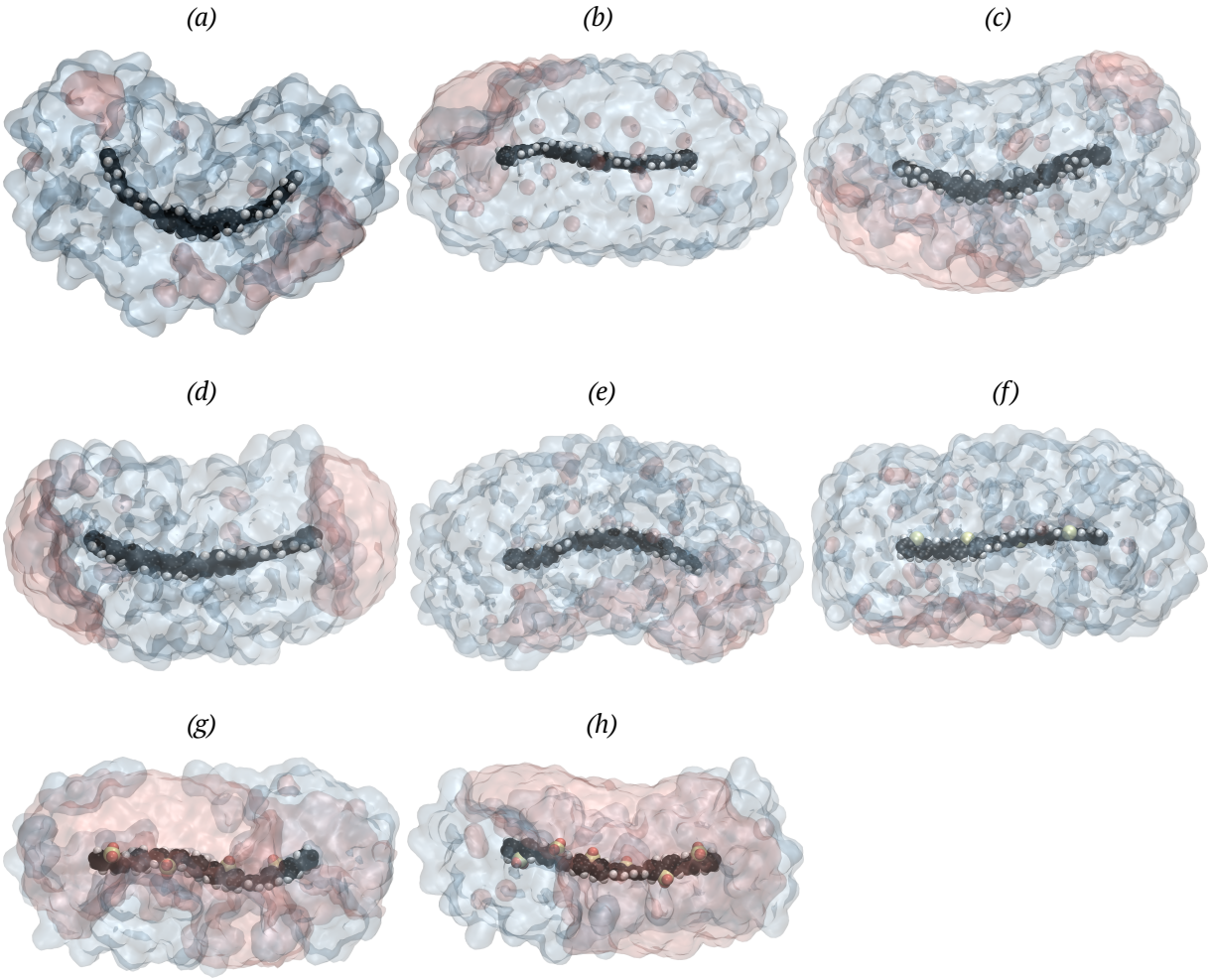


Figure 7.11: This figure shows the local solvent environment of a) FSM 6mer, b) P1 12mer, c) P2 4mer, d) P3 4mer, e) P4 4mer, f) P6 4mer, g) P7 4mer and h) P10 6mer in a 1:1 mixture of water and TEA at 300K.

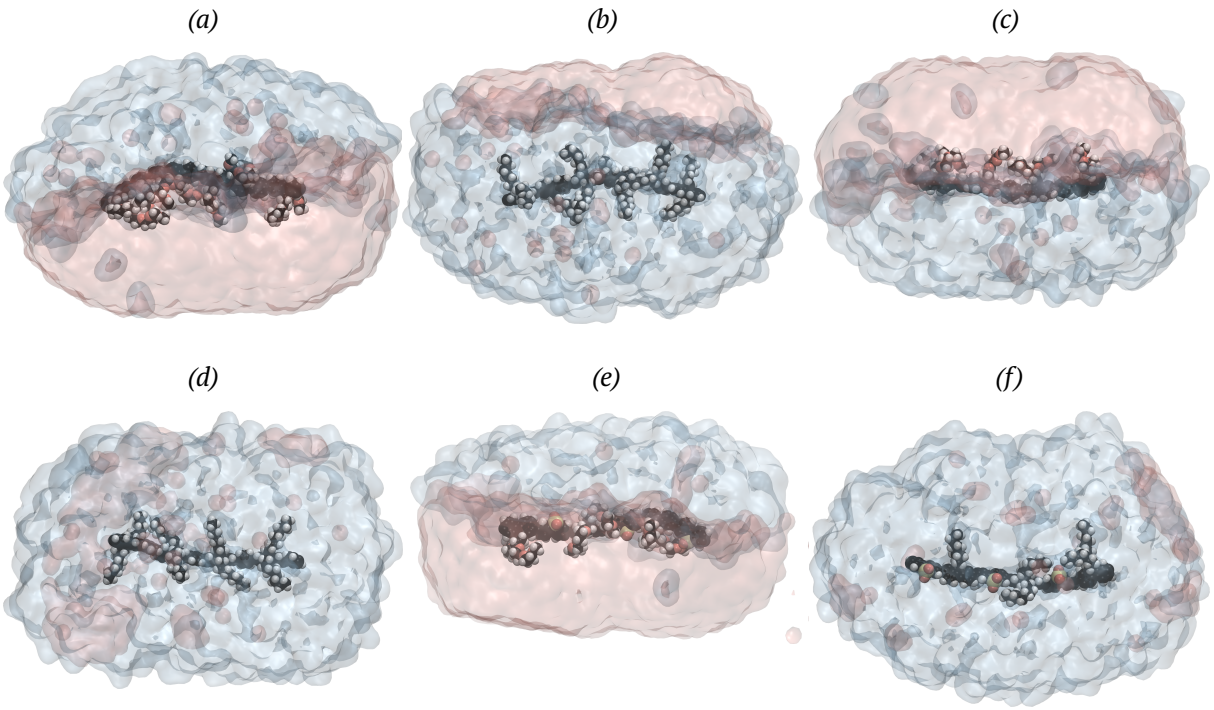


Figure 7.12: This figure shows the local solvent environment of a) FSMPEG, b) FSMOCT, c) FPPEG, d) FPOCT, e) FS5PEG and f) FS5OCT oligomer in a 1:1 mixture of water and TEA at 300K.

We calculate a radial distribution function for the duration of the simulation for all the polymers shown here. We then calculate the cumulative distribution to identify the average number of molecules of each component as a function of radius from the centre of mass of each monomer unit. We can then multiply this molar volume of each component to determine the proportion of the volume that contains each of the components. The results of this can be seen in Figure 7.13 and in Table 7.1. These have been taken at a cut-off radius of 2nm.

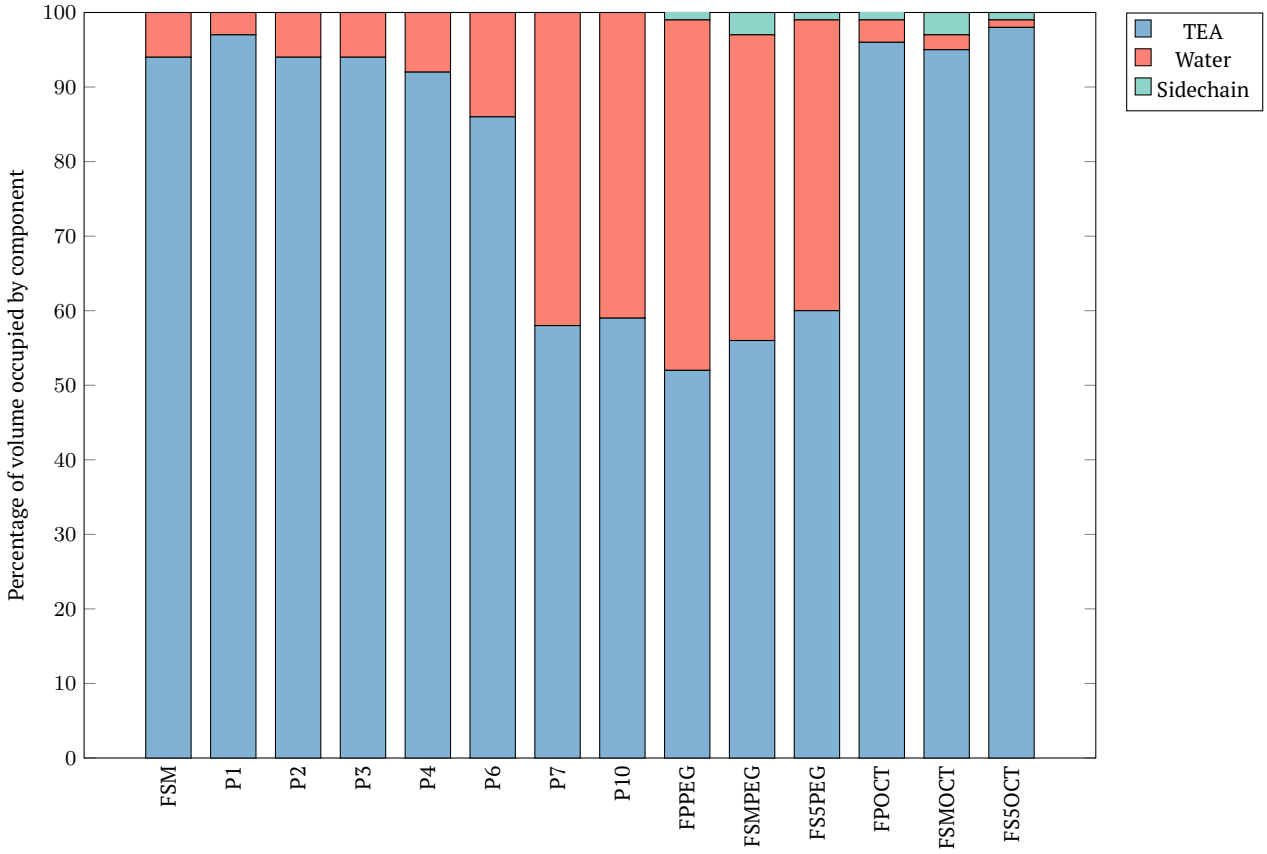


Figure 7.13: This figure shows the local environment (taken at a cutoff radius of 2nm from the center of mass of the oligomers' backbone) of the oligomers studied with MD.

There are several key things to note from the MD, firstly that with this expanded set the fundamental observation of the last chapter is intact, namely, that the more of the environment that is surrounded by water the better performing the polymer. This can be seen quite clearly in Figure 7.14. It shows that adding hydrophilic sidechains, which do not significantly adjust the energetics of the states involved in a reaction (for a given environment), can push a polymer from being inactive to active purely by adjusting the solvation properties (e.g comparing P2 with FPPEG). We can also see that for some polymers (P7, P10, FPPEG, FSMPEG, FS5PEG) the assumption utilised in the DFT calculations that the environment is monophasic and can be modelled by a continuum model of a solvent does not hold. This might explain in part why the correlation in Figure 7.8 is not that strong, the difference between the enviroment the calculations are performed in and the reality is very different and highly dependent on the polymer. In Figure 7.14 we plot the extracted fraction of water in the local environment against the experimental HER values.

Oligomer	TEA	Water	Sidechain
FSM	94.2	5.8	N/A
P1	97.1	2.9	N/A
P2	75.4	24.6	N/A
P3	94.2	5.8	N/A
P4	71.2	28.8	N/A
P6	85.9	14.1	N/A
P7	58.4	41.6	N/A
P10	59.3	40.7	N/A
FPPEG	51.7	46.6	1.75
FSMPEG	56.4	40.9	2.73
FS5PEG	59.3	39.5	1.26
FPOCT	95.5	3.2	1.73
FSMOCT	95.2	2.0	2.75
FS5OCT	97.8	0.9	1.28

Table 7.1: A table showing calculation percentage of the volume at 2nm from the oligomer backbone.

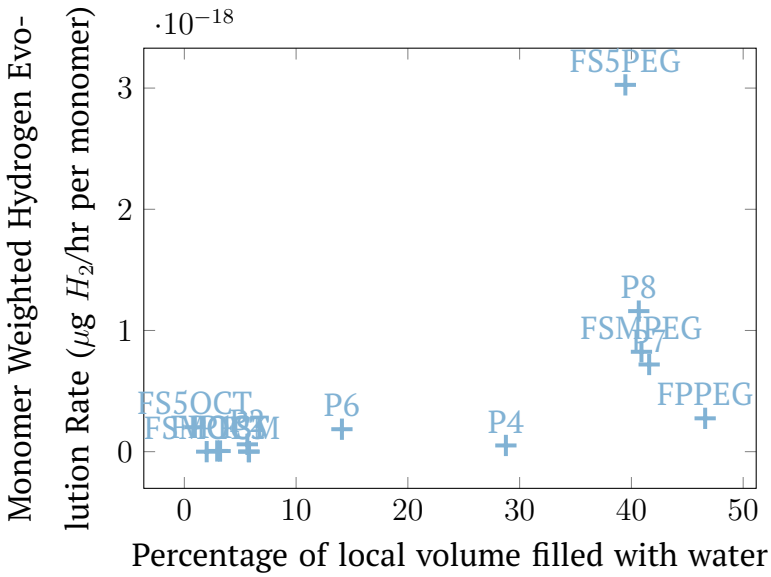


Figure 7.14: This figure shows the correlation between water volume in the surrounding environment on the oligomer from water/TEA(1:1) MD systems and the experimental HER values (performed in water/TEA/methanol solution in 1:1:1 ratio by volume).

From Figure 7.14 we can see that there is some correlation of HER with the fraction of water in the local environment, extracted from MD. However, a large fraction of water does not seem to be a sufficient condition for efficient hydrogen evolution, although it does seem to be a necessary one.

This tells us that to effectively model the driving forces of the TEA degradation pathway for these polymers we need to find a way of modelling the biphasic nature of the environment. For this we need to establish:

- How to effectively model the environment without recourse to computationally expensive MD simulations.
- The most effective and efficient way of calculating the driving forces in this effective medium.

The latter of these is explored separately in the next two subsections.

7.4.5 Driving Forces in Multi-Phasic Environment

On the assumption that we can quantify the nature of the local environment of the polymer, either via an expensive MD calculation or via DFT calculations coupled with a simple physics model like the one outlined in the last section, we still require the ability to determine the driving forces in this effective medium. We suggest several options:

1. Make an effective medium model, which would be used to estimate the quantities needed for the PCM given the make-up of the medium, and rerun DFT calculations for those parameters. This would have the potential to offer a DFT model for the multi-phasic nature of the system but it does, however, have one major drawback: water is well-known to be a unique and difficult to model solvent and as such the PCM used in the DFT calculations uses a bespoke model that is not compatible with the model of other solvents. Whilst more limited, we proceed by allowing the model to assume the medium is water but modify the polarity.

2. A simpler model would be to determine the effective polarity of the medium via an effective medium approach and perform an interpolation of the driving force between the two values we already have (in TEA and water). This is making the assumption that the

difference in driving force for charge separation will mostly be due to the polarity of the medium.

Given the first of these approaches is incompatible with considering the polymers in water, something vital for considering water splitting, we abandon it. Both approaches require an effective medium model to determine ϵ_{eff}. In the next subsection we outline models for determining the ϵ_{eff}, the effective polarity used in both approaches.

7.4.5.1 Polarity of Binary Mixtures

In the general case it is quite difficult to come up with a way of modelling the effective permittivity of an inhomogeneous medium as this will depend strongly on the concentration, the size of the phases and how ordered or random the distribution is. There are a number of effective medium models for estimation of the effective dielectric permittivity of a binary mixture from properties of the pure components, and the two most used are the Bruggeman model[16] and the Maxwell-Garnett model[250, 251]. The Bruggeman model assumes that we have two homogeneous and isotropic phases, that the molecules are small in comparison to system size, that each phase is randomly distributed in the system and that each domain is in an equivalent mean field. The last of these breaks down when the system is close to its percolation threshold[10]. The Maxwell-Garnett model assumes that one phase significantly dominates the other and the phase with less volume fraction can be modelled as small spherical inclusions. It breaks down if the volume fraction is too high. We use the Bruggeman model as in our case we will be dealing with situations where the volume fraction is high for both phases. Experiments and our molecular dynamics simulations suggest the reaction mixture is well mixed with small domains. Bruggeman's model gives the effective polarity of a binary medium,ε_{eff}, as the solution to:

$$\phi_A \frac{\varepsilon_A - \varepsilon_{\text{eff}}}{\varepsilon_A + \varepsilon_{\text{eff}}} + (1 - \phi_A) \frac{\varepsilon_B - \varepsilon_{\text{eff}}}{\varepsilon_B + \varepsilon_{\text{eff}}} = 0, \tag{7.18}$$

where ϕ_i is the mole fraction of medium i and ε_i is the permittivity of medium i in its pure form.

[10]The percolation threshold will be neared if the average cluster size tends to one, so section 4.4.4 can act as a guide to the validity. We know that for the reaction mixture this is not the case, as the system is well mixed. In the case of just Water-TEA systems we know that it can tend to the percolation threshold but this system is not the one used in experiments.

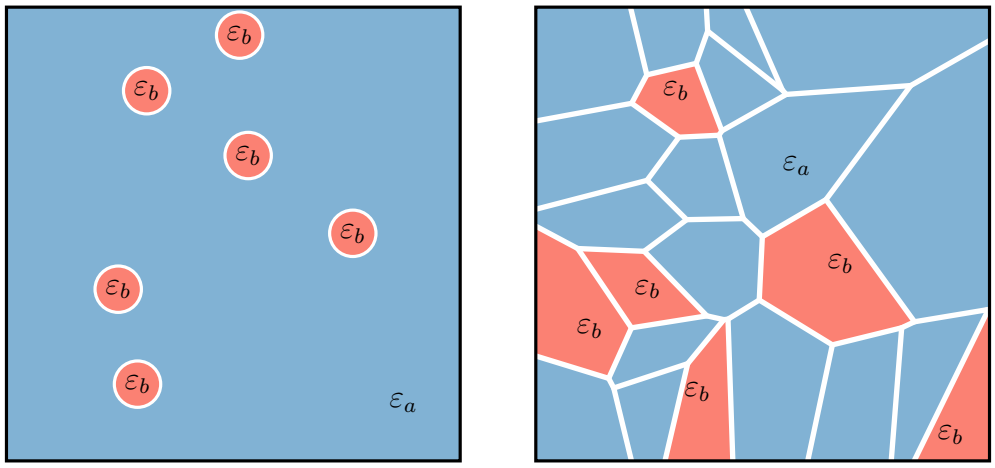


Figure 7.15: This figure shows the fundamental system assumed by each of the two main effective medium models, the Maxwell-Garnett[15] and Bruggeman[16]. The former uses different regions of each medium for a given mole fraction, whereas in contrast the Maxwell-Garnett model considers one of the mediums as the base medium and then adds small inclusions of the second medium.

7.4.5.2 Results

With an ability to model the effective permittivity of the binary mixture we can now apply both of the approaches outlined in Section 7.4.5 and compare the results. The driving forces we find using both of the approaches are summarised in Table 7.2.

Oligomer	ΔH_{cs} b3lyp	ΔH_{cs}, ωB97XD	ΔH_{cs}, M06HF
FSM	0.810	0.611	0.534
P1	0.541	0.406	0.173
P2	1.039	0.786	0.670
P3	1.022	0.770	0.653
P4	1.022	0.759	0.273
P6	0.717	0.388	0.329
P7	0.024	-0.333	-0.574
P10	-0.226	-0.486	-0.683

Table 7.2: A table showing driving forces when weighted by the MD volume fraction alongside the unweighted values in water.

We plot each of the approaches' driving forces against the experimental results for HER in Figure 7.16.

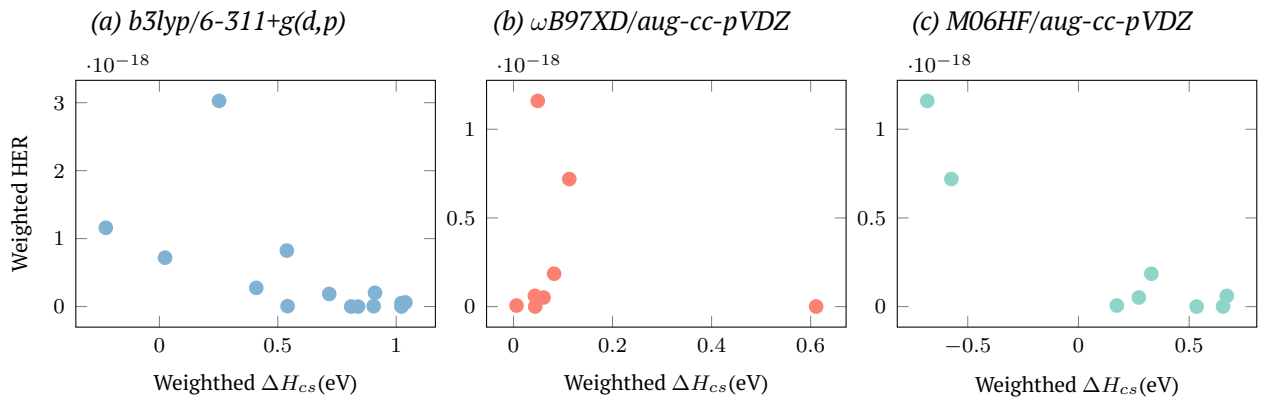


Figure 7.16: This figure shows the improved correlation of experimental HER data, in μg H_2/hr per monomer, with the charge separation driving force weighted by amount of water in the local environment from MD simulations. Results using b3lyp/6-311+g(d,p), ωB97XD/aug-cc-pVDZ and M06HF/aug-cc-pVDZ are shown in blue, red and cyan respectively.

We see from Figure 7.16 that this simple approach provides a powerful measure of hydrogen evolution. We have effectively harnessed the power of both MD and DFT to partially explain the differential performance of this set. Unfortunately, the use of MD would preclude this method from being an effective screening technique. It is worth noting that we have assumed a mixture of just water and TEA and the experiments take place in a mixture of TEA, water and methanol. We investigate how good this approximation is in the next section.

7.5 Ternary Enviroments: Full Reaction Mixture Model

In this section we attempt to extend our model of the previous section to the full experimental solvent mixture. The experimental set-up is complex and it can be hard to isolate the different factors involved in an overall performance. For example, methanol was added as it was necessary to ensure that the TEA mixed sufficiently with the water, but it is also known to act independently as a SED. To isolate this, experimental tests were also performed by our collaborators with just methanol and water and this did not evolve any hydrogen, suggesting that methanol indeed is acting as a simple mixing agent[14]. This, however, is very high level and there are still a lot of uncertainties about how the introduction of another liquid impacts the system. As such, we extend our model and investigation to look at the full ternary solvent system. This allows us to test the reliability of our findings. First, we look at the same systems with which we used MD, in the last section, but this time adding in methanol. We then return to the model we have developed using DFT calculations and extend it to a ternary system.

7.5.1 Molecular Dynamics

We use a TEA:water:methanol mixture in 1:1:1 ratio by volume for FSM, P1, P2, P3, P4, P6, P7 and P10 oligomers as well as for the series with different sidechains: FSMPEG, FSMOCT, FPPEG, FPOCT, FS5OCT and FS5PEG, the structures of which are shown in Figure 7.6. We use the same procedure as before to obtain fully equilibrated systems, where the solvent has relaxed. The snapshots at the end of the equilibration are shown in Figures 7.17 to 7.20.

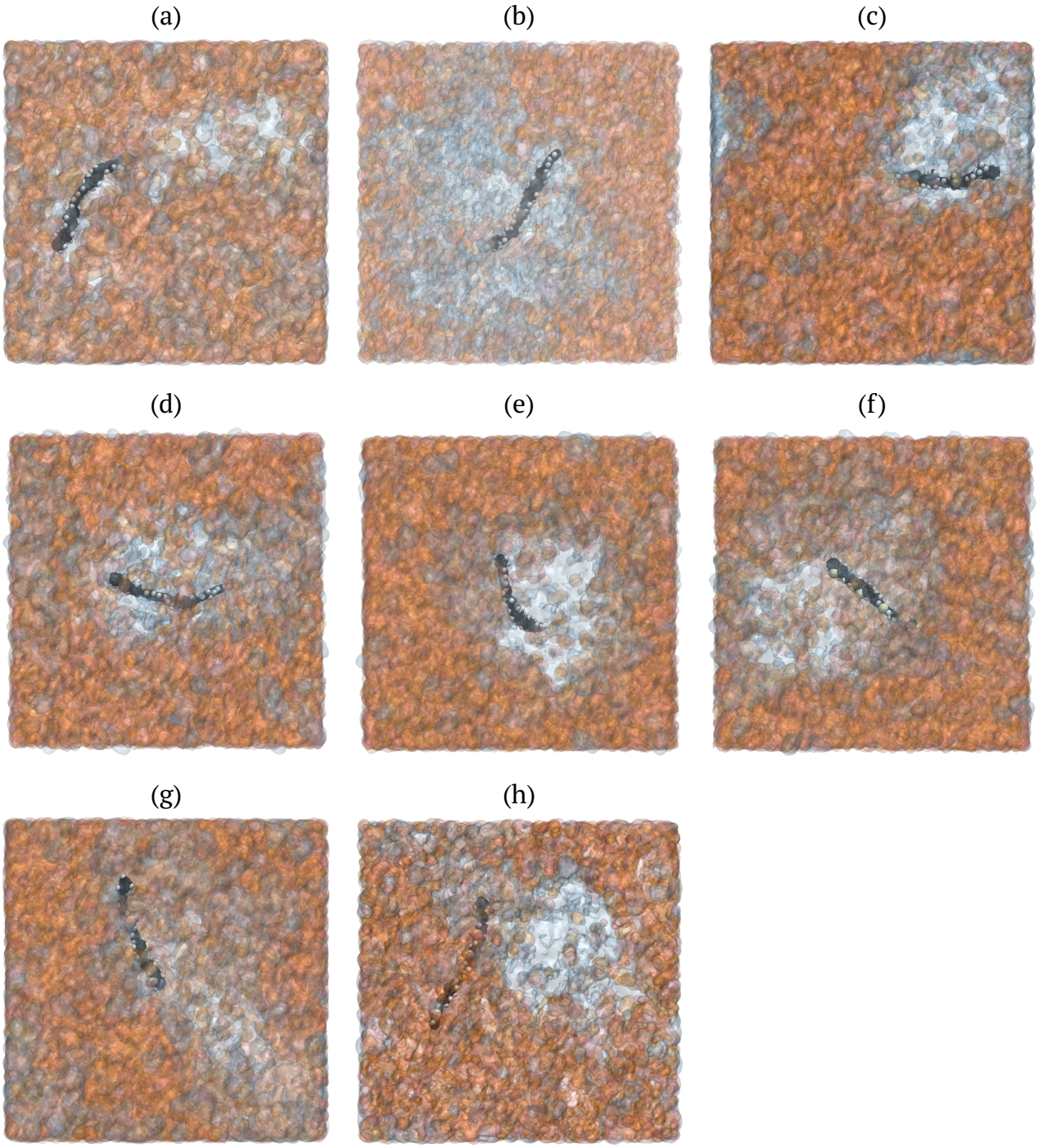


Figure 7.17: This figure shows the whole simulation box of a) FSM 6mer, b) P1 12mer, c) P2 4mer, d) P3 4mer, e) P4 4mer, f) P6 4mer, g) P7 4mer, and h) P10 4mer solvated in TEA, water and methanol in 1:1:1 ratio by volume. Water, TEA and methanol are shown in Red, Blue and Orange respectively but because of the level of mixing the definition between solvents is hard to see.

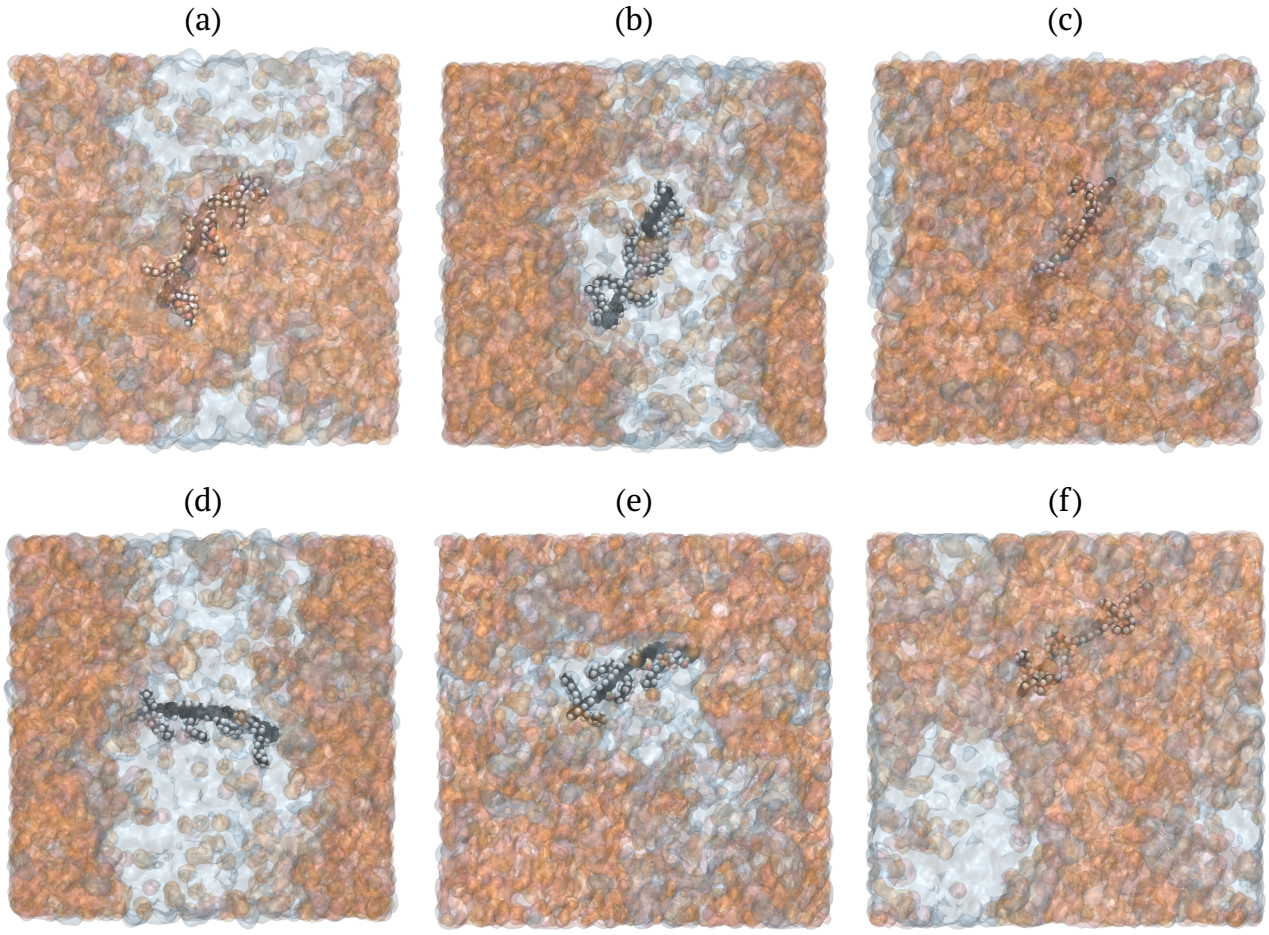


Figure 7.18: This figure shows the whole simulation box of a) FSMPEG 6mer, b) FSMOCT 6mer, c) FPPEG 4mer, d) FPOCT 4mer, e) FS5OCT 3mer, and f) FS5PEG 3mer solvated in TEA, water and methanol in 1:1:1 ratio by volume. Water, TEA and methanol are shown in Red, Blue and Orange respectively but because of the level of mixing the definition between solvents is hard to see.

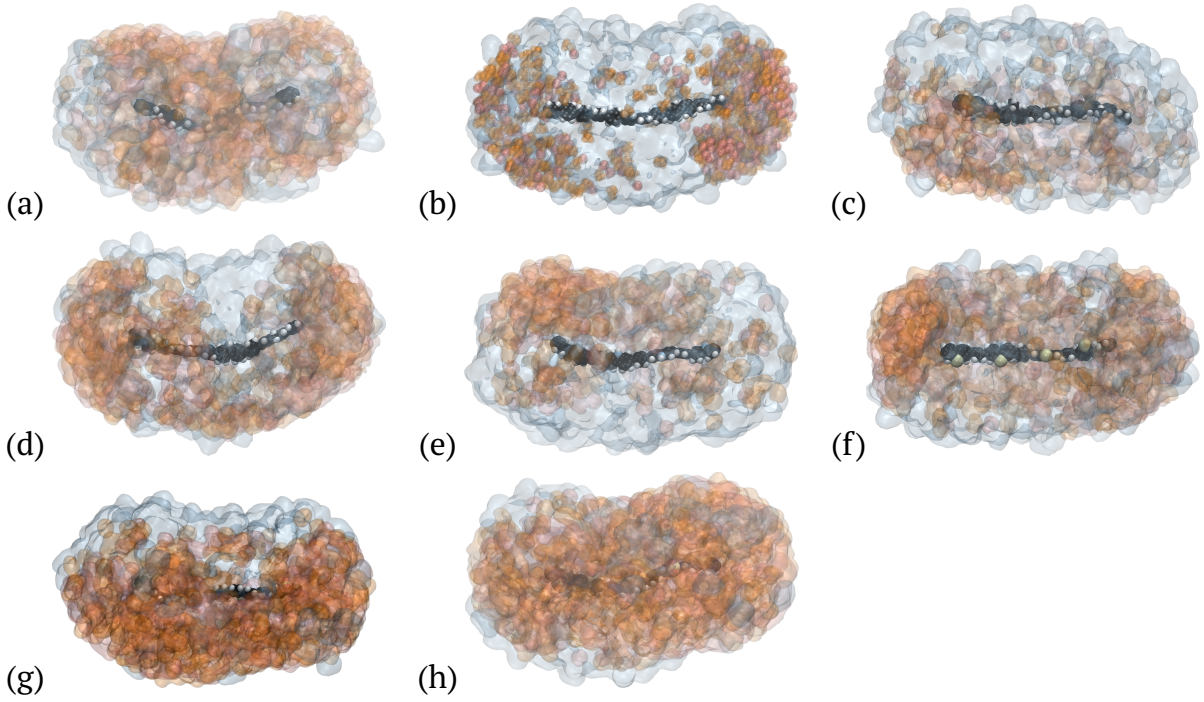


Figure 7.19: This figure shows the local environment of a) FSM 6mer, b) P1 12mer, c) P2 4mer, d) P3 4mer, e) P4 4mer, f) P6 4mer, g) P7 4mer, and h) P10 4mer solvated in TEA, water and methanol in 1:1:1 ratio by volume. Water, TEA and methanol are shown in Red, Blue and Orange respectively but because of the level of mixing the definition between solvents is hard to see.

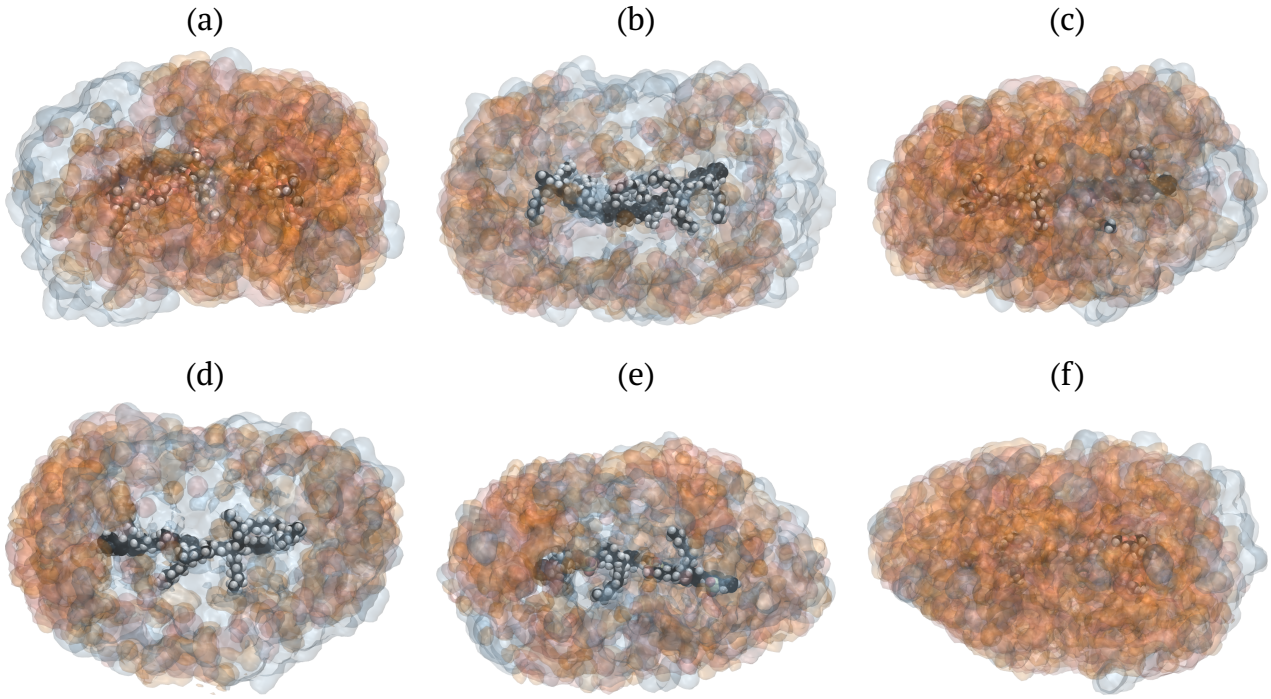


Figure 7.20: This figure shows the local environment of a) FSMPEG 6mer, b) FSMOCT 6mer, c) FPPEG 4mer, d) FPOCT 4mer, e) FS5OCT 3mer, and f) FS5PEG 3mer solvated in TEA, water and methanol in 1:1:1 ratio by volume. Water, TEA and methanol are shown in Red, Blue and Orange respectively but because of the level of mixing the definition between solvents is hard to see.

As before we need to extract, using the radial distribution function, the local environments surrounding each of the oligomers. The values obtained using this method can be seen in Figure 7.21 and are tabulated in Table 7.3.

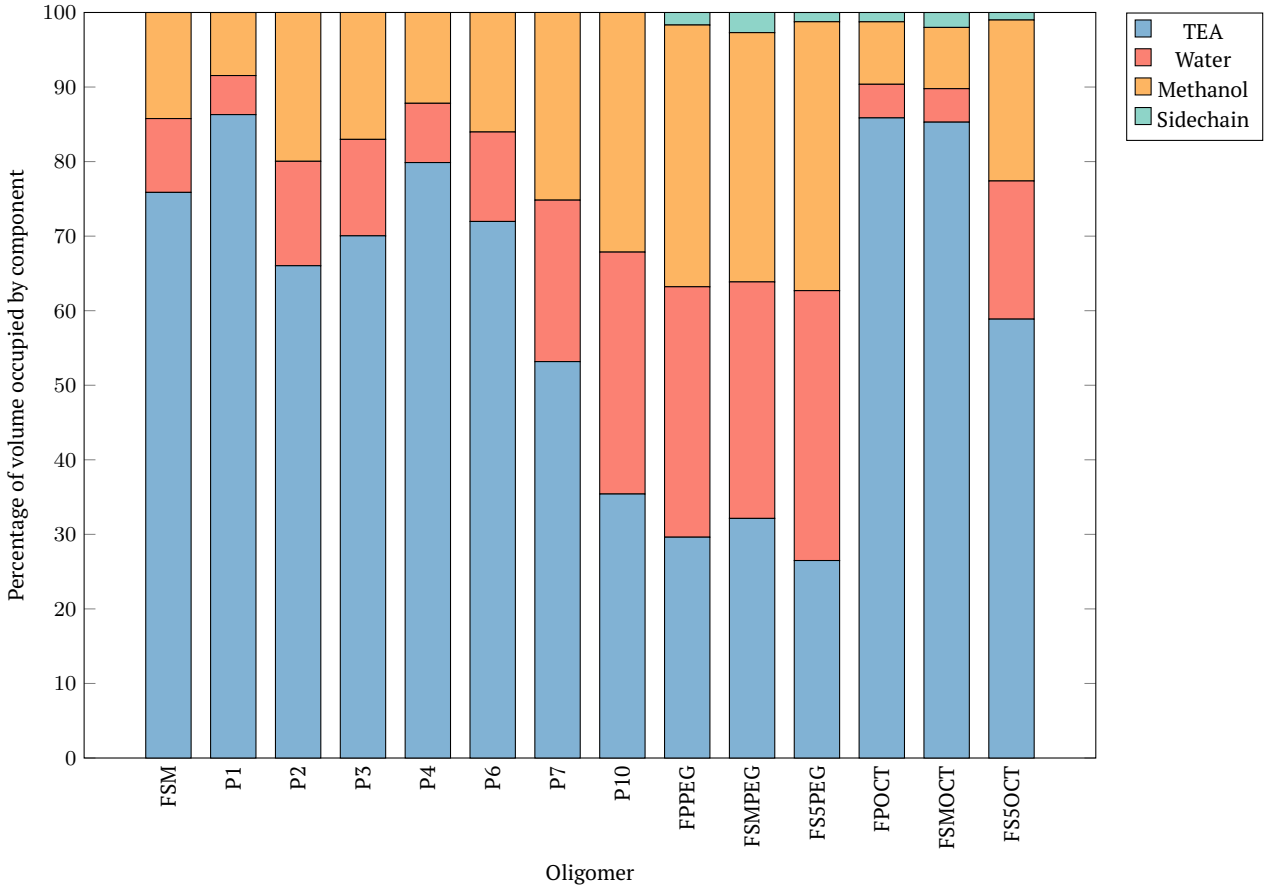


Figure 7.21: This figure shows the local environment (taken at the cutoff of 2nm) of the oligomers studied with MD.

Oligomer	TEA	Water	Methanol	Sidechain
FSM	75.9	9.9	14.2	N/A
P1	86.3	5.2	8.5	N/A
P2	66.0	14.0	20.0	N/A
P3	70.0	13.0	17.0	N/A
P4	79.9	8.0	12.1	N/A
P6	72.0	12.0	16	N/A
P7	53.2	21.7	25.1	N/A
P10	35.4	32.5	31.1	N/A
FPPEG	29.6	33.6	35.1	1.7
FSMPEG	32.1	31.7	33.5	2.7
FS5PEG	26.5	36.2	36.1	1.2
FPOCT	85.9	4.5	8.4	1.3
FSMOCT	85.3	4.5	8.2	2.0
FS5OCT	58.9	18.5	21.6	1

Table 7.3: A table showing the calculated percentage of the volume at a r_{cutoff} of 2nm from the oligomers' backbone.

We can see, primarily from Figure 7.21 but also from the snapshots in Figures 7.17 to 7.20, that our MD simulations agree with the experimental observations that methanol acts as an effective mixing agent (as we saw in Sections 4.5 and 6.4.3.2) even when the oligomer is present. It is also the case that we still observe a trend whereby more water (and methanol) rich phases surround oligomers which perform well for hydrogen evolution. A full treatment of this however would be necessary to say with certainty what the impact of the methanol would be by including methanol calculations and extending the Bruggeman approach to a ternary system. However, this is beyond the scope of this work.

7.6 Summary

In this chapter, we have seen that it is possible to rationalise the performance of different linear conjugated polymer dispersions as photocatalysts for hydrogen evolution. We have outlined a method that accounts for the electronic structure of the polymer and the solvation properties in the full reaction mixture. Whilst we know from experiment (and indeed the outcomes of the last chapter) that there are other factors that are important for determining the final performance

of the polymer, such as the amount of aggregation of the polymer in the reaction mixture, this moves us toward a method of pre-screening the large phase-space of polymers. Organic photocatalysts are a new, exciting and poorly understood field and this work represents a significant start to understanding what elements can predict which polymers will perform well at hydrogen evolution.

8

Conclusions and Future Work

8.1 Conclusions

This work has focused on exploring different organic materials for use in energy applications. We now overview the work that has been performed. In Chapter 4 we performed a study of simulations of organic solvents and water using molecular dynamics, choosing force fields to maximise the physicality of the simulation before studying the type of interactions and behaviours of multi-phase simulations. In Chapter 5 we studied, again using molecular dynamics, the behaviour of polymers (modelled as short oligomers) in solution and attempted to link that behaviour to properties in the solid-state. In Chapter 6 we looked at a class of organic photocatalysts for which there was experimental data on differing performances. We used MD and DFT to study a variety of possible explanations for why some polymers were able to evolve hydrogen whilst others were not. Finally, in Chapter 7, we continued to study organic photocatalysts, this time using a mixture of MD and DFT to study more closely the hydrogen evolution reaction and the factors that influence it. We do this to build towards a computational system of screening the wide chemical phase space to suggest polymers that are worth experimentally producing and measuring, in the hopes of being able to produce organic polymer photocatalyst systems with performances that could rival carbon-nitride or even metal-oxide systems.

The major findings of the work are:

1. MD can be used to study the phase segregation and miscibility of solvents as well as the free energy of solvation. This is particularly useful for examples where the phase diagrams for certain mixtures do not exist. There are a number of other methods for determining phase diagrams, such as monte carlo[252], and it is far from clear that MD would be the best approach.

2. A mixture of techniques arising from MD are capable of modelling conformational proper-

ties of polymers in solution. A relationship between the free energy of solvation of a polymer and properties like the persistence length was observed, with better solvation leading to higher persistence lengths. This likely arises from the polymer maximising the surface area when experiencing a favourable solvation interaction and otherwise minimising it which acts against the polymer's natural stiffness.

3. The free energy cost of planarising the backbone of PFO was calculated in chloroform and was found to be in line with some experimental observations. Namely, that it was significantly harder to planarise if the backbone had branched sidechains than straight ones.

4. I was able to study a highly complicated experimental system to rule out a number of causes of differential hydrogen evolution in a set of polymers, isolating that solvation effects were likely to play a key role. In particular, that a polymer with preferential solvation in water was able to bring significantly more water around it and that this correlated with higher evolution rates. I was unable to conclusively rule out the impact of aggregation effects or the role of the co-catalyst.

5. Aggregation effects were studied by simulating pairs of oligomer and solvating. I found that some polymers had strong interactions as a result of their large dipoles and that this was enough to overcome the solvation forces.

6. I went on to study the chemical reaction pathway of the hydrogen evolution and using DFT was able to isolate the reason that a higher concentration of water in the local area of the polymer led to high rates of hydrogen evolution. This was due to the water raising the polarity of the medium and thus acting to stablise the charge separation reaction.

7. I built a structure for testing the likely performance of organic polymers that used a mixture of MD and DFT to predict performance for a potential screening method.

8.2 Future Work

The work outlined in this thesis has also stimulated and opened up a number of exciting avenues that could be explored in the future. In this section we outline some of them.

- With a good metric for phase segregation it would be possible to produce a full ternary phase diagram of the reaction mixture: water:methanol:TEA. This would allow predictions of what proportions of each of them would lead to phase segregation. Given that

the results of this work suggest that the amount of water in local environment is key, it opens up the possibility that optimisation of the ratio could improve performance.

- We have made a start to the consideration of the formation of β-phase in solution but a full treatment of it should include both the planarisation effect, which we have studied here, and the aggregation effects. The aggregation effect could be studied using a technique known as the potential of mean force (PMF). This is where the distance between two oligomers is fixed at different values before simulations are run and an average force is found. This would allow us to see if planarising first before aggregating was more or less favourable than aggregating before planarising. With this approach one could then study the impact of solvent (or solvent mixtures), sidechain, and temperature.

- In the case of the polymer photocatalyst the use of the PMF technique could once again allow us to definitively categorise the difference in likely aggregation behaviour which impacts on the overall performance of the system.

- For predicting the performance of the photocatalyst we have relied on both MD and DFT. MD is a time intensive procedure in terms of both computational and human effort, relying on the parameterisation of the force field for a particular polymer as well as the simulations themselves. If we are to isolate an effective screening method, finding a way of determining or estimating the likely local environment using only DFT calculations would allow a fast way of searching in a wide chemical phase space. One way of doing this would be using free energy of solvations, calculated from DFT, and a simple physics model to estimate a volume fraction of each solvent. This would involve a number of assumptions including that B3LYP (or another chosen functional) is sufficiently accurate.

- With a procedure in place for examining the chemical reaction of water splitting with TEA, we could also apply the same methodology to much more complicated whole-water spliting reactions or to the oxygen evolution side of the reaction.

- Finally, we know that the choice of SED is very important and often a neglected part of study in the field. We could utilise a convenient similarity of reaction pathway between two commonly used SEDs. Triethanolamine (TEOA) is often used, and is known to follow a similar reaction pathway, shown in Figure 8.1, as TEA. TEOA is soluble with water and as such does not require methanol as a mixing agent. It was found to, on the whole, perform worse than TEA for our systems and as such would make an excellent test case for the methodology.

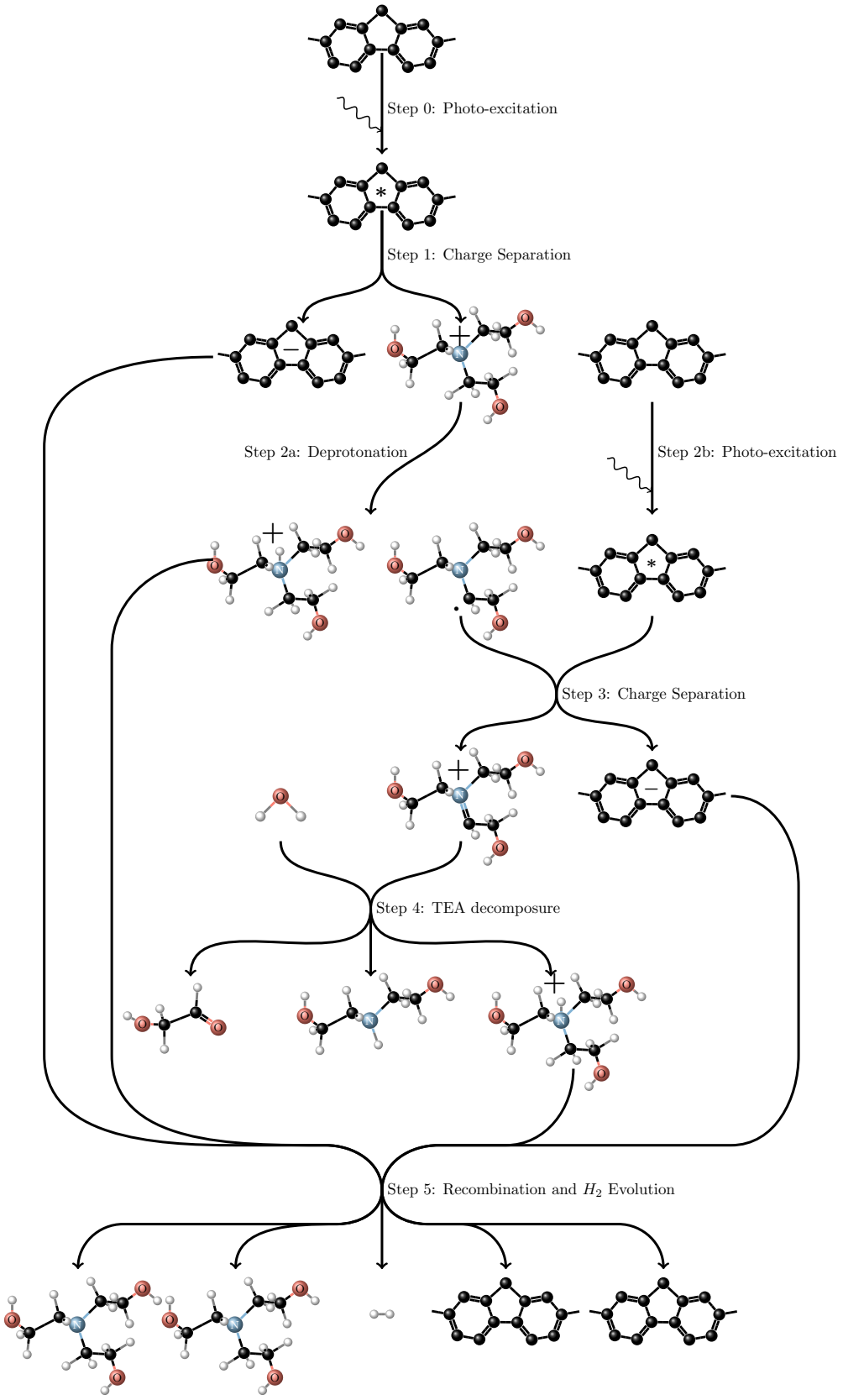


Figure 8.1: This figure shows the main reaction pathway for hydrogen evolution when Triethanolamine (TEOA) is used as the SED. The pathway is almost identical to that of the main SED of study in this work, TEA. It should be noted that there is an additional dead-end step not shown here that may limit performance.

[1] Giulia Tregnago. *Photophysics and applications of organic semiconductors*. PhD thesis, 2015.

[2] S. Himmelberger and A. Salleo. Engineering semiconducting polymers for efficient charge transport. *MRS Communications*, 5(3):383–395, 2015.

[3] J. P. Perdew. Jacob's ladder of density functional approximations for the exchange-correlation energy. In *AIP Conference Proceedings*, volume 577, pp. 1–20. AIP, 2001.

[4] R. C. Rizzo and W. L. Jorgensen. OPLS all-atom model for amines: Resolution of the amine hydration problem. *Journal of the American Chemical Society*, 121(20):4827–4836, may 1999.

[5] W. L. Jorgensen and J. D. Madura. Temperature and size dependence for monte carlo simulations of TIP4P water. *Molecular Physics*, 56(6):1381–1392, dec 1985.

[6] C. Caleman et al. Force field benchmark of organic liquids: Density, enthalpy of vaporization, heat capacities, surface tension, isothermal compressibility, volumetric expansion coefficient, and dielectric constant. *Journal of Chemical Theory and Computation*, 8(1):61–74, 2012.

[7] W. L. Jorgensen, D. S. Maxwell and J. Tirado-Rives. Development and testing of the OPLS all-atom force field on conformational energetics and properties of organic liquids. *Journal of the American Chemical Society*, 118(45):11225–11236, jan 1996.

[8] D. Eisenberg and W. Kauzmann. *The Structure and Properties of Water*, volume 9780198570. 2007.

[9] A. K. Adya, L. Bianchi and C. J. Wormald. The structure of liquid methanol by H/D substitution technique of neutron diffraction. *Journal of Chemical Physics*, 112(9):4231–4241, 2000.

[10] H. Bertagnolli and P. Chieux. The complete set of atom pair correlation functions of liquid chloroform as obtained from a final neutron scattering experiment with H/D isotopic substitution. *Molecular Physics*, 51:617–631, 1984.

[11] X. Shi. Unpublished Data. 2017.

[12] A. S. Gertsen, S. Xingyuan, J. Nelson and J. W. Andreasen. Provisionally titled: The mechanism of charge transport in a stiff conjugated polymer. *Manuscript in Preparation*, 2019.

[13] X. Wang et al. Sulfone-containing covalent organic frameworks for photocatalytic hydrogen evolution from water. *Nature Chemistry*, 10(12):1180–1189, 2018.

[14] M. Sachs et al. Understanding structure-activity relationships in linear polymer photocatalysts for hydrogen evolution. *Nature Communications*, 9(1):1–11, 2018.

[15] J. E. Sipe and R. W. Boyd. Nonlinear susceptibility of composite optical materials in the Maxwell Garnett model. *Physical Review A*, 46(3):1614–1629, aug 1992.

[16] S. M. Puranik, A. C. Kumbharkhane and S. C. Mehrotra. The static permittivity of binary mixtures using an improved bruggeman model. *Journal of Molecular Liquids*, 59(2-3):173–177, mar 1994.

[17] H. Flyvbjerg and H. G. Petersen. Error estimates on averages of correlated data. *The Journal of Chemical Physics*, 91(1):461–466, jul 1989.

[18] R. W. Brown and P. N. Stearns. The Industrial Revolution in World History, 2006.

[19] H. D. Jong. Global Handbook of Quality of Life. *Global Handbook of Quality of Life*, (2012):45–74, 2015.

[20] D. Moralee. *The Microelectronics Revolution*, volume 27. {MIT} press, 2010.

[21] B. Hevly, E. Braun and S. Macdonald. *Revolution in Miniature: The History and Impact of Semiconductor Electronics*, volume 25. Cambridge University Press, 2006.

[22] J. Mokyr. Is There Still Life in the Pessimist Case? Consumption during the Industrial Revolution, 1790-1850. *The Journal of Economic History*, 48(1):69–92, 1988.

[23] M. A. Cole and R. J. R. Elliott. Industrial Characteristics , Environmental Regulations and Air Pollution in a Developing Country : An Analysis of the Chinese Manufacturing Sector. 50(1):1–32.

[24] B. Clapp. *Environmental History of Britain since the Industrial Revolution, An*. Routledge, 2017.

[25] J.-P. Candelone, S. Hong, C. Pellone and C. F. Boutron. Post-Industrial Revolution changes in large-scale atmospheric pollution of the northern hemisphere by heavy metals as documented in central Greenland snow and ice. *Journal of Geophysical Research*, 100(D8):16605, 2004.

[26] M. A. Deboer and K. Lammertsma. Scarcity of rare earth elements. *ChemSusChem*, 6(11):2045–2055, 2013.

[27] J. Schipper et al. The status of the world's land and marine mammals: diversity, threat, and knowledge. *Science*, 322(5899):225–230, 2008.

[28] N. Chomksy and L. Polk. *Nuclear War and Environmental Catastrophe*. Seven Stories Press.

[29] IPCC 2013. *Summary for Policymakers*, volume 1542. Cambridge University Press, 2013.

[30] T. A. Boden, G. Marland and R. J. Andres. Global, regional, and national fossil-fuel CO2 emissions. *Carbon Dioxide Information Analysis Center, Oak Ridge National Laboratory, US Department of Energy, Oak Ridge, Tenn., USA doi*, 10:505–584, 2009.

[31] A. Malik, J. Lan and M. Lenzen. Trends in Global Greenhouse Gas Emissions from 1990 to 2010. *Environmental Science and Technology*, 50(9):4722–4730, 2016.

[32] W. Liu, J. Lu and S. P. Xie. Understanding the Indian Ocean response to double CO2 forcing in a coupled model. *Ocean Dynamics*, 65(7):1037–1046, 2015.

[33] K. Riahi et al. The Shared Socioeconomic Pathways and their energy, land use, and greenhouse gas emissions implications: An overview. *Global Environmental Change*, 42:153–168, 2017.

[34] S. Hatfield-Dodds et al. Assessing global resource use and greenhouse emissions to 2050, with ambitious resource efficiency and climate mitigation policies. *Journal of Cleaner Production*, 144:403–414, 2017.

[35] A. J. Bebbington et al. Resource extraction and infrastructure threaten forest cover and community rights. *Proceedings of the National Academy of Sciences*, 115(52):13164–13173, 2018.

[36] M. Hulme. 1.5 ÂřC and climate research after the Paris Agreement. *Nature Climate Change*, 6(3):222–224, 2016.

[37] F. Tancini et al. 1,1-Dicyano-4-[4-(diethylamino)phenyl]buta-1,3-dienes: Structure-property relationships. *European Journal of Organic Chemistry*, (14):2756–2765, 2012.

[38] R. Lacal Arantegui and A. Jäger-Waldau. Photovoltaics and wind status in the European Union after the Paris Agreement. *Renewable and Sustainable Energy Reviews*, 81(December 2016):2460–2471, 2018.

[39] E. Kabir, P. Kumar, S. Kumar, A. A. Adelodun and K. H. Kim. Solar energy: Potential and future prospects. *Renewable and Sustainable Energy Reviews*, 82(August 2017):894–900, 2018.

[40] K. Ullah et al. The insight views of advanced technologies and its application in bio-origin fuel synthesis from lignocellulose biomasses waste, a review. *Renewable and Sustainable Energy Reviews*, 82(August 2017):3992–4008, 2018.

[41] Z. Li, C. Han and T. Gu. Economics of biomass gasification: A review of the current status. *Energy Sources, Part B: Economics, Planning and Policy*, 13(2):137–140, 2018.

[42] Y. Yang, S. Bremner, C. Menictas and M. Kay. Battery energy storage system size determination in renewable energy systems: A review. *Renewable and Sustainable Energy Reviews*, 91(March):109–125, 2018.

[43] C. Zhang, Y. L. Wei, P. F. Cao and M. C. Lin. Energy storage system: Current studies on batteries and power condition system. *Renewable and Sustainable Energy Reviews*, 82(December 2016):3091–3106, 2018.

[44] M. Faisal et al. Review of energy storage system technologies in microgrid applications: Issues and challenges. *IEEE Access*, 6:35143–35164, 2018.

[45] Y. Chen, P. Xu, J. Gu, F. Schmidt and W. Li. Measures to improve energy demand flexibility in buildings for demand response (DR): A review. *Energy and Buildings*, 177:125–139, 2018.

[46] M. Uddin et al. A review on peak load shaving strategies. *Renewable and Sustainable Energy Reviews*, 82(February 2017):3323–3332, 2018.

[47] S. K. Hoekman and A. Broch. Environmental implications of higher ethanol production and use in the U.S.: A literature review. Part II-Biodiversity, land use change, GHG emissions, and sustainability. *Renewable and Sustainable Energy Reviews*, 81(June 2017):3159–3177, 2018.

[48] R. Herrmann, C. Jumbe, M. Bruentrup and E. Osabuohien. Competition between biofuel feedstock and food production: Empirical evidence from sugarcane outgrower settings in Malawi. *Biomass and Bioenergy*, 114:100–111, 2018.

[49] P. P. Edwards, V. L. Kuznetsov, W. I. F. David and N. P. Brandon. Hydrogen and fuel cells: Towards a sustainable energy future. *Energy Policy*, 36(12):4356–4362, 2008.

[50] Y. Bicer and I. Dincer. Clean fuel options with hydrogen for sea transportation: A life cycle approach. *International Journal of Hydrogen Energy*, 43(2):1179–1193, 2018.

[51] G. W. Crabtree and M. S. Dresselhaus. The Hydrogen Fuel Alternative. *MRS Bulletin*, (April 2008):421–429, 2019.

[52] S. Belz. A synergetic use of hydrogen and fuel cells in human spaceflight power systems. *Acta Astronautica*, 121:323–331, 2016.

[53] C. Winnefeld, T. Kadyk, B. Bensmann, U. Krewer and R. Hanke-Rauschenbach. Modelling and designing cryogenic hydrogen tanks for future aircraft applications. *Energies*, 11(1):1–23, 2018.

[54] F. Zhang, P. Zhao, M. Niu and J. Maddy. The survey of key technologies in hydrogen energy storage. *International Journal of Hydrogen Energy*, 41(33):14535–14552, 2016.

[55] S. R. Forrest and M. E. Thompson. Introduction: Organic Electronics and Optoelectronics. *Chemical Reviews*, 107(4):923–925, 2007.

[56] N. Thejo Kalyani and S. J. Dhoble. Organic light emitting diodes: Energy saving lighting technology - A review. *Renewable and Sustainable Energy Reviews*, 16(5):2696–2723, 2012.

[57] V. C. Bender, T. B. Marchesan and J. M. Alonso. Solid-State Lighting: A Concise Review of the State of the Art on LED and OLED Modeling. *IEEE Industrial Electronics Magazine*, 9(2):6–16, 2015.

[58] X. Guo, M. Baumgarten and K. Müllen. Designing π-conjugated polymers for organic electronics. *Progress in Polymer Science*, 38(12):1832–1908, 2013.

[59] Y. Yamashita. Organic semiconductors for organic field-effect transistors. *Science and Technology of Advanced Materials*, 10(2):24313, 2009.

[60] H. Sirringhaus. 25th anniversary article: Organic field-effect transistors: The path beyond amorphous silicon. *Advanced Materials*, 26(9):1319–1335, 2014.

[61] R. R. Søndergaard, M. Hösel and F. C. Krebs. Roll-to-Roll fabrication of large area functional organic materials. *Journal of Polymer Science, Part B: Polymer Physics*, 51(1):16–34, 2013.

[62] M. Ni, M. K. Leung, D. Y. Leung and K. Sumathy. A review and recent developments in photocatalytic water-splitting using TiO2 for hydrogen production. *Renewable and Sustainable Energy Reviews*, 11(3):401–425, 2007.

[63] M. G. Walter et al. Solar Water Splitting Cells. *Chemical Reviews*, 110(11):6446–6473, 2010.

[64] M. Irimia-Vladu, E. D. Głowacki, G. Voss, S. Bauer and N. S. Sariciftci. Green and biodegradable electronics. *Materials Today*, 15(7-8):340–346, 2012.

[65] Y. Zhang et al. Probing Carrier Transport and Structure-Property Relationship of Highly Ordered Organic Semiconductors at the Two-Dimensional Limit. *Physical Review Letters*, 116(1):1–6, 2016.

[66] P. Meredith, C. J. Bettinger, M. Irimia-Vladu, A. B. Mostert and P. E. Schwenn. Electronic and optoelectronic materials and devices inspired by nature. *Reports on Progress in Physics*, 76(3):34501, 2013.

[67] A. Gooneie, S. Schuschnigg and C. Holzer. A review of multiscale computational methods in polymeric materials. *Polymers*, 9(1), 2017.

[68] D. Andrienko. Modeling of phosphorescent organic light emitting diodes: from molecular to device properties (Conference Presentation). pp. 13, 2018.

[69] M. Irimia-Vladu. "Green" electronics: Biodegradable and biocompatible materials and devices for sustainable future. *Chemical Society Reviews*, 43(2):588–610, 2014.

[70] M. Chen et al. Intrinsic charge carrier mobility in single-crystal OFET by "fast trapping vs. slow detrapping" model. *Organic Electronics: physics, materials, applications*, 54(December 2017):237–244, 2018.

[71] S. G. Surya et al. Organic field effect transistors (OFETs) in environmental sensing and health monitoring: A review. *TrAC - Trends in Analytical Chemistry*, 111:27–36, 2019.

[72] R. Xue, J. Zhang, Y. Li and Y. Li. Organic Solar Cell Materials toward Commercialization. *Small*, 14(41):1–24, 2018.

[73] W. Lee et al. *Stimuli-responsive switchable organic-inorganic nanocomposite materials*, volume 23. Elsevier Ltd, 2018.

[74] M. E. Ragoussi and T. Torres. Organic photovoltaics. *Revista Virtual de Quimica*, 7(1):112–125, 2015.

[75] Y. Yang and F. Wudl. Organic Electronics: From Materials to Devices. *Advanced Materials*, 21(14-15):1401–1403, 2009.

[76] R. Noriega, A. Salleo and A. J. Spakowitz. Chain conformations dictate multiscale charge transport phenomena in disordered semiconducting polymers. *Proceedings of the National Academy of Sciences*, 110(41):16315–16320, 2013.

[77] M. S. Vezie et al. Exploring the origin of high optical absorption in conjugated polymers. *Nature Materials*, 15(7):746–753, 2016.

[78] F. M. Veronese and G. Pasut. PEGylation, successful approach to drug delivery, 2005.

[79] V. G. Kadajji and G. V. Betageri. Water soluble polymers for pharmaceutical applications, 2011.

[80] L. Vaisman, G. Marom and H. D. Wagner. Dispersions of surface-modified carbon nanotubes in water-soluble and water-insoluble polymers. *Advanced Functional Materials*, 16(3):357–363, 2006.

[81] T. Förster. *Electronic Absorption Spectra and Geometry of Organic Molecules*, volume 72. 2011.

[82] A. A. Bakulin et al. The role of driving energy and delocalized states for charge separation in organic semiconductors. *Science*, 335(6074):1340–1344, 2012.

[83] W. Chang et al. Spin-dependent charge transfer state design rules in organic photovoltaics. *Nature Communications*, 6:1–6, 2015.

[84] I. Kang, H. J. Yun, D. S. Chung, S. K. Kwon and Y. H. Kim. Record high hole mobility in polymer semiconductors via side-chain engineering. *Journal of the American Chemical Society*, 135(40):14896–14899, 2013.

[85] H. Yan et al. A high-mobility electron-transporting polymer for printed transistors. *Nature*, 457(7230):679–686, 2009.

[86] H. Li, F. S. Kim, G. Ren and S. A. Jenekhe. High-mobility n-type conjugated polymers based on electron-deficient tetraazabenzodifluoranthene diimide for organic electronics. *Journal of the American Chemical Society*, 135(40):14920–14923, 2013.

[87] J. Mei, D. H. Kim, A. L. Ayzner, M. F. Toney and Z. Bao. Siloxane-terminated solubilizing side chains: Bringing conjugated polymer backbones closer and boosting hole mobilities in thin-film transistors. *Journal of the American Chemical Society*, 133(50):20130–20133, 2011.

[88] C. B. Nielsen, M. Turbiez and I. McCulloch. Recent advances in the development of semiconducting DPP-containing polymers for transistor applications. *Advanced Materials*, 25(13):1859–1880, 2013.

[89] T. Liu and A. Troisi. Understanding the microscopic origin of the very high charge mobility in PBTTT: Tolerance of thermal disorder. *Advanced Functional Materials*, 24(7):925–933, 2014.

[90] D. T. Duong, M. F. Toney and A. Salleo. Role of confinement and aggregation in charge transport in semicrystalline polythiophene thin films. *Physical Review B - Condensed Matter and Materials Physics*, 86(20):1–5, 2012.

[91] A. Zen et al. Effect of molecular weight and annealing of poly(3-hexylthiophene)s on the performance of organic field-effect transistors. *Advanced Functional Materials*, 14(8):757–764, 2004.

[92] W. Li et al. Controlling molecular weight of a high efficiency donor-acceptor conjugated polymer and understanding its significant impact on photovoltaic properties. *Advanced Materials*, 26(26):4456–4462, 2014.

[93] A. Perevedentsev, P. N. Stavrinou, D. D. C. Bradley and P. Smith. Solution-crystallization and related phenomena in 9,9-dialkyl-fluorene polymers. I. Crystalline polymer-solvent compound formation for poly(9,9-dioctylfluorene). *Journal of Polymer Science, Part B: Polymer Physics*, 53(21):1481–1491, 2015.

[94] M. Grell, D. D. C. Bradley, M. Inbasekaran and E. P. Woo. A glass-Forming conjugated main-chain liquid crystal polymer for polarized electroluminescence applications. *Advanced Materials*, 9(10):798–802, 1997.

[95] M. Redecker, D. D. C. Bradley, M. Inbasekaran and E. P. Woo. Mobility enhancement through homogeneous nematic alignment of a liquid-crystalline polyfluorene. *Applied Physics Letters*, 74(10):1400–1402, 1999.

[96] A. Babel and S. A. Jenekhe. Charge carrier mobility in blends of poly(9,9-dioctylfluorene) and poly(3-hexylthiophene). *Macromolecules*, 36(20):7759–7764, 2003.

[97] P. Prins et al. Enhanced charge-carrier mobility in beta-phase polyfluorene. *Physical Review B*, 74(11):113203, sep 2006.

[98] H. H. Lu, C. Y. Liu, C. H. Chang and S. A. Chen. Self-dopant formation in poly(9,9-di-n-octylfluorene) via a dipping method for efficient and stable pure-blue electroluminescence. *Advanced Materials*, 19(18):2574–2579, 2007.

[99] M. G. Ramírez, M. A. Díaz-García and F. Montilla. Optimization of the Electrochemically Generated Luminescence of Polyfluorene Films. *Journal of Physical Chemistry C*, 122(6):3608–3616, 2018.

[100] A. J. Cadby et al. Film morphology and photophysics of polyfluorene. *Physical Review B - Condensed Matter and Materials Physics*, 62(23):15604–15609, 2000.

[101] W. Xue et al. Exploring side-chain length effect on beta-phase of polyfluorene derivatives in electrospinning and their optical behavior. *Polymer*, 153:338–343, 2018.

[102] H. J. Eggimann, F. Le Roux and L. M. Herz. How beta-Phase Content Moderates Chain-conjugation and Energy Transfer in Polyfluorene Films. *The Journal of Physical Chemistry Letters*, pp. acs.jpclett.9b00483, 2019.

[103] C. Wu and J. McNeill. Swelling-controlled polymer phase and fluorescence properties of polyfluorene nanoparticles. *Langmuir*, 24(11):5855–5861, 2008.

[104] D. W. Bright, F. B. Dias, F. Galbrecht, U. Scherf and A. P. Monkman. The influence of alkyl-chain length on beta-phase formation in polyfluorenes. *Advanced Functional Materials*, 19(1):67–73, 2009.

[105] G. Wang et al. Hydrogen-treated TiO2 nanowire arrays for photoelectrochemical water splitting. *Nano Letters*, 11(7):3026–3033, 2011.

[106] C. Y. Liu and S. A. Chen. Charge mobility and charge traps in conjugated polymers. *Macromolecular Rapid Communications*, 28(17):1743–1760, 2007.

[107] A. Fujishima and K. Honda. Electrochemical photolysis of water at a semiconductor electrode. *Nature*, 238(5358):37–38, 1972.

[108] Z. Wang, C. Li and K. Domen. Recent developments in heterogeneous photocatalysts for solar-driven overall water splitting. *Chemical Society Reviews*, 2018.

[109] P. V. Kamat and S. Jin. Semiconductor Photocatalysis: "Tell Us the Complete Story!". *ACS Energy Letters*, 3(3):622–623, 2018.

[110] K. Schwinghammer, S. Hug, M. B. Mesch, J. Senker and B. V. Lotsch. Phenyl-triazine oligomers for light-driven hydrogen evolution. *Energy and Environmental Science*, 8(11):3345–3353, 2015.

[111] L. Stegbauer, K. Schwinghammer and B. V. Lotsch. A hydrazone-based covalent organic framework for photocatalytic hydrogen production. *Chemical Science*, 5(7):2789–2793, 2014.

[112] K. Schwinghammer et al. Triazine-based carbon nitrides for visible-light-driven hydrogen evolution. *Angewandte Chemie - International Edition*, 52(9):2435–2439, 2013.

[113] W. Jones et al. A comparison of photocatalytic reforming reactions of methanol and triethanolamine with Pd supported on titania and graphitic carbon nitride. *Applied Catalysis B: Environmental*, 240:373–379, 2019.

[114] Y. Lai, J. Gong and C. Lin. Self-organized TiO2 nanotube arrays with uniform platinum nanoparticles for highly efficient water splitting. *International Journal of Hydrogen Energy*, 37(8):6438–6446, 2012.

[115] V. S. Vyas and B. V. Lotsch. Materials chemistry: Organic polymers form fuel from water, 2015.

[116] A. Kudo. New materials for photocatalytic and photoelectrochemical water splitting. In *AIP Conference Proceedings*, volume 1568, pp. 7–10, 2013.

[117] Y. Kwon, A. Soon, H. Han and H. Lee. Shape effects of cuprous oxide particles on stability in water and photocatalytic water splitting. *Journal of Materials Chemistry A*, 3(1):156–162, 2015.

[118] J. Joy, J. Mathew and S. C. George. Nanomaterials for photoelectrochemical water splitting-review, 2018.

[119] A. Fujishima, T. N. Rao and D. A. Tryk. Titanium dioxide photocatalysis, 2000.

[120] K. Nakata and A. Fujishima. TiO 2 photocatalysis: Design and applications, 2012.

[121] R. Asahi, T. Morikawa, T. Ohwaki, K. Aoki and Y. Taga. Visible-Light Photocatalysis in Nitrogen-Doped Titanium Oxides: books, journal articles and other publications in one search. *Science*, 293(5528):269–271, 2001.

[122] A. A. Ismail. Mesoporous PdO-TiO 2 nanocomposites with enhanced photocatalytic activity. *Applied Catalysis B: Environmental*, 117-118:67–72, 2012.

[123] N. R. Khalid et al. Graphene modified Nd/TiO2 photocatalyst for methyl orange degradation under visible light irradiation. *Ceramics International*, 39(4):3569–3575, 2013.

[124] G. L. Chiarello, M. H. Aguirre and E. Selli. Hydrogen production by photocatalytic steam reforming of methanol on noble metal-modified TiO2. *Journal of Catalysis*, 273(2):182–190, 2010.

[125] X. Wang et al. A metal-free polymeric photocatalyst for hydrogen production from water under visible light. *Nature materials*, 8(1):76–80, 2009.

[126] X. Wang et al. A metal-free polymeric photocatalyst for hydrogen production from water under visible light. *Nature materials*, 8(1):76–80, 2009.

[127] W. J. Ong, L. L. Tan, Y. H. Ng, S. T. Yong and S. P. Chai. Graphitic Carbon Nitride (g-C3N4)-Based Photocatalysts for Artificial Photosynthesis and Environmental Remediation: Are We a Step Closer to Achieving Sustainability?, 2016.

[128] J. Wen, J. Xie, X. Chen and X. Li. A review on g-C3N4 -based photocatalysts. *Applied Surface Science*, 391:72–123, 2017.

[129] M. Schröder et al. Hydrogen Evolution Reaction in a Large-Scale Reactor using a Carbon Nitride Photocatalyst under Natural Sunlight Irradiation. *Energy Technology*, 3(10):1014–1017, 2015.

[130] Z. Huang, F. Li, B. Chen and G. Yuan. Porous and low-defected graphitic carbon nitride nanotubes for efficient hydrogen evolution under visible light irradiation. *RSC Advances*, 5(124):102700–102706, 2015.

[131] L. Wang et al. Conjugated Microporous Polymer Nanosheets for Overall Water Splitting Using Visible Light. *Advanced Materials*, 29(38), 2017.

[132] X. Jiang, P. Wang and J. Zhao. 2D covalent triazine framework: A new class of organic photocatalyst for water splitting. *Journal of Materials Chemistry A*, 3(15):7750–7758, 2015.

[133] L. Wang et al. Conjugated Microporous Polymer Nanosheets for Overall Water Splitting Using Visible Light. *Advanced Materials*, 29(38):1–8, 2017.

[134] R. S. Sprick et al. Tunable organic photocatalysts for visible-light-driven hydrogen evolution. *Journal of the American Chemical Society*, 137(9):3265–3270, 2015.

[135] T. Shibata et al. Novel visible-light-driven photocatalyst. Poly(p-phenylene)-catalyzed photoreductions of water, carbonyl compounds, and olefins. *Journal of Physical Chemistry*, 94(5):2068–2076, 1990.

[136] S. Matsuoka, T. Kohzuki, A. Nakamura, C. Pac and S. Yanagida. Efficient visible-light-driven photocatalysis. Poly(pyridine-2,5-diyl)- catalysed hydrogen photoevolution and photoreduction of carbonyl compounds. *Journal of the Chemical Society, Chemical Communications*, (8):580–581, 1991.

[137] O. Winther-Jensen, B. Winther-Jensen and D. R. MacFarlane. Photostimulated electrocatalysis of water oxidation by conjugated polymers. *Electrochemistry Communications*, 13(4):307–309, 2011.

[138] X. Wang et al. Sulfone-containing covalent organic frameworks for photocatalytic hydrogen evolution from water. *Nature Chemistry*, 10(12):1180–1189, 2018.

[139] J. Kosco and I. McCulloch. Residual pd enables photocatalytic h_2 evolution from conjugated polymers. *ACS Energy Letters*, 3(11):2846–2850, 2018.

[140] J. C. Slater. The theory of complex spectra. *Physical Review*, 34(10):1293–1322, 1929.

[141] K. B. Lipkowitz. *Reviews in Computational Chemistry*. Reviews in Computational Chemistry. John Wiley & Sons, Inc., Hoboken, NJ, USA, jun 2007.

[142] W. Li, Z. Ni and S. Li. Cluster-in-molecule local correlation method for post-Hartree-Fock calculations of large systems. *Molecular Physics*, 114(9):1447–1460, may 2016.

[143] M. Schütz, G. Hetzer and H.-J. Werner. Low-order scaling local electron correlation methods. I. Linear scaling local MP2. *The Journal of Chemical Physics*, 111(13):5691–5705, oct 1999.

[144] G. E. Scuseria and P. Y. Ayala. Linear scaling coupled cluster and perturbation theories in the atomic orbital basis. *The Journal of Chemical Physics*, 111(18):8330–8343, nov 1999.

[145] C. Riplinger and F. Neese. An efficient and near linear scaling pair natural orbital based local coupled cluster method. *The Journal of Chemical Physics*, 138(3):034106, jan 2013.

[146] P. Hohenberg and W. Kohn. Inhomogeneous electron gas. *Physical Review*, 136(3B):391–402, 1964.

[147] W. Kohn and L. J. Sham. Self-consistent equations including exchange and correlation effects. *Physical Review*, 140(4A), 1965.

[148] M. Levy. Universal variational functionals of electron densities, first-order density matrices, and natural spin-orbitals and solution of the v-representability problem (Hohenberg-Kohn/Hartree-Fock/geminals/exchange-correlation). *Physics*, 76(12):6062–6065, 1979.

[149] G. Vignale and M. Rasolt. Density-functional theory in strong magnetic fields. *Physical Review Letters*, 59(20):2360–2363, 1987.

[150] W. Koch and M. C. Holthausen. *A Chemist's Guide to Density Functional Theory*. Wiley-VCH Verlag GmbH, Weinheim, FRG, jul 2001.

[151] N. Harrison and A. Cornelius. *Electronic structure*, volume 61. Cambridge University Press, Cambridge, 2000.

[152] G. L. Estiu. *Electrode catalysis versus enzyme catalysis: Theoretical modeling of a biological enzyme*. John Wiley & Sons, Inc., Hoboken, NJ, USA, mar 2010.

[153] R. O. Jones. Density functional theory: Its origins, rise to prominence, and future. *Reviews of Modern Physics*, 87(3), 2015.

[154] L. H. Thomas. The calculation of atomic fields. *Mathematical Proceedings of the Cambridge Philosophical Society*, 23(05):542, jan 2008.

[155] E. Teller. On the stability of molecules in the Thomas-Fermi theory. *Reviews of Modern Physics*, 34(4):627–631, oct 1962.

[156] E. H. Lieb and B. Simon. The Thomas-Fermi theory of atoms, molecules and solids. *Advances in Mathematics*, 23(1):22–116, 1977.

[157] K. Burke and L. O. Wagner. DFT in a nutshell. *International Journal of Quantum Chemistry*, 113(2):96–101, jan 2013.

[158] U. Jitropas and C. H. Hsu. Study of the first-principles correlation functional in the calculation of silicon phonon dispersion curves. *Japanese Journal of Applied Physics*, 56(7):070313, jul 2017.

[159] J. P. Perdew et al. Prescription for the design and selection of density functional approximations: More constraint satisfaction with fewer fits. *Journal of Chemical Physics*, 123(6):062201, aug 2005.

[160] J. P. Perdew and A. Zunger. Self-interaction correction to density-functional approximations for many-electron systems. *Physical Review B*, 23(10):5048–5079, may 1981.

[161] A. D. Becke. Perspective: Fifty years of density-functional theory in chemical physics. *Journal of Chemical Physics*, 140(18):18A301, may 2014.

[162] M. G. Medvedev, I. S. Bushmarinov, J. Sun, J. P. Perdew and K. A. Lyssenko. Density functional theory is straying from the path toward the exact functional. *Science*, 355(6320):49–52, jan 2017.

[163] C. Lee, W. Yang and R. G. Parr. Development of the Colle-Salvetti correlation-energy formula into a functional of the electron density. *Physical Review B*, 37(2):785–789, jan 1988.

[164] J. P. Perdew, K. Burke and M. Ernzerhof. Generalized Gradient Approximation Made Simple. *Physical Review Letters*, 77(18):3865–3868, oct 1996.

[165] Y. Zhao and D. G. Truhlar. A new local density functional for main-group thermochemistry, transition metal bonding, thermochemical kinetics, and noncovalent interactions. *The Journal of Chemical Physics*, 125(19):194101, nov 2006.

[166] J. Tao, J. P. Perdew, V. N. Staroverov and G. E. Scuseria. Climbing the Density Functional Ladder: Nonempirical Meta-Generalized Gradient Approximation Designed for Molecules and Solids. *Physical Review Letters*, 91(14):146401, sep 2003.

[167] A. D. Becke. Density-functional thermochemistry. III. The role of exact exchange. *The Journal of Chemical Physics*, 98(7):5648–5652, apr 1993.

[168] S. H. Vosko, L. Wilk and M. Nusair. Accurate spin-dependent electron liquid correlation energies for local spin density calculations: a critical analysis. *Canadian Journal of Physics*, 58(8):1200–1211, aug 1980.

[169] P. J. Stephens, F. J. Devlin, C. F. Chabalowski and M. J. Frisch. Ab Initio Calculation of Vibrational Absorption and Circular Dichroism Spectra Using Density Functional Force Fields. *The Journal of Physical Chemistry*, 98(45):11623–11627, nov 1994.

[170] J. D. Chai and M. Head-Gordon. Systematic optimization of long-range corrected hybrid density functionals. *Journal of Chemical Physics*, 128(8), 2008.

[171] J. D. Chai and M. Head-Gordon. Long-range corrected hybrid density functionals with damped atom-atom dispersion corrections. *Physical Chemistry Chemical Physics*, 10(44):6615–6620, 2008.

[172] U. Salzner. Electronic structure of conducting organic polymers: insights from time-dependent density functional theory. *Wiley Interdisciplinary Reviews: Computational Molecular Science*, 4(6):601–622, 2014.

[173] Y. Zhao and D. G. Truhlar. Density functional for spectroscopy: No long-range self-interaction error, good performance for Rydberg and charge-transfer states, and better performance on average than B3LYP for ground states. *Journal of Physical Chemistry A*, 110(49):13126–13130, 2006.

[174] Y. Zhao and D. G. Truhlar. Comparative DFT study of van der Waals complexes: Rare-gas dimers, alkaline-earth dimers, zinc dimer and zinc-rare-gas dimers. *Journal of Physical Chemistry A*, 110(15):5121–5129, apr 2006.

[175] Y. Zhao and D. G. Truhlar. The M06 suite of density functionals for main group thermochemistry, thermochemical kinetics, noncovalent interactions, excited states, and transition elements: Two new functionals and systematic testing of four M06-class functionals and 12 other function. *Theoretical Chemistry Accounts*, 120(1-3):215–241, may 2008.

[176] M. Walker, A. J. Harvey, A. Sen and C. E. Dessent. Performance of M06, M06-2X, and M06-HF density functionals for conformationally flexible anionic clusters: M06 functionals perform better than B3LYP for a model system with dispersion and ionic hydrogen-bonding interactions. *Journal of Physical Chemistry A*, 117(47):12590–12600, nov 2013.

[177] R. Ditchfield, W. J. Hehre and J. A. Pople. Self-Consistent Molecular-Orbital Methods. IX. An Extended Gaussian-Type Basis for Molecular-Orbital Studies of Organic Molecules. *The Journal of Chemical Physics*, 54(2):724–728, jan 2004.

[178] K. A. Peterson and T. H. Dunning. Accurate correlation consistent basis sets for molecular core-valence correlation effects: The second row atoms Al-Ar, and the first row atoms B-Ne revisited. *Journal of Chemical Physics*, 117(23):10548–10560, dec 2002.

[179] A. Karton, S. L. Waite and A. J. Page. Performance of DFT for C60 Isomerization Energies: A Noticeable Exception to Jacob's Ladder. *Journal of Physical Chemistry A*, 123(1):257–266, jan 2019.

[180] L. Goerigk and N. Mehta. A Trip to the Density Functional Theory Zoo: Warnings and Recommendations for the User. *Australian Journal of Chemistry*, 2019.

[181] M. Döntgen et al. Automated Discovery of Reaction Pathways, Rate Constants, and Transition States Using Reactive Molecular Dynamics Simulations. *Journal of Chemical Theory and Computation*, 11(6):2517–2524, 2015.

[182] T. T. Trinh, N. Meling, D. Bedeaux and S. Kjelstrup. Thermodynamic properties of hydrogen dissociation reaction from the small system method and reactive force field ReaxFF. *Chemical Physics Letters*, 672:128–132, mar 2017.

[183] W. L. Jorgensen and J. Tirado-Rives. The OPLS Potential Functions for Proteins. Energy Minimizations for Crystals of Cyclic Peptides and Crambin. *Journal of the American Chemical Society*, 110(6):1657–1666, mar 1988.

[184] C. I. Bayly et al. A Second Generation Force Field for the Simulation of Proteins, Nucleic Acids, and Organic Molecules. *Journal of the American Chemical Society*, 117(19):5179–5197, 1995.

[185] C. Oostenbrink, A. Villa, A. E. Mark and W. F. Van Gunsteren. A biomolecular force field based on the free enthalpy of hydration and solvation: The GROMOS force-field parameter sets 53A5 and 53A6. *Journal of Computational Chemistry*, 25(13):1656–1676, oct 2004.

[186] B. R. Brooks et al. CHARMM: A program for macromolecular energy, minimization, and dynamics calculations. *Journal of Computational Chemistry*, 4(2):187–217, 1983.

[187] A. D. MacKerell et al. All-atom empirical potential for molecular modeling and dynamics studies of proteins. *The journal of physical chemistry. B*, 102(18):3586–616, 1998.

[188] A. D. Mackerell, M. Feig and C. L. Brooks. Extending the treatment of backbone energetics in protein force fields: Limitations of gas-phase quantum mechanics in reproducing protein conformational distributions in molecular dynamics simulation. *Journal of Computational Chemistry*, 25(11):1400–1415, aug 2004.

[189] P. Robustelli, S. Piana and D. E. Shaw. Developing a molecular dynamics force field for both folded and disordered protein states. *Proceedings of the National Academy of Sciences*, 115(21):E4758–E4766, may 2018.

[190] S. Patel and C. L. Brooks. CHARMM fluctuating charge force field for proteins: I parameterization and application to bulk organic liquid simulations. *Journal of Computational Chemistry*, 25(1):1–15, jan 2004.

[191] C. R. Cioce, K. McLaughlin, J. L. Belof and B. Space. A polarizable and transferable PHAST N2 potential for use in materials simulation. *Journal of Chemical Theory and Computation*, 9(12):5550–5557, dec 2013.

[192] A. C. Van Duin, S. Dasgupta, F. Lorant and W. A. Goddard. ReaxFF: A reactive force field for hydrocarbons. *Journal of Physical Chemistry A*, 105(41):9396–9409, oct 2001.

[193] D. W. Hofmann, L. Kuleshova and B. D'Aguanno. A new reactive potential for the molecular dynamics simulation of liquid water. *Chemical Physics Letters*, 448(1-3):138–143, nov 2007.

[194] S. J. Marrink, H. J. Risselada, S. Yefimov, D. P. Tieleman and A. H. De Vries. The MARTINI force field: Coarse grained model for biomolecular simulations. *Journal of Physical Chemistry B*, 111(27):7812–7824, jul 2007.

[195] A. Korkut and W. A. Hendrickson. A force field for virtual atom molecular mechanics of proteins. *Proceedings of the National Academy of Sciences*, 106(37):15667–15672, sep 2009.

[196] D. C. Rapaport, R. L. Blumberg, S. R. McKay and W. Christian. *The Art of Molecular Dynamics Simulation*, volume 10. Cambridge University Press, Cambridge, 2013.

[197] W. C. Swope, H. C. Andersen, P. H. Berens and K. R. Wilson. A computer simulation method for the calculation of equilibrium constants for the formation of physical clusters of molecules: Application to small water clusters. *The Journal of Chemical Physics*, 76(1):637–649, jan 1982.

[198] A. Dullweber, B. Leimkuhler and R. McLachlan. Symplectic splitting methods for rigid body molecular dynamics. *Journal of Chemical Physics*, 107(15):5840–5851, oct 1997.

[199] S. O. Nielsen, C. F. Lopez, G. Srinivas and M. L. Klein. Coarse grain models and the computer simulation of soft materials. *Journal of Physics Condensed Matter*, 16(15), 2004.

[200] H. J. Berendsen, J. P. Postma, W. F. Van Gunsteren, A. Dinola and J. R. Haak. Molecular dynamics with coupling to an external bath. *The Journal of Chemical Physics*, 81(8):3684–3690, oct 1984.

[201] S. Nosé. A unified formulation of the constant temperature molecular dynamics methods. *The Journal of Chemical Physics*, 81(1):511–519, jul 1984.

[202] S. Jang and G. A. Voth. Simple reversible molecular dynamics algorithms for Nosé-Hoover chain dynamics. *Journal of Chemical Physics*, 107(22):9514–9526, 1997.

[203] M. Parrinello and A. Rahman. Crystal structure and pair potentials: A molecular-dynamics study. *Physical Review Letters*, 45(14):1196–1199, oct 1980.

[204] M. Parrinello and A. Rahman. Polymorphic transitions in single crystals: A new molecular dynamics method. *Journal of Applied Physics*, 52(12):7182–7190, dec 1981.

[205] M. J. Abraham et al. Gromacs: High performance molecular simulations through multi-level parallelism from laptops to supercomputers. *SoftwareX*, 1-2:19–25, 2015.

[206] J. Glaser et al. Strong scaling of general-purpose molecular dynamics simulations on GPUs. *Computer Physics Communications*, 192:97–107, jul 2015.

[207] P. Stadlbauer et al. Coarse-Grained Simulations Complemented by Atomistic Molecular Dynamics Provide New Insights into Folding and Unfolding of Human Telomeric G-Quadruplexes. *Journal of Chemical Theory and Computation*, 12(12):6077–6097, 2016.

[208] M. Ferraro, M. Masetti, M. Recanatini, A. Cavalli and G. Bottegoni. Mapping cholesterol interaction sites on serotonin transporter through coarse-grained molecular dynamics. *PLoS ONE*, 11(12), 2016.

[209] M. F. Hagan and R. Zandi. Recent advances in coarse-grained modeling of virus assembly. *Current Opinion in Virology*, 18:36–43, jun 2016.

[210] R. M. Betz and R. C. Walker. Paramfit: Automated optimization of force field parameters for molecular dynamics simulations. *Journal of Computational Chemistry*, 36(2):79–87, jan 2015.

[211] J. Blumberger. Recent Advances in the Theory and Molecular Simulation of Biological Electron Transfer Reactions. *Chemical Reviews*, 115(20):11191–11238, oct 2015.

[212] S. Kajimoto, N. Yoshii, J. Hobley, H. Fukumura and S. Okazaki. Electrostatic potential gap at the interface between triethylamine and water phases studied by molecular dynamics simulation. *Chemical Physics Letters*, 448(1-3):70–74, 2007.

[213] J. F. Ouyang and R. P. A. Bettens. Modelling Water: A Lifetime Enigma. *CHIMIA International Journal for Chemistry*, 69(3):104–111, mar 2015.

[214] B. Guillot. A reappraisal of what we have learnt during three decades of computer simulations on water. *Journal of Molecular Liquids*, 101(1-3):219–260, nov 2002.

[215] C. Vega, J. L. Abascal, M. M. Conde and J. L. Aragones. What ice can teach us about water interactions: A critical comparison of the performance of different water models. *Faraday Discussions*, 141:251–276, 2008.

[216] R. Mills. Self-diffusion in normal and heavy water in the range 1-45.deg. *The Journal of Physical Chemistry*, 77(5):685–688, 2005.

[217] J. R. Pliego and J. M. Riveros. Gibbs energy of solvation of organic ions in aqueous and dimethyl sulfoxide solutions. *Physical Chemistry Chemical Physics*, 4(9):1622–1627, 2002.

[218] G. Hura, J. M. Sorenson, R. M. Glaeser and T. Head-Gordon. High-quality X-ray scattering experiment on liquid water at ambient conditions. *Journal of Chemical Physics*, 113(20):9140–9148, nov 2000.

[219] J. N. Nayak, M. I. Aralaguppi and T. M. Aminabhavi. Density, viscosity, refractive index, and speed of sound in the binary mixtures of 1,4-dioxane + ethanediol, + hexane, + tributylamine, or + triethylamine at (298.15, 303.15, and 308.15) K. *Journal of Chemical and Engineering Data*, 48(5):1152–1156, sep 2003.

[220] C. D'Agostino, M. D. Mantle, L. F. Gladden and G. D. Moggridge. Prediction of mutual diffusion coefficients in non-ideal mixtures from pulsed field gradient NMR data: Triethylamine-water near its consolute point. *Chemical Engineering Science*, 74:105–113, may 2012.

[221] L. Michielan, M. Bacilieri, C. Kaseda and S. Moro. Prediction of the aqueous solvation free energy of organic compounds by using autocorrelation of molecular electrostatic potential surface properties combined with response surface analysis. *Bioorganic and Medicinal Chemistry*, 16(10):5733–5742, 2008.

[222] B. González, N. Calvar, E. Gómez and Á. Domínguez. Density, dynamic viscosity, and derived properties of binary mixtures of methanol or ethanol with water, ethyl acetate, and methyl acetate at T = (293.15, 298.15, and 303.15) K. *Journal of Chemical Thermodynamics*, 39(12):1578–1588, dec 2007.

[223] G. D. Hawkins, C. J. Cramer and D. G. Truhlar. Universal Quantum Mechanical Model for Solvation Free Energies Based on Gas-Phase Geometries. *The Journal of Physical Chemistry B*, 102(17):3257–3271, 2002.

[224] W. Jakes et al. Authentication of beef versus horse meat using 60 MHz 1 H NMR spectroscopy. *Food Chemistry*, 175:1–9, may 2015.

[225] L. Klíčová, E. Muchová, P. Šebej, P. Slavíček and P. Klán. Nature of CTAB/Water/Chloroform Reverse Micelles at Above- and Subzero Temperatures Studied by NMR and Molecular Dynamics Simulations. *Langmuir*, 31(30):8284–8293, aug 2015.

[226] S. J. Halstead and J. Li. Molecular dynamics simulations of acid/base induced switching of a bistable rotaxane. *Molecular Physics*, 115(3):297–307, feb 2017.

[227] J. Winkelmann. *Diffusion in Gases, Liquids and Electrolytes*. 2007.

[228] N. G. Tsierkezos, I. E. Molinou and G. A. Polizos. Relative permittivities, speeds of sound, viscosities, and densities of cyclohexanone + cis-decalin and cyclohexanone + trans-decalin mixtures at 283.15, 293.15, and 303.15 K. *Journal of Chemical and Engineering Data*, 47(6):1492–1495, nov 2002.

[229] C. K. Zéberg-Mikkelsen, A. Baylaucq, M. Barrouhou and C. Boned. The effect of stereoisomerism on dynamic viscosity: A study of cis-decalin and trans-decalin versus pressure and temperature. *Physical Chemistry Chemical Physics*, 5(8):1547–1551, 2003.

[230] F. Torrens. Free energy of solvation of solutes and their partition coefficients in methanol-water binary mixtures. *Chromatographia*, 53(S1):S199–S203, jan 2006.

[231] A. Perevedentsev, P. N. Stavrinou, D. D. C. Bradley and P. Smith. SolutionâĂŘCrystallisation and Related Phenomena in 9,9âĂŘdialkylâĂŘfluorene Polymers. I. Crystalline PolymerâĂŘSolvent Compound Formation for Poly(9,9âĂŘdioctylfluorene). pp. 1–21.

[232] A. Perevedentsev, P. N. Stavrinou, D. D. C. Bradley and P. Smith. Solution-Crystallisation and Related Phenomena in 9,9âĂŘdialkylâĂŘfluorene Polymers.

[233] Q. Zhang et al. An easy approach to control β-phase formation in PFO films for optimized emission properties. *Molecules*, 22(2):315, feb 2017.

[234] P. Chen et al. Optimization of opto-electronic property and device efficiency of polyfluorenes by tuning structure and morphology. *Polymer International*, 55(5):473–490, 2006.

[235] C. W. Cone, R. R. Cheng, D. E. Makarov and D. A. Vanden Bout. Molecular weight effect on the formation of β phase poly(9,9-dioctylfluorene) in dilute solutions. *Journal of Physical Chemistry B*, 115(43):12380–12385, 2011.

[236] M. Grell et al. Intrachain ordered polyfluorene. *Synthetic Metals*, 111:579–581, jun 2000.

[237] U. Scherf and E. J. W. List. Semiconducting PolyfluorenesâĂŤTowards Reliable Structure-Property Relationships. *Advanced Materials*, 14(7):477–487, apr 2002.

[238] H. Ahmad, S. K. Kamarudin, L. J. Minggu and M. Kassim. Hydrogen from photo-catalytic water splitting process: A review. *Renewable and Sustainable Energy Reviews*, 43:599–610, 2015.

[239] R. S. Sprick et al. Visible-Light-Driven Hydrogen Evolution Using Planarized Conjugated Polymer Photocatalysts. *Angewandte Chemie - International Edition*, 55(5):1792–1796, 2016.

[240] S. Hillman. *Understanding the role of the dibenzothiophene-sulfone group in linear conjugated polymers for photocatalytic hydrogen evolution from water*. Msc, Imperial College London, 2017.

[241] Y. Pellegrin and F. Odobel. Sacrificial electron donor reagents for solar fuel production. *Comptes Rendus Chimie*, 20(3):283–295, 2016.

[242] E. D. Cline, S. E. Adamson and S. Bernhard. Homogeneous catalytic system for photoinduced hydrogen production utilizing iridium and rhodium complexes. *Inorganic Chemistry*, 47(22):10378–10388, 2008.

[243] P. J. DeLaive, T. K. Foreman, D. G. Whitten and C. Giannotti. Photoinduced Electron Transfer Reactions of Transition-Metal Complexes with Amines. Mechanistic Studies of Alternate Pathways to Back Electron Transfer. *Journal of the American Chemical Society*, 102(17):5627–5631, 1980.

[244] J. A. MejÄśÌĄas and S. Lago. Calculation of the absolute hydration enthalpy and free energy of H+ and OHâĹŠ. *The Journal of Chemical Physics*, 113(17):7306–7316, nov 2000.

[245] J. L. MacCallum and D. P. Tieleman. Computer Simulation of the Distribution of Hexane in a Lipid Bilayer: Spatially Resolved Free Energy, Entropy, and Enthalpy Profiles. *Journal of the American Chemical Society*, 128(1):125–130, jan 2006.

[246] D. J. Woods et al. Side-chain tuning in conjugated polymer photocatalysts for hydrogen production from water. *Manuscript in Preparation*, 2019.

[247] S. A. J. Hillman et al. Mechanistic limitations of linear conjugated polymer photocatalysts for hydrogen evolution from water and the deposition of thin films as a microstructural solution. *Manuscript in Preparation*, 2019.

[248] R. S. Sprick et al. Maximising the hydrogen evolution activity in organic photocatalysts by co-polymerisation. *Journal of Materials Chemistry A*, 6(25):11994–12003, 2018.

[249] R. S. Sprick et al. Nitrogen Containing Linear Poly(phenylene) Derivatives for Photocatalytic Hydrogen Evolution from Water. *Chemistry of Materials*, 30(16):5733–5742, aug 2018.

[250] J. C. M. Garnett. Colours in Metal Glasses and in Metallic Films. *Philosophical Transactions of the Royal Society A: Mathematical, Physical and Engineering Sciences*, 203(359-371):385–420, jan 1904.

[251] J. C. M. Garnett. Colours in Metal Glasses, in Metallic Films, and in Metallic Solutions. II. *Philosophical Transactions of the Royal Society A: Mathematical, Physical and Engineering Sciences*, 205(387-401):237–288, jan 1906.

[252] R. G. Larson. Monte Carlo Simulations of the Phase Behavior of Surfactant Solutions. *Journal de Physique II*, 6(10):1441–1463, oct 1996.